Thermo-Mechanical Fatigue of Compacted Graphite Iron in Diesel Engine Components

Ph.D. Thesis

SEPIDEH GHODRAT

This research was performed in the department of Materials Science and Engineering of Delft University of Technology.

This research was carried out under project number MC2.06270b in the framework of the Research Program of the Materials innovation institute (M2i) in the Netherlands (www.m2i.nl).

Thermo-Mechanical Fatigue of Compacted Graphite Iron in Diesel Engine Components

Proefschrift

ter verkrijging van de graad van doctor
aan de Technische Universiteit Delft,
op gezag van de Rector Magnificus prof. ir. K.C.A.M. Luyben,
voorzitter van het College voor Promoties,
in het openbaar te verdedigen op maandag 10 juni 2013 om 15:00 uur

door

Sepideh GHODRAT

Master of Science in Metallurgy and Materials Engineering,
Iran University of Science and Technology (IUST), Tehran, Iran.
Geboren te Shiraz, Iran

Dit proefschrift is goedgekeurd door de promotoren:
Prof.dr.ir. L.A.I. Kestens
Prof.dr.ir. J. Sietsma

Samenstelling promotiecommissie:

Rector Magnificus,	voorzitter
Prof.dr.ir.L.A.I. Kestens,	Technische Universiteit Delft, Universiteit Gent, Belgium, promotor
Prof.dr.ir. J. Sietsma,	Technische Universiteit Delft, promotor
Dr.ir. M. Janssen,	Technische Universiteit Delft
Prof.dr.ir. T. Pardoen,	Université Catholique de Louvain, Belgium
Prof.dr. I.M. Richardson,	Technische Universiteit Delft
PD Dr. S. Zaefferer,	Max-Planck Institut für Eisenforschung, Germany
Dr.ir. J. Zijp,	Central Laboratory of DAF Trucks N.V., The Netherlands
Prof.dr.ir. H. Terryn,	Technische Universiteit Delft, reservelid

Dr.ir. M. Janssen heeft als begeleider in belangrijke mate aan de totstandkoming van het proefschrift bijgedragen.

Keywords: Thermo-Mechanical Fatigue, Compacted Graphite Iron, Volume Expansion, Oxidation, Pearlite Decomposition, Paris' Crack Growth Law, Holding Time, Orientation Contrast Microscopy, 3D Microscopy Analysis.

ISBN 978-90-77172-92-6

Sepideh.Ghodrat@gmail.com

Printed by: Proefschriftmaken.nl || Uitgeverij BOXPress

To Nasrin Sotoudeh,
and all women of my country who struggle for Human Rights…

Table of contents

1
Introduction

"The process of scientific discovery is, in effect, a continual flight from wonder".

Albert Einstein

1.1 Synopsis

In diesel engines of trucks, the repetition of the start-up and shut-down of engines causes severe mechanical loading in some parts of the engine, such as cylinder blocks and heads and this may lead to localized cracking due to stresses that develop as a result of thermal gradients and thermal mismatch. This phenomenon is known as Thermo-Mechanical Fatigue (TMF). TMF is believed to be the dominating process responsible for cracks developing in engine components [1].

In order to understand TMF cracking and the involved mechanisms, it is important to characterize the microstructure evolution and TMF behavior under realistic thermal and mechanical loads. Hence, with the purpose of studying the underlying microstructural mechanisms of TMF, the current project was defined, inspired by the localized cracking of cylinder heads due to the start-up/shut-down cycles of diesel truck engines.

In the cylinder head, temperatures run up to 420 °C when a (cold) engine is operated at full power (directly after starting) and after stopping the engine the temperature drops down to room temperature again. Severe temperature changes may induce yield in surface layers, which in turn can result in the initiation of cracks in a number of cycles less than 5 x10^4 [2]. In the cylinder head, TMF failure especially occurs at the valve bridges in cylinder heads, the areas between intakes and outlets (*cf.* Figure 1.1) as they are severely subjected to out-of-phase (OP) loading, *i.e.* maximum strain occurring at minimum temperature [3].

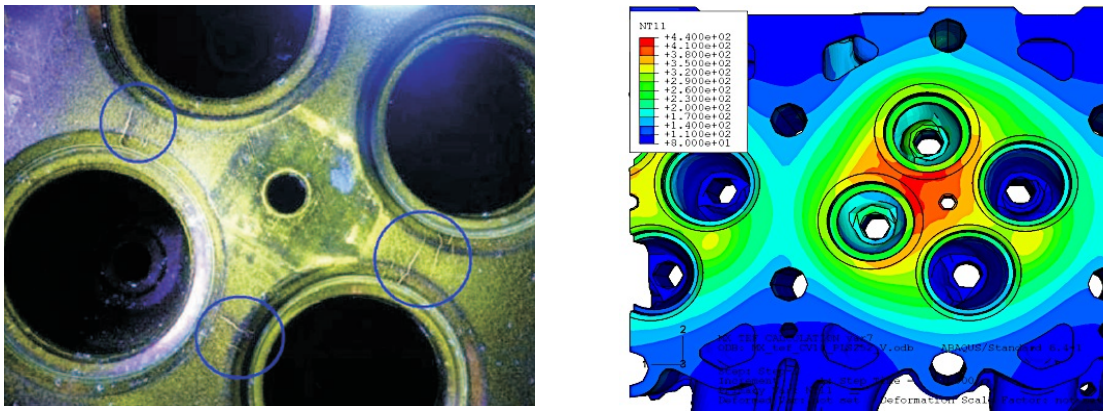

(a) (b)

Figure 1.1 Valve bridges in cylinder heads are the critical locations under TMF conditions (a) a cylinder head containing macroscopic cracks, (b) Temperature distribution under full load condition/comparison *(courtesy of DAF N.V. Trucks).*

Increase of fuel efficiency and good performance of cylinder heads at high temperatures are essential. The performance of any component is inherently related to the material properties and thus to its microstructure. Any variation in the microstructural aspects will lead to a variation of mechanical properties such as strength and fatigue toughness, but may also affect important physical properties such as thermal conductivity.

The most common material used in cylinder heads is pearlitic compacted graphite cast iron (CGI), which consists of two main components: coral-like graphite particles embedded in a pearlitic steel matrix (*cf.* Figure 1.2). This composite material provides a suitable combination of thermal and mechanical properties to achieve the desired performance of cast iron cylinder heads. The graphite provides favorable thermal properties (thermal conductivity), whereas pearlite is responsible for appropriate mechanical properties (strength and fatigue resistance). However, microstructure instability and evolution during operation may deteriorate the thermal and mechanical properties of CGI and accordingly the TMF properties. For instance, debonding of the graphite/matrix interface, internal oxidation or decomposition of pearlite to ferrite and graphite are examples of microstructural evolutions that may have a severe impact on the properties.

According to Löhe *et al.* [4], multiple mechanisms may take place during a thermo-mechanical cycle: plastic deformation, creep, oxidation, pearlite decomposition, coarsening of the microstructure, crack initiation and propagation. It is recognized that most of the micro-scale damage mechanisms are temperature and time dependent, which is relevant to TMF, since this takes place during prolonged periods of time at various temperatures.

With regard to oxidation in cast iron, it was found that during exposure to air at elevated temperature graphite at the surface starts to oxidize immediately and a rapid carbon loss takes place. Gradually oxygen penetrates into the structure along the graphite particles, leading to the oxidation of carbon (graphite) with the formation of gaseous reaction products (CO and CO_2) and eventually leaving empty cavities behind [5]. Buni *et al.* [6] describe that oxidation of the graphite phase weakens the bond between the matrix and the graphite, resulting in the creation of holes.

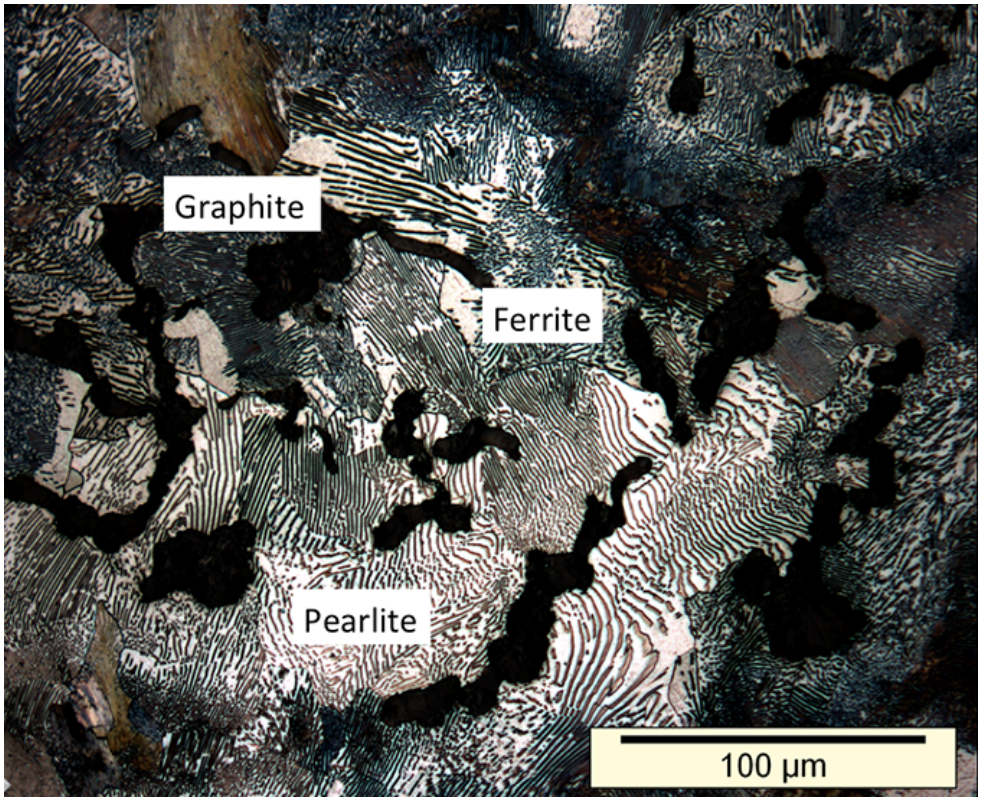

Figure 1.2 Microstructure of the pearlitic CGI under investigation.

The present research was carried out in a collaborative project between Delft University of Technology (TUDelft), on experimental research, Eindhoven University of Technology (TU/e), on modeling research, and supported by the industrial partner N.V. DAF Trucks (Eindhoven). In order to better design engine parts with CGI it is essential to be able to predict the TMF performance. To this purpose physical models are being built, which simulate the phenomena that operate in the material during combined mechanical and thermal loading. A profound understanding of the relation between structure and properties and microstructure evolution not only enables to predict the mechanical performance, it also provides the opportunity to optimize the microstructure of CGI and hence improve its performance.

The temperature cycle represents the situation during the many start-stop cycles during the operational life of the engine. In this way, the TMF test results are designed to represent potential TMF processes in real engines. In order to simulate real life conditions, in this research a series of TMF tests were performed between 50 °C and 420 °C under total constraint conditions with different holding times. This TMF test procedure is intended to mimic the thermal and mechanical conditions acting in cylinder heads. In order to reduce testing time and also to improve reproducibility, specimens were provided with a sharp circumferential notch.
Lifetimes in notched CGI specimens can be predicted by the Paris' fatigue crack growth model. This forms the basis to predict the lifetime of notched and smooth specimens with internal microstructural inhomogeneities, such as the graphite particles. Subsequently, the validity of the Paris law was meticulously tested by microscopic observation of crack length values, during the progress of a TMF test.
Moreover, microstructural characterization techniques, before and after exposure to elevated temperatures in static and cycling conditions were employed to provide insight into the microstructure evolution of CGI, with its complex morphology, under TMF conditions. The applied techniques for characterizing the microstructure were Energy and wave-length dispersive X-Ray Analysis (WDX), Electron Probe Micro Analysis (EPMA), X-ray 3D-computed tomography scans (CT). Furthermore, microstructural changes during deformation were evaluated by analyzing quantitative data obtained by orientation contrast microscopy based on the Electron Back Scattering Diffraction (EBSD) technique in 2D and 3D. Statistical processing of the crystallographic data was applied on a very wide scale of material on the order of millimeters.
It was our aim at TUDelft to combine the results of controlled TMF tests with the underlying microstructural changes and damage phenomena within the structure of the CGI. It is our conviction that our detailed microstructural observations and failure analyses, *i.e.* our interpretation of material knowledge and test results, contribute to the development of a microstructure-based material model that can be employed for thermo-mechanical fatigue simulations of cast iron cylinder heads.

1.2 Research Objectives

The main aim of the research project in which the present PhD thesis was embedded is formulated as follows:

To identify and understand the damage micro-mechanisms that control thermo-mechanical fatigue phenomena (TMF) in compacted graphite cast iron (CGI) to predict the lifetime and increase the reliability of diesel truck cylinder heads.

This aim translates into the following specific objectives of this research, which are seen as an approach to address the overall aim:

- To characterize the microstructure of the graphite morphology in 2D and 3D in order to obtain a comprehensive insight in the complex morphology of CGI.

- To investigate the effect of elevated temperatures and/or thermal cycling with and without the presence of an oxidizing atmosphere on the evolution of microstructure of CGI and more precisely the effect of oxygen on the graphite/metal interaction and its associated effect on volume.

- To explore the effect of the initial state of CGI (as-cast, annealed in open atmosphere (oxidized) and annealed in vacuum) on the room temperature tensile properties and fatigue lifetime.

- To characterize TMF lifetimes of specimens simulating the cyclic loads to which valve bridge area cylinder heads of real diesel engines are subjected.

- To evaluate the separate roles of crack initiation and crack growth in TMF and to determine the role of crack initiation and growth in the TMF lifetime of CGI.

- To develop a model to predict the TMF lifetime of CGI, which exhibits a satisfactory agreement with the measured lifetime, in order to understand the relation between microstructure and TMF lifetimes.

- To evaluate the effect of holding time at elevated temperature on TMF behavior of CGI.

- To reveal the subtle microstructural changes induced by microplastic strain and stress relaxation in CGI by analyzing quantitative data sets obtained by orientation contrast microscopy based on the EBSD technique.

- To meticulously characterize TMF crack paths, in relation to microstructural features and to find out how and by which mechanisms the cracks predominantly develop. To this purpose, 2D and 3D microscopy analyses were carried out.

1.3 Outline of Research

Addressing the objectives mentioned above, this thesis is structured as follows:

Chapter 2 "Background" describes what is known in the literature about TMF (mechanisms, parameters) with regard to realistic thermal and mechanical loads that are of relevance in cylinder heads of diesel engines. A detailed account will be presented on compacted graphite iron and its complex microstructure in relationship with TMF. A review is given on the test parameters of relevance and the predominant failure mechanisms that control TMF in CGI such as holding time, environmental factors and specific microstructural features such as the graphite morphology.

Chapter 3 "Experimental Set-up" gives details on the investigated material (CGI), the origin of the material, specimens fabrication and preparation, the hardware set-up of the thermo-mechanical fatigue experiments and the employment of dedicated software to configure and design the TMF procedures used to investigate TMF properties of CGI.
With regard to microstructural characterization, and more specifically to the purpose of revealing subtle microstructural changes in the material under investigation, several techniques were employed in this study. These techniques include X-ray 3D-computed tomography, scanning electron microscopy with energy and wave-length dispersive X-ray analysis (SEM-WDX) and the powerful technique of orientation-contrast microscopy, *i.e.* Electron Back Scattering Diffraction (EBSD). The essentials of these techniques are briefly reviewed in this chapter.

Chapter 4 "Characterization of Microstructure and Mechanical Properties of CGI at Ambient and Elevated Temperatures" presents the characterization of the microstructure of the graphite morphology in three dimensions (3D) in order to obtain a better insight in the complex morphology of CGI.
To investigate the effect of elevated temperatures and/or thermal cycling on the evolution of microstructure of CGI during thermo-mechanical fatigue and the microstructural origin of oxidation and its effect on the extent of volume change, annealing experiments were performed with and without the presence of an oxidizing atmosphere. The microstructural evolution was observed by scanning electron microscopy and electron probe microanalysis to investigate the formation of oxide layers around the graphite particles.
Moreover, in order to explore the effect of the initial state of CGI on the room temperature tensile properties and fatigue lifetime, three different initial conditions were considered: as-cast, annealed in open atmosphere (oxidized) and annealed in vacuum.

Chapter 5 "Measurement and Characterization of Thermo-Mechanical Fatigue in Compacted Graphite Iron" reports on lifetime assessment of CGI material measured and analyzed during TMF. We performed a test series with smooth and circumferentially sharp notched specimens, with depths ranging from 0.1 to 0.65 mm. TMF lifetimes were also simulated numerically by using the Paris crack growth equation. For three values of stress intensity range ΔK, the crack growth rate (da/dn) was accurately measured applying a new crack length measurement procedure. In addition, we evaluated to what extent the accumulation of cyclic plasticity of bulk material has an influence on the TMF crack growth in CGI.

Chapter 6 "Effect of Holding Time on Thermo-Mechanical Fatigue Properties of Compacted Graphite Iron through Tests with Notched Specimens" gives details on the effect of holding time at elevated temperature on the microstructural evolution and the TMF properties of notched specimens. The Paris model is used to differentiate between the individual effects of stress level and material related features on the TMF lifetime.
At some specific reference points of the TMF heating stage, the microstructures were characterized in detail by orientation contrast microscopy based on the EBSD technique. The images thus obtained could be processed numerically to the purpose of obtaining quantitative information of local strain distributions.

Chapter 7 "Microstructural Characterization of Compacted Graphite Iron with Orientation Contrast Microscopy" presents an analysis of the crack path evolution induced in CGI during thermo-mechanical fatigue conditions. Orientation contrast microscopy was employed to provide a detailed insight in the complex TMF crack morphology of CGI. To meticulously characterize TMF crack paths, in relation to microstructural features in more detail and to determine and characterize the mechanisms that the cracks predominantly develop, 2D and 3D microscopy analysis were employed.

The **"General Conclusions and Recommendations for Future Work"** are presented in **Chapter 8**.

1.4 References

[1] Hallstein R., Lang K.H, Löhe D., Macherauch E. Thermal-mechanical fatigue behaviour of vermicular cast iron, Proceedings of the 8th International Conference on Mechanical Behaviour of Materials (ICM8), Ellyin F., Provan J.W. (Editors), 1 (Victoria, Canada), May 16-21, 1999; 301-306.
[2] Remy L. Fatigue and thermomechanical fatigue at high temperature, Encyclopedia of Materials: Science and Technology, 2001; 2866-2877.
[3] Trampert S., Gocmez T., Pischinger S. Thermomechanical fatigue life prediction of cylinder heads in combustion engines, J. Eng. Gas Turbines Power, 2008; 130: 012806-1 (10 pages).

[4] Löhe D. Important aspects of cyclic deformation, damage and lifetime behaviour in thermo-mechanical fatigue of engineering alloys. In P. S. Portella (Ed.), Fifth International Conference on Low Cycle Fatigue, Berlin, Germany, 2004; 161-175.
[5] Merchant H.D. Oxidation kinetics of iron-carbon base alloys, Oxid. Met., Vol.2, No. 2, 1970; 145-153.
[6] Buni S.Y., Raman N., Seshan S., The role of graphite morphology and matrix structure on the low frequency thermal cycling of cast irons, Sadhana, 29(1), 2004; 117-127.

2

Background

"With the enormous CGI potential for manufacturing diesel engine components, especially cylinder heads and blocks, the real iron age is only just beginning".

Steve Dawson

In this chapter, a detailed account is presented on "Cast Iron" in general and a specific graphitic type of cast iron, compacted graphite iron (CGI), which is the material under investigation in this research. This chapter also presents a brief literature survey on the Thermo-Mechanical Fatigue (TMF) principle and material behavior when subjected to thermal and mechanical loads that are of relevance in cylinder heads of diesel engines.

2.1 Introduction to Cast Iron

Cast Iron: History

The origin of cast iron dates back to about 600 B.C., when in China iron castings were used for cooking utensils, ploughshares, and statuary. In the 15th century A.D. cast iron was introduced to Europe but its mass production was not until the 18th century [1]. In 1709, in Coalbrookdale, England, Abraham Darby developed a method for producing pig iron in a blast furnace fuelled by coke. Later on, the first large steel and cast iron constructions have appeared. The production for larger volumes was made possible by the use of coke rather than charcoal. In 1779 one of the earliest large cast iron constructions was built, *i.e.* the world famous Iron Bridge, which spans the Severn River in England. Ever since, cast iron has continued to be one of the most widely used and versatile of engineering materials. Prior to World War II the usage of cast irons was limited due to its relatively brittle nature. However, with the emergence of ductile iron in 1948, new market areas were opened for iron castings. Today, ductile cast iron with a wide range of properties obtained by several heat treatments is replacing steel for such components as gearboxes, gears, cylinders, crankshafts, valve bodies, and pump connections.

Optimum fluidity, low shrinkage, easy castability into complex shapes, good machinability, excellent damping capacity (4 to 20 times better than steel), resistance to deformation, wear resistance, and low cost are a number of arguments favoring the

widespread use of cast iron as the material of choice for a wide variety of industrial applications [1-4].

Cast iron, in the form of gray and ductile iron, represents the largest tonnage of cast-to-shape products produced worldwide*, i.e.* 57.5 million tons which is 71% of the total cast metal production according to a report of *Modern Casting Census of World Casting Production in 2010* (*cf.* Figure 2.1) [3]. Since 1999, gray iron production has increased 9.3%, ductile iron production has increased 39.6%, steel production has had 50% growth, and nonferrous production 41.1%.

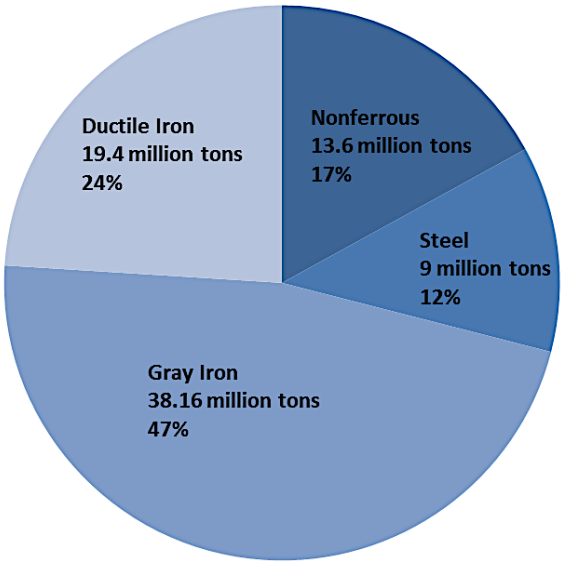

Figure 2.1 The global cast production pie chart of gray iron, ductile iron, steel and nonferrous metals [3].

Figure 2.2 shows that China is by far the biggest production of cast iron compared to the rest of the industrial regions.

Figure 2.2 Main producers of gray and ductile irons in 2010 [3].

Cast Iron: Definition

The term cast iron identifies a wide range of ferrous alloys, which contain as major alloying elements carbon and silicon (ranging from 2.1 to 4.0 wt.% and 1 to 3 wt.%, respectively). Additionally to the main alloying elements C and Si, other elements may be added: Ba, Bi, B, Ca in minor contents (<0.01 wt.%) and Al, Sb, As, Ce, Co, Cr, Cu in contents exceeding 0.01%. [1]. Compared to steel, cast iron has a much higher carbon and silicon content, which leads to the presence of the carbon-rich graphite phase in the microstructure of cast iron, which is generally absent in steel.
Referring only to the binary Fe-Fe_3C or Fe-Gr system (where Gr stands for graphite) cast iron can be defined as an iron-carbon alloy with more than 2 wt.% C. It is important to note that silicon and other alloying elements may considerably change the maximum solubility of carbon in austenite (γ). Therefore, in exceptional cases, alloys with less than 2 wt.% C can solidify with a eutectic structure and therefore still belong to the family of cast iron.
As shown in the binary iron-carbon diagram, *cf.* Figure 2.3, part of the solidification of cast irons takes place at the eutectic point. Since the compositions of most cast irons are around the eutectic point of the iron-carbon system, the melting temperatures are closely correlated to the eutectic temperature, usually ranging from 1,150 to 1,200 °C, which is about 300 °C lower than the melting point of pure iron. This contributes to the well-appreciated fluidity and castability of cast iron.

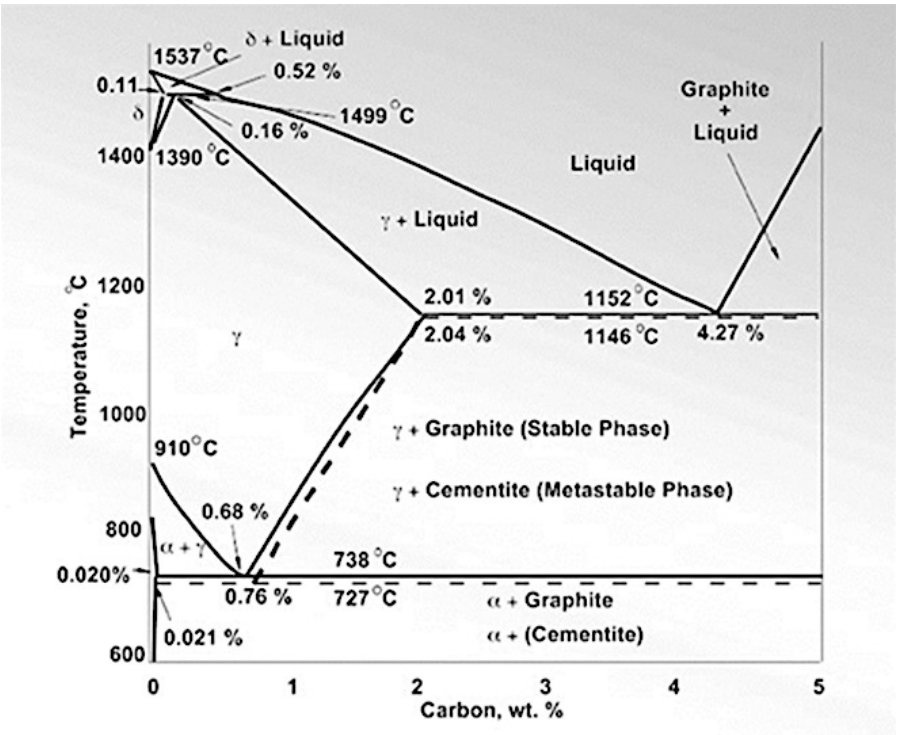

Figure 2.3 Iron-Carbon diagram with steel and cast iron areas [1].

Depending on the nucleation potential of the liquid, the chemical composition and the cooling rate, cast iron can solidify according to the thermodynamically metastable Fe-Fe_3C or the stable Fe-Gr phase diagram. The first two factors determine the graphitization potential of the iron, which promotes the formation of graphite instead of iron carbide [1-2, 5]. In the Fe-C diagram of Figure 2.3, both the metastable Fe-Fe_3C and the stable Fe-Gr systems are represented. If the solidification occurs according to the metastable Fe-Fe_3C diagram, the white eutectic consisting of austenite (γ) and cementite (Fe_3C) forms, whereas the gray eutectic austenite (γ)—graphite (Gr) is formed when solidification follows the stable diagram. These two types of eutectics, γ-Gr and γ-Fe_3C, display wide differences in properties such as strength, hardness, toughness, ductility or thermal conductivity.
Without silicon, the eutectic in a binary Fe-C alloy is at 4.3 wt.% carbon. Addition of silicon to the binary Fe-C alloy decreases the stability of Fe_3C, and increases the stability of ferrite as the α field is enlarged, and the γ field is constricted. With increasing silicon content in the ternary Fe-C-Si system, the carbon contents of the eutectic and eutectoid alloys decrease, while the eutectic and eutectoid temperatures increase [1]. The diagram of Maurer in Figure 2.4 shows the dependency of the microstructural constituents on the C and Si content for a conventional cooling rate and to what extent certain microstructures are stable [6]. It must be noted that either a high carbon and low silicon or low carbon and high silicon content give gray iron [5].

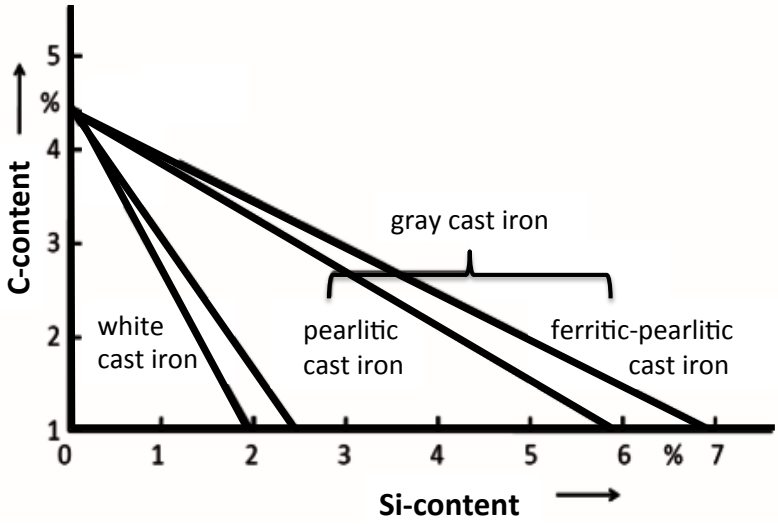

Figure 2.4 Diagram indicating the structures of cast iron resulting from variation of silicon and carbon contents in normal cooling [6].

Another element that may change the Fe-C diagram is phosphorous. When appreciable amounts of phosphorous are present in the alloy, the phosphorous content of the iron also will play a role on the transformation behavior. It is convenient to combine the effect of the silicon, carbon and phosphorous into a single factor, called Carbon Equivalent (CE) and expressed as a simple equation, *cf.* equation (2.1) [1]:

$$x^{e}_{c=} x_c \ + \frac{1}{3}(x_{si} + x_p \ ) \quad (2.1)$$

with x_M, the weight percept of element M.

The carbon equivalent is employed to determine how close a given composition of iron is to that of the eutectic composition (CE 4.3%), *e.g.* a CE of 3.9% represents an alloy corresponding to a hypo-eutectic composition, *i.e.* with the austenite (γ) phase solidifying first, whereas a CE of 4.6% represents an alloy corresponding to a hypereutectic composition, *i.e.* with the graphite or cementite to solidify first.

Solidification of the Hypoeutectic and Hypereutectic Gray Alloys

Depending on the chemical composition solidification of cast irons will occur in two different modes, either hypoeutectic (CE < 4.3%) or hypereutectic (CE > 4.3%). In the solidification of a hypoeutectic iron (shown in Figure 2.5), the primary solidified phase is austenite. At the austenite liquidus temperature, T_L, the proeutectic austenite dendrites grow into the liquid, which is enriched in carbon until the eutectic temperature, T_G, is reached. Cooling below T_G results in the equilibrium eutectic reaction L-->γ+Gr, producing a microstructure consisting of austenite dendrites surrounded by a eutectic mixture of of γ and Gr. By further cooling below T_G, the carbon content of austenite decreases as the C diffuses to the graphite phase contained in the eutectic. When the upper critical temperature is reached the austenite starts to transform to stable ferrite and graphite [2]. Ferrite will nucleate on the graphite/austenite interface, depositing carbon from austenite on the existing graphite particles as the carbon cannot be dissolved in the BCC ferrite (*cf.* Figure 2.6). In a slowly cooling casting, ferrite nuclei can continue to grow into the austenite. The final structure is composed by ferrite and graphite as predicted by the stable phase diagram. However, if the casting is cooled more rapidly, or in the presence of certain alloying elements, the austenite may transform to pearlite, which is a eutectoid mixture of ferrite and cementite (Fe_3C). In some cases, a shift may occur from stable to metastable transformations as the temperature decreases. *E.g.* the austenite may first transform to stable ferrite and graphite below the upper critical temperature (T_{UC}), whereas below the lower critical temperature (T_{LC}) austenite transforms to the eutectoid mixture of ferrite and cementite, known as pearlite, *cf.* Figure 2.5b.
On solidifying a hypereutectic cast iron, the primary phase that forms consists of graphite nodules, which may nucleate at temperatures below the graphite liquidus temperature. These primary nodules grow freely in the melt, while depleting carbon from the melt, and may reach a considerable size before the eutectic temperature is reached. At the eutectic temperature, the eutectic shell, composed of a mixture of austenite and graphite, starts to envelope the nodules. As the shell grows, graphite nucleation slows down. Eventually, as the undercooling increases a new population of eutectic nodules is formed. Upon further cooling, the solid state transformations continue in a similar manner as described before for the hypoeutectic alloy, *i.e.* with the austenite contained in the eutectic cells transforming to ferrite and Gr or pearlite. [2].

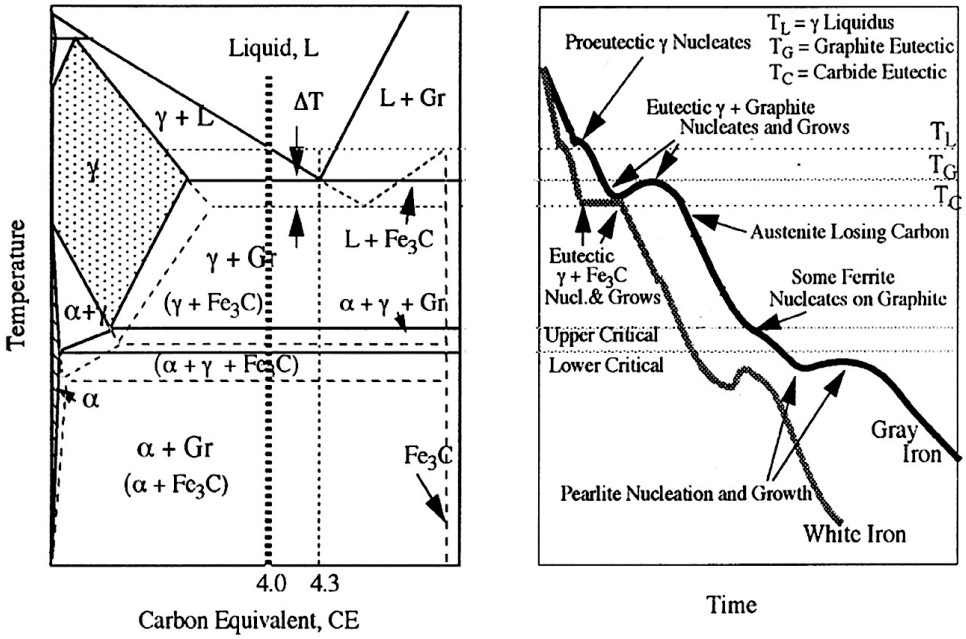

(a) (b)

Figure 2.5 (a) Schematic drawing showing the solidification of a hypoeutectic alloy, solid lines: stable (Gr), dashed lines: metastable (Fe_3C) (b) Cooling curves for a hypoeutectic alloy of CE=4.0 [*2*].

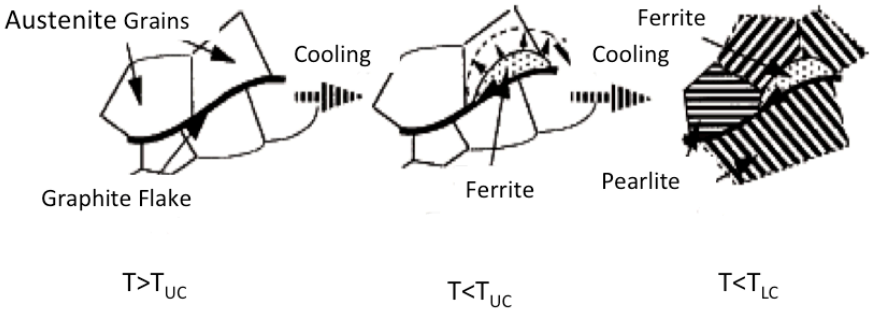

Figure 2.6 Nucleation and growth of ferrite below the upper critical temperature, T_{UC} and pearlite below the lower critical temperature, T_{LC} [2].

Structure of Graphite

In order to identify cast iron properties, the structure of the graphite phase must be well understood. The crystal structure of graphite consists of planes of hexagonal rings, called basal planes, which consist of arranged atoms stacked parallel to each other perpendicular to the *c* axis as shown schematically in Figure 2.7 [7]. In its outer shell each C atom possesses four valence atoms. Three of the four valence electrons are tied up in strong covalent bonds in the basal planes and the remaining electron establishes a bond with the adjacent basal planes with a weak Van der Waals force. The electrons

involved in the covalent bonds provide electrical and thermal conductivity of graphite in the basal planes. Since the bonding between the basal planes is weak, the layered structure of graphite allows sliding movement of the parallel basal plates. This feature explains a number of characteristic graphite properties such as its limited strength, self-lubrication and low shear strength.

The crystal growth mechanism of graphite evolves out of its anisotropic crystal structure; the crystal plane normal to the *c* <0 0 0 1> axis grows laterally in the <1 0$\bar{1}$ 0> directions. Certain elements, *e.g.* aluminum, antimony, arsenic, bismuth, magnesium, calcium and cerium, can inhibit growth in the preferred growth directions. This growth inhibition may lead to the formation of spheroidal or compacted morphologies (see section 2.2) [1, 7].

As a consequence of the different bonds in the *a* and *c* directions of the graphite crystal, it can be said that graphite exhibits a pronounced crystal anisotropy as the material behaves differently in a and c-directions. This anisotropic nature of the graphite crystal structures is reflected in its mechanical and physical properties. For example, it gives rise to a strong elastic anisotropy in the *c*- and *a*-directions. The elastic modulus in the basal planes (*i.e.* along the *a*-axis) and perpendicular to them (*i.e.* along the *c*-axis) are 686 and 27 GPa respectively [33]. The thermal conductivity along the *a*-axis varies between 293 and 419 W/m-K between 0-100 °C while along the *c*- axis it is 85 W/m-K (0-100 °C) as reported by Shao *et al.* [8].

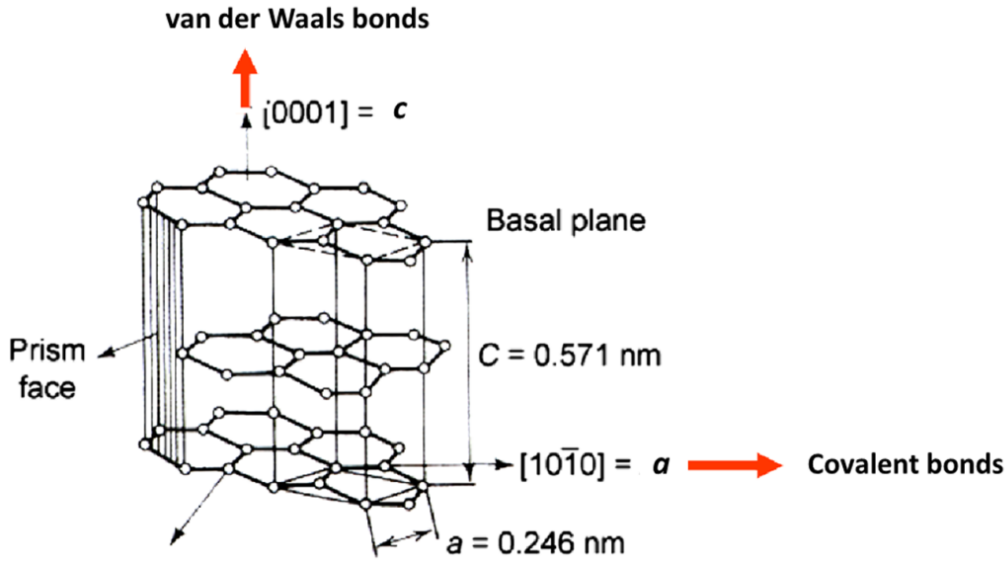

Figure 2.7 Crystalline structure of graphite in hexagonal shape showing the unit cell (heavy line) with *a* and *c*, possible growth directions [1].

2.2 Classification of Cast Irons

Historically, the first classification of cast iron was based on the visual aspect of its fracture surface. Two types of iron were primarily known:

White iron: Exhibits a white, crystalline fracture surface because fracture occurs along the iron carbide plates (Fe_3C).
Gray iron: Exhibits a gray fracture surface because fracture occurs along the graphite plates (Gr).

A schematic of the common types of commercial cast irons based on the graphitization potential, as well as the final processing stage in obtaining common cast iron is summarized in Figure 2.8.

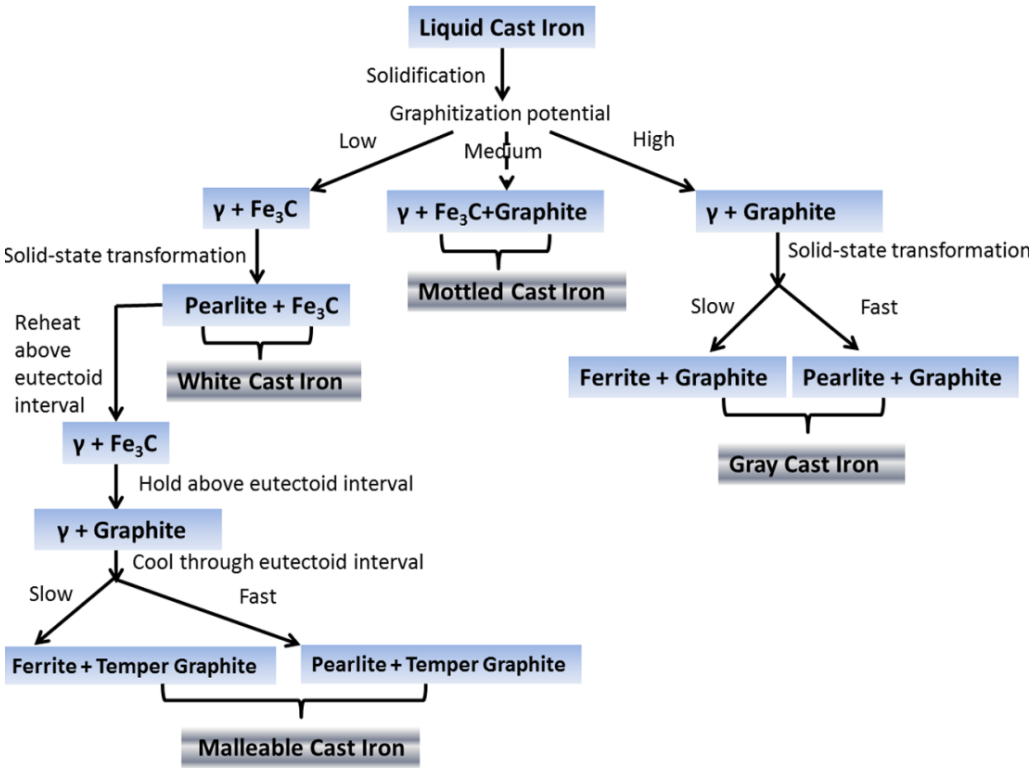

Figure 2.8 Basic microstructures and processing for obtaining common commercial cast irons [1].

With regard to the microstructural features, other classifications are possible, since cast iron is a composite material comprised of graphite or Fe_3C particles in an iron matrix. For instance, cast irons can be classified based on the morphology of the graphite and/or the metal matrix. This metal matrix may consist of ferrite, pearlite, austenite, martensite, bainite or a combination of these phases. The graphite morphology depends

on the dominant growth direction, which may control the final graphite morphology of a cast iron. There are different graphite growth directions during solidification as illustrated in Figure 2.9. It can be seen that the preferential graphite growth may occur either along the *a*- or the *c*- crystal direction or along both directions concurrently.
As a consequence, a variety of graphite morphologies solidify as part of the austenite-graphite eutectic, depending on the chemical composition, the ratio of the temperature gradient to growth rate and the cooling rate. The graphite morphologies have a crucial effect on the thermo-mechanical properties of cast irons, *i.e.* these properties depend strongly on the shape and the interconnection of the graphite particles. Nodular shapes improve mechanical properties, whereas elongated shapes weaken mechanical properties due to stress concentration points. As cast irons are classified according to the morphologies of graphite particles, in this respect three main graphitic cast irons are classified as follows (*cf.* Figure 2.10) [9]:

- Flake or lamellar Graphite Iron (FGI),
- Compacted or vermicular Graphite Iron (CGI),
- Spheroidal or nodular Graphite Iron (SGI).

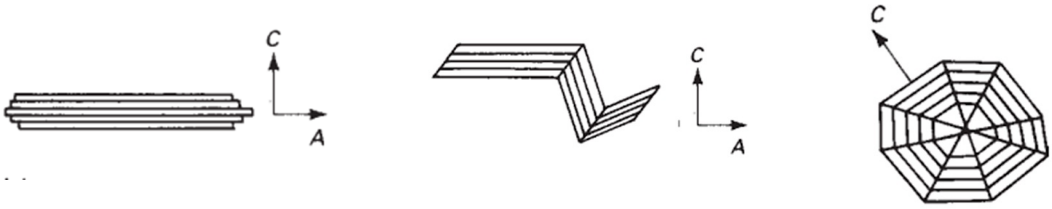

(a) (b) (c)

Figure 2.9 A schematic illustration of graphite types found in cast irons. a) Flake/lamellar graphite, b) Compacted/vermicular graphite, c) Spheroidal/nodular graphite [1].

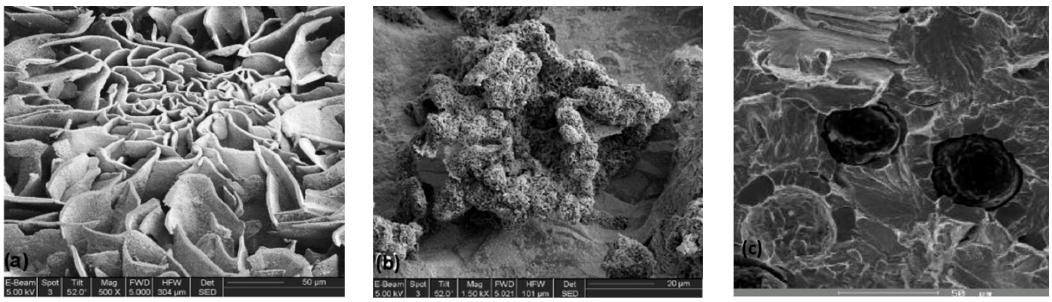

Figure 2.10 Three main graphite morphologies observed in deep etched graphitic cast irons: a) Flake or lamellar graphite (FG), b) Compacted or vermicular graphite (CG), c) Spheroidal/nodular graphite (SG) [9].

Flake (Lamellar) Graphite Iron (FGI)

The predominant graphite growth direction in FGI is the *a*-direction. Thus, the basal planes are oriented parallel to the graphite flakes [1]. Based on chemical composition and cooling conditions, there are five patterns for flake graphite designated by the letters A through E according to the ASTM A 247 standard [10].
From a mechanical point of view, the principal drawback of FGI is its toughness associated with the morphology of the graphite flakes, which promote the initiation and propagation of microcracks. In fact, by applying an external tensile stress, the sharp edges of the graphite flakes (*cf.* Figure 2.10) may act as stress raisers. Strength and ductility are much higher, however, under compressive loads. As a result of its heterogeneous microstructure, FGI exhibits a non-linear elastic behavior because of the formation of multiple micro-cracks at the flake tips, even at low tensile stresses causing the graphite to delaminate from the metal matrix [1, 4, 7]. In section 2.3 the mechanical properties of FGI are compared with other graphitic cast irons.
There are various means of modifying the graphite morphology to improve mechanical properties, including toughness. For example, by the use of appropriate liquid inoculants it is possible to produce fine flakes instead of coarse flakes.
A variety of FGIs are used in highly competitive, low-cost applications where founding properties are of importance. A wide range of applications may be considered such as elevator counterweights, fences and frames, enclosures for electrical equipment, and fire hydrants, automotive castings and process furnace parts.

Spheroidal (Nodular) Graphite Iron (SGI)

Ductile spheroidal graphite (SG) cast iron was discovered in the 1950s. It is somewhat of a coincidence that flake graphite iron is the one that was developed first. This is due to the use of coke for iron melting. Since coke is rich in sulphur it contributes to the directional solidification of carbon, which is required for the formation of graphite flakes. If high purity ores had been used then ductile iron with spherical graphite nodules would have been the most common type of cast iron. Actually this is precisely what happened in China where spheroidal graphite irons were produced over 2000 years ago [7]. The morphology of graphite in SGI is illustrated in Figure 2.10. The graphite morphology in the form of roughly spherical nodules is obtained by means of an appropriate liquid metal treatment. Because their ductility is significantly improved (tensile elongation is 17 % higher than of FGI), an alternative designation is *ductile* cast irons [7].
The carbon equivalent of SGI is higher and its sulphur content much lower than in FGI. The silicon content can range from 1.8 to as high as 6 wt.% when good oxidation resistance is required. However, high silicon and carbon contents promote flotation of the graphite nodules, while low carbon enhances solidification shrinkage and low silicon leads to carbide formation instead of graphite.
SGIs are produced directly by the solidification of a melt containing sufficient silicon to ensure graphite formation, after careful removal of sulphur and oxygen by inoculants (magnesium, calcium, yttrium or some other rare earth elements) [1-7]. These elements

provide the necessary conditions for the precipitation of the carbon atoms on the {0001} planes of the graphite crystals. For instance, by adding magnesium to the melt it can drastically change the graphite growth morphology. The simple way to explain the mechanism of the spheroidising effect by magnesium is that oxygen and sulphur are adsorbed preferentially on the hexagonal planes of graphite, {0001}, inhibiting growth parallel to the *C* axis, leading to a lamellar morphology. By adding Mg, it reacts with oxygen and sulphur and forms MgO and MgS, which can float to the melt surface and can be skimmed off. The removal of sulphur and oxygen by magnesium allows for a more isotropic growth. However, since magnesium has low solubility in the metal and is volatile, the reactions can become reversed if Mg-losses are too great. Therefore, to avoid this, silicon in the form of ferro-silicon is generally added to provide additional deoxidation [7]. Cerium is another element that forms highly stable oxides and sulphides and is less volatile than magnesium, with which it is often used in combination. It is clear that a careful choice of alloying additions is used to appropriately adjust the deoxidation, graphitising and nucleation effects.
SGI is used for many structural applications, particularly those requiring strength and toughness combined with good machinability and low cost. The cast iron pipe industry is the largest user of SGI representing nearly 44% of total SGI production.

Compacted (Vermicular) Graphite Iron (CGI)

Efforts to develop CGI production techniques and product applications began in the early 1960's. Since then, many CGI applications have been successfully established in series production [12, 13]. According to the AFS Metalcasting Forecast and Trends, 66,000 tonnes of these CGI products were produced in the USA in 2001 [13].
The graphite particles in CGI are elongated and randomly oriented as in flake graphite iron, however they are shorter and thicker, and have rounded edges, *i.e.* CGI represents an intermediate structure between FGI and SGI in the metal matrix. As the compacted graphite particles appear worm-shaped viewed in two dimensions, this type of cast iron is also called vermicular cast iron. Deep-etched scanning electron micrographs (*cf.* Figure 2.10) show that the individual worm-shaped particles are connected to their nearest neighbours within the eutectic cell. The complex coral-like graphite morphology, together with the rounded edges and irregular bumpy surfaces of the graphite particles, results in strong adhesion between the graphite and the iron matrix.
In general, CGI is produced in a similar way as SGI, but with a lower concentration of magnesium (0.01 to 0.02 wt.% Mg) in the molten cast iron [2]. In general, the chemistry of CGI is more complex than for the other cast iron types; compositions of inoculant elements (magnesium, cerium), spheroidizing elements (magnesium, calcium, and/or rare earth metals) and antispheroidizing (titanium and/or aluminum) elements must be controlled in order to produce a microstructure that contains the worm-shaped vermicular particles [1]. CGI invariably includes some nodular (spheroidal) graphite particles. For proper castability and machinability performance, the fraction of nodular graphite particles or the degree of graphite nodularity is also limited to a range of 0 to 20% nodularity [12]. According to the *SinterCast* nodularity rating chart [14], nodularity is defined as the ratio of the area fraction exceeding a critical curvature (for which the

graphite particles are considered as nodular shaped) to the total area fraction of graphite. It should be noticed that for optimum machinability, the Ti-content should not exceed 0.015 wt.% [15]. Titanium results in the formation of titanium carbide and carbonitride inclusions, which are harder than many tool materials, significantly increasing the abrasive wear resistance. Titanium also inhibits the formation of pearlite in the matrix. Simultaneously, apart from avoiding too much nodularity, the formation of flake graphite is prohibited to prevent local weakness [12, 15].
The most widely used procedure to cast CGI is the *SinterCast* method. In the *Sintercast* method the magnesium content is controlled based on in-situ thermal analysis of molten iron [12]. As shown in Figure 2.11 the Mg content needs to be controlled within a narrow window of +/- 0.004 wt.% in order to obtain CGI. In practice, the usable Mg-range for CGI is even smaller, because active magnesium fades at a rate of approximately 0.001% every five minutes, and hence the initial composition of the cast iron must be sufficiently far away from the abrupt CGI-to-FGI transition [12].
Concurrently, the initial composition (*cf.* Figure 2.11) must not be too close to the high-Mg side of the plateau in order to minimize the formation of nodular graphite in the faster-cooling thin sections. If the active oxygen and/or sulphur contents are high, they will consume the active magnesium and shift the plateau towards higher Mg-concentration. Conversely, if the oxygen or sulfur levels are relatively low, the CGI plateau will shift towards lower Mg-concentration. For these reasons, variations in the composition, cleanliness, oxidation and humidity of the charge material make it impossible to define a fixed chemistry specification for CGI.

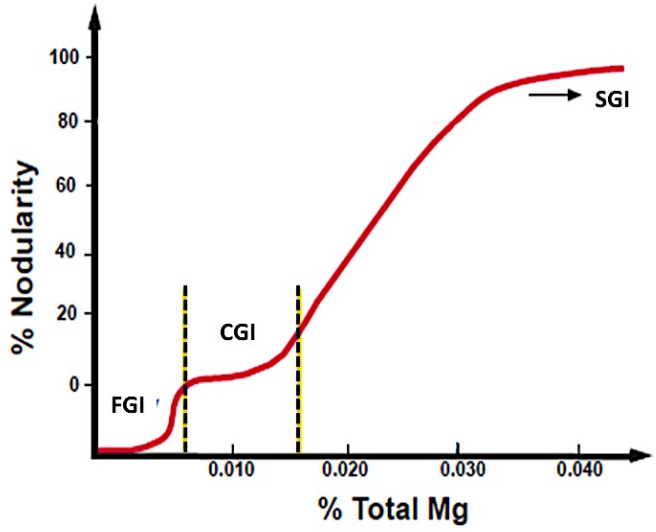

Figure 2.11 Effect of total magnesium content on nodularity and graphite morphology [12].

The different morphologies result in different mechanical and thermal properties. More details are given in section 2.3.
Some main applications of CGI are in exhaust manifolds, bedplates, brake components, pump housings, flywheels and brackets. The enormous CGI potential for manufacturing diesel engine components, especially cylinder heads and blocks, stimulated Dawson (2001) to state that "*The real iron age is only just beginning*" [16].

Aluminum alloys are also used in cylinder heads due to their low density and high thermal conductivity. However, aluminum alloys will hardly endure the high peak firing pressures, which are approximately between 160 and 180 bar for diesel passenger cars and 200 bar for heavy-duty truck engines. Also the mechanical strength of aluminum drops rapidly with raising temperature. Whereas, CGIs have reasonable tensile strength (up to 550 MPa), which can remain stable with increasing temperatures up to 400 °C [16]. Figure 2.12 compares the tensile and thermal properties of CGI, FGI and one type of aluminum alloy. As can be seen, the Young's Modulus and UTS of CGI is 2.2 and 1.7 times higher than those of the aluminum alloy, respectively, whereas the thermal conductivity and the thermal expansion of aluminum alloy is 4.25 and 2 times the ones of CGI.

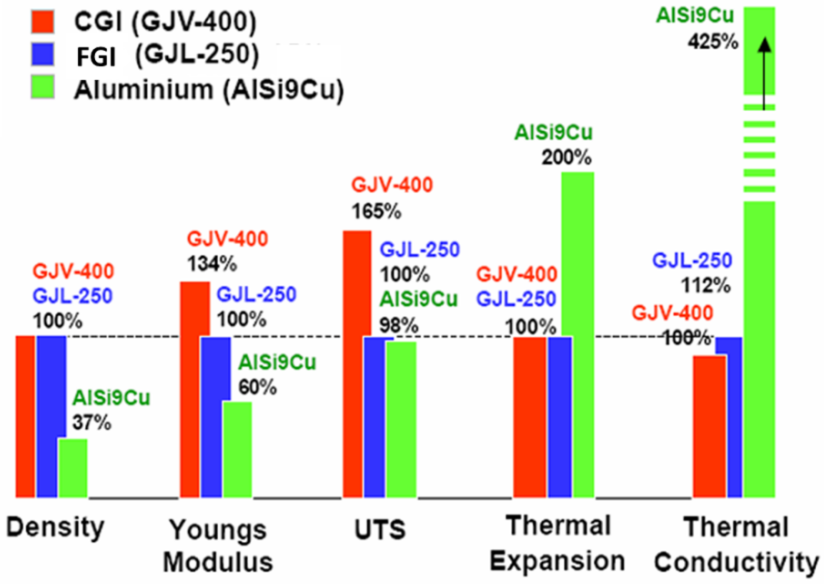

Figure 2.12 Material properties, comparing CGI, FGI and AlSi9Cu [16].

2.3 Mechanical and Thermal Properties

In general, the properties of cast iron are ultimately determined by the shape of the graphite particles as well as the structure of the iron matrix. Temperature is also an important parameter, which affects properties of cast irons.

To optimize the properties of a particular cast iron component under critical thermo-mechanical conditions, a compromise is necessary between mechanical and thermal properties. These two properties balance each other, *i.e.* a high mechanical strength is accompanied by a low thermal conductivity, and vice versa [2]. The main reason for this phenomenon is the shape and the anisotropy of the graphite phase. The relation between nodularity and mechanical and thermal properties is schematically presented

in Figure 2.13. As graphite particles become rounder, the strength and stiffness increase, but at the expense of thermal conductivity and damping capacity [2]. Therefore, a SGI has the best mechanical properties (in terms of strength) with nearly 100 % nodularity. On the contrary, an FGI with a nodularity close to 0 % has relatively poor mechanical properties but high thermal conductivity. CGI provides for many applications a suitable combination of both thermal and mechanical properties. On that account, in engine components, especially in cylinder blocks and heads, CGI is the most common material of choice. In such applications an optimum graphite morphology is of crucial importance to accomplish both mechanical and thermal properties.

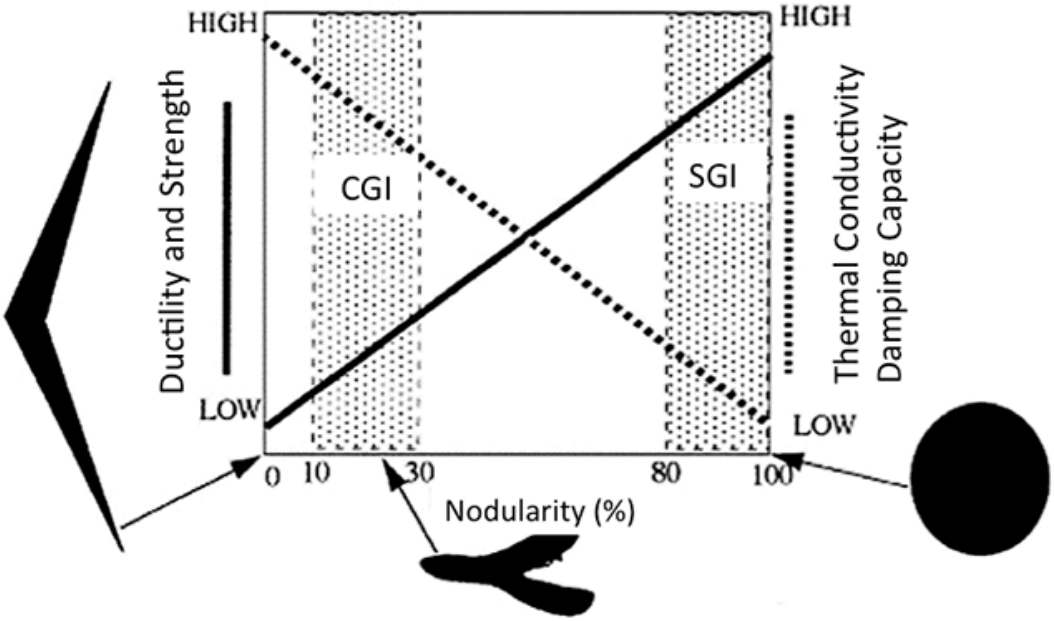

Figure 2.13 Variation of thermal and mechanical properties of cast irons as a function of the percentage of nodularity [2].

The influence of temperature on mechanical and thermal properties of different grades of cast iron has been evaluated by many researchers [1, 8, 9, 17-27]. In general the mechanical and thermal properties of cast iron deteriorate with increasing temperature, which may impede high temperature applications, such as *e.g.* in engine blocks in which commonly an operating temperature of 450°C is obtained.
A general comparison of mechanical properties of FGI, CGI and SGI with the same pearlitic matrix at room temperature and 540° C is summarized in Table 2.1 [17]. FGI and CGI exhibit the larger deterioration of tensile properties at elevated temperatures. This can be related to the interconnectivity of their graphite particles and consequently their higher oxidation and crack-propagation rates in comparison with SGI.

Table 2.1 Tensile properties of unalloyed FGI, CGI and SGI with the same 100 % pearlitic matrix at room temperature and 540 ° C [17].

	Room Temperature							540 ° C			
Type of Cast Iron	Y.S. (MPa)	T.S. (MPa)	%El	Young's Modulus (GPa)	BHN	Fatigue limit (MPa)	Fatigue Ratio	Y.S. (MPa)	T.S. (MPa)	%El	Young's Modulus (GPa)
FGI	212	268	1.3	109	185	117	0.436	159	185	2.5	65
CGI	324	405	2.0	130	215	180	0.445	183	220	3.5	72
SGI	424	676	2.8	158	210	288	0.426	232	336	2.5	122

Research results of Lòhe [9] on high-temperature mechanical properties of three main graphitic cast irons indicate that with increasing temperature to 130°C, the flow stress decreases. A flow stress-temperature plateau region is observed from 130 (400 K) to 327°C (600 K). As the temperature reaches to 327°C (600 K), the flow stress drops sharply (*cf.* Figure 2.14a).

In addition, Lòhe [9] displays the temperature dependence of the elongation (*cf.* Figure 2.14b). A minimum ductility in SGI is found to occur at 327 °C (600 K). The main reason for this sudden drop in ductility, as a result of which the material becomes brittle, is associated with dynamic strain ageing (DSA). This is similar to the blue brittleness of steel caused by diffusion of interstitial solute atoms, such as nitrogen or carbon, interacting with moving dislocations. However, the temperature of minimum ductility is different for different types of cast irons. Figure 2.14b also illustrates the influence of test temperature on the yield stress and tensile flow stress (*e.g.* at 3% strain) with increasing temperature.

T. S. Lui *et al.* [27] studied the tensile properties and fatigue life of different ferritic CGIs, with various carbon and silicon contents, at intermediate temperatures. Their results show that the flow stress plateau and serrated flow stress both occur from 200 to 400 °C owing to DSA.

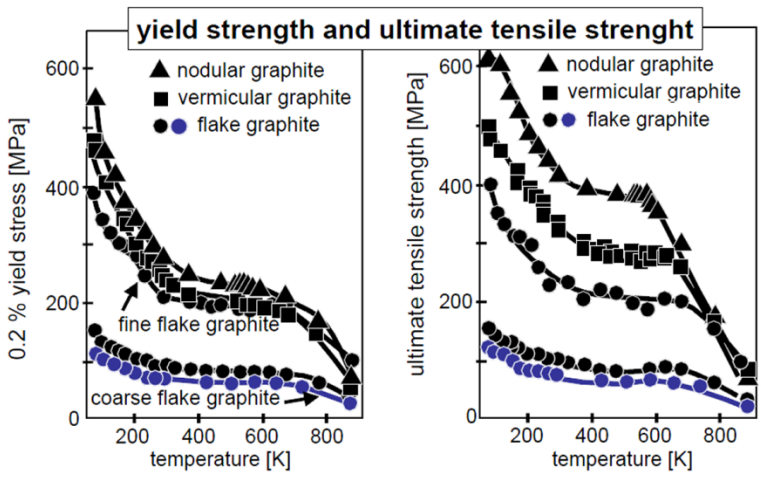

(a)

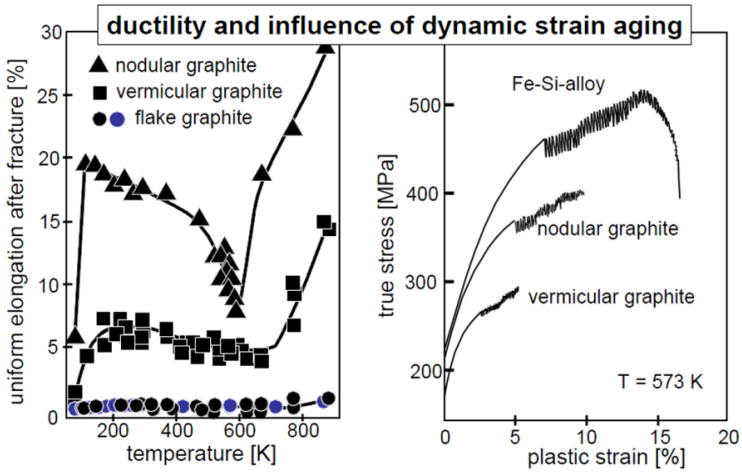

(b)

Figure 2.14 Influence of temperature on tensile properties (a) and ductility (b) of FGI, CGI and SGI [9].

The influence of temperature on fatigue life of ferritic CGI is presented in Figure 2.15 [9]. This figure shows that in stress- (*cf.* Figure 2.15a) and strain-controlled (*cf.* Figure 2.15b) conditions the fatigue life has more or less a similar trend, as it decreases with increasing temperature up to 200 °C. At this temperature, a first minimum in number of cycles-to-failure is observed. With increasing temperature, the number of cycles to failure starts increasing, up to approximately 400 °C, before another decrease occurs. Also the stress or strain level noticeably affects the fatigue life, the higher the value of stress or strain level, the lower the number of cycles to failure.

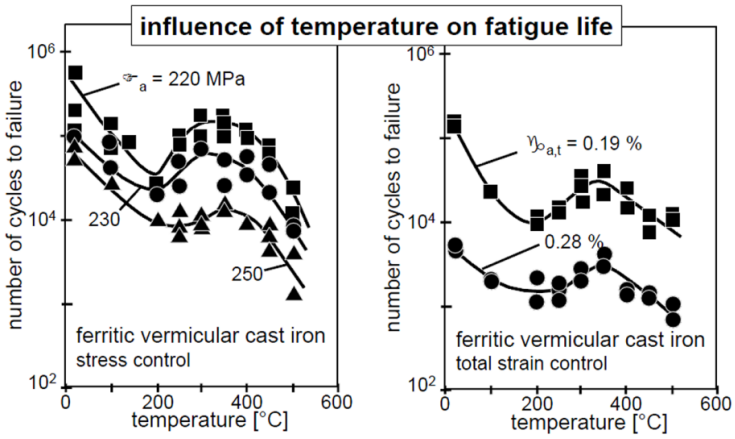

(a) (b)

Figure 2.15 The effect of temperature on fatigue life in ferritic CGI (a) Stress controlled condition (b) Strain controlled condition [9].

The *thermal conductivity (TC)* of materials under TMF conditions plays an important role on the TMF lifetime. The higher the TC, the lower the temperature gradients within the material, and therefore the lower the thermal stresses and the longer the fatigue lifetime.
Thermal conductivity depends on many factors, for instance, in cast iron TC is influenced by the graphite morphology, matrix microstructure, alloying additions, and temperature. Of these elements, the graphite shape is the most important [17, 20, 23]. A lamellar graphite structure provides very efficient heat conduction paths, due to the interconnected structure of the graphite. Additionally in FGI, graphite basal planes, along which the conductivity is high, are oriented in the same direction as the flakes. Alternatively, SGI, with a nearly circumferential platelet arrangement, provides a much more tortuous heat conduction path as the graphite particles are isolated one from the other and the metal matrix exhibits a TC that is 5 to 8 times less than that of the graphite [8] (*cf.* Figure 2.16).
The TC of CGI is close to that of FGI and thus significantly higher than the TC of SGI. As for FGI and CGI, increasing the carbon equivalent results in a higher TC. Also as the temperature in CGI is increased, the TC reaches a maximum at about 200°C, an effect also shown by SGI, but not by FGI [20], *cf.* Figure 2.17.

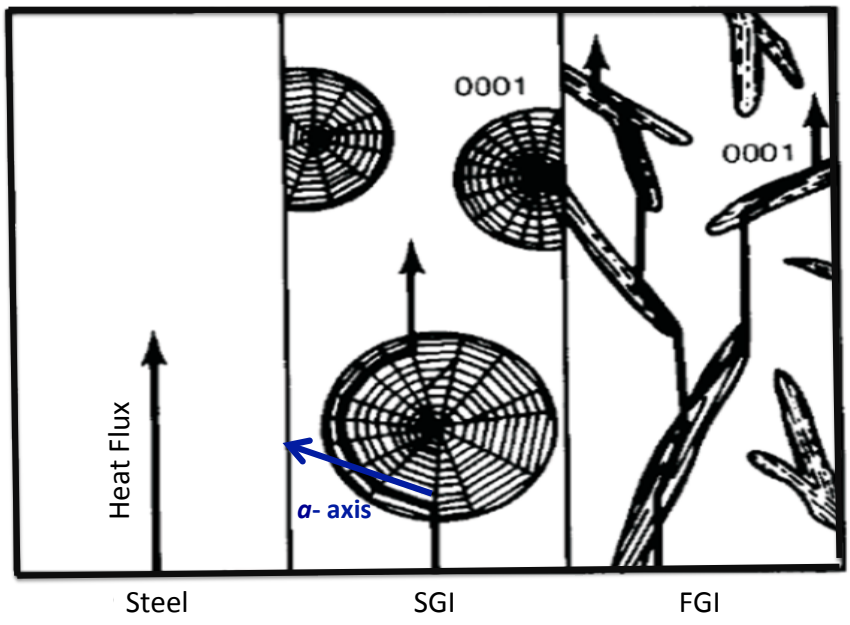

Figure 2.16 Mechanism of heat induction in Fe-C system [1].

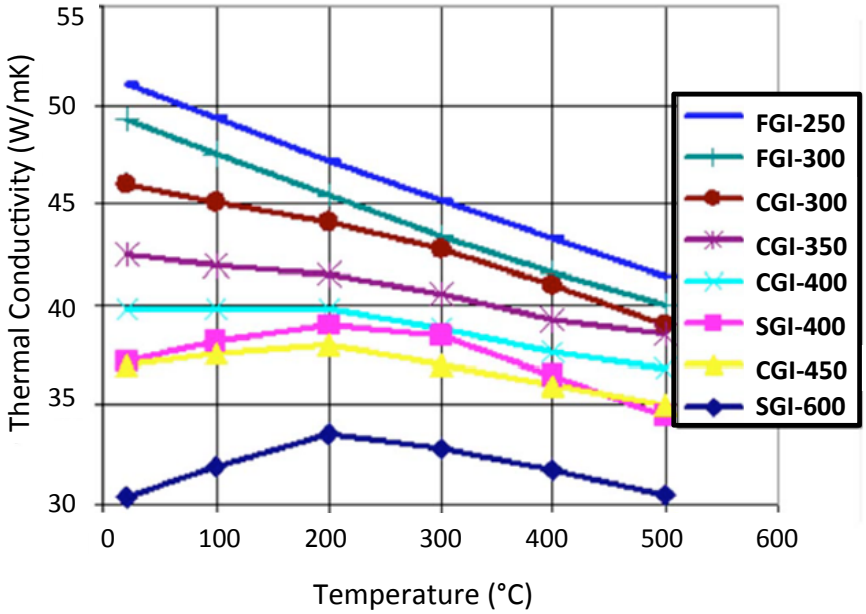

Figure 2.17 Thermal conductivity as a function of temperature in several cast irons [20]. In the legend, the number after each cast iron is the tensile strength in MPa.

The coefficient of thermal expansion (CTE) is the change of a unit of length accompanying a unit change of temperature. The CTE of cast irons is influenced to some extent by the macrostructure, to a minor extent by temperature and slightly by the composition, *i.e.* for cast irons of similar chemical composition, there seems to be no difference in total expansion. Ziegler *et al.* [17] point out that pearlitic CGI has a lower thermal expansion coefficient than FGI and SGI with the same pearlitic structure. There are only small differences in the expansion of the pearlitic and ferritic CGI and more or less the thermal expansion of pearlitic-ferritic CGI is similar to that of fully ferritic or pearlitic iron. The addition of 0.5% Mo significantly reduces the expansion of the pearlitic iron, but has little effect on ferritic iron. The stabilizing effect of Mo on pearlite accounts for the small expansion of alloyed pearlitic iron, whereas further alloying beyond 0.5% Mo has no effect.

CGI, with a predominantly pearlitic matrix, is currently the material of choice for cylinder blocks and heads. CGI provides an appropriate strength, stiffness and hardness. Within the range of 60-80% pearlite, CGI has approximately the same hardness (BHN 190-225) as a conventional fully pearlitic gray cast iron. Table 2.2 lists the mechanical and physical properties of CGI with 10% nodularity and two levels of pearlite volume fraction, at three different temperatures.

Table 2.2 Mechanical and Physical Properties of 10% Nodularity CGI [13].

Property	Temp (°C)	70% Pearlite	100% Pearlite
0.2% Yield Strength (MPa)	25 100 300	315 295 284	370 335 320
Ultimate Tensile Strength (MPa)	25 100 300	420 415 375	450 430 410
Young's Modulus (GPa)	25 100 300	145 140 130	145 140 130
Rotary-Bending Fatigue limit (MPa)	25 100 300	195 185 165	210 195 175
Thermal Conductivity (W/m°C)	25 100 300	37 37 36	36 36 35
Thermal Expansion coefficient (μm/m°C)	25 100 300	11.0 11.5 12.0	11.0 11.5 12.0
0.2% Compressive Yield Strength (MPa)	25 400	400 300	430 370
Density (g/cc)	25	7.0-7.1	7.0-7.1
Brinell Hardness (BHN)	25	190-225	207-255
Ultrasonic Velocity (km/s)	25	5.0-5.2	5.0-5.2

2.4 Introduction to Thermo-Mechanical Fatigue (TMF)

The phenomenon of fatigue is a very important research area within the field of materials science, since it is known that fatigue accounts for at least 90% of all service failures due to mechanical causes [21]. Brooks and Choudhury indicated that 61% of aircraft failures is caused by fatigue, whereas other failures include overload (18%), stress corrosion (8%), excessive wear (7%), corrosion, high temperature oxidation (5%) and stress rupture (1%) [22].

Fatigue is often thought of as resulting from a cyclically applied load on a material that shows a gradual crack growth rate *da/dN* as a response until ultimate failure. This form of purely mechanical fatigue does not give a complete picture, however, when dealing with material performance in applications involving temperature gradients and temperature time-dependent behavior.

In general, depending on the level of stress and strain involved, there are three commonly recognized forms of fatigue: high cycle fatigue (HCF), low cycle fatigue (LCF) and thermo-mechanical fatigue (TMF). *HCF* is associated with low stress levels, correspondingly low amplitude elastic strains and a high number of cycles to failure (N> 10^5). *LCF* is fatigue in which the strain range exceeds the elastic strain range and causes macroscopic inelastic deformation, so that the material exhibits a relatively low number of cycles to failure (N< 10^4 or 10^5) [21].

Thermal or Thermo-mechanical fatigue is often considered as a subcategory of LCF [18], mainly because of the presence of cyclic plastic strains and the low number of cycles to failure. TMF is caused by stresses and strains that develop during changes in both thermal and mechanical loads [19-23]. If the stresses in a component develop under thermal cycling without external loading, the term thermal fatigue (TF) or thermal stress fatigue is used.

Moreover, a distinction also should be made between isothermal LCF (IF), *i.e.* cyclic straining under constant nominal temperature, and TMF. Many researchers have developed models to treat TMF based on IF information. Remy [18] claims that "*such a comparison is often meaningless since strain rate and frequency at a given temperature in a thermomechanical cycle are often different from the one in the isothermal cycle*". In most cases IF tests do not capture all damage mechanisms that occur under variable strain-temperature conditions in TMF, *i.e.* TMF loading can be more damaging by more than an order of magnitude compared with IF at maximum operating temperature.

One of the major differences between IF and TMF is constraint. When a structure heats up, the structure develops a thermal gradient as it expands. Expansion near stress concentrators is often constrained by the surrounding cooler material. In this case thermal strain is converted into mechanical strain, which causes fatigue damage in the structure. Total constraint exists when all of the thermal strain is converted into mechanical strain.

TMF is life limiting for turbine blades and vanes in gas turbines used in jet aircraft engines, combustion chambers, railway wagon wheels, high pressure and intermediate pressure rotors of steam turbines used in fossil-fuel-fired power plants, components of diesel engines such as pistons used and cylinder heads, exhaust systems, hot working tools, and heat exchanger tubes in power and chemical plants [18]. Most of these components are made of ferritic or austenitic steels, forged or cast aluminum alloys, titanium alloys, nickel-based superalloys or cast irons and therefore, most of the published TMF knowledge pertains to these alloys [18]. However, many companies are not interested to publish or report their results. As TMF tests are highly demanding in terms of cost and time, there is a strong reluctance among leading companies to communicate their results in the open literature.

In the automotive industry, driven by the demand for low emission, there is an evolution towards higher torques and high specific power at increasing operating temperatures. Therefore, TMF has become a big challenge for the relevant industries, especially in engine design. In truck-manufacturing industry, most of the combustion-engine components, such as cylinder blocks and heads, are made of cast irons. This is mainly because of the fact that cast iron offers an excellent balance between mechanical and thermal properties. These components are exposed for long periods of time to elevated

temperatures (approximately 450 °C) and subjected to large numbers (approximately 4000 cycles in 5 years) of heating and cooling cycles. As a result of these cycles, the mechanical and thermal properties of the subjected material deteriorate, and accordingly an acceleration of fatigue damage is induced, which can finally lead to localized cracking. This is due to stresses that develop as a result of thermal gradients and thermal mismatch. It is stated by many researchers [20, 24] that the TMF phenomenon in a combustion engine is related to the start-operate-stop cycles and not to the combustion cycles. Also, strong engine load changes, *e.g.* from full load to coasting or idle operation mode, contribute to the TMF of the relevant component. Cylinder heads especially in the valve bridges, the areas between intakes and outtakes (*cf.* Figure 1.1 in the Introduction chapter), are severely subjected to so called out-of-phase (OP) TMF loading, where the material is under a maximum tensile stress at the minimum temperature of the cycle and vice versa (*cf.* Figure 2.18) [20]. Another type of TMF loading is in-phase (IP) loading, where a material is under a maximum tensile stress at the maximum temperature of the cycle and vice versa.

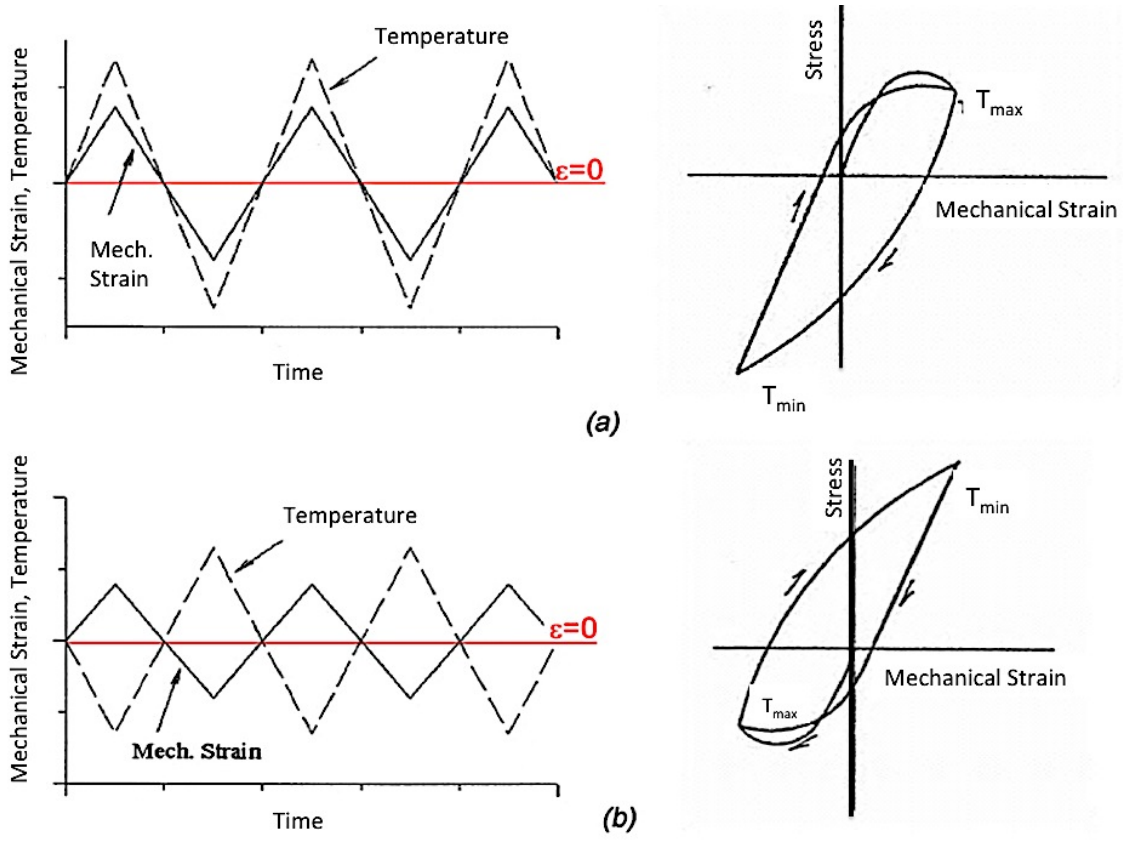

Figure 2.18 Mechanical strain and temperature variation in TMF IP and TMF OP, together with stress-strain responses.

(a) In-phase TMF loading (TMF IP).
(b) Out-of-phase TMF loading (TMF OP).

2.5 TMF and Damaging Micromechanisms in Cast Irons

For TMF conditions, the most dominant damage mechanisms are mechanical damage by fatigue, viscous phenomena by stress relaxation and creep and environmental damage by oxidation [18-20, 22-29]. Figure 2.19 summarizes these damage mechanisms under TMF conditions which may act independently or can interact, depending on various material characteristics (*e.g.* thermal conductivity, thermal expansion coefficient, Young's modulus, plastic properties) and operating conditions (maximum and minimum temperatures, mechanical strain range, strain-temperature phase, strain rate, holding time, and environmental factors).

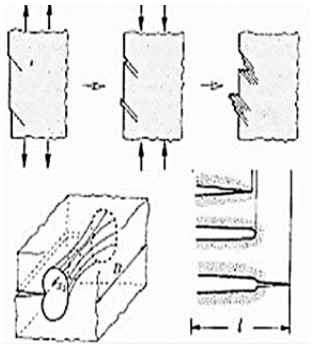

- Slip of dislocations
- Crack initiation (due to intrusions and extrusions)
- Crack growth by localized deformation and slip in the plastic zone at crack tip.

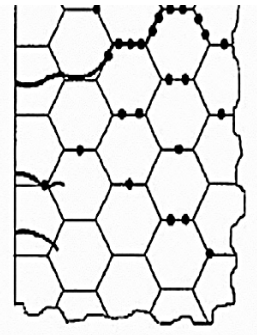

- Formation of voids
- Voids act as crack initiation
- Intergranular crack growth

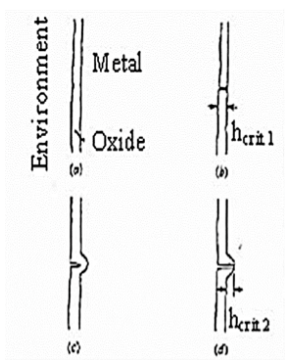

- Formation of an oxide layer
- Rupture of the oxide layer at a critical thickness
- Oxidation of fresh metal
- New oxide layer again grows and ruptures

Figure 2.19 Multiple damage mechanisms taking place during a thermo-mechanical cycle [25].

Fundamental studies on high-purity single crystals have shown that at low temperatures fatigue cracks initiate at persistent slip bands at the surface of the specimen. Crack initiation can occur in polycrystalline materials in the same way if not initiated first by inclusions or other second phases. If the surface of the specimen is smooth, slip-band extrusions and intrusions can be observed after cyclic loading (Figure 2.19a), and, with further cycling, a microscopic crack initiated along the slip band can be seen. In other words, fatigue failures can be initiated by slip [22].
Slip-band extrusions develop on the plane of maximum shear stress, which is often at 45° to the normal load, and the first stages of crack growth are known as the initiation stage. After initiation, the extrusions and intrusions basically form stress concentrations

from which a crack can grow to a macroscopic size. During crack growth, the controlling damaging mechanism is localized at the crack tip. Ultimately, the cyclic plasticity within the plastic zone causes the crack to grow a certain amount each cycle. This fatigue crack typically grows on the plane perpendicular to the maximum normal stress. Ultimately, it can lead to an instable crack, *i.e.* failure. In the case of cast iron, the initiation phase of fatigue is shortened or even not present due to the presence of graphite particles acting as inherent stress concentrations (*cf.* chapter 5).

Both mechanical and oxidation damage mechanisms are temperature and time dependent, which is relevant for TMF, since this takes place during prolonged periods of time at various temperatures. In general, creep deformation must be considered at temperatures starting at about 40% of the melting point [21]. Nevertheless, it is reported that cast irons under TMF conditions undergo short-term stress relaxation within time periods of the order of only minutes [26]. For instance, the results of relaxation experiments performed for nodular cast iron show that after half an hour the stress decreased by 30 % at 723 K (450 °C) and 50% at 773 K (500 °C) [29]. It should be noted that for fatigue in general it is not apparent to consider stress relaxation as a damaging mechanism, since reduction of stresses is more likely to slow down fatigue processes. However, in the specific case of TMF under total constraint conditions, stress relaxation during the compressive part of a TMF cycle causes a higher tensile stress in the subsequent tensile part of the TMF load cycle. This increased stress level in tension is considered to induce damage and hence reduce the TMF lifetime. The matter of increasing tensile stresses due to relaxation of compressive stresses is discussed in more detail in chapter 5.

The stresses developed in a real engine operation are schematically explained in Figure 2.20. As the engine starts up, temperature rises and compressive stresses develop. Once the operating temperature is reached, depending on the temperature and holding time, elastic and probably plastic strains will develop subsequently followed by stress relaxation, during holding at elevated temperature. At the end of the running time, the engine shuts down and it cools down to room temperature. This cooling down produces residual tensile stresses, which lead to plastic deformation in tension. The repetition of these start-stop cycles during the operational life of the engine may produce TMF cracking, particularly in the thinner parts of the engine such as the valve bridges in cylinder heads.

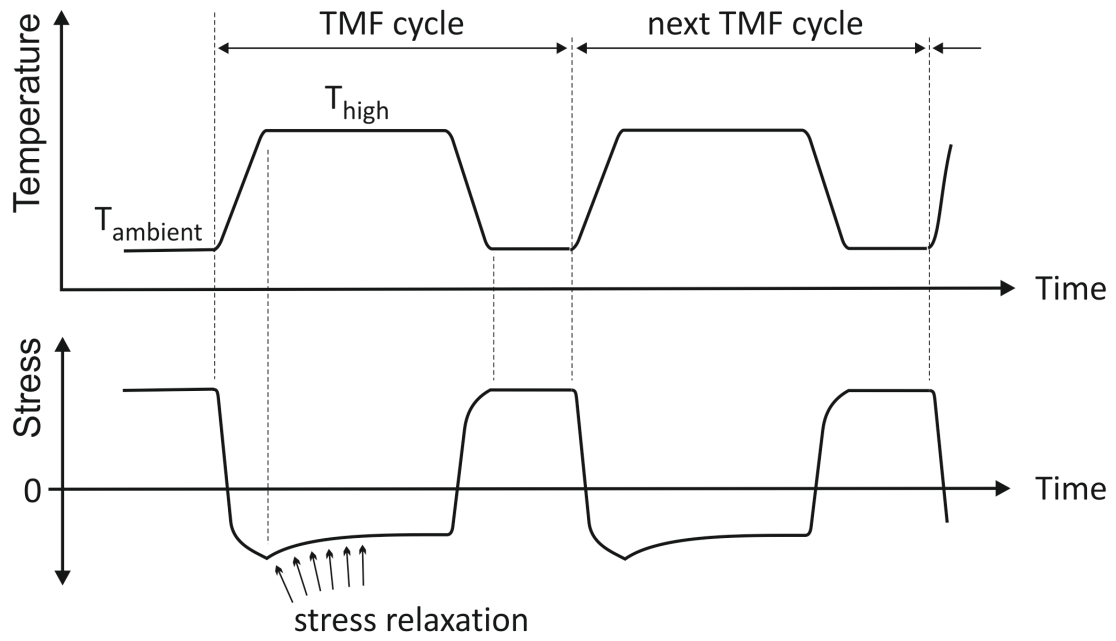

Figure 2.20 Schematic plot of TMF loading showing compressive stresses during heating cycle, stress relaxation during holding time and residual tensile stress during cooling cycle.

With regard to environmental effects, fatigue in air might be considered as corrosion fatigue, and, in fact, crack initiation may occur at slip-band extrusions and intrusions due to the absorption of oxygen atoms on the exposed slip planes. There are two types of oxidation that occur in cast iron: (i) metallic oxidation known as scaling and (ii) internal oxidation of carbon, leading to decarburization. Mass is lost by decarburization, while mass is gained by the formation of scale layers. Thus, the mass change is the balance between scaling (mass gain) and decarburization (mass loss) [30]. It has been found that during exposure to air at elevated temperature graphite at the surface starts to oxidize immediately and a rapid carbon loss takes place. Gradually oxygen penetrates into the structure along the graphite particles, oxidizing the carbon and forming reaction products CO and CO_2 and eventually leaving empty cavities behind. Buni *et al.* [31] describe that oxidation of the graphite phase reduces the bond between the matrix and the graphite, resulting in the creation of holes. Many studies conclude that internal oxidation is influenced by the graphite morphology; *i.e.* the interconnectivity of the graphite provides favorable paths for oxygen transport through the material.
At the same time scaling occurs, *i.e.* iron oxide layers (Fe_3O_4, FeO, Fe_2O_3) form at and near the surface. It was found that the iron oxide layers, which develop at elevated temperatures, are brittle and they crack during the cooling cycle of TMF. The cracking results from tensile stresses developing during the cooling cycle. Therefore, they may facilitate crack advance into the substrate and create paths for easy access of oxygen into the material. Fatigue cracks that develop also show oxidation at their flanks [23].

The effect of oxidation on the extent of volume change in CGI and the kinetics of change during exposure at elevated temperatures is investigated in the current research and the results are comprehensively discussed in chapter 4.

In addition to the damage phenomena mentioned before, microstructural degradation can also occur under TMF conditions as the material becomes unstable with respect to microstructural modification. A number of microstructural evolution processes might take place such as spheroidization of pearlite, grain coarsening, strain aging in the case of solute-hardened systems, precipitation of second-phase particles, phase transformation within the temperature limits of the cycle (*e.g.* graphitization of the carbide in pearlite), overaging, grain-boundary segregation or precipitation.

In addition to all this, in the case of cast iron, the graphite particles affect the deformation. As discussed by Seifert *et al.* [28, 29], graphite particles in SGI weaken the material in tension by decreasing the stiffness, since the graphite particles partly delaminate from the matrix. Cracks propagate also through the graphite inclusions due to the weak Van der Waals bonding along the *c*-direction (*cf.* section 2.1: *Structure of Graphite)*. In compression, though, interfacial microcracks are closed and a higher stiffness results. This leads to an asymmetrical tension-compression behavior of cast iron [28]. Also, variations in mechanical and thermal properties between the matrix and graphite result in local stresses and cracking. These mechanisms affect the deformation characteristics of the material, which unavoidably couple with damage processes [23].

Different underlying physical processes and interacting microstructural mechanisms that can occur during thermo-mechanical loading is shown in Figure 2.21 [25]. For cast iron with the melting point of 1,150 to 1,200 °C and a maximum working temperature of 420°C, T/T_m is equal to 0.36. Assuming a maximum stress of 300 to 350 MPa built up during TMF tests (*cf.* chapter 5, Figure 5.4) and ultimate tensile stress of 450 MPa (at 420°C, *cf.* chapter 3, Table 3.2), σ/σ_{UTS} is calculated to be 0.66 to 0.77. The area of possible active mechanisms for CGI is marked by the dotted lines in this figure, which covers dislocation movements, strain hardening and static/thermal recovery.

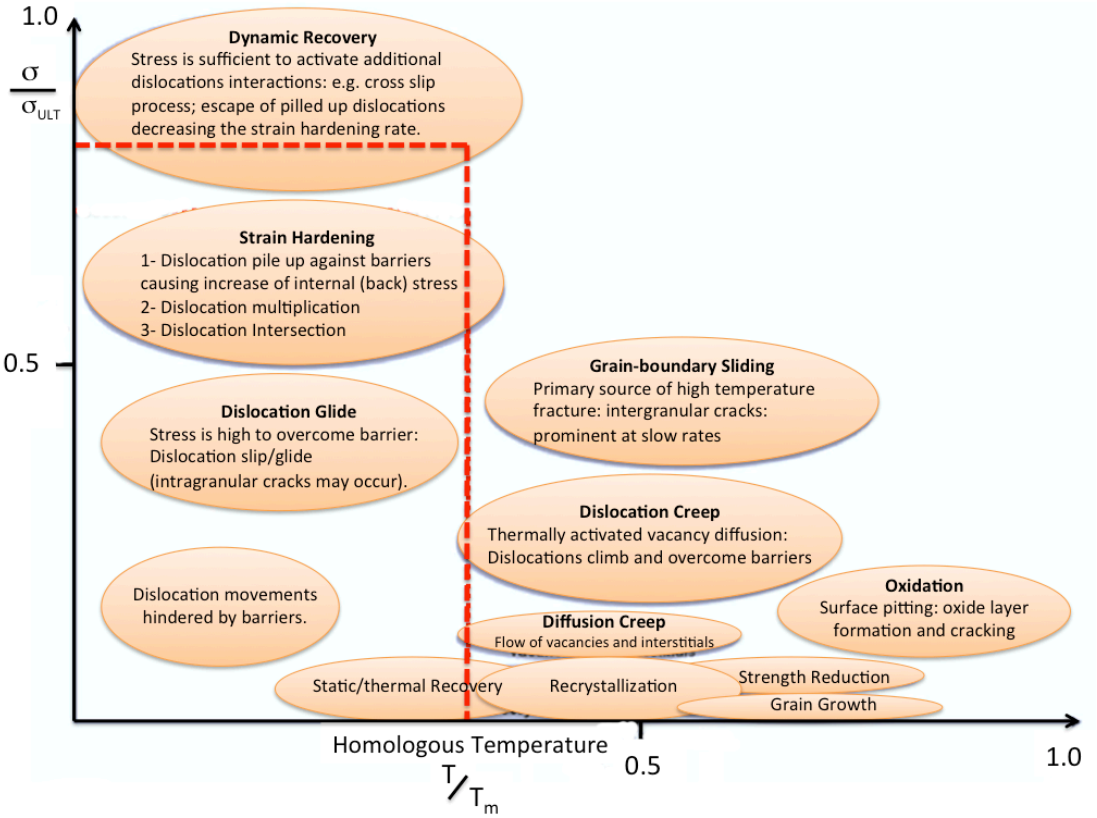

Figure 2.21 Different interacting microstructural processes that can occur during thermo-mechanical loading. T_m: melting temperature [25].

2.6 References

[1] Davis J.R. (Ed.) ASM Specialty Handbook: Cast Irons, ASM International, United States of America, Materials Park, OH 44073-0002, 1996; 3-6, 16-20.
[2] Rundman K.B. Cast Irons, Encyclpedia of Materials, Science and Technology, 2003; 1003-1010.
[3] 44th Census of World Casting Production, A MODERN CASTING Staff Report, December 2010.
[4] Callister W. D. Materails Science and Engineering, An Introduction, Book published by John Wiley & Sons, Inc., 7th edition.
[5] Knowledge Article, www.Key-to-Steel.com: Cast irons.
[6] Velichko A. Quantitative 3D Characterization of Graphite Morphologies in Cast Iron using FIB Microstructure Tomography. PhD thesis, University of Saarlandes, 2008.
[7] Durand-Charre M. Microstructure of steels and cast irons, Springer, 2003. 3-6,9.
[8] Shao S., Dawson S., Lampic M. The Mechanical and Physical Properties of Compacted Graphite Iron, Mat.-wiss. u. Werkstofftech, 29, 1998; 397-411.
[9] Löhe D. Properties of vermicular cast iron at mechanical and thermal-mechanical loading, Institutfur Werkstoffkunde I, Universitat Karlsruhe (TH), MACHINING WORKSHOP 2005 for Powertrain Materials, Darmstadt, November 24-25, 2005.
[10] Standard Test Method for Evaluating the Microstructure of Graphite in Iron Castings, ASTM A247.

[11] Gomes O.F.M., Paciornik S. Automatic Classification of Graphite in Cast Iron, Microsc. Microanal, 11, 2005; 363–371.
[12] Dawson S. Process Control for the Production of Compacted Graphite Iron, presentation 106th AFS Casting Congress Kansas City 4–7 May 2002.
[13] Dawson S., Schroeder T. Practical Applications for Compacted Graphite Iron, AFS Transactions American Foundry Society, Des Plaines IL USA, Paper 04-047(05). 2004; 1-9.
[14] 'SinterCast Nodularity Rating Chart'; 1997.
[15] Vermicular Cast Iron, Un-Alloyed. DAF Standard, 02:1–3, March 2006.
[16] Guesser W. L., Compacted Graphite Iron for Diesel Engine Cylinder Blocks. Congrès Le diesel: aujourd'hui et demain Ecole centrale, P. 1 -11,12 et. 13 May, Lyon, France, 2004.
[17] Ziegler K.R., Wallace J.F. The Effect of Matrix Strucutre and Alloying on the Properties of Compacted Graphite Iron, Transactions of the American Foundrymen's Society, 92, 1984; 735-748.
[18] Remy L. Fatigue and thermomechanical fatigue at high temperature, Encyclopedia of Materials: Science and Technology, 2001; 2866-2877.
[19] Charkaluk E., Remy L. Fatigue of Materials and Structures, Application to Design and Damage, In Bathias, C., & Pineau A. (Eds.), Chapter 7: Thermal fatigue, John Wiley & Sons Inc., USA, 2011; 271-338.
[20] Trampert S, Gocmez T, Pischinger S. Thermomechanical fatigue life prediction of cylinder heads in combustion engines, J. Eng. Gas Turbines Power, 2008; 130: 012806-1 (10 pages).
[21] George E. Dieter, Mechanical metallurgy, Book published by McGraw-Hill Co, 1988.
[22] Brooks C., Choudhury A., Mettalurgical Failure Analysis, Mc Graw-Hill, 1993.
[23] ASM Metals Handbook, Volume 19, Fatigue and Fracture. Thermal and Thermomechanical Fatigue of Structural Alloys, ASM International, United States of America, 1996; 1313-1402.
[24] Riedler M., Leitner H., Prillhofer B., Winter G., Eichlseder W. Lifetime simulation of thermo-mechanically loaded components, Meccanica 42, 2007; 47-59.
[25] Gocmez T., Awarke A., Pischinger S. A new low cycle fatigue criterion for isothermal and out-of phase thermomechanical loading, Int. J. Fatigue, 32, 2010; 769-779.
[26] Zieher F., Langmayr F. Engine Simulation in View of Reduced Development Time. Technical, Paper Code: F02V081, AVL List GmbH, Austria, 2002.
[27] CHAO C. G., LUI T. S., HON M. H. A study of tensile properties of ferritic compacted graphite cast irons at intermediate temperatures, Journal of Materials Science 24, 1989; 2610-2614.
[28] Seifert T., Riedel H., Mechanism-based thermomechanical fatigue life prediction of cast iron: Part I, Int. J. Fatigue, 32, 2010; 1358-1267.
[29] Seifert T., Maier G., Uihlein A., Lang K.H., Riedel H. Mechanism-based thermomechanical fatigue life prediction of cast iron: Part II: Comparison of model predictions with experiments, Int. J. Fatigue, 32, 2010; 1368-1377.
[30] Merchant H.D. Oxidation Kinetics of Iron-carbon Base Alloys, Oxid. Met., Vol.2, No. 2, 1970; 145-153.
[31] Buni S.Y., Raman N., Seshan S., The role of graphite morphology and matrix structure on the low frequency thermal cycling of cast irons, Sadhana, 29(1), 2004; 117-127.
[32] Neu RW., Sehitoglu H. Thermomechanical fatigue, oxidation, and creep: part II. Life prediction, Metal Trans A, 20A, 1989; 495-508.
[33] Era H., Kishitake K., Nagai K., Zhang Z.Z. Elastic modulus and continuous yielding behaviour of ferritic spheroidal graphite cast iron, Materials Science and Technology, 8(3): 1992; 257-261.

3

Experimental Set-up

"Experience without theory is blind, but theory without experience is mere intellectual play".
Immanuel Kant

In this chapter, a detailed account is presented on the investigated material (Compacted Graphite Iron: CGI), the origin of material, specimens fabrication and preparation, the hardware set-up of the Thermo-Mechanical Fatigue (TMF) experiments and the employment of dedicated software to configure and design the TMF procedures used to investigate TMF properties of CGI.
With regard to microstructural characterization, and more specifically to the purpose of revealing subtle microstructural changes in the material under investigation, several techniques were employed in this study. These techniques include X-ray 3D-computed tomography, scanning electron microscopy with wave-length dispersive X-ray analysis (SEM-WDX) and the powerful technique of orientation-contrast microscopy, *i.e.* Electron Backscatter Diffraction (EBSD). The essentials of these techniques are briefly reviewed in this chapter.

3.1 Material: Compacted Graphite Iron (CGI)

Chemical Composition

The material investigated in this study is CGI with a pearlitic matrix (*cf.* Figure 3.1). The nominal chemical composition is given in Table 3.1 [1]. The determination of carbon and sulfur concentrations was carried out by a high-frequency induction furnace (LECO CS-225® [1]) for samples taken from different areas of the cylinder heads. For the measurement of other elements an X-ray fluorescence analyzer (XRF) was used.

[1]The LECO CS-225® is an instrument for the determination of carbon and sulfur in solid materials, *i.e.* iron, steel. The sample is combusted in a high-frequency induction furnace instrument. The products of combustion are passed through a moisture trap to the sulfur IR cell where sulfur is measured as sulfur dioxide. The gases exiting the sulfur cell pass through a catalyst where carbon monoxide is converted to carbon dioxide. SO_3 is removed, then carbon is measured as carbon dioxide in the carbon IR cell.

Table 3.1 Nominal chemical composition of the CGI (wt.%) (courtesy of DAF: [1]).

C	Si	Cu	Mn	Cr	Ti	Sn	Pb
3.60-3.90	1.90-2.20	0.75-0.95	0.15-0.40	< 0.10	< 0.015	0.06-0.10	< 0.002

Depending on the specification of the casting, different elements are added to the melt. According to DAF specification [1], the specified limit value for the elements carbon (C), titanium (Ti) and chromium (Cr) is mandatory, and the limit value for manganese (Mn), copper (Cu) and tin (Sn) are guide values. Cu and Sn are added to provide 70-90% pearlitic matrices with the hardness of 190-250 HB [1]. Sn is a strong pearlite stabilizer and the addition of 0.1% Sn can reduce the rate of decomposition of pearlite into ferrite and graphite even at 700 ˚C. Combination of Cr and Sn also stabilizes the pearlitic structure up to 450 ˚C. Mn is a mild carbide and pearlite former, and Pb is a strong carbide promoter. Ti at concentration below 0.25% is a graphitizer, *i.e.* it promotes graphite formation, but it suppresses the growth of SGI, thus allowing CGI production at higher magnesium contents. Ti-concentrations greater than 0.1% must be avoided, because they promote the formation of titanium-carbonitride inclusions, which increase abrasive wear and cannot be tolerated in machining-intensive components such as cylinder heads.

Figure 3.1 shows the microstructure of CGI, which is composed of a complex morphology of compacted graphite particles, pearlite with a variety of lamellar structures, and a small fraction of ferrite. The heterogeneous pearlitic structure ranges from a fine (0.4 µm) to coarse pearlite interlamellar spacing of cementite (2.6 µm). According to application requirements [1], the optimum microstructure should consist of a composite containing a pearlitic matrix and graphitic carbon and avoid primary carbides. In CGI, graphite may occur with a maximum nodularity of 20% but flake or lamellar morphology must be avoided.

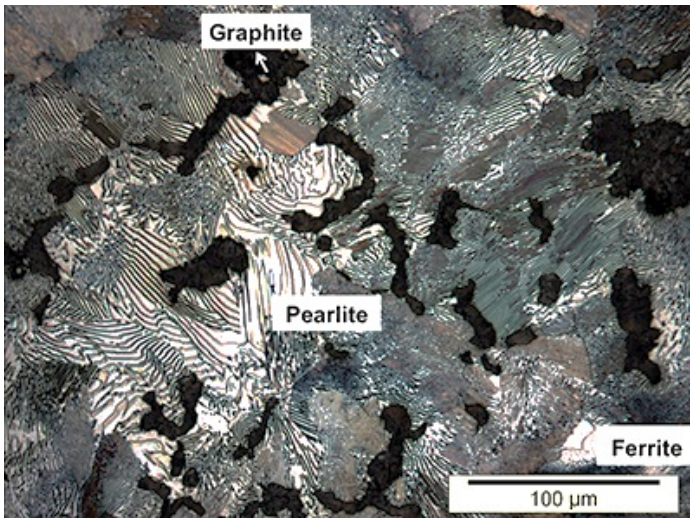

Figure 3.1 Microstructure of the pearlitic CGI.

Mechanical properties

The mechanical properties of the present material are given in Table 3.2 for room temperature and 420 °C. Tensile tests were conducted in accordance with the standard test methods for tension testing of metallic materials at room temperature and elevated temperature, ASTM-E8/E8M and ASTM-E21 respectively [2, 3]. It can be observed that the mechanical properties are temperature dependent, *i.e.* the yield strength and tensile strength decrease by 24% and 14%, respectively, while the elongation at fracture increases by 17% and the Young's modulus drops by 20% upon a temperature increase to 420 °C.

Table 3.2 Mechanical properties of CGI at RT and 420°C.

	σ_y (MPa)	σ_{UTS} (MPa)	$E_{Modulus}$ (GPa)	Elongation at break (%)
RT	330	520	150	2.9
420 °C	250	450	120	3.5

3.2 TMF Testing

The main objective of TMF tests is to characterize the failure mechanism by the number of cycles to failure, and identify the controlling factors. The experimental set-up, testing specimen, methods and tools employed are addressed in this section.

3.2.1 Origin of Material

All TMF specimens were extracted from a specific type of currently produced CGI cylinder heads*, cf.* Figure 3.2. In total seven cylinder heads were used to obtain all TMF test specimens.
TMF failures typically occur in the valve bridge area of cylinder heads, and therefore, it would be ideal to cut out TMF specimens from this region. Especially since in this thin region the casting conditions (*i.e.* high cooling rates) can possibly cause a locally different microstructure (which ideally should contain not less than 90% pearlite). Unfortunately, the valve bridge area is too small to allow the extraction of TMF specimens of practical dimensions. As the next best option, material was taken out from the 19 positions shown in Figure 3.2, located as closely as possible to the valve areas. It was considered also sensible to cut out the material nearby from the top surface of the cylinder head, since TMF cracks are likely to initiate from the flame deck.

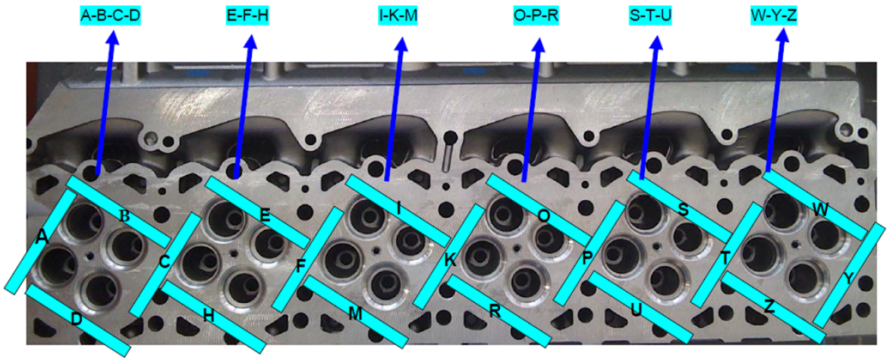

Figure 3.2 A typical cylinder head with the locations for testing specimens and the corresponding coding system.

3.2.2 Out-of-Phase (OP) TMF Testing: Employed Standard TMF Test Procedure

As mentioned before, in complex cast iron components, such as cylinder blocks and heads, heating and cooling cycles can lead to localized cracking due to stresses that develop as a result of thermal gradients and thermal mismatch. Especially the valve bridges in cylinder heads, the areas between intakes and outlets, are severely subjected to out-of-phase (OP) loading, *i.e*. maximum strain occurs at minimum temperature.
TMF tests were intentionally designed to represent the conditions occurring within valve bridge areas of cylinder heads. Therefore, TMF tests were performed under total constraint, meaning that the total strain measured by the extensometer was kept constant with the reference at 50 °C. By cycling the temperature between 50 and 420 °C, OP TMF loading was accomplished. Holding times of 30 s were introduced during both maximum and minimum temperatures in order to stabilize temperature levels throughout the specimen[2]. The basic equations for strains applied during TMF loading by temperature cycles are presented in the following (equations 3.1 and 3.2) and also presented in Figure 3.3.

$$\varepsilon_{meas.} = \varepsilon_{el.} + \varepsilon_{pl.} + \varepsilon_{thermal} \qquad (3.1)$$

With $\varepsilon_{meas.}$ being the strain measured by the extensometer (*i.e.* the total strain), $\varepsilon_{el.}$ being the elastic strain calculated as the stress divided by the Young's modulus (σ/E), and $\varepsilon_{thermal}$ the thermal expansion strain, calculated by $\alpha\Delta T$ (with α being the coefficient of thermal expansion and ΔT being the temperature difference). As a result, the plastic strain is known by subtracting the elastic strain and thermal strain from the total strain (*cf.* equation 3.2).

$$\varepsilon_{pl.} = \varepsilon_{meas.} - \sigma/E - \alpha\Delta T \qquad (3.2)$$

[2] It is recognized that the holding times of 30 s do not represent service conditions of real engines. This matter is addressed in the section 3.2.3 "Investigating the Effect of TMF Holding Times".

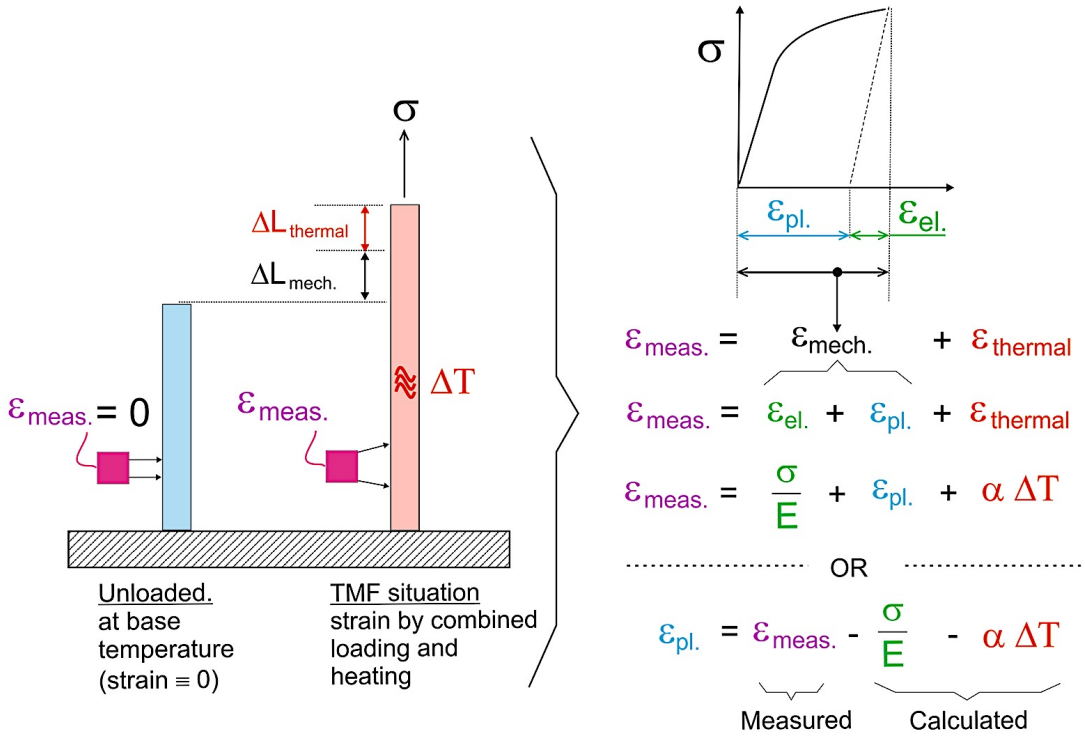

Figure 3.3 Basic equations for strains induced during TMF loading.

The heating and cooling rates were 9 and 6 °C s^{-1}, respectively. Reducing the TMF test 'cycle time' proportionally shortens the total test time and motivates a careful choice of heating/cooling rates and holding times, with the intension of shortening the TMF test cycle time as much as possible while preserving the basic TMF failure mechanism. The chosen value of 9 °C s^{-1} was considered safe with respect to radial temperature gradients produced during heating[3]. The cooling rate of 6 °C s^{-1} was basically the maximum value attainable with the cooling system available.

This TMF test procedure will be referred to as the *standard TMF test procedure* and an example of the designed and recorded signals of stress, strain and temperature is given in Figure 3.4. At the start of the TMF tests, the load is initially kept to a zero level while the specimen temperature was ramped to 50 °C (*i.e.* free expansion) and this condition served as the reference starting point from which TMF cycling was launched. At the beginning of the first TMF cycle the control mode of the test is switched from load control to strain control, maintaining the strain signal to the initial level, as it is present at the start of the first TMF cycle (*i.e.* an unloaded specimen at a temperature of 50 °C). The first TMF cycle differs from subsequent TMF cycles by the fact that heating starts from an unloaded specimen, causing a distinctive high mechanical strain level during the first TMF cycle (*cf.* Figure 3.4b). This situation is also present for material in cylinder

[3] Although not reported, the existence of radial thermal gradients is acknowledged and also analysed by numerical simulations, showing an acceptable maximum temperature difference between skin and core of about 10 °C for the standard TMF test conditions described in this section.

heads of real engines, when started for the first time. Therefore, the TMF procedure used is considered to be representative for the actual service situation of diesel engines.
TMF testing under total constraint is equivalent to cyclically inducing a fixed amount of mechanical strain. This amount is equal (and opposite in sign) to the value of the thermal strain, which is 0.6% for the temperature range of 50 to 420 °C, indicating that cyclic plasticity is bound to occur and a limited amount of cycles to failure is most probable (*cf.* Figure 3.4a).
The Coefficient of linear Thermal Expansion (CTE or α) was obtained by measurement of the strain during heating from RT to 420 ˚C in free expansion. The measurement was not carried out for each individual test but obtained on a few specific samples at the beginning of the project. By plotting the axial strain measured as a function of the temperature, a linear expansion curve was observed, of which the slope is equal to 15.6 $\times 10^{-6}$ /˚C for the coefficient of thermal expansion.

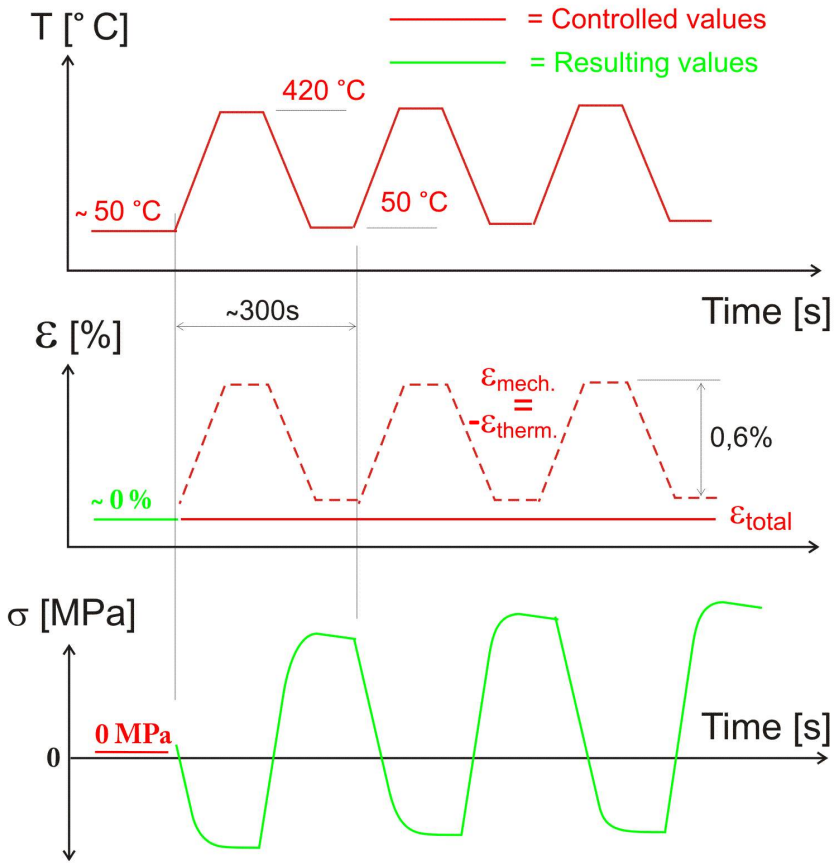

(a)

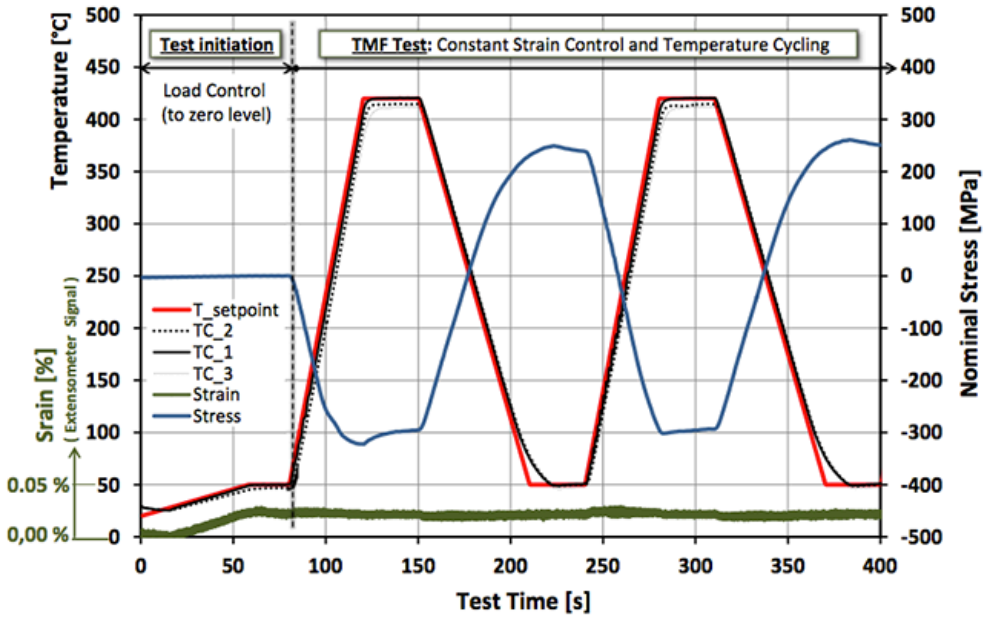

(b)

Figure 3.4 TMF Out-of-Phase (OP) schematic loading (a) TMF designed test signals, (b) TMF recorded test signals at test start-up and initial two cycles. TC_1, TC_2 and TC_3 indicate thermocouples readings of center, upper and lower positions in the gauge length region.

3.2.3 Investigating the Effect of TMF Holding Times

For CGI, the number of TMF cycles to failure was found (*cf.* chapter 5, section 5.3.2) to range from 1000 to 2000 cycles, corresponding to a testing time up to 100 hours (*i.e.* four days with all testing preparation), using holding times of 30 s during both maximum and minimum temperatures. However, to represent the in-service conditions that valve bridges are subjected to, realistically longer holding times were used. Four holding times of 180 (used for testing smooth specimens), 480, 1800 and 18000 s (5 h) at the maximum temperature of 420 °C were chosen in combination with 30 s for the minimum temperature of 50 °C. These holding times were selected to limit the tests to reasonable times. Using these holding times at 420 °C allows stress relaxation to occur which at 50 °C no significant stress relaxation is expected. The choice of holding times is based on performed compressive stress relaxation experiments at 420 °C [4]. The thermal cycles are shown schematically in Figure 3.5.

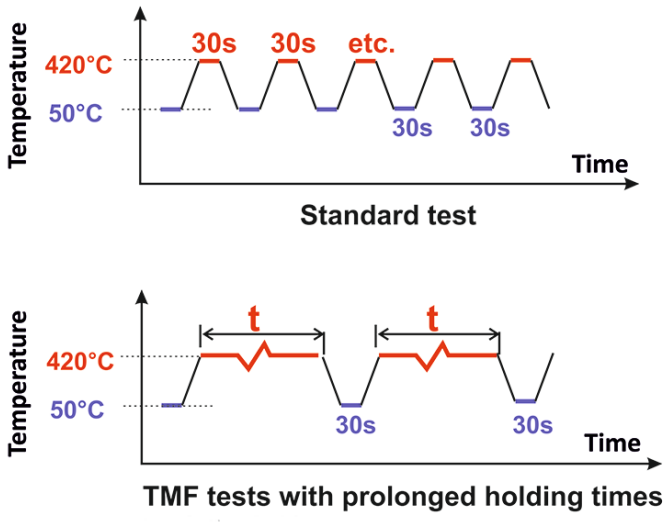

Figure 3.5 Five different holding times of t= 30, 180, 480, 1800 s (30 min) and 18000 (5 h) at maximum temperature of 420 °C were chosen in combination with holding during 30 s at the minimum temperature of 50 °C.

3.2.4 TMF Specimen Preparation

In a first step, the 19 pieces of material from locations A to Z (*cf.* Figure 3.2) were removed from the cylinder heads by means of a water-jet-cutting operation. This produced parts with a length of about 150 mm and a more or less square cross section (with sides of approximately 15 mm). At a second step, the pieces were shaped into cylindrical specimens (D = 12 mm, $L \approx$ 150 mm) using electro-discharge machining (EDM)[4]. Finally, solid dog-bone TMF specimens were machined by a turning operation (*cf.* Figure 3.6a). The gauge length of the specimen is 22.00 ± 0.25 mm with a diameter of Ø6.000 ± 0.025 mm, with the final two turning steps removing 0.05 mm only, to prevent the introduction of internal stresses near the surface. This resulted in an average roughness value of about 0.6 µm, which is much smaller than the microstructural features of this material (> 1 µm).

3.2.5 Employment of Notched TMF Specimens

Commonly, TMF behavior is studied by cyclically loading smooth dog bone specimens until failure. The resulting number of cycles to failure (N_f) constitutes a single parameter

[4] Starting a turning operation from a work piece having a rectangular cross section will first chip off corners, introducing some degree of impact loading on the work piece. It was initially not known if this impact loading (during the turning) would affect the TMF failure mechanisms of CGI material. To avoid any ambiguity, EDM, which does not involve any impact loading, was chosen to produce cylindrical shapes from the rectangular cross sections. However, for economic reasons a last series of specimens was produced by directly turning the rectangular cross sections. These specimens were found to produce consistent TMF results, when compared to results of specimens produced involving EDM. Therefore, for CGI material, turning TMF specimens from rectangular cross sections can be considered an economically good practice, not influencing TMF test results.

that can be used to predict actual service life. Both the crack-initiation phase and the crack-growth phase may contribute to the overall lifetime, but unfortunately standard test methods do not distinguish between crack initiation and crack propagation. Another aspect of the conventional testing procedure is the long testing time involved and the considerable scatter in test results (*cf.* chapter 5).
In this research these drawbacks were addressed by not only performing tests on smooth specimens, but by also using an alternative experimental approach, in which specimens are provided with a sharp circumferential notch. Individual specimens were provided with circumferential notches with depths of 0.1, 0.2, 0.35, 0.5 and 0.65 mm and a 0.04 mm tip radius. For a notch depth of 0.2 mm the geometry is shown in Figure 3.6b. Details on TMF testing of smooth specimens and the reasons of testing also notched specimens are explained in more detail in chapter 5. In order to avoid that the notch affects the test results, it is of utmost importance that the notch is machined with the highest possible accuracy. The way this is done is explained in appendix A.

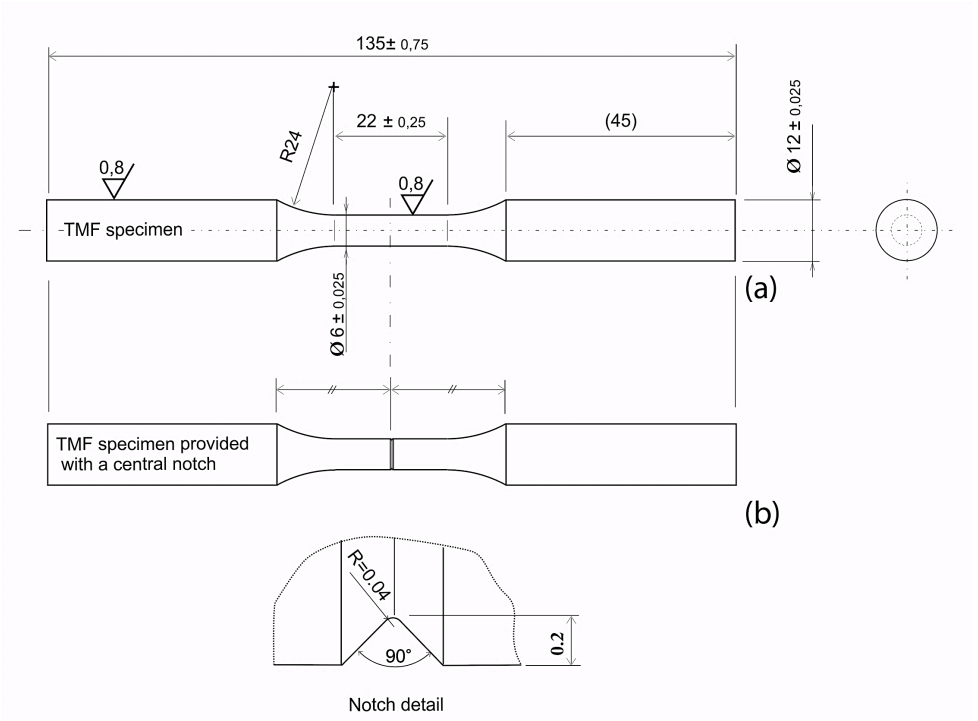

Figure 3.6 (a) Solid smooth dog-bone specimens. (b) Circumferential notched specimens with depth of 0.2 (as an example) and a 0.04 mm tip radius. Dimensions are indicated in mm.

3.2.6 Employed TMF Equipment

In order to study damage phenomena and micromechanisms for TMF crack initiation and growth, well-controlled TMF experiments were designed. To this aim, a TMF experimental set-up, as shown in Figure 3.7, was built around a servo-hydraulic fatigue machine. At the beginning of the TMF research program (2009), a TMF testing setup was

not yet available in the department of Material Science and Engineering (MSE), at Delft University of Technology (DUT). Therefore, no detailed experience was initially present for setting up the required TMF test facilities.

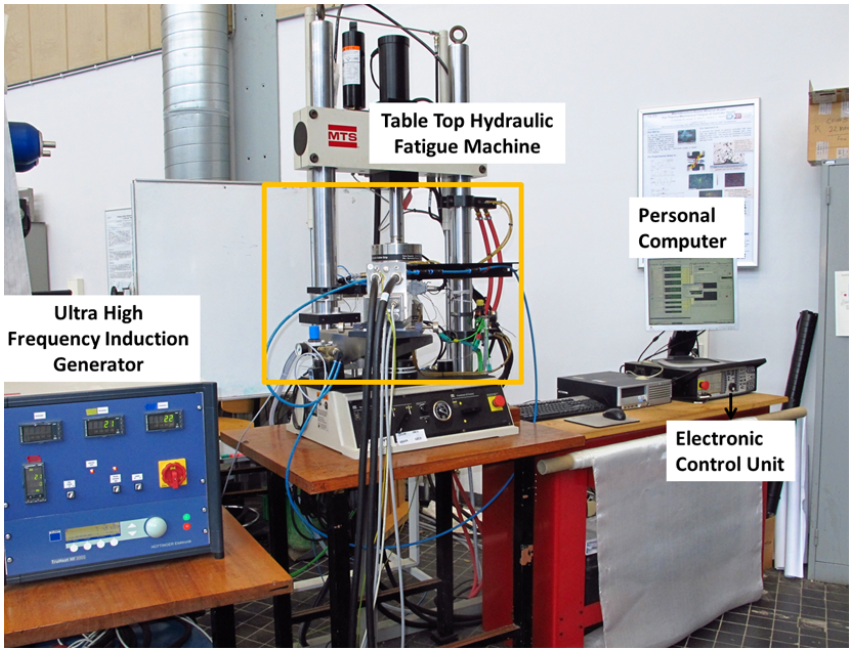

(a)

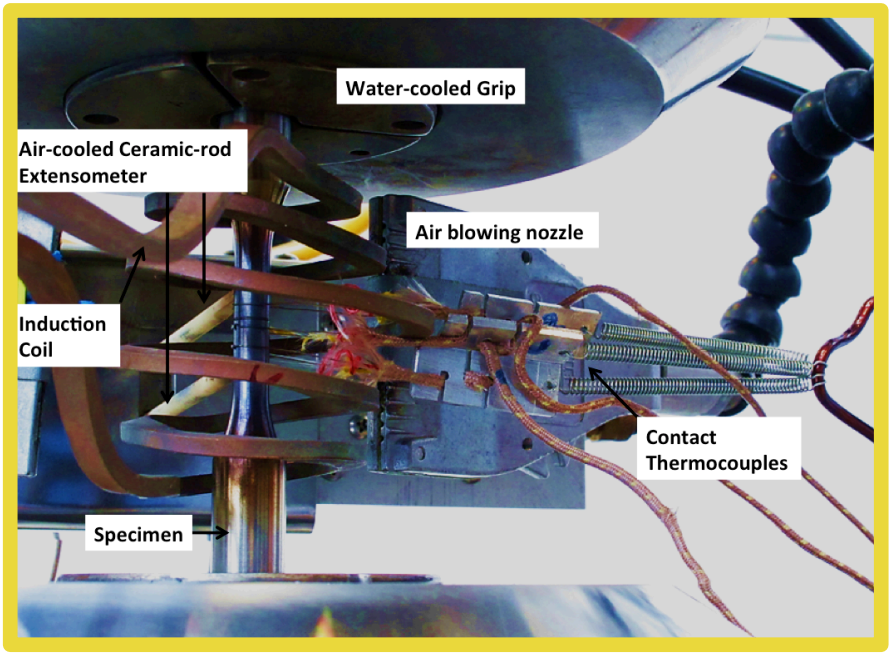

(b)

Figure 3.7 TMF set-up machine (a) The entire TMF test set-up (b) A close-up view shows the induction coil for heating and air blowing system for cooling the specimen, and thermocouples for temperature measurement and control.

An Overview of the Components Used for TMF Tests

i) Controlling the TMF Set-up Equipment

The central part of the test setup comprises a table-top hydraulic fatigue machine[5] with a load capacity of 25 kN, in both tension and compression (*cf.* Figure 3.7a). A Personal Computer (PC) with dedicated software[6] is incorporated to design and control a set of actions to be performed by the fatigue machine. The commands are linked to an electronic control unit[7], which regulates the actual physical execution of the commands in a control loop. For operating the fatigue machine, there is a choice of three control modes[8], *i.e.* control by load, by displacement and by strain. These control modes (also called channels) can be active only one at the time, since their signals are interdependent. In addition, the specimen temperature and the flow rate of cooling air can be controlled independently from all other channels. Both specimen temperature and air flow value are incorporated in the "Multiple Purpose Testing" (MPT™) software[6] and can be addressed as channels[9].
It was found to be of crucial importance to optimize the stability and response of the servo control loop for each specific test set-up employed. This implies that so called Proportional-Integral-Derivative (PID) tuning procedures were executed for all types of specimens used and all control modes involved[10].
The software MPT™ includes a graphical test-programming environment and allows the user to define different test segments, data acquisition processes, and trigger processes. Typically, MPT™ software is used to define a set of sequential actions (or tasks) to be performed by the fatigue machine, with the ability to choose an arbitrary control channel per action. Such a set of actions is designated a "*test procedure*".

ii) Heating and Cooling Components

The heating cycle in the TMF test has been achieved by employing a Ultra High Frequency (UHF) induction generator[11], equipped also with an induction coil (Figure

[5] MTS 858 table top system.
[6] Model 793.00 system software in combination with Multiple Purpose Testware™ (MPT)
[7] Flextest™ SE, version 4.0B 1978.
[8] There is an additional control mode designated as the "Channel Limited Channel" control mode or CLC mode, being displacement control with a load feedback. Using CLC, the displacement is controlled in the first place, but when for some reason a certain load level builds up, further displacements are halted even if the displacement set-point is not yet attained. The CLC mode is dedicated for safely manipulating the grip positions, for instance during the installing of a specimen.
[9] For clarity it is mentioned that the temperature is regulated only with the induction power as controlling output signal, with the thermocouple readings as feedback signals. Although air cooling from the nozzles also affects the temperature response of the system, a change in flow rates of cooling air just causes the induction power to be regulated to the point that the measured temperature equals the temperature set-point again.
[10] Because the load and strain control modes are used in combination with a gripped TMF specimen, the adequate PID values have to be determined when a specimen is gripped. The stiffness of the system basically governs the setting of the PID values.
[11] Trumpf type TruHeat HF 3005, with Huttinger Electronic, with a heating capacity of about 6 kW.

3.7b). The coil is positioned around the gauge of the specimen. Induction heating constitutes a non-contact heating principle, producing eddy currents in a thin surface layer of an electrically conductive specimen, heating only the outer skin of the specimen. The inner part of the specimen is heated by thermal conduction of heat from the hot outer skin layer to the colder core of the specimen. Induction heating enables a relatively high heating rate, for instance during most TMF tests a heating rate of 9 °C/s was used.
Cooling down from a high temperature level is achieved in the first place by reducing the heat input from the UHF generator. At some point during cooling, even without any heat input, the cooling rate requirements can only be fulfilled by actively cooling the specimen. For this purpose air can be blown with air blowing nozzles from three sides towards the gauge area[12] (*cf.* Figure 3.7b). During most TMF tests a cooling rate of 6 °C/s was applied. Details about control loops involved during the heating and cooling cycles are discussed in the next section (see section 3.2.7).

iii) Temperature Control of the TMF Specimen

Temperatures of the specimen were measured by three K-type thermocouples. It was not an option to weld the thermocouples directly onto the surface of the specimen in the gauge region, since the weld itself would probably serve as a TMF initiation spot. Instead, ends of thermocouple wires were welded together, producing a junction. The junction was subsequently flattened by plastic deformation, producing a so-called ribbon type thermocouple. The ribbon is wrapped around the cylindrical part of the gauge and stretched by a spring configuration, as shown in Figure 3.7b. The employment of a ribbon thermocouple is one of the suggestions mentioned in reference [5] and is found to give a good contact with the specimen surface, resulting in a consistent temperature measurement.
One thermocouple was placed in the middle of the gauge (smooth specimens) or in the case of notched specimens, at a location of about 0.5 to 1.0 mm above the notch. This central thermocouple was used to control the temperature. The two other thermocouples were positioned about 5 mm above and 5 mm below the middle of the specimen, respectively. This was specifically done to monitor the temperature gradient within the gauge. Typically, the readings of the upper and lower thermocouple were about 410 °C, at the moment that the controlled temperature was 420 °C. The temperature gradient in the gauge length observed is within the requirements listed in reference [5].

iv) Gripping and Alignment

Hydraulic grips provided with smooth collets were used[13], gripping the cylindrical ends of the specimen. This type of grips is ideal because it does not show backlash at the

[12] Heat is also transferred to the water-cooled grips. This heat flow cannot be controlled directly, but merely depends on the physical principles of heat conduction, with a major controlling factor being temperatures of the specimen gauge length and grip collet temperature.
[13] MTS model 646 hydraulic collet grips, for specimens with cylindrical gripping ends of Ø 12 mm.

reversal points from tension to compression loading (and vice versa) during the TMF cycles. The axial loads are transmitted completely by friction between the grips and the specimen ends, even though both grips and specimens have smooth surfaces. This is advantageous compared to the use of serrated grips, which bite into the specimen ends and potentially compromise the proper alignment of the specimen.
Finally, it should be noted that the set-up was provided with a fixture allowing the adjustment of both concentric and angular alignments[14]. A good alignment is considered essential to prevent buckling of the specimen during the compression parts of the TMF cycles. The alignment of the fixtures was checked regularly.

v) Strain Measurement

The axial strain was measured employing a customary type of strain gage extensometer[15], which is dedicated for measurements up to a maximum temperature of 1200 °C, fitted with solid ceramic contact rods and having a gauge length of 12 mm, which was kept constant during the actual TMF test with an absolute accuracy better than 10^{-5}, corresponding to a relative accuracy of 0.3 % for the strain measurements in this work. The delicate parts of the extensometer are shielded from heat radiated from the specimen and in addition cooled by a moderate flow of compressed air.

3.2.7 Configuration of the TMF Test Procedure (MPT™ Test Commands)

Using MPT, an OP-TMF test procedure was configured and regarding the set-up of the test procedure some aspects are mentioned here and shown in Figure 3.8. The TMF test procedure begins with activating the criteria for data acquisition and safety limits, while also a criterion for stopping the test in a controlled way is triggered[16].
In addition, the load is ramped to a zero level, because usually some small load level was found to develop during the specimen fitting and gripping[17] operation. Also, while keeping the load at a zero level, the specimen temperature was set to 50 °C in free expansion. After reaching the mentioned load and temperature levels, the control mode is switched from load control to strain control. The current strain signal (at the moment of switching to strain control) is used as set-point for keeping the strain constant from that point on, during the entire TMF test duration. The aforementioned actions are intended to bring the specimen in a well-defined condition, serving as a reference point from which TMF cycling can be consistently launched for all TMF tests.
In general, repetitions of identical processes can be performed by using a looped procedure. The MPT™ software is appropriately equipped with an option for looping actions designated as “group procedure” which can be incorporated in a test procedure

[14] MTS Model 609 alignment fixture and the accompanying software.
[15] MTS extensometer model 632.53 F-14.
[16] Details about the data acquisition strategy and the stopping test procedure are treated in appendix B.
[17] The fatigue machine can be controlled also with “manual command”, allowing the operator to enter values for either load, displacement or strain levels, and to which the machine immediately responds. This manual command was used to manipulate the position of the grips in order to fit the specimen in the grips.

to contain a looped set of actions. The OP- TMF cycle employed in this research consists of four successive steps that are included in a looped group procedure. Steps *i)* to *iv)* include the following actions:

i) The specimen is heated by linearly increasing the temperature from 50 °C to 420 °C in 40 s (using a ramping action). A gentle cooling air flow is used during this stage, which proved to be beneficial for the stability of the temperature controlling loop.

ii) The temperature set-point is maintained at 420 °C for 30 s (using a hold action), enabling the temperature to homogenize throughout the specimen. Simultaneously, the cooling air flow is gently shut down, which proved to be beneficial for an accurate temperature measurement of the ribbon type thermocouple.

iii) The specimen is cooled in the first place by linearly decreasing the temperature set-point from 420 °C to 50 °C in 60 s (using a ramping action). Simultaneously, the air flow rate is linearly intensified to provide sufficient cooling capacity at lower temperature levels.

iv) The temperature set-point is maintained at 50 °C for 30 s (using a hold action), enabling the temperature to homogenize throughout the specimen. Simultaneously, the cooling air flow is gently shut down, for the same reason as mentioned in *ii)*. At the end of this step the specimen temperature reaches the start condition of the TMF cycle again.

In order to avoid sudden and brutal fracture of the sample, which may possibly damage the extensometer, it is necessary to terminate the test in a mechanically controlled manner. This is explained in detail in Appendix B.

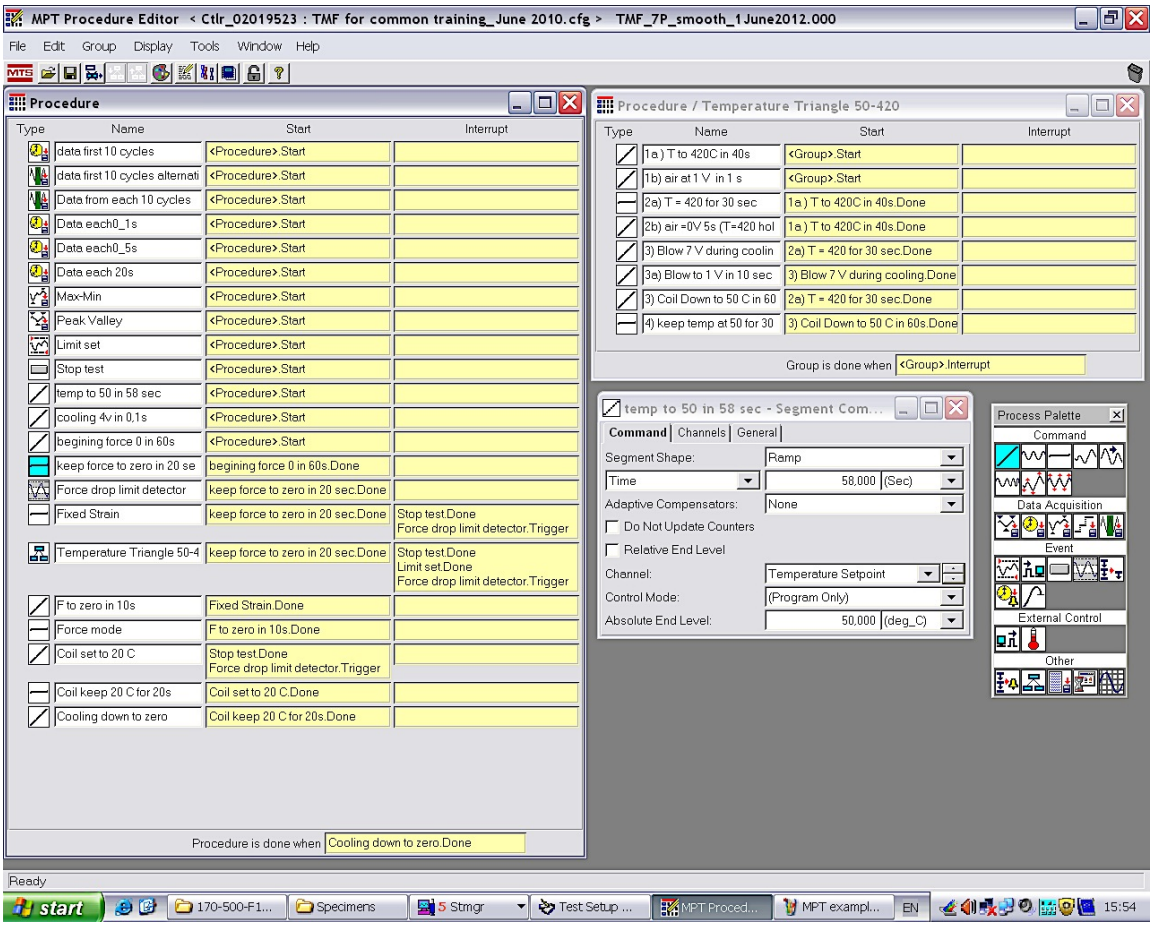

Figure 3.8 The configuration of most TMF tests performed, as defined by the actions in the Multiple Purpose Testing (MPT) procedure.

Data Acquisition Strategy

The duration of the performed TMF tests ranged from a few hours to some weeks. For analyzing test results and the data post-processing involved, it is convenient to work with a manageable file size. If the data file is too large it can become impractical (or even impossible) to handle files with standard software like Excel. Therefore, the data acquisition sampling rate must be optimized for each fatigue test, keeping data processing workable while maintaining a sufficient sampling rate for accurate analysis of the fatigue data. Also, analyzing different phenomena usually requires different data acquisition strategies. For this reason, several data acquisition processes were activated simultaneously, each dedicated to facilitate the evaluation of a particular phenomenon.
In general, three types of data acquisition were performed simultaneously during each TMF test, *i.e.*, peak-valley data acquisition, continuous (timed) acquisition and periodical acquisition. The simultaneous acquisitions each produced individual data files. The acquisition methods are treated in some more detail hereafter.

A peak-valley data acquisition option is provided in the MPT™ software. This feature is used to detect and store the maximum and minimum load levels[18] occurring during consecutive TMF cycles. The data file produced is compact and enables a quick evaluation of progressing minimum and maximum load levels during consecutive TMF cycles.
Timed acquisition constitutes the sampling of data at fixed time intervals throughout the duration of the test. Timed acquisition is employed mainly because it is a simple and trustable method to collect data, potentially serving as back-up file when other (more sophisticated) sampling methods would fail. Typically, the signals of load, strain, displacement and temperatures[19] were included with sampling rates of 1, 0.5 or 0.05 Hz, depending on the expected test duration. Especially during the initial TMF cycles the mechanical response of the material is expected to change significantly. For this reason, the first ten cycles of each test were recorded using timed acquisition with a sampling rate of 20 Hz.
Periodical data acquisition[20] involves logging data during certain preferred periods of the test only. It enabled the use of a high sampling rate to obtain detailed information for the selected test periods, while keeping the total file size within reasonable limits. Typically, an individual TMF cycle was logged for every ten intermediate TMF cycles, using a sample rate of 10 Hz.

3.3 Characterization Techniques and Analytical Procedures

3.3.1 3D X-ray Computed Tomography (CT)

In the present work a three-dimensional (3D) quantitative analysis is carried out in order to obtain an unambiguous characterization and objective classification of the complex graphite morphology of CGI. To this aim, the non-destructive technique of X-ray Computed Tomography (CT) with a phoenix Nanotom® scanner (Figure 3.9a) is applied for revealing the 3D image of the graphite network with sufficient resolution, down to several micrometers. The CT technique was applied to establish the graphite volume fraction as well as the graphite interconnectivity in CGI. Results are presented in chapter 4, section 4.2.
A schematic view of the apparatus is shown in Figure 3.9b. X-rays are generated when accelerated electrons hit a target material, which in this case was molybdenum. During a measurement the sample rotates over 360°, while a detector records the projections.

[18] In the MPT™ software the load signal was selected as so called “master signal”, while also instantaneous values of temperature, strain and displacement were added to the file.
The additional signals stored did not on forehand have a dedicated purpose but were just considered redundant information with potential to become useful later on.
[19] The TMF tests performed comprise the cycling of the temperature under a total constraint condition, involving the simultaneous operation of a temperature and strain control loop. For both control loops, the values of the command signal (*i.e.* set-point) and the actual value were recorded, enabling the monitoring of control loop deviations.
[20] In the MPT™ software, the option of periodical data acquisition is incorporated and designated as “cyclic acquisition”.

The projections contain information on the variation in X-ray attenuation within the specimen. With the use of an algorithm all projections are used to assign a grey value to coordinates in the cross section, reflecting the X-ray intensity, thus constructing an image of a single xy-slice [6]. With these 2D xy-slices, a 3D image will be reconstructed.

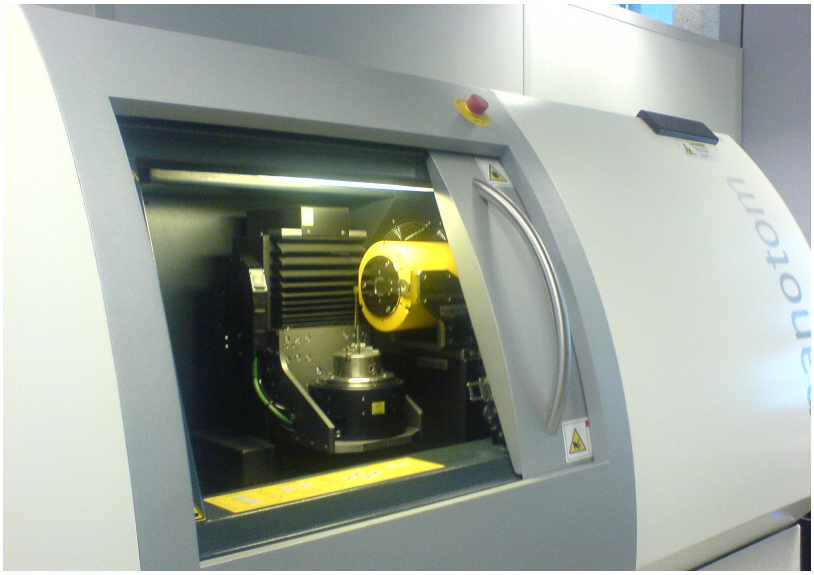

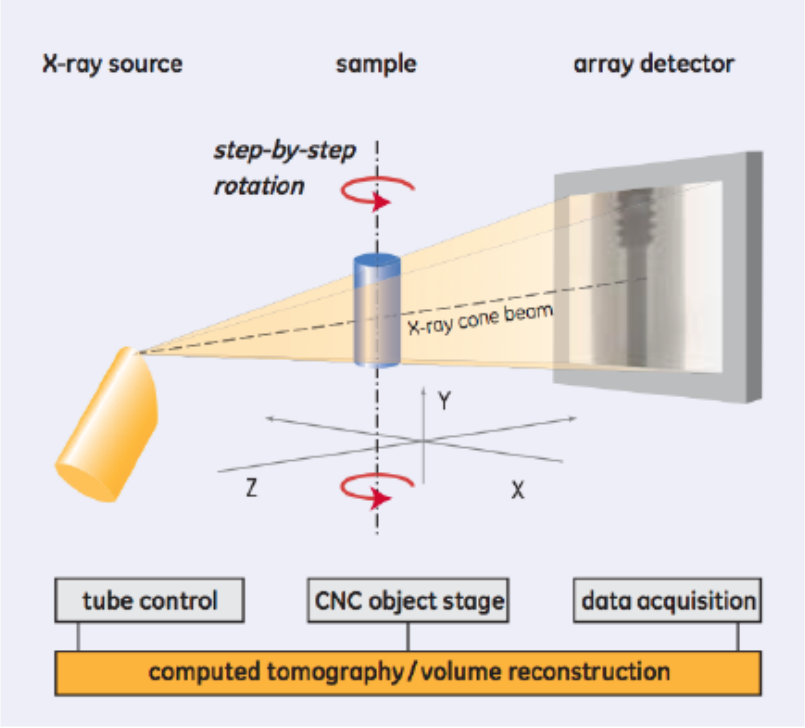

Figure 3.9 (a) The phoenix Nanotom® scanner used for scanning with X-ray computed tomography (CT). (b) A schematic view of the CT-scanner [6].

Before starting an X-ray scan on the specimen, it is important to optimize the settings of the scanner to achieve the highest resolution and hence the highest image quality, in

terms of sharpness and contrast (*cf.* Table 3.3). The resolution is dependent on a number of factors [6]:

- The distance between the source and the sample, *i.e.* the focus-object-distance (FOD);
- The distance between the source and the detector, *i.e.* focus-detector-distance (FDD);
- The resolution of the detector itself.

The highest resolution can be achieved by decreasing the FOD and increasing FDD, while the sample is kept within the total detector width and is sufficiently exposed. For a detector with a pixel size *P*, this results in a voxel resolution *V* of, *cf.* equation 3.3:

$$V = P\frac{(FOD)}{(FDD)} \qquad (3.3)$$

The sharpness of the image depends on the spot size of the beam. To achieve a maximum sharpness, the spot size should be as small as possible. The sharpness is also affected by thermal fluctuations in the system caused by heating of the specimen due to exposure by the X-ray source.
The contrast of the image, apart from the sample characteristics, depends on the X-ray spectrum and exposure time. Generally, a low-energy X-ray beam creates more contrast than a high-energy X-ray beam because the low energy radiation is more easily attenuated. Therefore, the ratio of strongly to weakly absorbed photons will be larger with low energy radiation. Hence, a larger contrast between the areas of different thickness is obtained.
However, the downside of this is that low-energy X-rays are attenuated more easily, especially for metals and therefore a lower signal-to-noise ratio is obtained. For CGI the attenuation of X-rays is very severe for low- energy beams, *i.e.* beams generated with a low acceleration voltage. Hence a suitable optimum must be found between contrast on the one hand and signal-to-noise ratio on the other hand.
As the low-energy X-rays are absorbed by the sample, the remaining X-rays become harder and thus the beam becomes more penetrating. This phenomenon is known as beam hardening. As a result of beam hardening, the effective attenuation coefficient of a material depends on the thickness of the crossed material. The effect causes so-called beam-hardening artefacts to occur in CT images. If beam hardening is not appropriately corrected for, a reduction of the reconstructed attenuation coefficient toward the exit surface of the sample occurs.

CT: Sample Preparation

A small cylindrical specimen (mm-sized) of CGI is used to obtain a high resolution and sharp image. If the sample is too large, the attenuation of X-ray is too large and then there is a risk of insufficient intensity to capture a sharp image. Therefore, comparatively small samples are taken out of the cylinderhead by electrical discharge machining (EDM)

and afterwards machined to the appropriate dimensions, *cf.* Figure 3.10. The height of the sample that is actually scanned is 2 mm and has a diameter of 1 mm. The sample consists of the volume to be scanned with an additional socket and is made out of one piece [6].
The samples are mounted on a sample holder made out of Invar[21], which is specially designed for CT-analysis. It is known that the sample must be as close to the X-ray source as possible and that the sample may not show any translations during a measurement. No linear expansion due to thermal changes may occur, despite heating of the specimen and holder by the beam. Normally, the sample is mounted on a tube made from quartz, because of its low linear thermal expansion coefficient. Quartz is quite brittle, however, and cannot be machined. Invar has the same low linear thermal expansion coefficient and the additional advantage is that it can be machined. A technical drawing can be found in Figure 3.10 [6]. The cap made of invar and the scaffold on which the specimen rests comprise the sample holder.

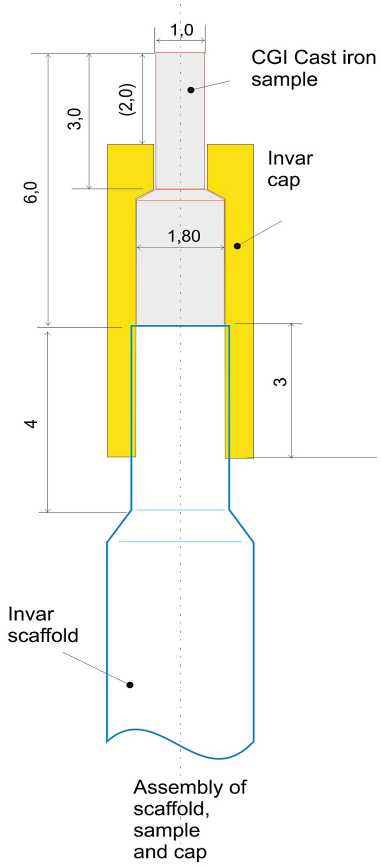

Figure 3.10 Technical drawing of the CT-specimen and sample holder. Sample mounted in the holder; the holder consists of a cap screwed on the scaffold with the CGI sample tightened in between. Dimensions are indicated in mm [6].

[21] Invar is a metal with a chemical composition of 36 % Ni, trace elements of Si, Mo, and C and balanced by Fe ≈ 64%. It is favored for its extremely low thermal expansion coefficient.

CT: Measurement Settings

For each measurement, the settings leading to the highest image resolution are used. At each measurement the distance between source and sample (FOD) is approximately 6 mm, and the distance between source and detector (FDD) is 300 mm. This leads to a voxel size of 1.04 μm^3 [6]. To achieve maximum sharpness, spot mode 1 (second largest spot size) of the beam has been used throughout the measurement with an exposure time of 1.5 s per projection. For each projection 3 images were taken of which only the last two were averaged and the first one was eliminated in order to avoid the effect of afterglow. For the CGI samples in initial state an acceleration voltage of 140 kV and a current of 30 µA were used for the generation of X-rays. In order to make sure the settings yield the best result, a live image grey-value histogram is recorded, to obtain optimum intensity and contrast. The range of grey values is optimized to completely capture all the grey values present in the sample, which results in good contrast in the reconstructed image. The settings of voltage and electrical current are set to yield sufficient lateral resolution in grey values to obtain maximum contrast. The settings of the CT-scanner used for CGI in the present work are shown in Table 3.3.

Table 3.3 Settings of the CT-scanner used for analysis on CGI samples [6].

Parameter	Value	Unit
Magnification	50	[-]
Voxelsize	1.04	[μm^3]
Correlation value	0	[-]
FOD	6	[mm]
FDD	300	[mm]
Tilting angle	0	[°]
Number of images	720	[-]
Total rotation	360	[°]
Exposure time	1500	[ms]
Voltage	140	[kV]
Current	30	[µA]
Spot mode	1	[-]
X-ray filter	None	[-]

CT: Image Reconstruction

Each scan produces a series of grey scale projections for consecutive slices of the sample. A reconstruction has to be made out of this set of projections. The program datos|X-®reconstruction is used to build up a 3D image. The program makes use of subsequent image files to combine the 720 (2D) projection images of the sample. Before a reconstruction can be started, the data from the scan have to be optimized. First, a geometrical correction must be applied which involves alignment of the images by the function *'automatic geometry calibration'.* This correction procedure calculates the

deviation of the first and last projections, so as to map both one-to-one on each other. Second, the beam hardening correction has to be applied. The correction values highly depend on the voltage and electrical current of the generated beam and the sample material. The purpose of this correction is to obtain a homogeneous distribution of grey values in the matrix for a featureless sample. Afterwards, a scan optimization on the first and last image projections is performed. Scan optimization is necessary as the sample moves during the scan, which can cause a slight deviation between the first and last cross section image. With the scan optimization this can be corrected, by moving the first and last image in any direction to let them fit.

3.3.2 Orientation Contrast Microscopy (Electron Backscatter Diffraction — EBSD)

Polycrystalline materials can be considered as aggregates of single crystals, which each have a specific crystallographic orientation. The distribution of the crystallographic orientations in a material is very often described quantitatively by means of the Orientation Distribution Function (ODF). This function can be determined by X-Ray Diffraction (XRD) or by Electron Backscatter Diffraction (EBSD) [7]. In our research, the latter technique was used to study crystallographic orientations. Electron Backscatter Diffraction patterns (EBSP) were first observed in Transmission Electron Microscopy (TEM) by Kikuchi in 1928. Therefore, EBSD patterns are also known as backscatter Kikuchi diffraction patterns (BKD). EBSD is based on the principle of Bragg's law but the much smaller beam diameter (a few nm) allows obtaining very local microstructural information. It is used to perform quantitative microstructure analysis in the Scanning Electron Microscope (SEM), on a millimetre to a nanometre scale with good spatial resolution (20 nm) and excellent angular resolution for the crystallographic orientation (~0.7°). Since the 1990's EBSD has developed into the most powerful microstructural visualization technique, which allows for a quantitative characterization of crystallographic phases, crystal orientation, grain and subgrain size on a length scale varying from mm to nm. One of the main advantages of EBSD images is their potential for quantification and statistical data processing. Whereas image contrast in the more conventional metallographical techniques is often obtained by chemical etching of the sample surface, the contrast in an EBSD image is based on crystallographic data, which can be readily used for further numerical analysis.
In EBSD a stationary electron beam strikes a crystalline sample tilted by approximately 70° relative to the electron beam of the SEM. This glancing angle condition is required to optimize both the contrast in the diffraction pattern and the fraction of electrons scattered from the sample. The electron beam is diffracted by the crystal lattice of the sample at the incident beam point on the specimen surface (*cf.* Figure 3.11a). Electrons that satisfy the Bragg condition for a crystal plane are diffracted and show the Kikuchi bands (*cf.* Figure 3.11b). A series of data points obtained by scanning the beam across the sample may be plotted as pixels to form an orientation map [8-11].

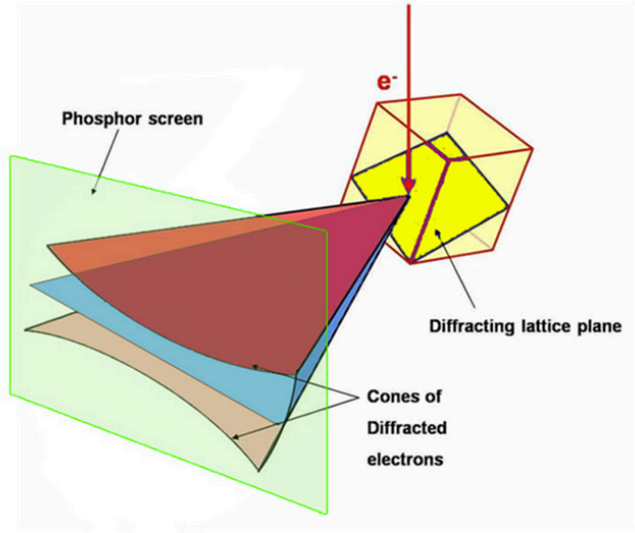

(a)

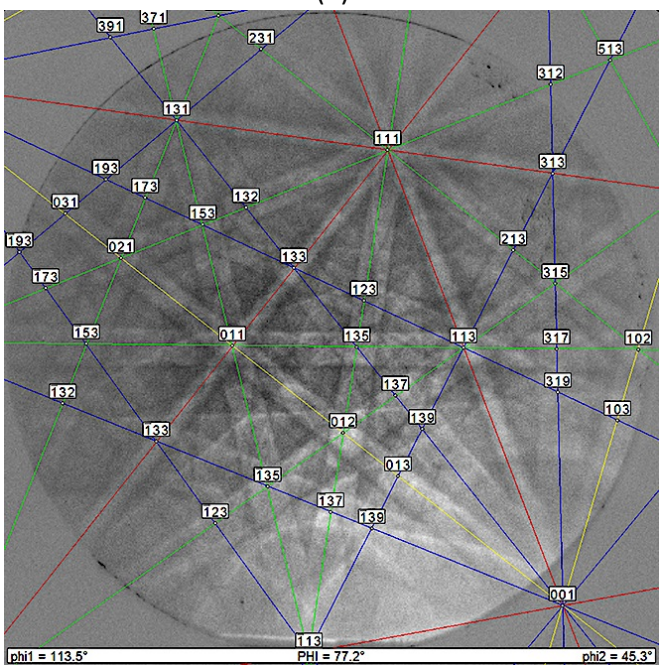

(b)

Figure 3.11 Formation of the electron backscatter diffraction pattern. (a) A schematic drawing shows electrons from a source incident on crystal planes at the Bragg angle are diffracted into a pair of cones to form Kikuchi bands in the diffraction pattern. (b) A high contrast electron diffraction pattern from CGI collected at 20 kV accelerating voltage [10].

EBSD: Basic Set-up

The EBSD acquisition hardware generally comprises a sensitive Charge Coupled Device (CCD) camera, and an image processing system for pattern averaging and background subtraction. Figure 3.12 represents a schematic diagram showing the main components of an EBSD system, which is typically configured of the following components [8-11]:

- A phosphor screen which is fluoresced by electrons from an exposed sample to form the diffraction pattern.
- A digital high-sensitive CCD camera together with optics for viewing the diffraction pattern on the phosphor screen. Nowadays, modern digital cameras may record up to 600 patterns per second.
- A lead glass radiation shield behind the phosphor screen to block the radiation.
- Vacuum seals that allow the camera to operate at atmospheric pressure without degrading the chamber pressure.
- A computer to control EBSD experiments; collect and analyze the diffraction patterns as well as display results and do further processing.
- Electronic hardware that controls the SEM scanning.
- Communication control of SEM stage and column.

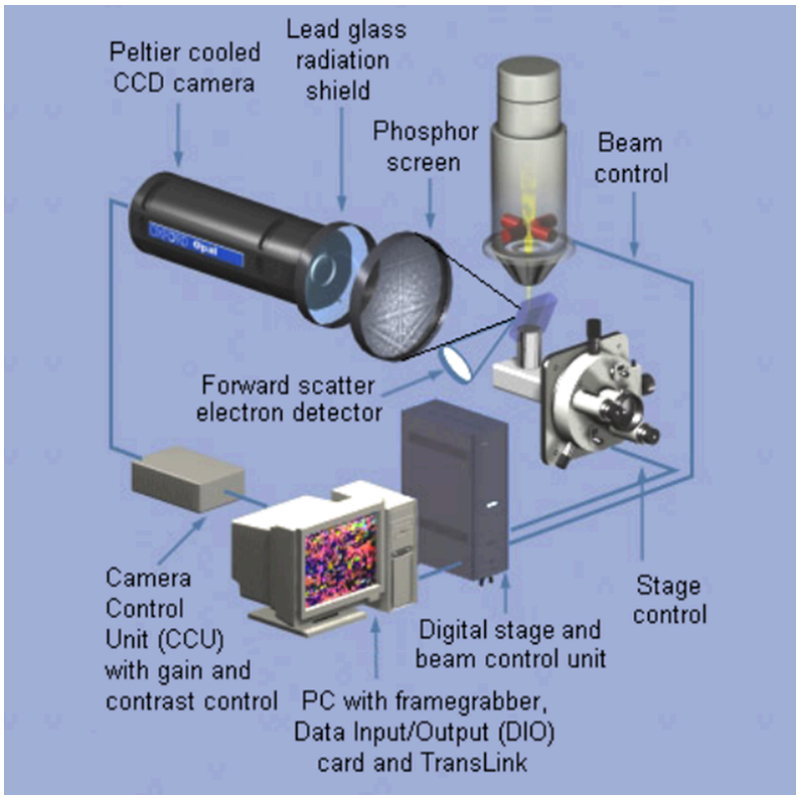

Figure 3.12 Schematic diagram of a typical EBSD installation in an SEM chamber [10].

EBSD: Sample Preparation

EBSD is very sensitive to crystalline imperfections and a very careful sample preparation is required to remove any surface damage. The preparation of an outer surface layer of 10 to 50 nm with the characteristic condition of the sample is of critical importance for a successful EBSD experiment, *i.e.* no mechanical damage (*e.g.* caused by grinding) should be present, hazardous surface layers (*e.g.* oxides, coatings or contamination) should be

removed. Conventional metallographic techniques can normally be used successfully: for metals and insulators, mounting in conductive resin, mechanical grinding, diamond polishing and final polishing with colloidal silica or electropolishing are suggested. The final and the most important preparation step for the CGI material currently under investigation consists of manually polishing the surface up to 40 minutes with an abrasive oxide polishing suspension, *i.e.* colloidal silica (OP-S) with a particle size of 0.25 µm.

EBSD: Measurement Settings

The EBSD system of type EDAX-TSL® that was used in the current study was mounted on a FEI quanta 450® microscope with Field Emission Gun (FEG) filament. In the current measurement setup a tilt angle of 70° was used (*i.e.* the angle between the sample surface normal and the beam) and a working distance of 25 mm. In EBSD operating conditions, a medium to high acceleration voltage of 20 to 30 kV is applied with an incident beam current from 1 to 15 nA. Unfortunately, these operating conditions do not allow obtaining the highest possible resolution (~1 nm) as in conventional secondary electron imaging mode. Conversely, the EBSD operating conditions only allow resolution of the order of 20-30 nm.
A series of data points is obtained by scanning the beam across the sample. With each data point a record is registered that contains the following information:

- X, Y coordinates of the data point;
- The three Euler angles that characterize the crystallographic orientation of the data point;
- A specific number that refers to the crystal phase of the data point;
- The image quality of the data point (*cf.* infra);
- The confidence index of the data point (*cf.* infra).

The image quality (IQ) is a parameter that quantifies the sharpness of the EBSD pattern. It is very sensitive to a variety of features such as sample preparation, chemical composition, crystal phase and crystal orientation, but most importantly to the density of crystal defects *e.g.* dislocations.
The confidence index (CI) is a measure of the reliability of the orientation determination (*i.e.* calculation of Euler angles on an indexed pattern representing a solution of that pattern). As the EBSD pattern contains ample redundant information for orientation determination, it implies that the Euler angles associated with the Kikuchi pattern can be calculated may times over. The *CI* is defined in the following way, *cf.* equation 3.4:

$$CI = \frac{V_1 - V_2}{V_{tot}} \qquad (3.4)$$

with V_{tot} the total number of solutions, V_1 and V_2 are the largest and the second largest number of identical solutions, respectively.

EBSD: Scanning Step Size

The appropriate scanning step size was chosen in function of the characteristic length scale of the microstructure, in order to obtain a sufficient statistical representation of the microstructural elements. Typically the step size is one order of magnitude smaller than the characteristic microstructural length scale. In the case of the heterogeneous pearlitic CGI under investigation with a typical graphite particle size of 47± 25 µm (*cf.* chapter 4, section: 4.2) and the grain size of 120-150 µm, the employed step size varied from 1 to 5 µm, depending on the optimum scanning time.

EBSD: Data Acquisition Program and Post-processing: Orientation Imaging Microscopy (OIM®)

The EBSD acquisition software controls the data acquisition, solves the diffraction patterns and stores the data. Further software is required to analyse, process and display the data.
One of the fully automated data acquisition programs used is the Orientation Imaging Microscopy (OIM®), which collects and processes EBSD patterns. The principle of OIM program is illustrated in Figure 3.13.

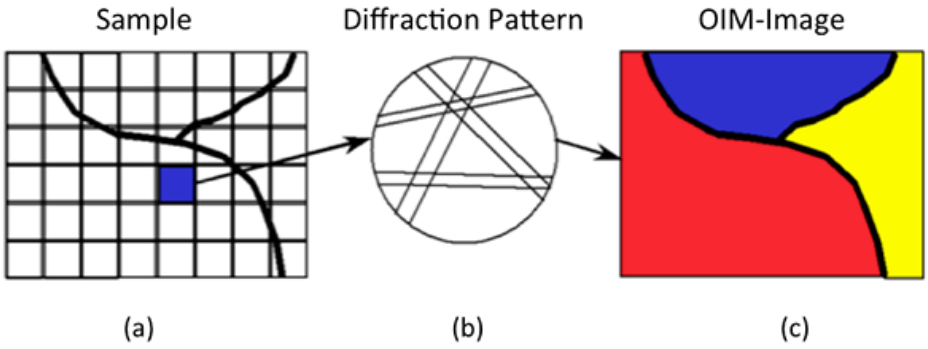

Figure 3.13 Principle of the OIM measurement [7].

As the electron beam scans the microstructure (Figure 3.12a), the EBSD patterns (Figure 3.13b) are collected, stored and analyzed. This implies that the crystal structure is identified, the pattern is indexed and the orientation is calculated. During post processing these data are transformed into an image in which crystallographic orientations are represented according to a certain color code (Figure 3.13c). One of the most used color codes is the so-called Inverse Pole Figure map (IPF) in which each crystal is given specific color depending its orientation with respect to specific sample reference direction. Other colored maps are also possible, like *e.g.* unique grain colored maps in which each specific grain is assigned an arbitrary color. One has to realize though that the EBSD data do not recognize data as such. Grain boundaries are identified by specifying a misorientation threshold, *e.g.* 15 ° for high angle grain boundaries (HAGB). More detailed information about the principal of EBSD is given in chapter 7, section 7.1: Background: orientation contrast microscopy.

3.4 References

[1] Vermicular Cast Iron, Un-alloyed, DAF Document, Reference Number: MAT 08080/08099, July 2004 Issue02.
[2] ASTM E8, Standard Test Methods for Tension Testing of Metallic Materials.
[3] ASTM E21, Standard Test Methods for Elevated Temperature Tension Tests of Metallic Materials.
[4] Zieher F., Langmayr F. Engine Simulation in View of Reduced Development Time. Technical, Paper Code: F02V081, AVL List GmbH, Austria, 2002.
[5] Hähner P, et al., Research and development into a European code-of-practice for strain-controlled thermo-mechanical fatigue testing, Int. J. Fatigue 2008; 30: 372-381.
[6] Verkleij N. Thermo-Mechanical Fatigue of Compacted Graphite Iron, MSc Thesis, Delft University of Technology, Faculty of Materials Science and Engineering, Department of Joining and Mechanical Behavior, In assignment of DAF Trucks N.V. a PACCAR company, October 2011; 54-60.
[7] Gaggiano R. Study of the Deposition and Interaction Mechanics of Aluminium and Copper Designed Surfaces, PhD thesis, 2012; ISBN 978 90 5718 140 5.
[8] Humphreys F.J. Hatherly M. Recrystallization and Related Annealing Phenomena, 2nd Ed., 2004 Elsevier Ltd.
[9] ENGLER O., RANDLE V. Introduction to Texture Analysis, Macrotexture, Microtexture, and Orientation Mapping, 2nd Ed. CRC Press, 2010; Taylor and Francis Group, LLC.
[10] www.EBSD.com
[11] Decocker R. Modeling the Crystallography of the Transformation of Austenite to Low Temperature Phases in Fe-based Alloys, PhD thesis, 2006; ISBN 90-8578-078-0.

4

Characterization of Microstructure and Mechanical Properties of CGI at Ambient and Elevated Temperature

"The true worth of an experimenter consists in his pursuing not only what he seeks in his experiment, but also what he did not seek".

Claude Bernard

In this chapter, a detailed account is presented on the characterization of the microstructure of the graphite morphology in three dimensions (3D) in order to obtain a better insight in the complex morphology of CGI.
Additionally[1], to investigate the effect of elevated temperatures and/or thermal cycling on the evolution of microstructure of CGI during thermo-mechanical fatigue and the microstructural origin of oxidation and its effect on the extent of volume change, annealing experiments were performed with and without the presence of an oxidizing atmosphere. The microstructural evolutions of such experiments were probed by scanning electron microscopy and electron probe microanalyses to investigate the formation of oxide layers around the graphite particles.
Moreover, in order to explore the effect of the initial state of CGI on the room temperature tensile properties and fatigue lifetime, three different conditions were considered: as-cast, annealed in open atmosphere (oxidized) and annealed in vacuum.

[1] This section of chapter is based on: S. Ghodrat, M. Janssen, L.A.I. Kestens, and J. Sietsma, Volume Expansion of Compact Graphite Iron Induced by Pearlite Decomposition and the Effect of Oxidation at Elevated Temperature, Oxidation of Metals, March 2013, DOI: 10.1007/s11085-013-9406-y.

4.1 Introduction

To quantitatively correlate the cast iron microstructure with its mechanical and thermal properties, the graphite particles need to be characterized according to their shape and morphology. The most widely used parameters in two dimensions (2D) are roundness, nodularity and aspect ratio.

The roundness *R* of a graphite particle is defined by equation (4.1):

$$R = \frac{4A}{\pi l_{\max}^2} \tag{4.1}$$

with *A* is the surface area of the particle as observed in a metallographic image and l_{max} the longest dimension of the particle. It is obvious that for a spherical particle $R = 1$, whereas *R* decreases to zero with increasing deviation from the *spherical* shape. For an entire population of graphite particles the nodularity *N* is defined by equation (4.2):

$$N = \frac{\sum_i A_i + \frac{1}{2}\sum_j A_j}{\sum_k A_k} \tag{4.2}$$

with index *i* including the nodular graphite particles,
with index *j* including the intermediate graphite particles,
with index *k* including the total graphite particles with l_{max} >10 μm.
The nodularity corresponds to the area fraction of particles that exhibit a roundness exceeding a certain critical limit; these are the so-called nodular particles with area fraction A_i. The particles of intermediate nodularity are the ones with a roundness just below this limit, with area fraction A_j. According to the *SinterCast* classification of graphite particles with respect to roundness [1], particles are considered to be *nodular* if $R > 0.625$, whereas particles with $0.525 < R < 0.625$ are considered as particles of intermediate nodularity. In the entire analysis, only particles with a size l_{max} larger than 10 μm are considered. This is somewhat arbitrary, but chosen just to exclude non-graphite particles such as inclusions, or defects.
If the volume *V* of a graphite particle is approximated by the following equation (4.3):

$$V = \frac{4}{3}\pi\, a\, b^2 \tag{4.3}$$

With *a* the longest dimension of the particle, then the aspect ratio is determined by the division of the smallest length by the largest length, *i.e. b/a*. This assumes that *a* and *b* can be determined by microscopy observations.

The complex and irregular graphite morphology, such as the one in CGI, makes the 2D characterization rather inaccurate, since the size and shape in the third dimension is not considered. However, the ability to characterize the shape of compacted graphite is very important in order to better understand the behavior of the material under thermo-mechanical fatigue conditions. Therefore, in the present work a three-dimensional (3D) quantitative analysis is carried out in order to obtain a more complete characterization and objective classification of the complex microstructure of CGI. To this aim, the non-destructive technique of X-ray computed tomography (CT) is applied for revealing the 3D image of the graphite network with a sufficient resolution, down to several micrometers. CT technique was applied to establish the graphite volume fraction as well as the graphite interconnectivity in CGI. The degree of interconnectivity is important to assess effects of oxidation and the associated mechanisms of damage initiation and growth (*cf.* section 4.2).
In addition, it is known that during exposure to elevated temperatures, a *growth* phenomenon can occur in cast irons. This growth represents a volume increase resulting from oxidation and from structural breakdown of the pearlite matrix, *i.e.* the decomposition of pearlite to ferrite accompanied by the formation of the lower-density graphite (graphitization) [1]. To investigate the effect of elevated temperatures and/or thermal cycling on the evolution of microstructure of CGI during thermo-mechanical fatigue, this effect is first investigated in a static condition. To this purpose, the results of annealing experiments with and without the presence of an oxidizing atmosphere were compared.
In section 4.3, the effect of an extended annealing treatment at 420 °C (corresponding to the maximum working temperature in diesel engines) on the microstructure of a pearlitic CGI is investigated. The growth results as a function of exposure time are presented, together with related microstructural evolution including phase transformations and oxidation. These results are completed by scanning electron microscopy and electron probe micro analyses to investigate the formation of oxide layers around the graphite particles. Furthermore, annealing treatments in the high-vacuum furnace of a dilatometer allowed to measure the growth in an atmosphere without oxygen and to assess the influence of the oxidation process.
Moreover, in order to know whether the mechanical behavior of CGI (mainly its tensile and fatigue properties) is influenced by the initial state of the microstructure and if so, to what extent it is of importance, tests were performed on CGI with different initial states. The initial states correspond to as-cast, oxidized (*i.e.* annealed in an open atmosphere) and vacuum annealed. By comparing the properties of materials in different annealing conditions with that of the as-cast one, the influence of the initial state on the properties of CGI can be investigated. These results are presented and discussed in section 4.4.

4.2 Characterization of CGI Microstructure with 3D X-ray Computed Tomography (CT)

With optical microscopy and the help of image analysis software (Analysis Pro®) microstructural images taken from different locations in valve bridge areas of a cylinder head were analysed. After analysing these images, the graphite volume comprised 10 %

of the volume of cast iron. Only graphite particles larger than 10 µm were considered for the roundness *R* characterization (*cf.* section 4.1). Measured for 2126 graphite particles, an average value of 0.35 was obtained for the roundness. Knowing the area fraction of graphite nodules ($R > 0.625$), the intermediate graphite particles ($0.525 < R < 0.625$), and the total area fraction of graphite, the nodularity is calculated as the ratio described by equation (4.2). The average of nodularity from the image analysis is found to be 9.6%.
From the same set of graphite particle images, an average particle size of 45 µm has been established. A typical micrograph used for this analysis is shown in Figure 4.1. In this analysis the standard deviation of the graphite particle-size distribution was found to be 25 µm.

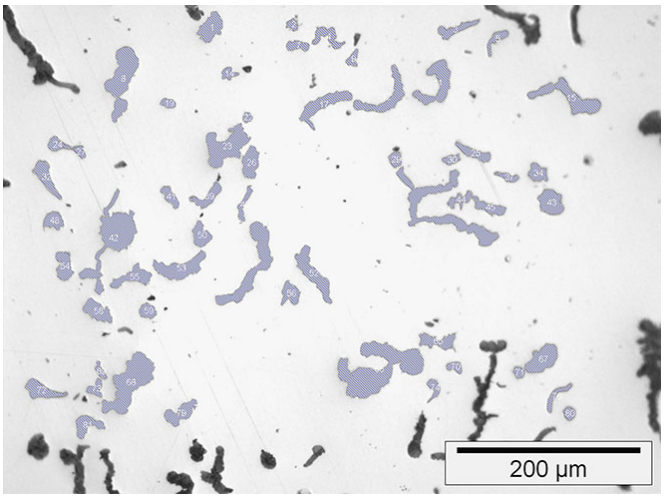

Figure 4.1 A typical micrograph processed by image analysis software for analyzing graphite particles.

In order to non-destructively visualize the graphite phase in 3D and its interconnectivity, a Phoenix Nanotom X-ray computed tomography scanner is used (chapter 3, section 3.3.1). A cylindrical specimen (diameter 1 mm and height 2 mm, volume 1.57 mm^3) was scanned and after the scanning, reconstruction was performed to visualize the microstructure and to measure the volume fraction of graphite and also to measure the cells within which the graphite particles are interconnected. Figure 4.2 represents a 2D reconstructed X-ray image of the specimen cross-section. In this figure, a ring is defined inside the 2D reconstructed image (blue circle). With this area-of-interest, there is a volume inside the sample in which the effect of edges as well as the graphite particles at the surface of the sample is eliminated. The calculated volume fraction of graphite depends on the threshold gray-value *G* that is determined by the operator. Choosing the correct threshold is a delicate issue, since the transition from graphite particles to matrix is not very sharp due to the limited spatial resolution of 5 µm.
It was found that by changing the threshold of gray-value *G*, the graphite volume changes remarkably. In this study the best threshold value was determined to be the one that yielded a total volume fraction of graphite that corresponds best to the one determined with the optical metallography images in 2D. If the entire gray-value domain

is considered between 0 and 1, with 0 corresponding to black and 1 corresponding to white, the optimum graphite domain was determined to be between 0.29 and 0.71. The domain with $G > 0.71$ corresponds to the region outside the specimen (air) and $G < 0.29$ is the matrix, *cf*. Figure 4.2. This threshold leads to a volume of 0.09 mm^3 of graphite, which corresponds to 14% of the reconstructed volume of the cylindrical specimen that was considered in the data analysis, *i.e.* the volume-of-interest (0.62 mm^3), which is within the entire volume of 1.57 mm^3 of the sample.

To define the interconnectivity of the graphite particles, the so-called eutectic cell definition given in Ref. [2] is used. The eutectic cell is a contiguous volume of graphite in which the graphite particles are interconnected. Eight representative eutectic cells were selected randomly and evenly spread over the sample volume, avoiding intersection with the edge of the sample.

These eight eutectic cells are shown in Figure 4.3, and the size is listed in Table 4.1. From these 8 eutectic cells the average cell size was determined to be 2.2 10^{-3} mm^3. With a total graphite volume of 0.09 mm^3, it ensues that there are approximately 40 eutectic cells within the volume under consideration of 0.62 mm^3. Hence, the number of graphite cells per unit volume is calculated to be 64/mm^3. In a spherical volume an average eutectic cell would have a diameter of 160 µm.

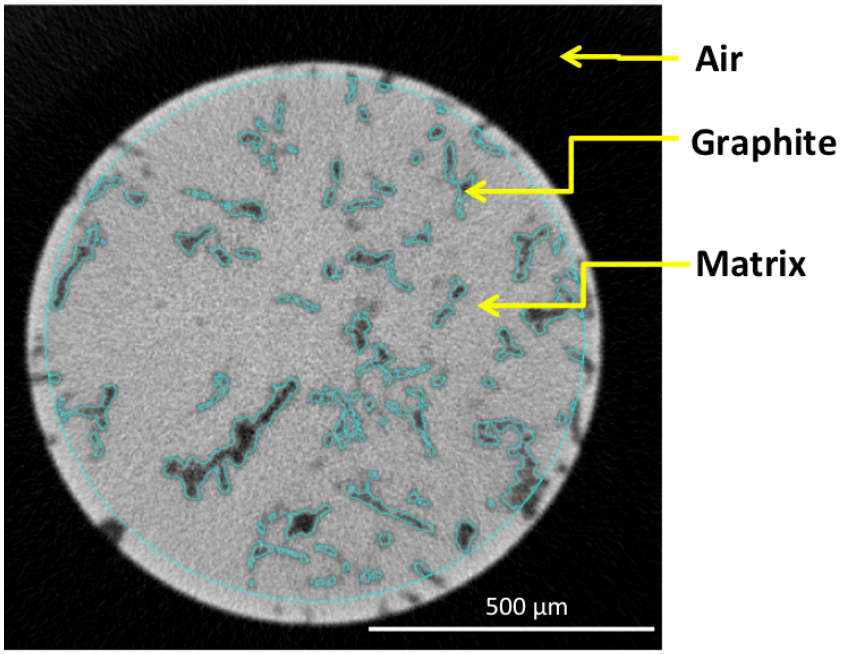

Figure 4.2 One 2D section of the reconstructed specimen.

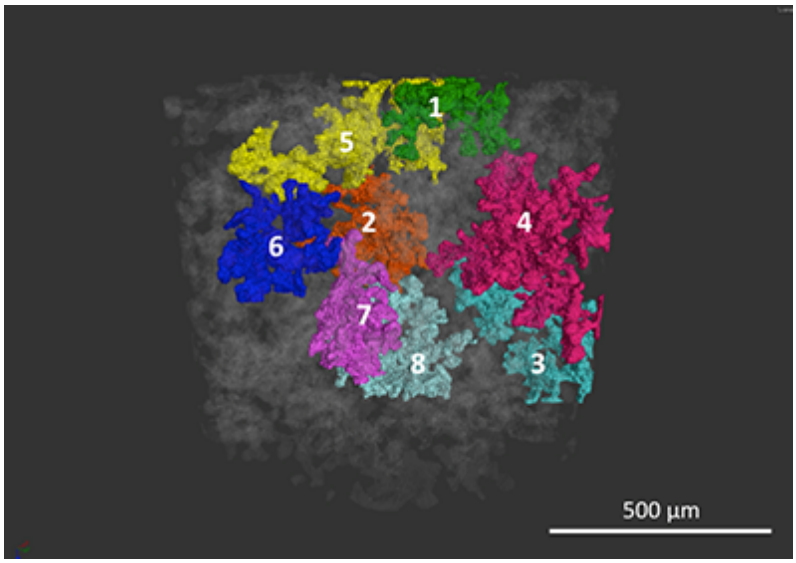

Figure 4.3 3D X-ray tomography of a cylindrical specimen (*d* = 1 mm, *h* = 2 mm) with 8 eutectic cells, voxel size = 1 µm^3/vox.

Table 4.1 The eight eutectic cell sizes measured in different locations inside the scanned specimen.

1	2	3	4	5	6	7	8	Avg. Eutectic cell
Size (mm^3)								
$9.2\ 10^{-4}$	$1.9\ 10^{-3}$	$3.0\ 10^{-3}$	$3.5\ 10^{-3}$	$2.2\ 10^{-3}$	$1.6\ 10^{-3}$	$1.7\ 10^{-3}$	$3.3\ 10^{-3}$	**$2.2\ 10^{-3}$**

4.3 Microstructural Evolution and Growth Phenomenon in CGI at Elevated Temperature Annealing[2]

Engine cylinder blocks and heads are subjected to prolonged periods of cyclic heating and cooling during engine operation at elevated temperatures. These conditions may give rise to the evolution mechanisms of microstructure, such as decomposition of the pearlite matrix accompanied by the formation of lower-density graphite and oxides, which leads to an increase of material volume, *i.e.* the so-called *growth* phenomenon. The growth phenomenon in cast iron, in this study CGI, affects the physical and mechanical properties at elevated temperatures and accordingly the thermal fatigue properties.

[2] This section of chapter is based on: S. Ghodrat, M. Janssen, L.A.I. Kestens, and J. Sietsma, Volume Expansion of Compact Graphite Iron Induced by Pearlite Decomposition and the Effect of Oxidation at Elevated Temperature, Oxidation of Metals, March 2013, DOI: 10.1007/s11085-013-9406-y.

One way to measure the effect of structural changes taking place at a microlevel in cast iron is through growth testing. In a growth test, the length and mass of a standard specimen are measured before, during and after exposure to an air environment at elevated temperature. The observed change in length reflects microstructural changes taking place in the specimen. To study these changes, the as-cast material was exposed in air at a selected elevated temperature for different exposure times. Additionally, annealing experiments were carried out under high vacuum conditions in order to compare the growth behavior with and without the presence of an oxidizing atmosphere. These growth experiments were carried out in vacuum (10^{-4} mbar) in a dilatometer, which allowed for precise characterization of the volume change. Consequently, in the dilatometer tests, phenomena like decarburization and internal oxidation were prevented from taking place.

4.3.1 Background

Several investigations [2-8] on cast iron indicate that the degree of pearlite decomposition and oxidation depends on temperature, exposure time and chemical composition. Decomposition of pearlite into ferrite and graphite and the resulting increase in graphite volume fraction are potentially the main changes occurring in the matrix of a pearlitic CGI, composed of graphite particles, pearlite, with a variety of lamellar structures, and a small fraction of ferrite. Yuzvak *et al.* [3] indicate that pearlite decomposition into ferrite and graphite in graphitic cast irons is accompanied by a 2.04 % increase in volume. In terms of mechanical properties, this decomposition gives rise to softening of the iron matrix.

With regard to oxidation in cast iron, it was found that during exposure to air at elevated temperature, graphite at the surface starts to oxidize immediately and a rapid carbon loss takes place. Gradually oxygen penetrates into the structure along the graphite particles, leading to the oxidation of carbon (graphite) with the formation of gaseous reaction products CO/CO_2 and eventually leaving empty cavities behind [8]. Buni *et al.* [4] describe that oxidation of the graphite phase reduces the bond between the matrix and the graphite, resulting in the creation of holes.

References [7-10] suggest that metal oxidation starts at the surface and that this superficial oxidation in general relates to the formation of a scale of iron oxides (Fe_3O_4, FeO, Fe_2O_3) [2, 10]. Silicon interaction with oxygen cannot be neglected in cast iron as its content is much higher (typically 3 at.%) than in steel [10]. Therefore the internal layer of the oxide scale might be composed of a mixture of FeO and Fe_2SiO_4. According to Jedrzejczyk *et al*. [10] silicon can cause a decrease of the metal oxidation rate, both during superficial and internal corrosion. The more silicon is added, the more oxidation protection is expected. For example, it is known that silicon in ductile cast iron is highly effective in oxidation protection through the formation of a silicon-rich oxide layer [2].

Many studies [2, 4-7] conclude that internal oxidation is influenced by the graphite morphology. Oxygen can penetrate more easily in flake graphite iron (FGI) and also in CGI than in nodular iron, due to the interconnecting arrangement of graphite, which provides favorable paths for oxygen transport into the material. Nevertheless, most of the previous work in the area of graphitic cast iron has been focused on FGI and

spheroidized graphite iron (SGI). Since in the past most of the engine parts were made of these two cast-iron grades, much less is known on the influence of the graphite morphology of CGI on internal oxidation and microstructure development. For a better understanding, however, of a complicated phenomenon such as thermomechanical fatigue, it is necessary to have better knowledge on the microstructural evolution of CGI at elevated temperatures and/or during thermal cycling.

Growth tests in unalloyed cast irons point out that structural decomposition might already take place at 400 ˚C [6, 7], although at a low rate. At 450 ˚C pearlite decomposition becomes significant for dwell times above 2000 h, while only for temperatures higher than 500 ˚C, the decomposition can be found after less than 1000 h [6, 7]. However, it is known that pearlite decomposition can be retarded by increasing the silicon content and by alloying with tin, chromium and molybdenum [2]. Addition of elements such as Cr, Sn or Cu can produce structural stabilization up to 450 ˚C and for shorter exposure times up to 550 ˚C. Results of Roehrig [6] show that above 550 ˚C, unalloyed cast irons exhibit pearlite decomposition after a few hundred hours while iron alloys with a Cr content up to 0.7% show decomposition only after approximately 1000 h.

With regard to oxidation, there are two types of oxidation that occur in cast iron: metallic oxidation, known as scaling, and oxidation of carbon, leading to decarburization. The latter process occurs because the chemical potential of carbon in CO or CO_2 is lower than that in the graphite of the cast iron. Therefore, mass is lost by decarburization, whereas mass is gained by the formation of scale layers. Thus, the mass change is a balance between scaling (mass gain) and decarburization (mass loss) [8]. According to Roehrig [6], the rate of oxidation strongly depends on temperature. For example, if the temperature is increased from 450 to 500 ˚C the oxidation rate is doubled, while for a temperature increase from 550 to 650 ˚C, the oxidation rate increases by a factor of 8 leading to an effective activation energy of 97.8 kJ/mol [6].

The oxidation kinetics of a cast iron might occur in the following five stages, according to Merchant [8]:

(i) Oxidation of graphite directly exposed to the oxidizing gases at the surface, denuding the graphite connected to the surface and leaving empty cavities.

(ii) Nucleation and growth of iron oxide nodules on the surface.

(iii) Oxide penetration along the graphite particles and covering of graphite cavities with iron oxide scales.

(iv) Reduction of the iron oxide by the remaining graphite in the cavities

(v) Oxidation of dissolved carbon at the metal-metal oxide interface, and transport of the reaction products (CO and CO_2) through the oxide scale.

Stages *(i)* and *(ii)* proceed simultaneously and stage *(v)* takes place during the entire period of exposure. Merchant [8] clarifies that carbon tends to lower the iron oxide-metal adhesion strength, suggesting a possible gap formation between metal and oxide during the diffusion of carbon and oxygen through the oxide.

Other investigations [4, 7-10] show that the kinetics of carbon oxidation and scaling are influenced by the quantity and morphology of the graphite, which is strongly dependent on the type of cast iron. It is mentioned that the degree of scaling increases markedly as the *fraction* of graphite increases, while the matrix structure apparently has little effect

on scaling. Likewise, Merchant [8] indicated that although an increase in carbon content increases the degree of oxidation of carbon, the rate of carbon loss is more sensitive to the graphite *morphology*. For example, the isolated nodules in nodular cast iron have less free surface and do not provide a path for oxygen transport. The surface area of flake and compacted graphite is larger than that of nodular graphite and these particles are partly interconnected, resulting in a higher oxidation rate of graphite in these iron alloys [4].

References [2, 11] refer to work of Evans *et al*., who performed growth and scaling tests of some FGIs and CGIs. Specimens were annealed at a temperature of 600 ˚C during 32 weeks (approximately 5400 h). For CGI and FGI the growth, defined as the relative length change, was found to be 0.25 % and 1.5 % respectively. This means that the flake graphite morphology accelerates growth by a factor of 6, compared to the compacted morphology. The carbon equivalent (CE) of both irons is approximately the same (4.1 %). This is important because the CE, which also is a measure of the chemical composition near the graphite, can affect growth significantly. For instance, cast irons with the same flake morphology but with a CE of 4.05% and 4.3 % were found to produce growth levels of 1.5 % and 2.5 % respectively [11].

The amount of scaling, defined as the mass change per unit surface area, was found to be 0.5 kg/m^2 for CGI and 0.9 kg/m^2 for FGI, both with the same CE of 4.1 % and the same matrix structure [11]. It is found that an increase of the CE also affects the amount of scaling, but to a lesser extent compared to the effect on growth. For instance, a change in CE from 4.1 % to 4.3 % results in an increase in scaling from 0.8 to 1.0 kg/m^2 [11].

4.3.2 Experimental Procedure

The material investigated in this study is CGI with a pearlitic matrix (*cf.* Figure 3.1, chapter 3). The nominal chemical composition of the material is given in Table 3.1 in chapter 3. Two cylindrical specimens A and B of equal dimensions (length 25 mm, diameter 6 mm) together with 10 cubic specimens (6×6×6 mm^3) were taken out from the valve bridges in a cylinder head and prepared for the growth tests. To obtain accurate length measurements, the ends of the cylindrical specimens were protected against oxidation by covering them with stainless-steel caps, fusion welded on the specimen prior to the test, *cf.* Figure 4.4*a*. Welding was done in such a way that the microstructure of both ends was not significantly affected, *cf.* Figure 4.4*b*.

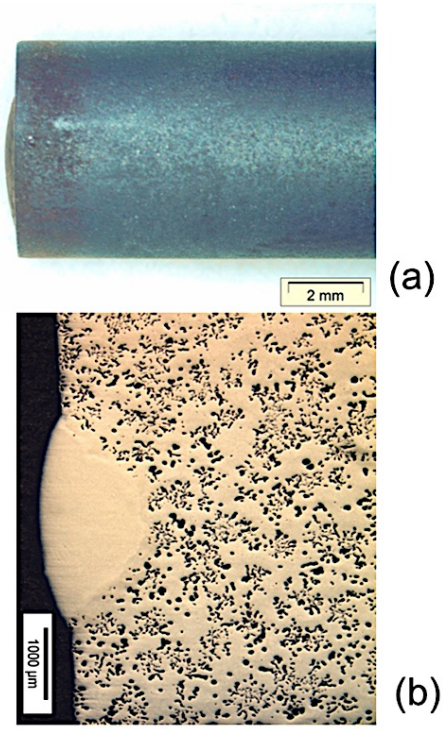

Figure 4.4 (a) End of the cylindrical specimen covered with a stainless-steel cap by fusion welding. (b) Microstructure of the end of the specimen is not significantly affected by the fusion welding.

All specimens were inserted in an atmospheric box oven equipped with resistance heating elements and set to a temperature of 420 ˚C. After exposing the specimens during a specific time interval (*cf.* Table 4.2), some of the specimens were removed from the furnace and cooled down to room temperature. The growth test consisted of measuring the length and the mass of the cylindrical specimens at each of the exposure times given in Table 4.2. The specimen length was measured by a digital micrometer with a gauge length of 30 mm with an accuracy of 1 µm. The mass was measured with a digital balance Denver® to an accuracy of 0.1 mg.

Table 4.2 Exposure times for growth tests.

Exposure times (h)								
8	24	56	120	255	567	1137	2277	4557

Also after each exposure time, one of the cubic specimens was selected for a microstructural study. Subsequently, one cylindrical specimen, labeled A, and the rest of the cubic specimens were again put in the furnace at the same temperature (420 ˚C). This process continued until the longest exposure time *i.e.,* 4557 h (189.8 days). Furthermore, the other cylindrical specimen, labeled B, and one cubic specimen were held continuously in the furnace at 420 ˚C up to the longest exposure time (4557 h). This

leads to a single growth value and reveals the microstructure changes for the case the temperature is not periodically decreased to room temperature.
Metallographic examination was carried out after the specimens were sectioned, ground, polished and etched with 2 % Nital. An optical microscope (OM) and a scanning electron microscope with wave-length dispersive X-ray analysis system (SEM-WDX) were used to evaluate the microstructures. In order to determine the stoichiometry of oxide layers and the local element distribution, especially the silicon content, an electron probe micro-analysis system (EPMA) was used to acquire quantitative chemical analyses by wave-length-dispersive spectroscopy (WDS) operated at spot sizes of 1 to 2 μm.
In order to study the growth phenomena in the absence of oxidation, a dilatometer test was carried out in vacuum (1.3 10^{-7} atm). Standard dilatometer specimens (length 10 mm, diameter 4 mm) were tested at 500, 550, 600, 650 and 700 ˚C for 16 h. The reason for choosing these temperatures was to accelerate the decomposition process relative to the test carried out at 420 ˚C.
In addition, to the purpose of characterizing the pearlite microstructural changes at elevated temperature, a specimen was polished to 1 μm and put into an argon atmosphere (to avoid oxidation) at 700 ˚C for 8 h. Several local pearlite structures in the specimen were observed before and after exposure with an optical microscope. To reveal the lamellar pearlite structures no etchant was used, and the observations were made with the help of objective lenses optimized for Nomarski interference microscopy [12] in order to obtain reflection phase contrast. A double quartz wedge was inserted in the optical system in the 45˚ position and the specimen was viewed in polarized light. The contrast obtained in Nomarski interference reflects small topological differences, which is a technique very similar to phase contrast. The contrast allows distinguishing cementite and ferrite layers in different pearlite colonies. The specimen after exposure was slightly polished with an oxide polishing suspension (OPS) of 0.25 μm, in order to remove the thin oxide layer on the surface of the specimen.

4.3.3 Growth Results

Results in terms of length and mass changes of the cylindrical CGI specimens A and B as a function of time are shown in Figure 4.5. The measured growth after 4557 h at 420 ˚C of cyclic exposure is +0.11 % and the concurrent scaling is +0.012 kg/m^2.

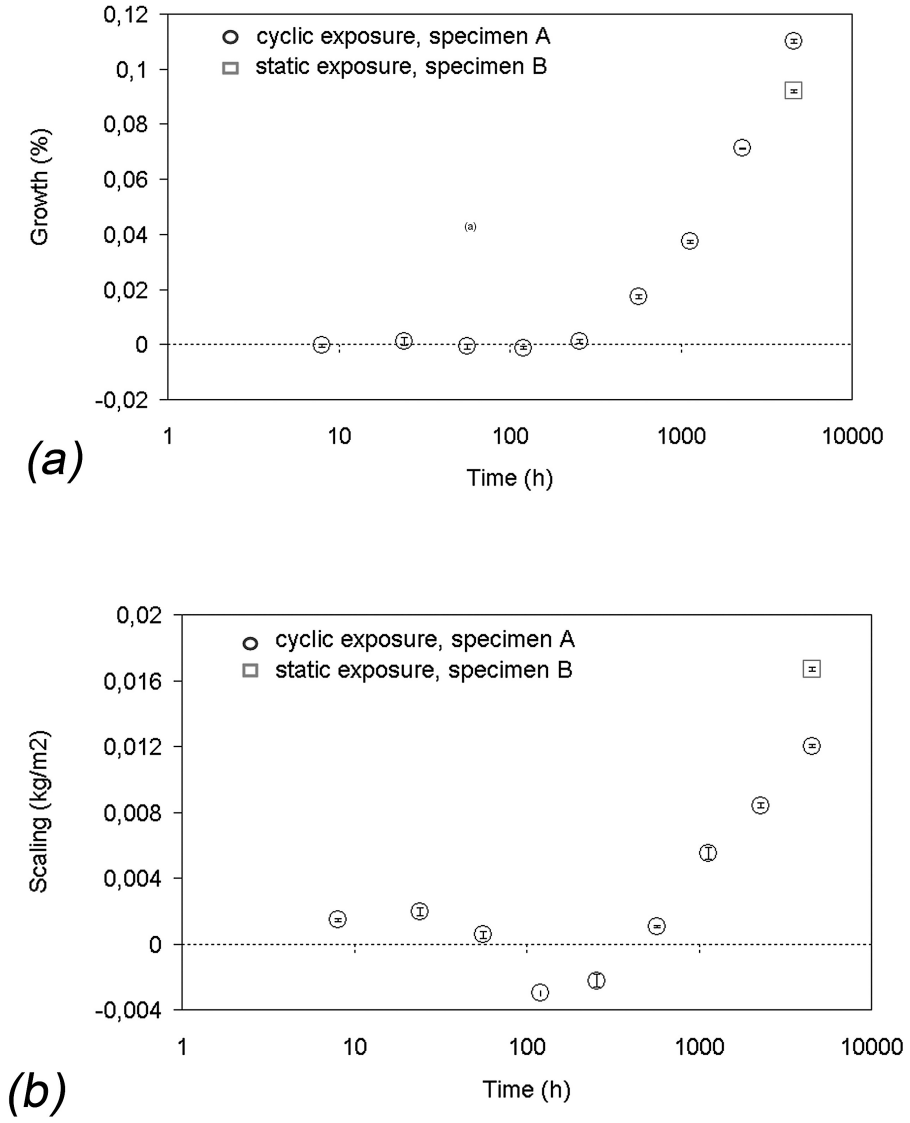

Figure 4.5 Growth (a) and scaling (b) as a function of exposure time at 420 ˚C.

The effect of having either cyclic (specimen A) or static exposure (specimen B) on growth is also shown in Figure 4.5*a*. It can be seen that the growth is accelerated by thermal cycling: for the specimen held continuously in the furnace (square single point) it is less (0.09 %) than for the specimen exposed cyclically (0.11 %). Growth test results by Roehrig [6] show a similarity with this study. He reported that for the case of unalloyed FGI, which was exposed at 650 ˚C, the amount of growth just after 50 h caused by thermal cycling was 125 % more than that for static exposure.

In contrast with this, growth results presented by Kattus and McPherson [9] show that cast irons held continuously in the furnace grow more than those under cyclic exposure. In their study, six FGIs and one spherical graphite iron were tested at a temperature of

538 ˚C. However, when comparing growth test results of Evans *et al.* [11], discussed in section 4.3.1, it can be seen that the growth of the CGI in this study is approximately half the value observed in Evans' study. The reason for this difference after the same exposure time can be related to the difference of applied temperatures, *i.e.* by increasing the temperature from 420 to 600 ˚C, the growth has doubled.

The scaling results of the growth tests show three distinct stages, as presented in Figure 4.5*b*. The first stage shows an initial increase in mass that can be explained by the initial nucleation and growth of iron oxide nodules at the outer surface of the specimen. This caused an increase in mass of 0.0019 kg/m^2 after 24 h exposure. Note that the possible increase in the surface area by appearing cavities was not included in the total surface area.

The second stage is the decrease in mass during the time period between 24 and 120 h exposure. In this stage graphite particles exposed directly to air are oxidized, leading to carbon loss. In the end, the graphite particles are denuded and empty cavities are left behind. Decrease in mass in this stage is believed to be due to decarburization outrunning scaling at the surface of the specimen. Eventually, a third stage starts after 120 h, where the curve starts to show a distinctly increasing trend. By formation of the cavities in the second stage more surface area is available for oxidation to take place. This explains the increasing trend of the third stage of the scaling curve. It is clear that ultimately the rate of metallic oxidation, including the formation of oxide scales in graphite cavities, outruns the carbon oxidation rate, leading to a scaling of +0.012 kg/m^2 at the end of the test after 4557 h of exposure. Moreover, it can be seen that the scaling during static exposure (specimen B) is more than that during cyclic exposure (specimen A).

During exposure to air at 420 °C, oxidation of graphite connected to the surface starts immediately. Gradually oxygen penetrates deeper along the graphite particles, leaving empty cavities behind, *cf*. Figure 4.6 *a* and *b*. The distance from the surface of the formed cavities was measured to be approximately 115 µm after 120 h. This corresponds to the average eutectic cell size measured with the help of X-ray CT with an estimated diameter of 160 µm (*cf.* section 4.2). Consequently, during these first 120 h, it can be estimated that approximately 8 % of the entire bulk volume of the cylindrical growth specimen is affected by internal oxidation. Beyond 120 h, iron oxide scales are found to continue to fill the cavities, explaining the scaling behavior shown in Figure 4.5. Possibly this process also contributes to the volume expansion that leads to the observed growth behavior. It was noticed that the formation of cavities did not significantly continue after 570 h. As revealed in Figure 4.7, the oxide penetration depth saturates at the value of approximately 240 µm after 570 h of exposure time. Presumably the interconnectivity of the graphite has a dominant influence on the kinetics of the oxidation process.

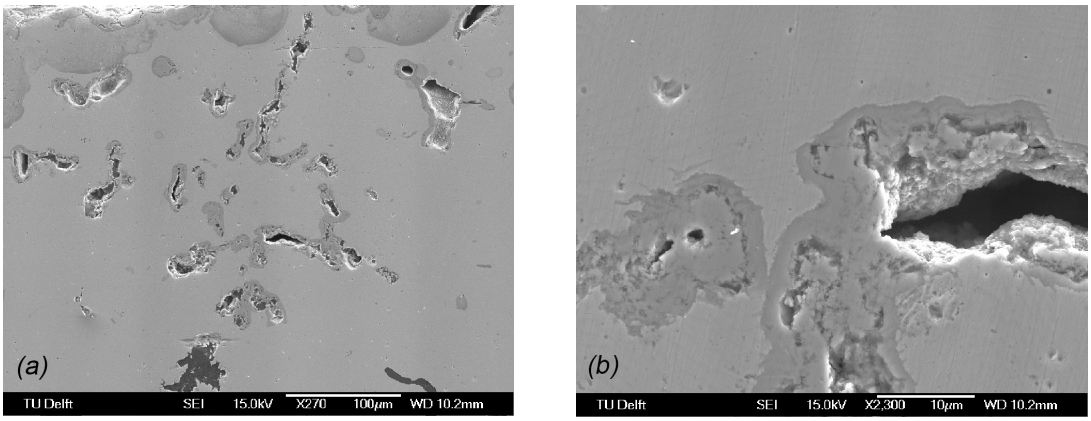

Figure 4.6 SEM micrographs of a cross section near the surface of a specimen exposed to air of 420 ˚C for 120 h: (a) oxidation of graphite particles and the formation of connected cavities near the surface; (b) detail showing the formation of cavities filled with oxides.

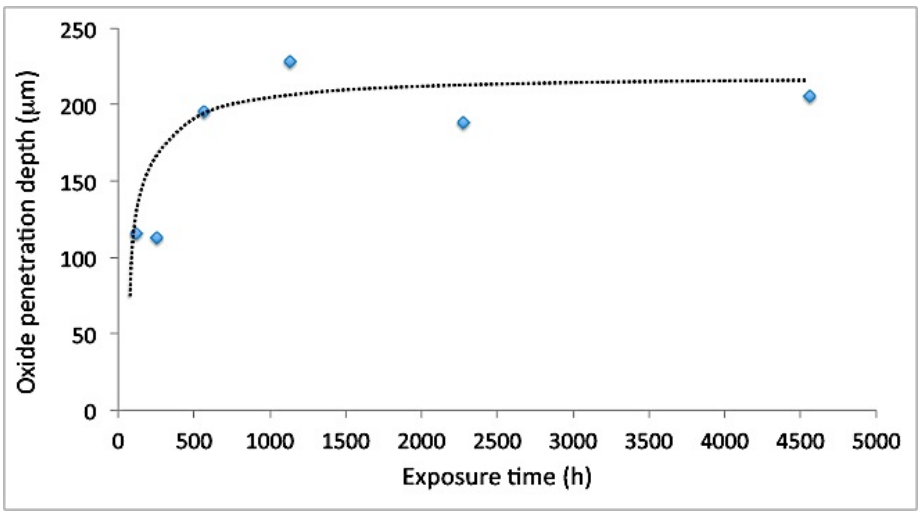

Figure 4.7 The oxide penetration depth as a function of exposure time.

4.3.4 Dilatometer Results

In addition to the growth test, the change in length of CGI specimens at elevated temperatures was measured using a dilatometer, which offers the possibility of carrying out the annealing under low-pressure conditions of 13 mPa, which corresponds to 1.3 10^{-7} atm. The result after 16 h of testing at 500, 550, 600, 650 and 700 ˚C are shown in Figure 4.8. These temperatures were chosen because they are below the A_1-temperature (*i.e.* the pearlite-to-austenite transformation temperature). Therefore, similar to 420 ˚C, no austenite formation occurs, and the microstructural process taking place is pearlite decomposition into ferrite and graphite.
From these graphs we can see that the growth for temperatures below 600 ˚C is small (less than 0.05 %), whereas the growth percentage at 650 ˚C and 700 ˚C is 0.40 % and

0.55 % respectively. The growth below 600 ˚C within a time period of 16 h is below the detection limit of the dilatometer.

In order to see whether the carbon diffusion through iron is the rate-determining process in the absence of oxygen, the activation energy was calculated, by comparing the growth rates at 650 and 700 ˚C, assuming that the activation energy is temperature independent in this temperature range. An average apparent activation energy was found of 94 kJ/mol (±15 kJ/mol). Comparing this value with the activation energy reported by Kucera and Stransky [13], *i.e.* 75.6 kJ/mol, the present material exhibits a higher activation energy for C diffusivity. This is probably caused by the addition of alloying elements such as Sn and Cr, which reduce the rate of pearlite decomposition [6].

Microstructural observations show that the pearlite structure was drastically changed after 16 h at 700 ˚C. Formation of the lower-density graphite (graphitization) is the dominant phenomenon in the microstructure (*cf*. Figure 4.9). The microstructural evolution is discussed in detail in the following section 4.3.5.

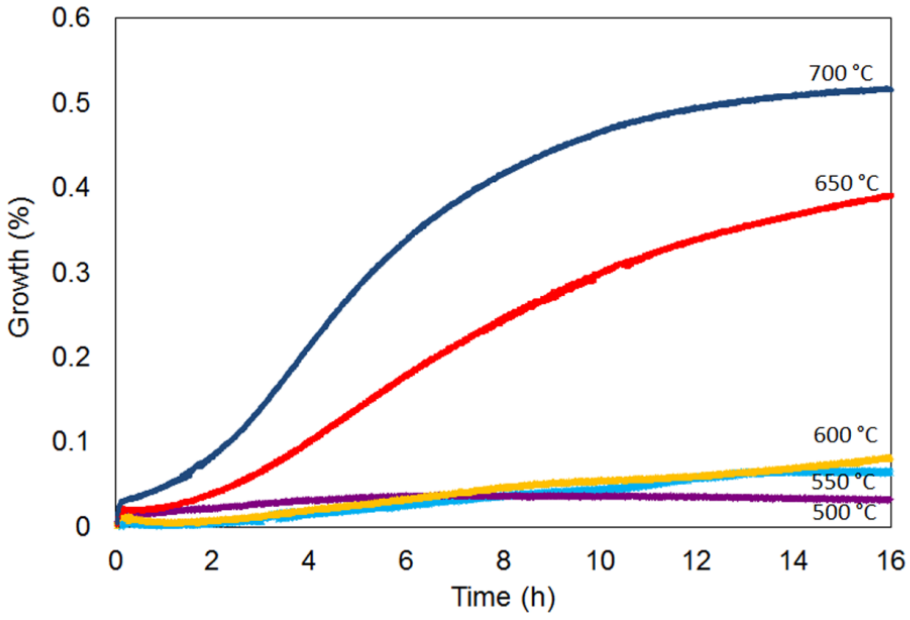

Figure 4.8 Growth of a dilatometer specimen, exposed to 500, 550, 600, 650 and 700 ˚C in vacuum for 16 h.

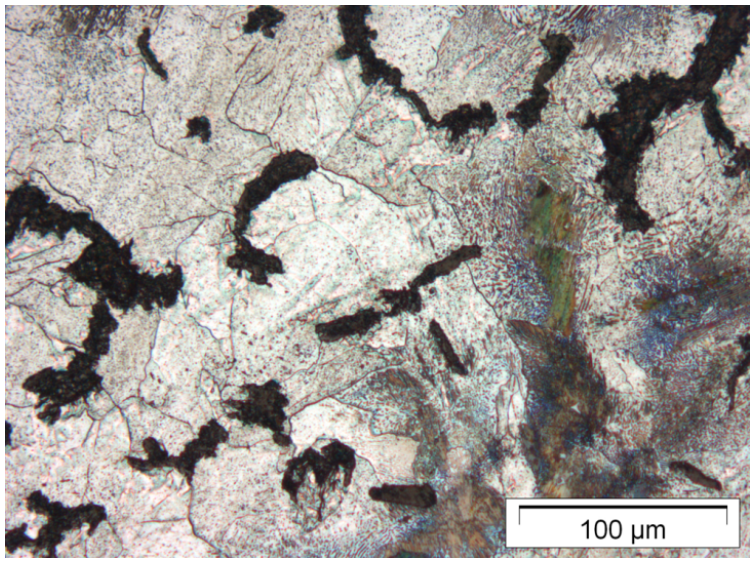

Figure 4.9 Pearlite structure after 16 h at 700 ˚C in vacuum showing significantly more spheroidized carbides with newly formed ferrite grains (when compared with Figure 3.1 in chapter 3).

4.3.5 Microstructural Evolution

As described in the introduction, the microstructural evolution in a pearlitic cast iron is controlled by two main phenomena: oxidation and decomposition of the pearlite. In this section micrographic observations and composition analyses will be presented and discussed.

Oxidation

EPMA line scans were carried out on specimens exposed for 0, 1137 and 4557 h. Figure 4.10 *a* to *c* show the results of scans for the elements C, O, Fe and Si. It can be seen that the composition trends of carbon and silicon go in opposite directions. In as-cast material (Figure 4.10*a*) the silicon content on average reaches 2.2 wt.% outside the graphite and less than 0.2 wt.% inside, *i.e.* silicon is expelled from the graphite during solidification. These results are consistent with the result of the bulk chemical analysis for silicon (1.9 wt.%), taking into account that the volume fraction of graphite in the iron is approximately 10 %.
In the annealed material the silicon content immediately next to the graphite is clearly larger than the nominal content (Figure 4.10 *b* and *c*). As indicated before, in cast iron silicon is expected to interact with the oxidation process [2]. According to Jedrzejczyk *et al.* [10] in oxidized cast irons the silicon content close to the graphite-matrix interface is higher than the nominal value. The Si enrichment in the vicinity of graphite is due to the formation of silicon oxides, which preferentially occurs at the graphite/metal interface. Probably the formation of SiO_2 prevents a more extensive corrosion of the metal matrix. Because of the larger silicon content the internal scale layer would be composed of a mixture of wustite (FeO) and fayalite (Fe_2SiO_4) [10].

As shown in Figure 4.10*b*, the graphite particles near the surface appear to be surrounded by two or three different gray layers after exposure to air of 420 ˚C for 1137 h. The EPMA results indicate that the inner oxide layer directly surrounding the graphite particle is hematite (Fe_2O_3) and the outer layer is magnetite (Fe_3O_4).
Figure 4.10*c* shows a scan over a graphite particle in a specimen exposed for 4557 h at 420 ˚C. The concentration of carbon measured with EPMA in the middle of the particle reaches to 25 wt.%. This was also found in other oxidized graphite particles, indicating that the oxidation of graphite was not completed even after the longest exposure time of 4557 h. Thus, similar to what Jedrzejczyk proposed [10], complete denuding of the graphite particles is not always taking place and some residues of graphite exist before iron oxidation starts to take place.
Although during exposure almost all graphite near the surface quickly disappears by oxidation and as a result cavities form (*cf.* Figure 4.6), some non-oxidized of graphite particles adjacent to oxidized particles remain (*cf.* Figure 4.11). The reason for this is probably related to the interconnectivity of the graphite particles, which provides a continuous path for oxygen penetration. It is surmised that the graphite particles that are not oxidized are not connected to the surface.

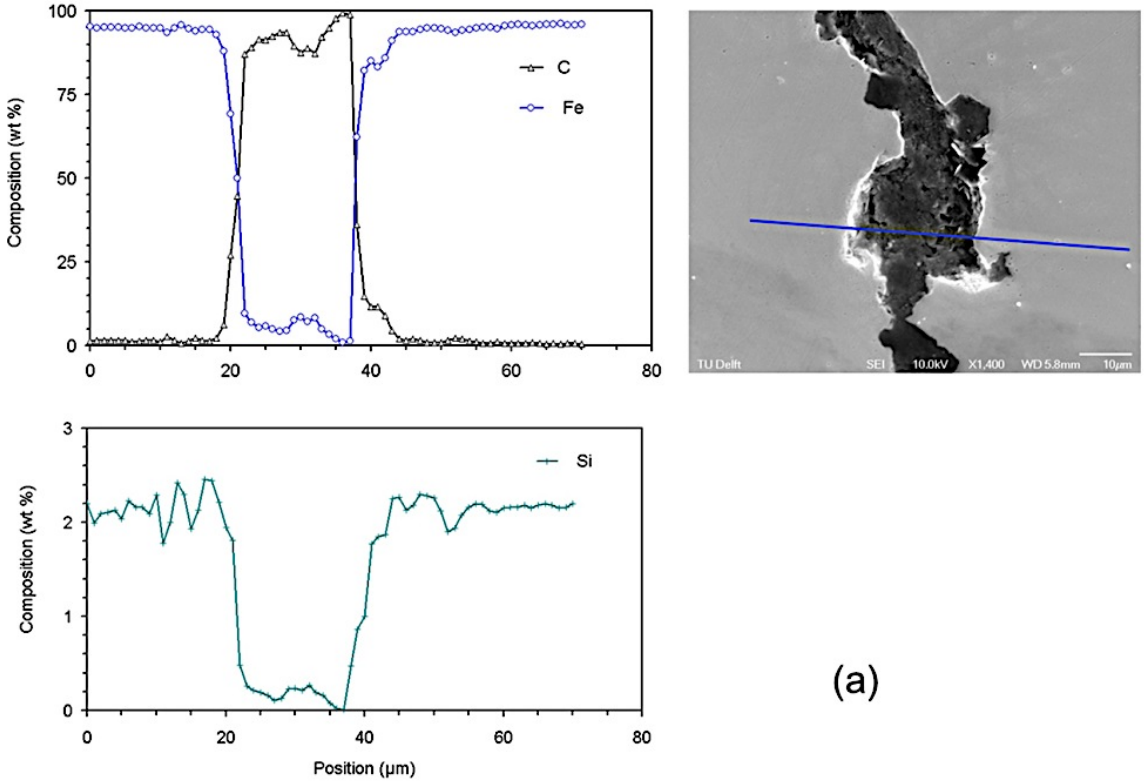

(a)

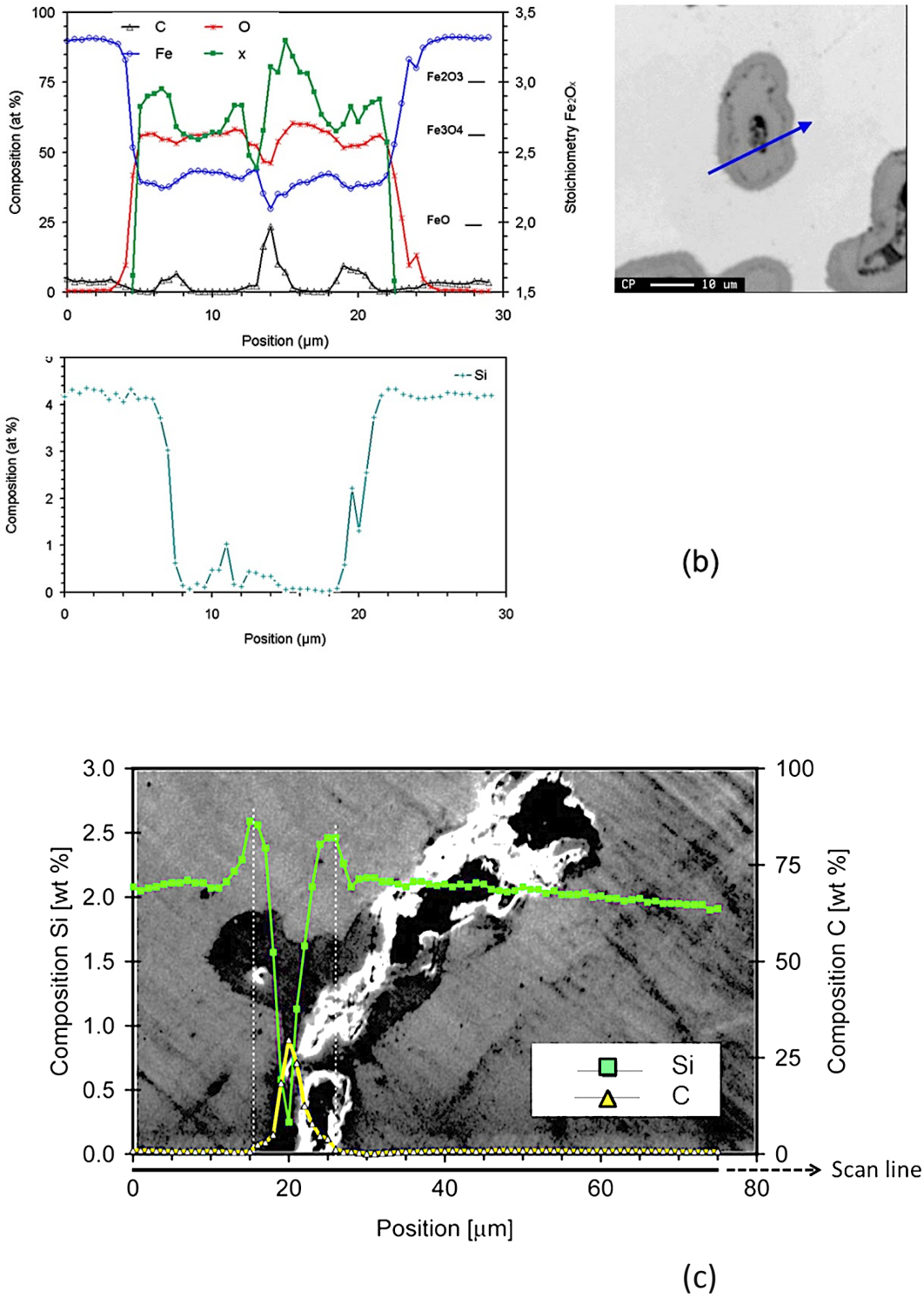

Figure 4.10 (a) Composition of as-cast material along the line for elements C, Fe and Si. (b) Composition after 1137 h exposure to air of 420 ˚C along the arrow for elements C, O, Fe, Si. Also the iron oxide stoichiometry x in Fe_2O_X is plotted. (c) Composition after 4557 h exposure to air of 420 ˚C for elements C and Si. The scan line is the x-axis.

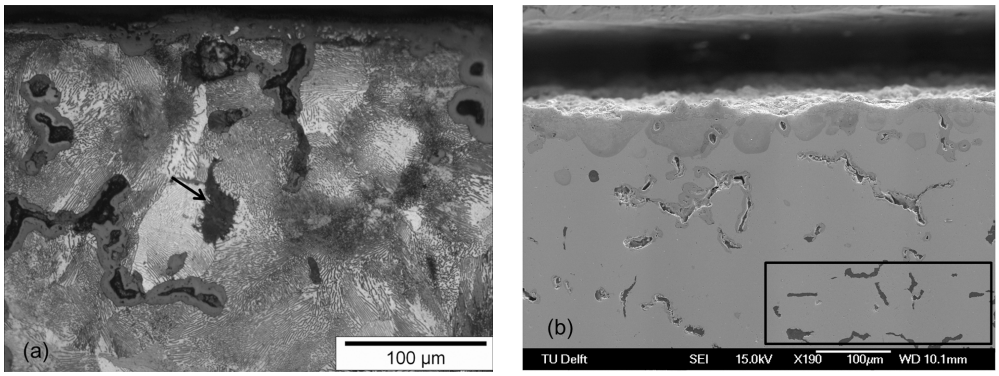

Figure 4.11 (a) Optical micrograph of specimen exposed cyclically for 1137 h to air of 420 ˚C showing a non-oxidized graphite particle (arrow in figure) which is nearer to the surface than the adjacent oxidized graphite particles. (b) SEM micrograph of specimen exposed cyclically for 576 h o air of 420 ˚C showing non-oxidized graphite particles (box in figure) adjacent to oxidized particles.

Pearlite Decomposition

The lamellar pearlite structure showed traces of spheroidization after 1100 h at 420 ˚C and a substantial volume fraction of the pearlite (approximately 15%) had spheroidized after the longest exposure time of 4557 h. This spheroidization of pearlite is believed to coincide with the initial stage of carbide decomposition and graphitization.

The typical diffusion distance of carbon in ferrite at 420 ˚C can be estimated by the expression $\sqrt{(D.t)}$, where D is the diffusion coefficient of carbon in ferrite at this temperature (5.8 10^{-13} m^2/s) and t is the exposure time. Thus 4557 h at 420 ˚C implies a diffusion distance for carbon that is larger than 3 mm, which, if this is the rate-determining process for pearlite decomposition, is expected to accomplish significant microstructural changes. However, because there is a wide variation in the pearlite structure, the changes in the pearlite structure, pertaining to decomposition, cannot be directly characterized by average characteristics; instead the microstructure in a specific region should be observed both before and after exposure.

Optical micrographs of one specific location before and after annealing in a protective argon atmosphere at 700 ˚C for 8 h are shown in Figure 4.12 *a* and *b* respectively. As can be seen, the fine lamellar structure of the pearlite partly changed into a spheroidized structure after exposure or even completely transformed to ferrite in the vicinity of a graphite particle (arrows). By this process of carbon diffusion from decomposing cementite layers in the pearlite to the nearest graphite particle, the graphite particle has grown.

Note that it can be expected that at 420 ˚C the same microstructural evolution occurs after roughly 877 h, assuming an activation energy for this carbon diffusion process equal to 94 kJ/mol, as calculated from the dilatometry experiments. Particularly the effect of Sn in the prevention of pearlite decomposition should not be ignored. It is

reported that the addition of 0.1% Sn reduces the rate of decomposition of pearlite and subsequent graphitization even at 700 ˚C [2, 6]. It is probable that the Sn-concentration in this material is important for its structural stability at 420 ˚C.

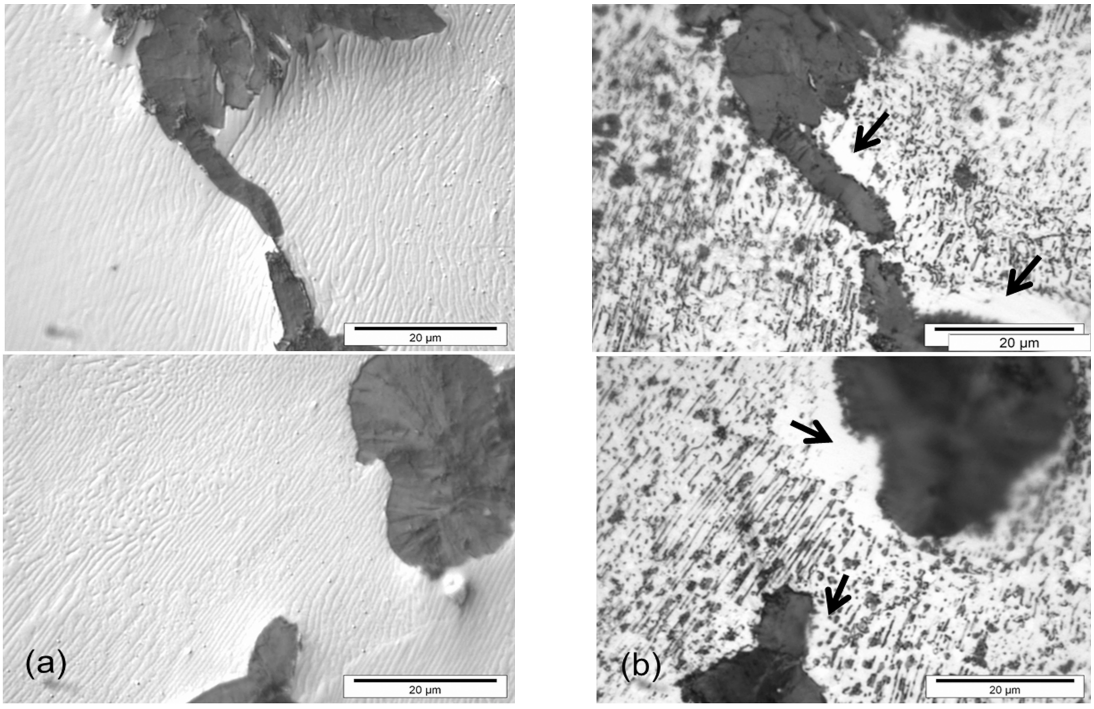

Figure 4.12 (a) Tracing of pearlite structure changes *i.e.*, spheriodization and formation of ferrite and bulkier graphite, observed before (b) and after 8 h at 700 ˚C in argon.

4.3.6 Discussion of the Growth Results

The growth results presented in Figure 4.5 show that after 4557 h of cyclic exposure, the relative length increase is +0.11 %. Since this length increase corresponds to a volume increase of the cast iron, it can be attributed to an increase in graphite volume fraction and/or the filling of cavities with iron oxides.

A full pearlite decomposition, *i.e.* the breakdown of all cementite into ferrite and graphite, would give rise to a relative volume increase of 2.04 % [3], which corresponds to a relative length increase of 0.68 %. When comparing this to the observed value of 0.11 % as found after 4557 h at 420 ˚C, it can be inferred that only a minor fraction of pearlite has actually decomposed into ferrite and graphite (presumably only 16 % of the pearlite).

Also taking into account that part of the growth may have been caused by the formation of oxide scale, the actual fraction of pearlite that has decomposed might even be lower. By microstructural observation it was determined that approximately 15 % of the pearlite has spheroidized, *i.e.* the lamellar structure of the cementite Fe_3C has taken a spherical shape. It is obvious that this cannot cause the volume change as no phase transformation is involved in spheroidization.

Additionally, it can be noticed that no large increase in ferrite volume fraction was observed in the oxide-affected zone of the specimen, which is indicative of the fact that no large-scale pearlite decomposition had occurred. Conversely, in the inner core of the specimen and also in the specimen annealed under protective atmosphere not only pearlite spheroidization had occurred but also a much larger volume fraction of ferrite had formed in the vicinity of the graphite particles, which is indicative of pearlite decomposition, *cf.* Figure 4.12.

The present data suggest that the oxidation phenomena occurring during the open atmosphere annealing are largely responsible for slowing down the pearlite decomposition kinetics. This is confirmed by comparing the open atmosphere growth data with the dilatometer data. The degree of carbon diffusion at 700 ˚C during 16 h is roughly equal to that at 420 ˚C during 1754 h. When comparing the relative length changes measured in the dilatometer test in vacuum after 16 h (0.5 %) with that in the growth test after 1754 h (0.055 %, *cf.* Figure 4.5*a*) in open atmosphere, it can be inferred that the relative length increase in the dilatometer test is roughly 10 times higher than in the growth test. The lower relative length increase obtained in the growth test compared to that in the dilatometer test could be due to oxide layers hindering the diffusion of carbon from the decomposing cementite to the graphite. As reported by Merchant [8], carbon has a low solubility in Fe_2O_3, about 0.003 %. Therefore, diffusion of carbon through the oxide scale and subsequent oxidation at the surface is expected to be very slow. The presence of the inhibiting oxide layer is abundantly illustrated in the micrographs of Figure 4.10*b* and *c*. The role of graphite as carbon sinks in the pearlite decomposition reaction is instrumental as it strongly reduces the surface-energy penalty that would appear if new small graphite particles would have to form in the absence of pre-existing graphite particles.

The fact that oxidation inhibits pearlite decomposition is not only supported by dilatometry results, but also by comparing the characteristics of the cyclically exposed specimen (specimen A), to statically exposed specimen (specimen B), see Figure 4.5*a* and *b*. Specimen A exhibits the lower weight gain, and consequently also the larger growth.

In the specimen annealed in open atmosphere, there is an outer layer, which consists of an oxide-affected zone and an inner core, which is partly decomposed. The extent of the oxide-affected zone (±240 mm) only represents a minor fraction (±16 %) of the entire volume of the sample. Hence, it is not immediately obvious why such a layer may inhibit the growth to such a large extent. We would like to point out, however, that in determining bulk material properties one cannot just apply a proportionality rule on the material volume. Because of the interaction between different parts of the volume, it may very well be conceivable that the oxide-affected layer (with virtually no decomposed pearlite) has restricted the growth of the inner softer part, which is decomposed and exhibits a far larger fraction of ferrite. The unequal distribution of the strain in the specimen will give rise to an internal stress distribution, which could be experimentally verified (*e.g.* by X-ray diffraction). However, the real the mechanism is not understood at this stage and requires further study in the future.

4.4 Effect of the Initial State of CGI on its Tensile and Fatigue Properties

In order to study the influence of the initial microstructural and physical state of CGI on its mechanical properties, a further study is carried out by performing tensile and fatigue tests at room temperature on *i)* as-cast, *ii)* oxidized and *iii)* vacuum annealed CGIs.
Here, the *as-cast material* corresponds to the as-cast CGI taken out of unused cylinder heads. The specimens were machined in the form of solid smooth dog-bone specimens with a final smooth cylindrical gauge length of 22.00 ± 0.25 mm and a diameter of 6.000 ±0.025 mm. For the specimen fabrication the same procedure was used as explained in chapter 3, section 3.2.4. *Oxidized material* refers to the specimens annealed in an atmospheric furnace at 420 ˚C for 720 h (1 month). Oxidized specimens have been divided in two categories: *specimens with scaling* and *specimens without scaling*. The latter ones were investigated to check whether the oxide scale affects the mechanical properties. In the specimens without scaling, this outer layer was removed. To be on the safe side, 500 µm was machined from the surface of each specimen in the gauge length section and therefore the diameter of this section was decreased from 6.0 to 5.0 mm. Since machining of the specimen may produce residual stresses near the surface region, which might affect the test results, specimens were reduced by using an appropriate final machining procedure, which consisted in removing the final 0.2 mm (*i.e.* removing from 5.2 to 5.0 mm) in two steps of 0.05 mm. A final set of specimens was annealed in a vacuum furnace at 420 ˚C for 720 h (1 month), *i.e.* the same temperature and exposure time as oxidized specimens.

4.4.1 Tensile Properties Results

Table 4.3 summarizes the tensile properties of the four initial states of CGI as as-cast, oxidized with and without scaling and vacuum annealed, whereas Figure 4.13 compares the tensile curves of these categories.

Table 4.3 Tensile-tests results of the four initial states of CGI as as-cast, oxidized with and without scaling and vacuum annealed. Together with the absolute values of the mechanical properties also the values relative to the as-cast state are shown between brackets.

Initial State	Yield Strength offset 0.2% (MPa)	Ultimate Tensile Strength (MPa)	Elongation at fracture %
As-cast	333 [100%]	524 [100%]	2.85 [100%]
Oxidized with scaling	367 [110%]	535 [102%]	3 [107%]
Oxidized without scaling	362 [109%]	536 [102%]	3 [107%]
Vacuum annealed	352 [106%]	569 [109%]	3.85 [135%]

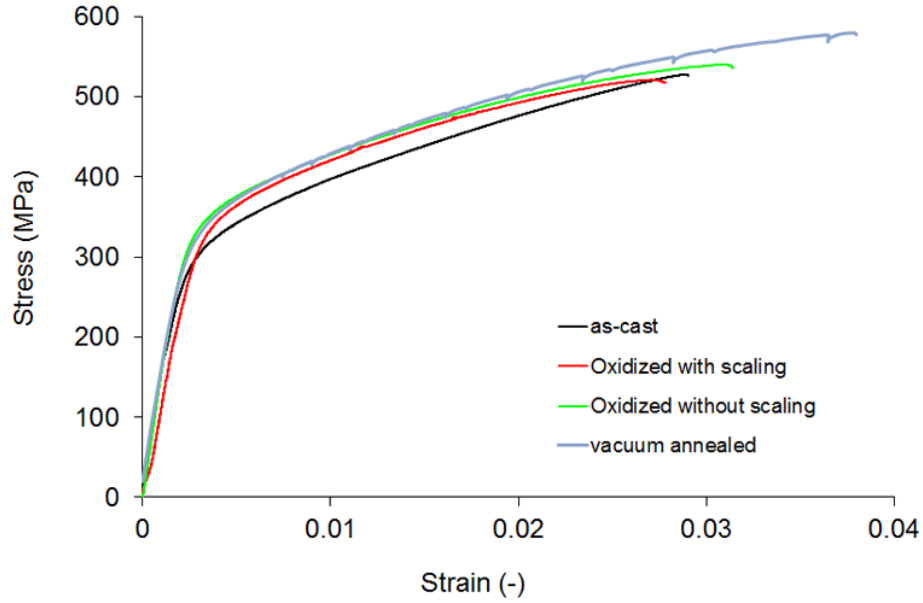

Figure 4.13 Tensile curves of as-cast, oxidized (with and without scaling) and vacuum-annealed specimens.

It can be noticed that the annealed specimens exhibit better mechanical properties both in terms of strength and ductility. After annealing under atmospheric conditions (oxidized), compared to the as-cast material, an increase of the yield strength and the UTS by 10% and 2%, respectively, was observed. This was the case for the specimens both with and without scaling. The elongation at fracture increased as a result of open air annealing by 7%. Subsequently, the results for vacuum annealing, compared to the as-cast material, showed an increase of the yield strength and the UTS by a percentage of 6% and 9%, respectively, together with a noticeable increase of the elongation at fracture by 35%. The increase of strength and at the same time ductility for all exposed specimens should be related to the microstructural changes occurring in the material. Some possible active mechanisms are suggested and explained in the discussion, section 4.4.3. It also can be noticed that there is no yield point elongation in these tensile curves, irrespective of the initial condition of the specimen.

4.4.2 Fatigue Properties Results

The fatigue tests were performed by applying a stress range of ±350 MPa, (a stress ratio of $R = -1$), *i.e.* stress-controlled tests. This stress level was chosen as slightly higher than the yield strength of 330 MPa of the as-cast state in tensile. In this way the yield strength of the material (during the first load cycle) will increase to 350 MPa by the mechanism of strain hardening. The fatigue load then is close to the situation of low cycle fatigue for all specimens. Table 4.4 presents the average cycles to failure for the four initial states of CGI as-cast, oxidized with and without scaling and vacuum annealed.

Table 4.4 Fatigue tests results (frequency: 1 Hz). Between brackets values relative to the as-cast condition are given.

	Average cycles to failure, N_f	Standard deviation
As-cast	1221 [100%]	421
Oxidized with scaling	1472 [120%]	365
Oxidized without scaling	2011 [165%]	454
Vacuum annealed	3728 [305%]	646

Similarly to the static mechanical properties, it can be observed that the annealing treatment induced a positive effect on the number of cycles to failure. The fatigue lifetimes for atmospheric annealing (oxidized), compared to the as-cast material, showed an increase by 20% (with scaling) and 65% (without scaling), respectively. The results for vacuum annealing, compared to the as-cast material, showed an increase of the number of cycles to failure with a factor of 3. The similar tendency for tensile and fatigue properties is consistent with the fact that fatigue properties are well known to be related to the yield strength.

In addition, Figure 4.14 shows the plastic strain range as a function of the number of cycles of as-cast, oxidized and vacuum-annealed specimens. The plastic strain, which may vary from cycle to cycle, is calculated by subtracting the elastic strain from the total strain. In turn, the elastic strain is calculated as the stress divided by the Young's modulus. Depending on the initial state, a metal may undergo cyclic hardening, softening or remain cyclically stable. The results show that during the first 10 cycles, the plastic strain range is increased, *i.e.* it seems that initially softening occurs in view of the stress-controlled situation. It should be noticed that the increase in plastic range is more pronounced for the vacuum-annealed samples and less for the oxidized samples. For the latter, the plastic strain is already quite high in the first cycle and shows only a limited increase in the subsequent cycles. In the second region, after the first 10 cycles, the plastic strain decreases consistently, indicating that a cyclic strain hardening process is active in the matrix. In the third region, near to the end of the lifetime of the samples, a softening process prevails, which may be related to the formation of cracks or to other damage mechanisms.

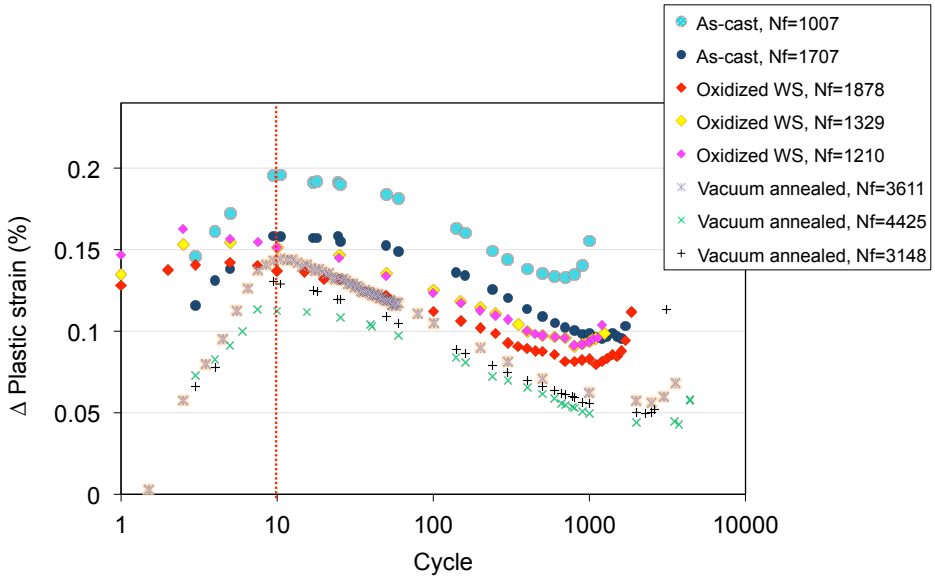

Figure 4.14 Measured plastic strain range versus number of cycles.

4.4.3 Discussion of Static and Dynamic Mechanical Behavior

4.4.3.1 Static Tensile Loading

In order to explain the mechanical properties measured under static conditions, one has to consider the microstructural processes that might have occurred during annealing at 420 °C, whilst taking into consideration that vacuum annealing has caused the largest effect both on the strength and the ductility. The following microstructural processes might have played a role.

Strain Ageing

Strain ageing is a mechanism that occurs in the metal matrix of the cast iron composite, when solute atoms (*C* and *N*) diffuse towards free dislocations. This generally results in an increase of yield strength as the dislocations are pinned and extra energy is required to unlock them from their solute atmospheres. Typically for strain ageing is the occurrence of a yield point elongation. A yield point elongation was not observed in CGI, which may be attributed to two phenomena: *i)* the presence of a heterogeneous stress state at the onset of yielding, and *ii)* the occurrence of delamination of graphite particles from metal matrix. However, for strain ageing to occur, it is necessary that a minimum density of free dislocations is present in the metal matrix at the onset of annealing.

Precipitation Hardening

Cast irons have a rather complicated chemistry, which allows interstitial elements such as C and N to precipitate in the form of carbides or nitrides at the applied annealing

temperature of 420 °C. It is well-known that the appearance of small (partially) coherent precipitates strengthen the metal matrix by impeding the movement of dislocations in the crystal lattice. The precipitation hardening mechanism gives rise to a characteristic hardening curve with an ageing peak and a declining slope of the hardness due to overageing at extended annealing times. Although the hardness data displayed in Figure 4.15 exhibit a peak value after ~1000 h of annealing, the general shape of the curve does not correspond to the one of a typical age-hardening curve, although it cannot be excluded that precipitation has affected the mechanical properties. It also was observed that high temperature annealing in this case has produced both an increase in strength *and* an increase in ductility. This is rather uncommon for the classical strengthening mechanism, such as precipitation hardening, as they generally increase the strength at the expense of ductility.

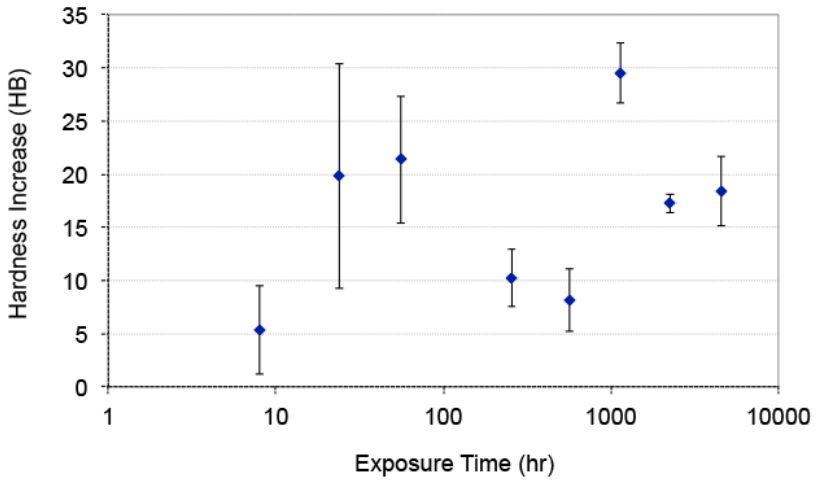

Figure 4.15 Macro-hardness (HB) change, the value after exposure at 420 ˚C subtracted from the value before exposure, shown as a function of exposure time.

Spheroidization and Decomposition of Pearlite

Another microstructural evolution mechanism that might have played a role is spheroidization and/or decomposition of the pearlite phase. The lamellar structure of the pearlite can change into a spheroidized structure during long exposure. In the growth tests (*cf.* section 4.3.5) spheroidization was observed in the present material after annealing under atmospheric conditions for 1100 h at 420 °C. This morphological transformation is driven by the reduction of interfacial energy at the cementite-ferrite phase boundary. In the vicinity of graphite particles a phase transformation might occur in which pearlite decomposes to ferrite and graphite (*cf.* section 4.3.5). As ferrite and the lower-density graphite are not as strong as the parent pearlite, it will give rise to a decrease in strength. Concurrently, however, ferrite is a more ductile phase and therefore the overall ductility may increase, and hence it could be concluded that decomposition of pearlite leads to a decrease of strength and an increase of ductility.

Figure 4.16 shows the microstructural evolution in a vacuum-annealed specimen at 420°C after annealing during 720 h. As it is shown in Figure 4.16*a* ferrite formed directly in the vicinity of the graphite particles, nearly enveloping the entire circumference of each graphite particle. Figure 4.16*b* shows one specific case of a graphite particle surrounded by ferrite with some decomposed and/ or spheroidized pearlite colonies in the vicinity.

In addition to the traditional hardening and softening mechanisms associated with the motion of dislocations in the metal matrix, the present composite material also might exhibit the consequences of stress and strain distribution between the metal matrix and the graphite particles. For instance, it is well-known that composite structures may be subject to delamination at the interface between matrix and inclusions. If one assumes that the ferrite/graphite interface exhibits a stronger and more stable bond than the pearlite/graphite interface, this might explain the concurrent observation of increasing ductility (ferrite is more ductile) alongside increasing strength after the annealing treatment. It also explains why the vacuum-annealed samples exhibit the larger change in tensile properties. It was already argued in section 4.3.6 that the presence of an oxidizing atmosphere has a considerable retarding effect on the decomposition kinetics.

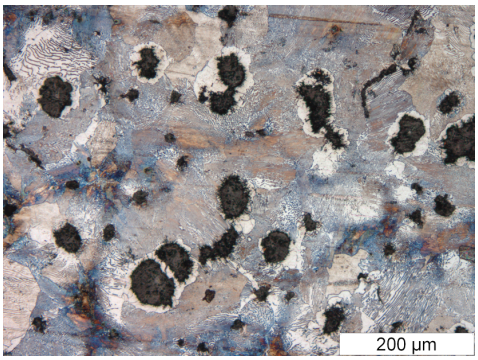

(a)

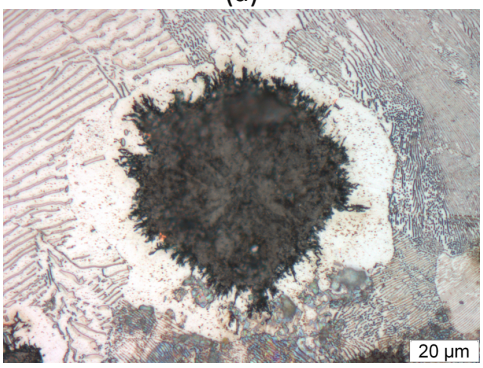

(b)

Figure 4.16 (a) Microstructure of a specimen annealed in a vacuum at 420 ˚C for 720 h showing newly formed ferrite grains around the graphite particles with some decomposed and/ or spheroidized pearlite colonies. (b) At higher magnification (500X) one graphite particle is shown enveloped by the ferrite phase and the lamellar pearlite at the left side of the graphite and spheroidized carbides at the right middle side of it.

4.4.3.2 Dynamic Fatigue Loading

The general trend of cyclic plastic strain as shown in Figure 4.14 shows that all specimens exhibit a certain amount of unrecoverable strain when the stress is reduced to zero. For the as-cast specimens, the applied stress level of 350 MPa is slightly above the elastic limit, thus the plastic strain is expected. However, for the annealed specimens, we do not expect plastic strain since the applied stress level is below the yield stresses (*cf.* Table 4.3).
Classic dislocation-carried plasticity below the yield point may have two reasons: *(i)* well-known microplasticity phenomena before the onset of homogeneous yielding and *(ii)* the stress exceeding the elastic limit at stress concentration points at the tip of the graphite particles. Additionally, there may be an effect of plastic deformation (in the sense of non-recoverable deformation) caused by delamination of graphite particles from the metal matrix. There is a strong indication here that the initial plastic strain may be the result of a delamination effect. This can be derived from the following observations: *(i)* there is initial plastic softening instead of plastic hardening and *(ii)* the hysteresis stress-strain curves of the first 10 cycles (*cf.* Figure 4.17) exhibit a distinct shift towards the tensile strain domain for as-cast and vacuum-annealed specimens (somewhat less pronounced for the specimens annealed in the open atmosphere).
In case plastic deformation is carried by dislocation glide, it is very unlikely that work softening precedes work hardening. In the normal sequence of events, dislocations first would be immobilized (hardening) and relaxed afterwards (softening). Delamination, on the other hand, may readily occur after a certain critical stress is applied, which may be well below the yield stress.
The fact that the permanent strain gradually shifts towards the tensile strain domain in the first 10 cycles is another indication that delamination may play a crucial role in the first stages of cyclic loading (*cf.* Figure 4.17). Indeed, it can be conceived that delamination only has an effect during the tensile part of the stress cycle, whereas in the compressive part the delamination voids between graphite inclusions and metal matrix are closed again and hence, there is less irrecoverable strain. A similar behavior is observed during loading of composite materials.
The fact that the specimens annealed in vacuum showed the least plastic strain after the first cycle, compared to specimens as-cast and annealed in open air, can be explained by the formation of ferrite surrounding graphite (*cf.* Figure 4.16). This may indicate that the bonding between graphite and ferrite is stronger than the bonding between graphite and pearlite, *i.e.* less delamination occurs at the onset of cyclic loading in the vacuum-annealed specimens. Towards the end of the first 10 cycles, however, also for the vacuum-annealed specimens delamination presumably occurs, giving rise to somewhat delayed plastic softening.
In addition, in the specimens annealed in open air conditions, less plastic softening is observed during the first 10 cycles compared to vacuum-annealed conditions, although also for these specimens a substantial part of the strain does not recover at zero stress and hence can be labeled as *plastic*. In this case however, the plastic domain is nearly constant during the first 10 cycles, hence there is neither plastic softening nor hardening. This corresponds with the observation for the oxidized specimen that the

initial plastic domain of the first 10 cycles is nearly constant, and does not shift to the higher strain as observed for the as-cast specimens and the vacuum-annealed specimens. This different behavior of the oxidized specimen may have been caused by the fact that part of the graphite/pearlite interfaces was embrittled by an oxide layer that has formed at the interface. Hence, such embrittled interface is more likely to be subject to instantaneous delamination, rather than of gradually increasing delamination as observed for the vacuum-annealed and as-cast specimens.

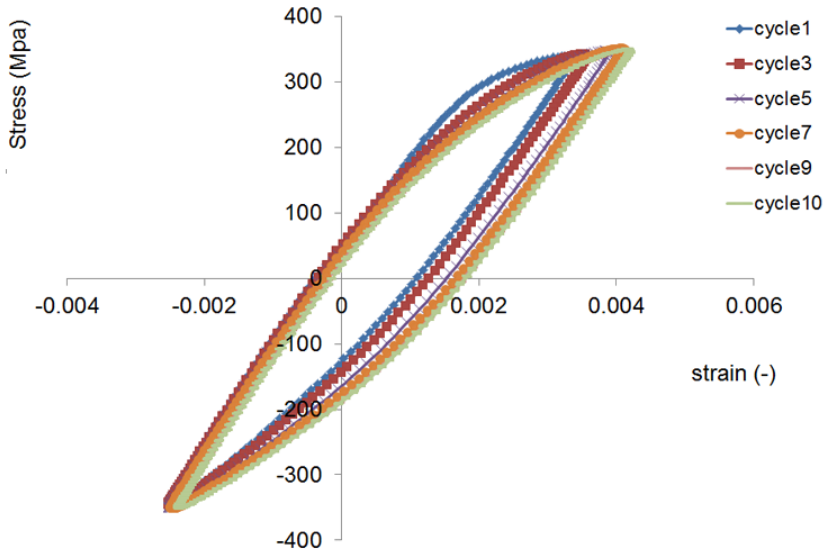

Figure 4.17 The average plastic strain for an as-cast specimen shifts towards the tensile strain domain in the first 10 cycles.

The fact that the specimen exposed in vacuum shows a pronounced prolongation of the (associated) fatigue lifetime (N_f = 3728) compared to the one of the oxidized specimens without scaling (N_f = 2011) indicates that the effect of oxidation may reach further into the core of the material than expected.
The increase of lifetime for oxidized specimens without scaling (36% increase compared to the specimen with scaling) may be related to the fact that the oxide scale has promoted crack initiation starting at the surface of the specimen. By removing this oxidised layer, the chance of crack initiation (at locations where the graphite particles were burnt away) was eliminated.

4.5 Conclusions

Growth Phenomenon in CGI at Elevated Temperature Annealing

With regard to open air annealing of CGI at 420 °C, it can be concluded that after 4557 h (189.8 days) of cyclic exposure, the length increase is +0.11 % and the mass increase due to oxide scaling is +0.012 kg/m^2. However, after this exposure time, only a minor fraction (less than 9 %) of pearlite has decomposed into ferrite and graphite, *i.e.* a

complete decomposition of pearlite needs longer exposure times than the presently applied 4557 h at 420 ˚C. It was also found that internal oxidation largely inhibited the progress of pearlite decomposition and therefore much smaller growth rates were obtained as compared to the ones observed under vacuum conditions. After 16 h of annealing time at 700 ˚C, comparable in terms of carbon diffusion to 1754 h at 420 ˚C, the vacuum conditions exhibited 10 times faster growth kinetics. The observed oxide layers at the internal metal/vapour interface of cavities (left behind by denuded graphite) cause the obstruction of carbon diffusion and thus hindering the pearlite decomposing process.
In addition, the saturation distance from the surface of the formed cavities was measured to be approximately 240 µm after 570 h. This is not very much different from the average eutectic cell size measured with the help of Computed Tomography (CT) with an estimated diameter of 160 µm. This suggests that the interconnectivity of the graphite has a dominant influence on the kinetics of the oxidation process.

Initial State of CGI: Tensile and Fatigue Properties at Room Temperature

An extended annealing treatment of 720 h at 420 °C was carried out to generate different initial conditions of the CGI microstructure. It can be concluded that this extended annealing treatment causes an increase in yield strength, and at the same time an increase in ductility during static tensile loading at room temperature. During dynamic cyclic loading at room temperature an increase of lifetime was observed after the annealing treatment. These variations of mechanical properties were measured both after annealing under atmospheric and vacuum conditions, but were far more pronounced after vacuum annealing. In the fatigue tests a decrease in cyclic plastic strain was associated with the increase in yield strength obtained by the extended annealing, which in turn has produced an increase of lifetime, with the strongest increase observed for the specimens annealed in vacuum. Specimens annealed in vacuum show the least plastic strain after the first cycle compared to specimens as-cast and annealed in open air. In the vacuum-annealed material this behavior can be explained by the decomposition of the pearlite phase during annealing and the formation of new ferrite at the graphite/metal interface. It is assumed that the ferrite/graphite interface exhibits a stronger bond than the pearlite/graphite interface. As this stronger bond will be better resistant to delamination it will strengthen the material both in static and dynamic loading. That such effects were far less pronounced in the open air annealed material could be associated with the fact that it was shown that internal oxidation strongly reduced the kinetics of decomposition.

4.6 References

[1] SinterCast Nodularity Rating Chart', 1997; SinterCast.
[2] Davis J.R. (Ed.), ASM Specialty Handbook: Cast irons, ASM International, United States of America, Materials Park, OH 44073-0002, 1996.

[3] Yuzvak V.M., Volchok I.P., Gontarenko V.I. Micromechanism of fracture of cast irons, Met. Sci. Heat Treat. 1983; 25(8): 569-573.
[4] Buni S.Y., Raman N., Seshan S. The role of graphite morphology and matrix structure on the low frequency thermal cycling of cast irons, Sadhana 2004; 29(1): 117-127.
[5] Ziegler K.R., Wallace J.F. The Effect of Matrix Structure and Alloying on the Properties of Compacted Graphite Iron, AFS Transactions 1984; 92: 735-748.
[6] Roehrig K. Thermal Fatigue of Gray and Ductile Cast Irons, AFS Transactions 1978, 78-02: 75-88.
[7] White D.G., L. I. M., A. C. T., Growth and Scaling Characteristics of Cast Irons with Undercooled and Normal Flake Graphite, BCIRA Journal, 11(Report 689); 1963: 223-230.
[8] Merchant H.D. Oxidation Kinetics of Iron-carbon Base Alloys, Oxid. Met. 1970; Vol.2, No. 2: 145-153.
[9] Kattus J.R., McPherson B. Report on Properties of Cast Iron at Elevated Temperatures, ASTM Special Technical Publication 1959; No. 248. Philadelphia.
[10] Jedrzejczyk D., Hajduga M., Lorek R. High Temperature Oxidation as the Method of Surface Treatment of Cast Iron, METAL 2008; 13–15 May, Hradec nad Moravici.
[11] Walton C.F., Oper T.J. (Eds), Text Book, Iron Casting Handbook, Published by Iron castings society, Cleveland, Ohio, 1981.
[12] Brandon D., Kapplan W.D. Text book, Microstructural Characterization of Materials, 2nd ed., John Wiley and Sons, Inc., 2008.
[13] Kucera J., Stransky K. Diffusion in Iron, Iron Solid Solutions and Steels, Mater. Sci. Eng. 1982, 52, 1-38.
[14] Löhe D. Properties of vermicular cast iron at mechanical and thermal-mechanical loading, Institutfur Werkstoffkunde I, Universitat Karlsruhe (TH), MACHINING WORKSHOP 2005 for Powertrain Materials, Darmstadt, November 24-25, 2005.

5

Measurement and Characterization of Thermo-Mechanical Fatigue in Compacted Graphite Iron

"The best way to predict the future is to invent it".

Alan C. Kay

In this chapter[1], a detailed account is presented on Thermo-Mechanical Fatigue (TMF) lifetimes of Compacted Graphite Iron (CGI) material. A TMF test series was performed using both smooth and sharply notched specimens (with notch depths ranging from 0.10 to 0.65 mm). The TMF lifetimes measured were also simulated numerically by using the Paris crack growth equation. Furthermore, for three distinct typical ΔK values the crack growth rate (da/dn) was measured by applying a new crack length measurement procedure. Finally, it was evaluated to what extent the accumulation of cyclic plasticity of bulk material affects TMF crack growth in CGI.

5.1 Introduction

As mentioned already in the introduction of chapter 2, in complex cast iron components, such as cylinder blocks and heads, heating and cooling cycles can lead to localized cracking due to stresses that develop as a result of thermal gradients and thermal mismatch. This phenomenon is known as Thermo-Mechanical Fatigue (TMF). In a combustion engine the TMF phenomenon is related to the start-operate-stop cycles [1-7]. Especially the valve bridges in cylinder heads, the areas between intakes and outlets, are severely subjected to out-of-phase (OP) loading, *i.e*. maximum strain occurs at minimum temperature [1-8]. Pearlitic Compacted Graphite Iron (CGI) provides a suitable combination of thermal and mechanical properties to satisfy the performance of engine components. In CGI, the phases of interest are the matrix (*i.e.* pearlite) and the graphite particles, *cf.* Figure 3.1 of chapter 3.

[1]This chapter is based on: S. Ghodrat, A.C. Riemslag, M. Janssen, J. Sietsma, and L.A.I. Kestens, Measurement and Characterization of Thermo-Mechanical Fatigue in Compacted Graphite Iron, International Journal of Fatigue 48 (2013) 319–329.

Fatigue of graphitic cast iron is largely affected by the high volume fraction of relatively large graphite particles. Under tensile loading these particles can be considered as internal defects or notches. Therefore, the initiation of a fatigue crack is likely to be accelerated by the presence of graphite. For instance, in the case of High Cycle Fatigue (HCF) of nodular cast iron, a clear relation between fatigue lifetime and graphite dimensions was established [9, 10]. Cracks in graphitic cast iron probably already initiate at the graphite particles during the first TMF cycles. As discussed by Seifert *et al.* [11, 12], graphite particles in cast iron weaken the material in tension by decreasing the stiffness, since the graphite particles partly delaminate from the matrix. On the other hand, in compression interfacial microcracks are closed resulting in a higher stiffness. This leads to an asymmetrical tension-compression behaviour of cast iron.

Commonly, TMF behavior is studied by cyclically loading smooth dogbone specimens until failure. The resulting number of cycles to failure (N_f) constitutes a single parameter that can be used to predict actual service failures. Both the crack initiation phase and the crack growth phase may contribute to the overall lifetime but unfortunately standard test methods do not distinguish between crack initiation and crack propagation.

One of the goals of this study was to identify the different roles of crack initiation and crack growth during TMF of CGI, and possibly to quantify their respective contributions to the TMF lifetime. To this purpose using both smooth and notched specimens (*cf.* chapter 3, sections 3.2.4 and 3.2.5), TMF tests were performed and measured lifetimes were compared to calculated lifetimes.

Another issue in TMF studies is to assess the performance of materials subjected to TMF cycling by performing isothermal low cycle fatigue (LCF) tests [5, 7]. Rémy [5] claims, however, that "*such a comparison is often meaningless since strain rate and frequency at a given temperature range in a thermomechanical cycle are often different from the one in the isothermal cycle*". In most cases isothermal fatigue tests do not capture all damage mechanisms that occur under variable strain-temperature conditions in TMF.

There are various approaches for TMF lifetime prediction, as is well summarized in reference [8]. According to this reference three main types of models can be distinguished: *i)* phenomenological models, *ii)* cumulative damage models and *iii)* crack growth models. Because of the likely fast initiation of TMF cracks in CGI material, it was considered appropriate here to employ the third approach *i.e.* using a crack growth model to evaluate the TMF lifetime for which the method employed by Rémy *et al*. [13] was adopted. They successfully calculated lifetimes under high cycle fatigue for a powder metallurgy (PM) material containing defects, using the hypothesis that a defect can be considered a crack. To calculate the HCF lifetimes, Rémy employed Paris' fatigue crack growth equation, which describes the crack growth rate (da/dn) as a function of the stress intensity range (ΔK), taking a representative dimension of a particle as the initial crack size. In the current work regarding TMF in CGI, the Paris model was also employed, with the graphite particles considered as defects, whilst still observing the simplifying assumptions of linear elastic fracture mechanics (LEFM) and ignoring the micromechanical nature of stress/strain heterogeneities at the crack tip.

The role of the graphite particles as defects (and initial cracks) and the validity of the Paris crack growth model was further evaluated by testing (and modeling) TMF lifetimes

of specimens provided with a sharp circumferential notch. Notches introduce locally increased stress levels (*i.e.* stress gradients) accelerating crack initiation, and thus affecting fatigue lifetime. However, it should be emphasized that in the case of CGI, the notches were *not* treated as stress concentrators (*i.e.* stress-lifetime methodology) but as crack length extensions (*i.e.* fracture mechanical approach). The idea behind this is the hypothesis that graphite particles within the notch tip region can act as notch tip sharpeners leading to a relatively quick crack initiation, basically causing the notch to behave as a crack. Therefore, in the numerical calculations (using the Paris model) the effect of the notch depth is taken into account by the higher value for ΔK associated with the longer initial crack length (being the notch depth). The use of more sophisticated models for TMF lifetime predictions [11-16] that go beyond the assumptions of LEFM known from the literature are acknowledged, but will not be employed in this work.
The use of the Paris equation relates to the crack growth during TMF. In contrast to high cycle fatigue, during TMF the crack advances through a ligament with changing properties, which is related to the accumulation of cyclic plasticity of bulk material and prolonged exposure to high temperatures. It is interesting to know to what extent these changing properties affect the TMF crack growth mechanism. This matter is evaluated in TMF tests using pre-cycled CGI material. In order to confirm the Paris model, a number of three TMF tests were performed with direct measurement of crack lengths, using a new crack size measurement technique.

5.2 Experimental Procedures: Dedicated Test Procedures

Basic information about CGI material and TMF procedures[2] and specimens used are addressed primarily in chapter 3. However, two additional test procedures used for the validation of the Paris crack growth model are explained separately in this chapter, referred to as “crack growth measurements” and “pre-cycled tests” (*cf.* infra).

Crack Growth Measurements

To verify the Paris crack growth equation, the length of TMF cracks was meticulously measured microscopically using specimens with notch depths of 0.20, 0.25 and 0.50 mm. For each notch depth, the number of cycles to produce a crack extension of approximately 150 μm was estimated, employing the Paris equation (*cf*. section 5.3.2). It is assumed that cracks initiate almost instantaneously from the notch tip, *i.e.* the notch depth is taken as initial crack length. This resulted in estimations of 125, 100 and 30 cycles, to produce crack extensions of about 150 μm in specimens containing notches of 0.20, 0.25 and 0.50 mm, respectively. The different notch depths are meant to obtain three distinctive crack growth rates, resulting from the different levels of ΔK associated with the distinct initial crack lengths (being the notch depths).

[2]TMF test procedure used in this chapter is the “standard TMF test procedure” with 30 s holding time explained in chapter 3, section 3.2.2.

The three specimens used for the microscopic crack length observation were provided not only with a central circumferential notch, but also two additional notches were machined at a distance of 4 mm above and 4 mm below the central notch[3] (*cf.* Figure 5.1). The extra notches are meant to enable a larger number of crack extension measurements for a better statistical analysis. The axial distance between the notches (4 mm) is considered large enough to prevent any interaction between developing TMF cracks.
After the estimated number of TMF cycles mentioned above, the gauge length region was cut from each specimen, producing a cylindrical sample (∅ 6 mm) with an axial length of about 16 mm. This gauge length sample was embedded in a polymer cylinder with an orientation as shown in Figure 5.1. In a first step, the sample was grinded off to an extent of 0.5 mm and subsequently polished. The crack extensions emanating from the six notch tips were measured using an optical microscope with magnifications up to 500×.
The crack extensions measured from the polished surface have to be corrected to obtain the values in radial direction. The details of this correction procedure are given in Figure 5.1 and Appendix D. This correction depends on the distance *h* between the polished surface and the center of the specimen. After measuring the crack extensions from all six notch tips, a next cross section is obtained by further grinding and polishing, and for the new value of *h*, the measurement procedure is repeated. A number of nine cross sections were obtained for the samples with notches of 0.20 and 0.50 mm, while the sample with a 0.25 mm notch was sectioned only five times[4]. In some occasions the crack extension could not be determined unambiguously and these measurements were not taken into account. In the end, a number of 48, 30 and 50 crack extension measurements were obtained for the 0.20, 0.25 and 0.50 mm notched specimens respectively. Finally, the measured crack extensions can be compared to the numerically calculated crack extensions (*i.e.*~150 μm) to evaluate the validity of the Paris crack growth equation.

Pre-cycled Tests

Another approach to study the TMF mechanism was introduced by TMF cycling a smooth specimen for a defined number of cycles (400 cycles), after which the test was interrupted. This procedure is designated *pre-cycling* and is intended to provide the (bulk) material with a certain amount of cyclic damage. After pre-cycling, the specimen was removed from the TMF test set-up and provided with a 0.20 mm circumferential notch. The notched (and pre-cycled) specimen was replaced in the TMF machine and the TMF test was restarted and continued until failure (N_{10} criterion, *cf.* section 5.3.2). The entire procedure is schematically depicted in Figure 5.2. Results of the pre-cycled specimens are compared to results of the standard TMF procedure, to the purpose of evaluating the role of cyclic damage of the bulk material on TMF lifetime.

[3]Individual specimens contained three notches of identical depths.

[4]It would have been more consistent to also evaluate nine sections here, but unfortunately (in the spur of the moment) only five sections were taken.

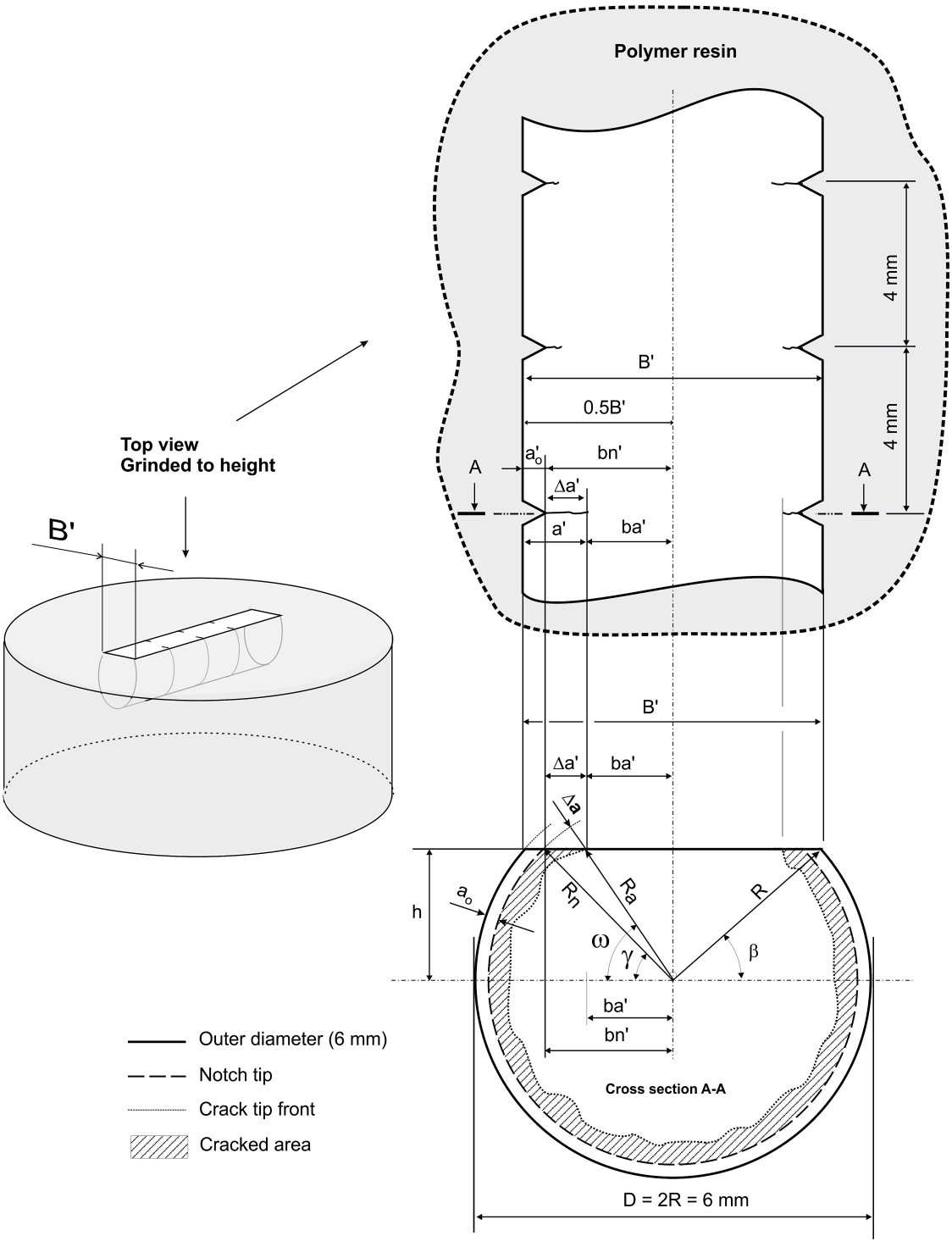

Figure 5.1 The set-up for the measurement of crack extensions from notch tips. *Cf.* Appendix D for the equations used to calculate the crack extension in the radial direction.

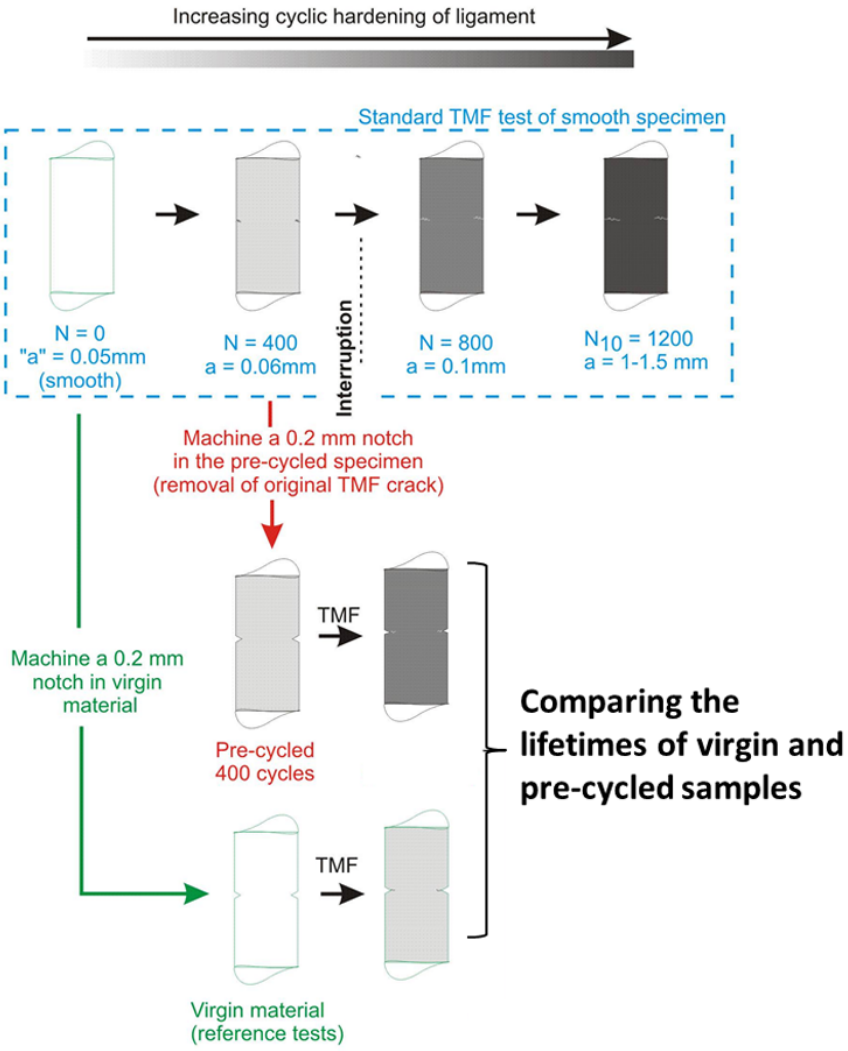

Figure 5.2 Principle of pre-cycling test procedure.

5.3 Results and Discussion

5.3.1 Development of Stress and Strain during TMF

The typical development of stress and mechanical strain (which is total strain minus thermal strain) during a TMF test can be illustrated by considering the results for a smooth specimen subjected to a holding time of 30 s, ultimately leading to failure after 1689 cycles. Figure 5.3 shows the first two cycles for this TMF test. Distinct points on the curves are identified with letters A to H. Note that the mechanical strain in the plot is calculated by defining a zero thermal strain at the average temperature during the TMF process, *i.e.* at 235 °C.

The test starts with applying a condition of total constraint at 50 °C (A). As a result of heating up from 50 °C a compressive stress builds up and plastic deformation starts at

–200 MPa (B). During further heating, up to 420 °C, the specimen shows plasticity with little hardening and ultimately even a slight softening until point C is reached. During the holding time of 30 s at 420 °C, the stress relaxes from an initial stress level of –325 MPa, to –288 MPa (C → C'). Through subsequent cooling, first elastic unloading and then elastic loading in tension takes place until the onset of plasticity at a tensile stress level of about 100 MPa (E) at a temperature of 225 °C. On further cooling down to 50 °C, the material shows pronounced hardening from 100 MPa to 255 MPa (F). During the holding time of 30 s at 50 °C, the stress relaxation is limited to a decrease of only 5 MPa. By heating up again, first the tensile stress is elastically released to a zero level (at 205 °C, point G), and upon further heating a compressive stress builds up. Below a stress level of –100 MPa, plastic deformation starts (H). Upon further heating to 420 °C, strain hardening occurs up to a level of –310 MPa. Note that for the total constraint condition, the applied fixed temperature range (50 to 420 °C) in combination with the coefficient of thermal expansion of the CGI (15.6×10^{-6} K^{-1}, *cf.* chapter 3, section 3.2.2) leads to a fixed mechanical strain range of almost 0.6 %.

As can be seen from Figure 5.4, a mean tensile stress develops with increasing number of cycles. This is typical for the out-of-phase nature of the TMF loading that results from the total constraint condition to which the specimen is subjected. The positive mean stress shift is caused by the fact that the material exhibits a lower yield strength in the compressive region (at high temperature) compared to the one in the tensile region (at low temperature).

At the same time the amount of stress relaxation at 420 °C gradually decreases and the shape of the hysteresis loop becomes narrower, indicating a reduction of cyclic plasticity. This reduction is more clearly visible in the stress-plastic strain loops plotted in Figure 5.5. The plastic strain is calculated by subtracting the elastic strain from the mechanical strain. In turn, the elastic strain is calculated as the stress divided by the Young's modulus.

For each cycle the Young's modulus was calculated separately for tension and compression by linear regression of the stress-mechanical strain data during unloading from +100 MPa to zero and –100 MPa to zero, respectively. It should be noted that this procedure inevitably leads to Young's moduli at slightly different temperatures, but the effect of temperature is considered to be relatively small.

Since the total constraint condition was applied at minimum temperature, the first TMF cycle produces a large compressive plasticity in the CGI. In the 2^{nd} cycle (the first complete cycle) a cyclic plastic strain range, $\Delta\varepsilon_p$, of 0.1% was obtained. At larger numbers of cycles, the width of the hysteresis loop, *i.e.* $\Delta\varepsilon_p$, gradually reduces to 0.04% at 1000 cycles. The reduction in cyclic plasticity is in accordance with an increase in yield strength found at increased numbers of cycles. This increase in strength indicates the occurrence of cyclic strain hardening, since the total strain is kept to zero and the cyclic mechanical strain range is fixed to a value of 0.6%. It ensues that the plastic strain range is reduced with increasing yield stress, implying a mechanism of strain hardening, *cf.* Figure 5.5.

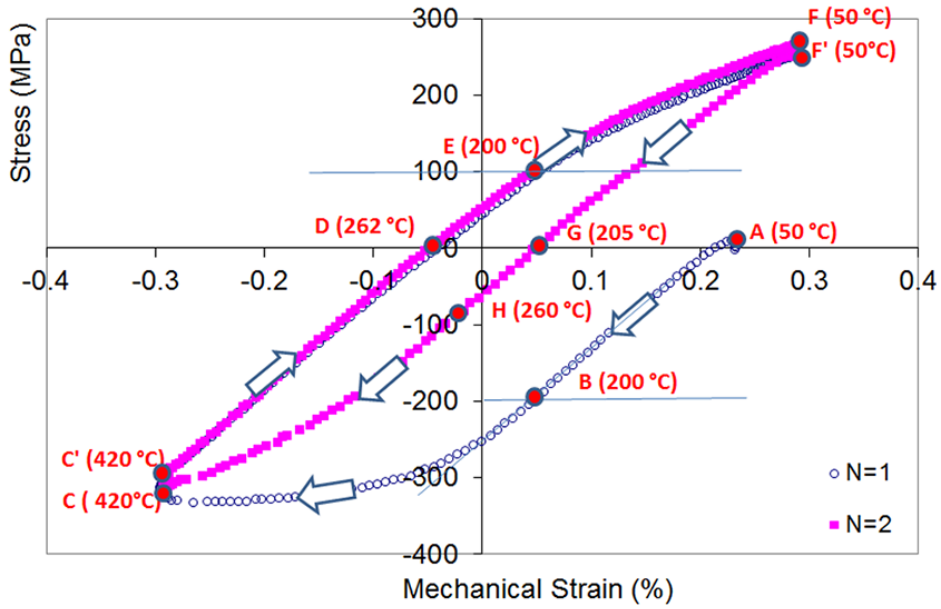

Figure 5.3 Stress-mechanical strain hysteresis loop for the first two cycles of TMF loading for a smooth specimen with 30 s holding times.

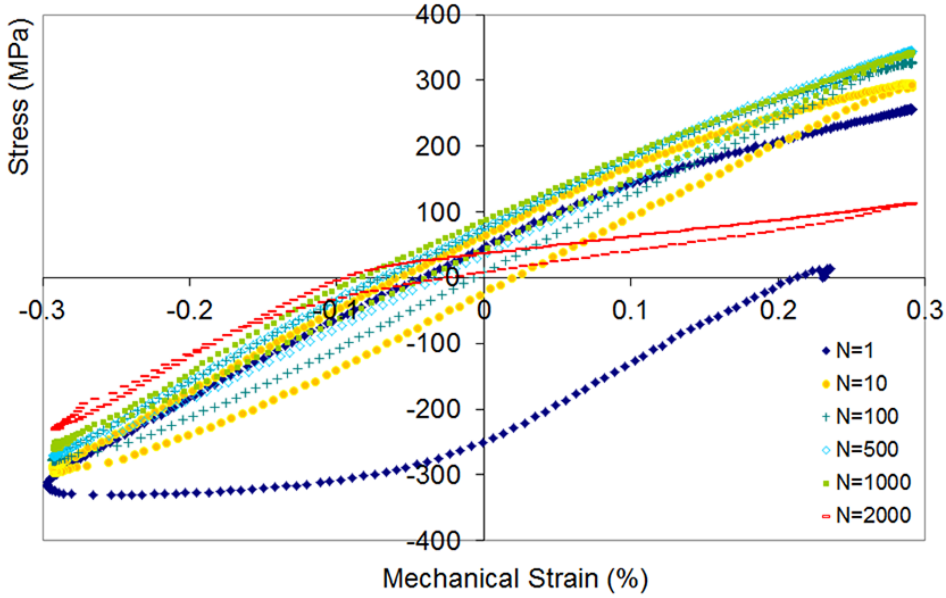

Figure 5.4 Development of stress-mechanical strain loops during TMF lifetime for a smooth specimen applying holding times of 30 s.

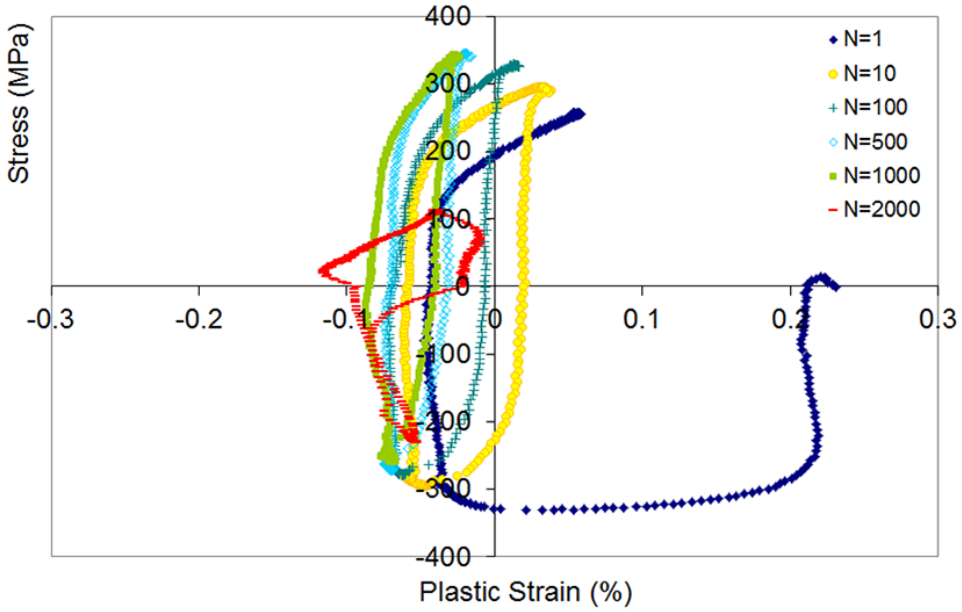

Figure 5.5 Development of stress-plastic strain loops during TMF lifetime for a smooth specimen with 30 s holding times at the maximum and minimum temperatures.

5.3.2 Effect of Notch Depth on TMF Life and Numerical Estimations

The results of the TMF test series on smooth and notched specimens are listed in Table 5.1. In this table TMF lifetime is defined as the number of cycles at which the maximum (tensile) stress that developed during the test, has decreased by 10% relative to the maximum value that developed during the entire test (N_{10}). The reason for using this criterion is described in appendix C. As it can be read from the results in this table, lifetime decreases monotonically with increasing notch depth. Also the scatter for 0.2 mm notched specimens appears to be less compared to the scatter for the smooth and 0.1 mm notched specimens.

Table 5.1 Experimental and calculated results for TMF tests performed on smooth and notched specimens with a holding time of 30 s at maximum and minimum temperature. All stress levels are nominal, *i.e.* based on the nominal circular cross section of 6 mm diameter.

Notch size	Experimental values			Calculated values	
	Lifetime N_{10}	Average lifetime N_{10} (st. dev./avg.) %	Maximum stress level $\sigma_{max.}$	Lifetime N_{Paris}	Average lifetime N_{Paris}
mm	cycles	cycles	MPa	cycles	cycles
"Smooth" (0.045 mm graphite particle size)	1525	**1443** (37%)	347	1629	**1278**
	968		359	1375	
	992		357	1413	
	2268		374	1120	
	1460		395	852	
0.10	254	**415** (40%)	371	291	**389**
	639		350	383	
	421		349	401	
	344		336	480	
0.20	172	**202** (16%)	311	198	**169**
	149		311	198	
	200		330	147	
	245		331	145	
	221		320	172	
	208		326	157	
	218		323	164	
0.35	89	**89** (0%)	290	88	**88**
	89		290	88	
0.50	49	**45** (12%)	265	57	**49**
	41		283	41	
0.65	28	**30** (7%)	265	26	**27**
	31		262	28	

The notch constitutes a stress concentration, which itself promotes crack initiation. In addition, the graphite particles located near the root of the notch still remain effective as inherent stress concentrators, just as is the case for smooth specimens. It has been found that both in macroscopically smooth specimens as well as in notched specimens, the graphite particles are the preferential locations for crack initiation, *cf.* Figure 5.6. In other words, the initiation mechanisms in notched and smooth specimens can be regarded to be of a similar nature, *i.e.* both determined by the graphite particles.

Another aspect of using notched specimens is the fact that it results in a shorter TMF lifetime of the specimen. This is because the notch in combination with graphite

particles near the notch tip constitutes a longer initial crack length compared to a smooth surface with only graphite particles. The corresponding higher initial crack growth rate is an advantage as it reduces the duration of the usually time-consuming TMF test procedures.

The maximum stress levels developed during the tests consistently decreased with increasing notch depth of the specimens. Figure 5.7 shows the typical evolution of maximum, minimum and mean stress levels together with the stress range during the subsequent TMF cycles (for smooth and notched specimens). A logarithmic scale is used for the horizontal axis to enable a clear comparison in stress development for the wide range in lifetimes presented. Initially, all smooth and notched specimens tested, show an increase in maximum and mean stress levels with the number of load cycles. On the one hand, this observation may be related to the occurrence of stress relaxation at high temperature and the associated reduction of compressive stress, subsequently giving rise to an increase of tensile stress at low temperature. On the other hand also cyclic hardening may be partly responsible for this observation. It can be deduced from the hysteresis stress-strain curve that the plastic strain range decreases with increasing number of cycles, *cf.* Figure 5.4 and Figure 5.5. However, at a distinct number of cycles, the maximum stress level developed reaches an absolute peak value and subsequently starts to drop during the final stage of the test. The final drop in maximum stress is related to the formation of a macroscopic crack, lowering the stiffness of the specimen. The lower stiffness, in combination with the condition of total constraint, causes the drop in maximum stress.

The absolute peak stress level reached for specimens with larger notches is relatively low (see also Table 5.1). Just as a macroscopic TMF crack, a machined notch also decreases the stiffness of the specimen compared to a smooth specimen. For instance, it can be seen in Figure 5.7 that for a 0.65 mm notched sample the maximum stress level, built up during the first cycles, is notably lower compared to stress levels developed in smooth specimens during the first TMF cycles. In addition, for the 0.65 mm notched specimen a macroscopic crack is created at a relatively small number of cycles, restricting the accumulated amount of cyclic hardening of the bulk material, and therefore also limiting the peak value of the maximum stress level developed. Therefore, for big notches the drop in maximum stress level has two reasons, (*i*) a decreased stiffness due to a larger contribution of the crack opening displacement, *i.e*. an elastic property, and (*ii*) a limited amount of cyclic hardening, *i.e.* a plastic property.

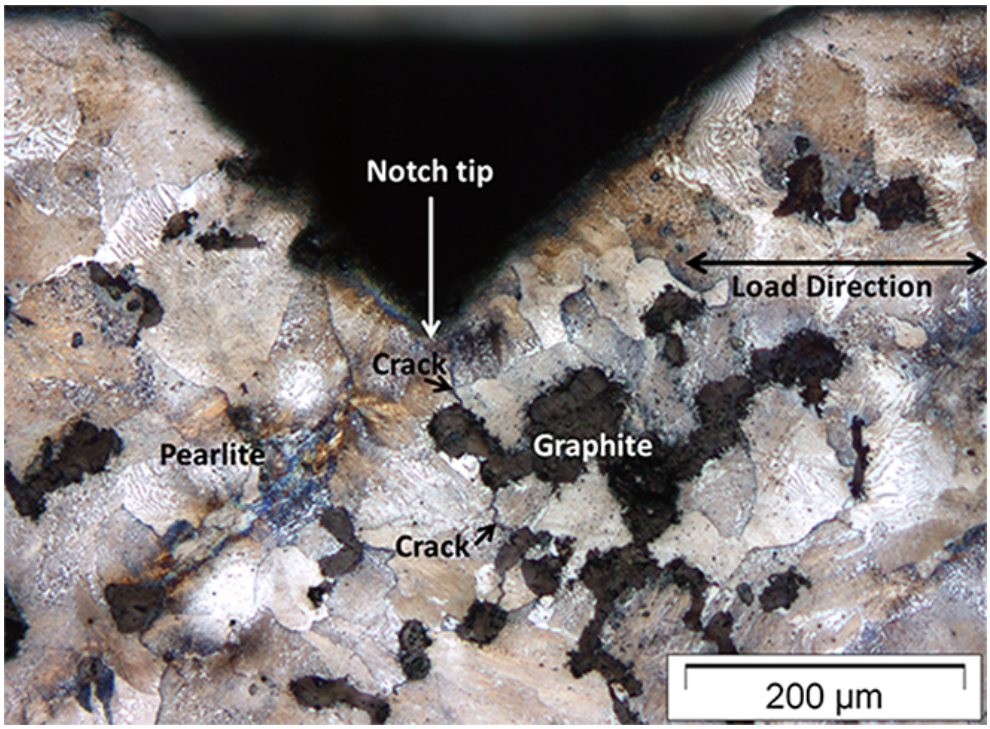

Figure 5.6 Cross section of a TMF loaded specimen, with a notch of 0.2 mm, showing graphite particles in the vicinity of the notch root and cracks emanating from the graphite particles (etched).

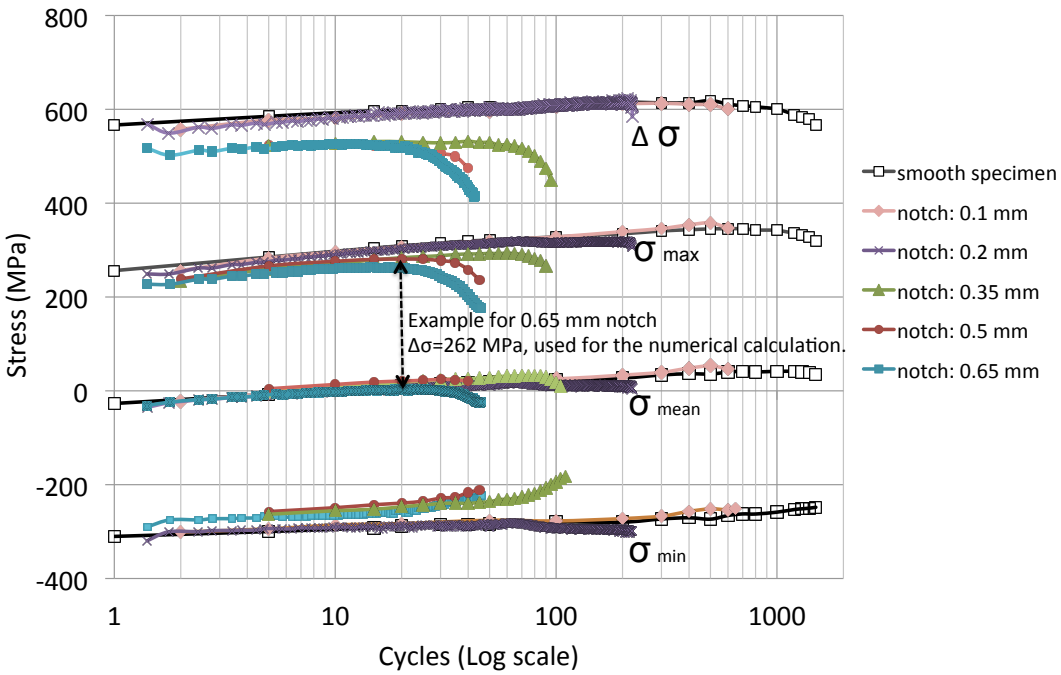

Figure 5.7 Development of maximum, minimum and mean stress levels together with the stress range as a function of elapsed TMF cycles, for smooth and notched specimens.

For specimens with small notches (0.1-0.2 mm) the stiffness is not affected much by the presence of the notch. The maximum stress levels developed during the initial TMF cycles are found to be comparable to levels that occur for the smooth specimen, *cf*. Figure 5.7. Nevertheless, for small notches, the maximum stress developed is still limited by the smaller amount of TMF cycles to failure, and the associated smaller amount of cyclic hardening (compared to smooth specimens).
To summarize, the lifetime of notched specimens may be affected in two ways: it is shortened by the longer initial crack length and lengthened by the reduced maximum stress levels. Consequently TMF results obtained with smooth specimens or with specimens containing different notch sizes cannot be compared directly. However, it will be discussed below how such results can be brought in accordance with each other by introducing a numerical lifetime estimation.
For this purpose, it is assumed that the stress intensity range ΔK can be used to correlate TMF crack growth by implementing the Paris crack growth equation (5.1) [19]:

$$\frac{\mathrm{d}a}{\mathrm{d}N} = C(\Delta K_{\mathrm{I}})^m \qquad (5.1)$$

where a is the crack size, N the number of load cycles, ΔK_{I} the stress intensity range and C and m are material-dependent parameters.
Despite the extensive plasticity occurring during TMF, it is believed that this approach is applicable, as is confirmed also by other TMF researchers, who successfully applied equation (5.1) to experimental growth rates as a function of ΔK, producing straight lines on double logarithmic scales [20]. The Paris model has also been used successfully in other fatigue situations, where deformation of the uncracked ligament is also not purely elastic. For instance, during fatigue of visco-elastic polymers the ligament will creep at the stress levels present during fatigue. However, for most polymers, the Paris model is used successfully to describe fatigue crack growth behavior [21-22]. In addition, it should be mentioned that the basic mechanism of fatigue crack growth described by ΔK is cyclic plasticity, not of the bulk material (*i.e.* the uncracked ligament), but locally at the crack tip. The cyclic plasticity of the ligament during TMF (apart from the first half cycle) is only approximately 0.15%, while the level of the crack tip cyclic plasticity is probably much higher than this. Therefore it is assumed that also in the TMF considered here, cyclic crack tip plasticity dominates fatigue crack growth. In section 5.3.4 it is shown that accumulation of bulk plasticity does not have a considerable effect on TMF crack growth rates (*i.e.* on TMF lifetime).
In the calculation it is assumed that a crack initiates immediately from the notch, *i.e.* the depth of the circumferential notch is taken as the initial crack length. Assuming specific values for the Paris parameters C and m, the number of cycles is calculated for the first 0.01 mm of crack extension around the entire circumference of the specimen. This process is repeated for subsequent steps of 0.01 mm, adjusting ΔK in each step in accordance with the increased crack length. Summing the results of all steps gives the total number of cycles to failure.

To calculate Δ*K*, the solution reported in [23] is used for a cylindrical specimen containing a circumferential notch loaded in tension (equation 5.2):

,

$$K_I = \sigma\sqrt{\pi a}\,\frac{1}{\left(1-\frac{a}{r}\right)^{3/2}}\left\{1.122 - 1.302\left(\frac{a}{r}\right) + 0.988\left(\frac{a}{r}\right)^2 - 0.308\left(\frac{a}{r}\right)^3\right\} \qquad (5.2)$$

where *r* is the radius of the cylindrical specimen.

The stress intensity range is corrected for crack closure at compressive loads by simply assuming $\Delta K = K_{max}$. Furthermore, as can be seen in Figure 5.4 and Figure 5.7, the maximum stress levels changed somewhat as the test progressed. However, for the numerical estimation of lifetime, a single stress range is used as being representative for the entire test. To this purpose the maximum tensile stress is used that developed during the test of each individual specimen. Typically, the smooth specimens developed a maximum stress of approximately 366 MPa, while the maximum stresses systematically dropped with increasing notch sizes. For example, for the deepest notch used (0.65 mm) a maximum stress level developed of only 265 MPa.

Results of the lifetime calculations were correlated with experimental lifetimes by choosing appropriate Paris parameters *C* and *m*. Using only a single notch depth, an infinite number of combinations of the parameters *C* and *m* can result in the value of the lifetime measured. Therefore, the correct combination of these two parameters is obtained by using all test results for specimens with different notch depths. The best correlation was found for $m = 5$, $C = 9.5 \cdot 10^{-12}$ and, where *da/dN* is expressed in m/cycle, Δ*K* in MPa√m and *C* in MPa^{-5} m $^{(-3/2)}$. These values are used in all subsequent calculations.

Results are shown in Figure 5.8, with both measured and calculated cycles to failure (N_f) plotted as a function of notch depth. It clearly appears to be possible to describe the experimentally observed variation of the cycles to failure of the differently notched specimens with calculations employing the Paris' crack growth equation. Figure 5.8 also contains two additional curves, showing calculated lifetimes as a function of notch depth for fixed maximum tensile stresses of 366 MPa and 263 MPa, respectively. These stress levels are the ones involved in tests on the smooth specimens and the 0.65 mm notched specimen, respectively. The curves are an illustration of how lifetime changes as a function of notch depth for a fixed maximum stress level.

The average lifetime of the five TMF tests on smooth specimen with a 30 s holding time was 1443 cycles. From the lifetime curve corresponding to the stress level of 366 MPa, *cf.* Figure 5.8, it can be read that a machined notch of approximately 45 µm would also give this lifetime. Therefore, 45 µm can be considered as an inherent notch size for this CGI, a value that corresponds well with the typical dimensions of the graphite particles.

To visualize the effect of stress level on TMF lifetime in a straightforward way, Figure 5.9 shows calculated TMF lifetimes as a function of stress levels, while individual curves in the figure represent specific values taken for the notch depth (or theoretical graphite particle size). Also the data points for the experimental TMF results are illustrated in this graph. It must be mentioned that the shown combinations of stress levels and notch

sizes may not be realistic for actual service TMF conditions, in other words, other properties such as thermal conductivity may play a role, but it illustrates the dependence of lifetime on stress level. This type of graph could be used as a design tool for predicting TMF lifetimes of real engine components, provided that the actual *in service* stress levels are known.

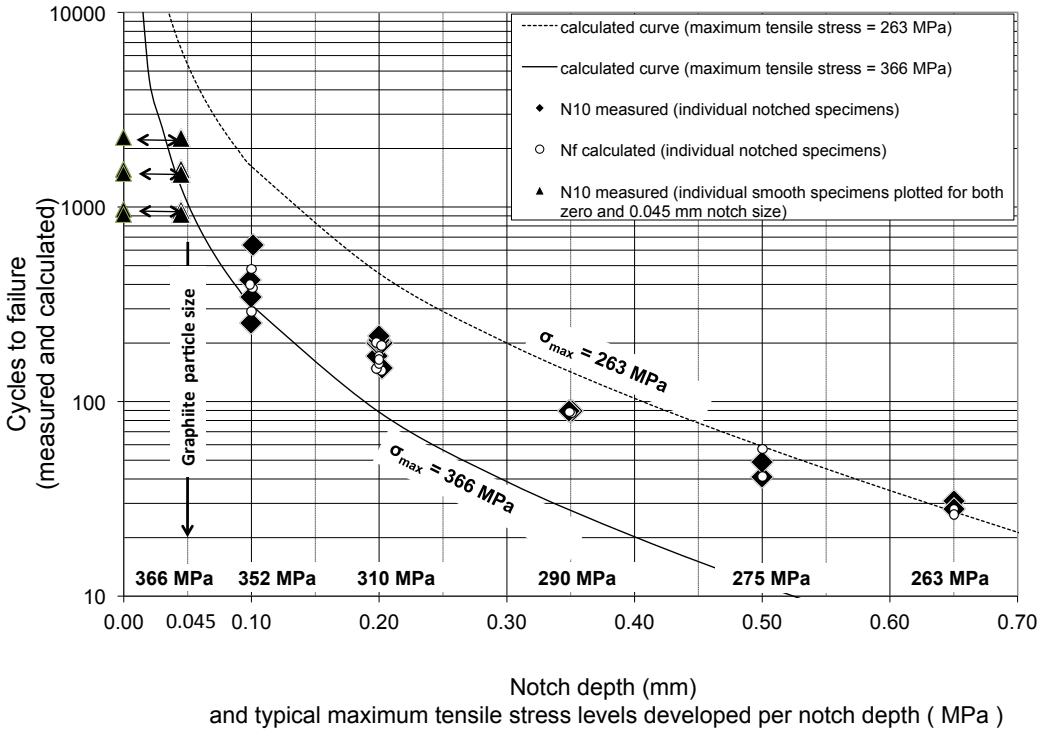

Figure 5.8 Results of TMF tests using notched and smooth specimens, in terms of measured and calculated cycles to failure, for different notch depths. The two solid lines represent the lifetime as a function of notch depth for the stress levels involved in tests on specimens with 0.045 mm (*i.e.* smooth specimen) and 0.65 mm notches, respectively.

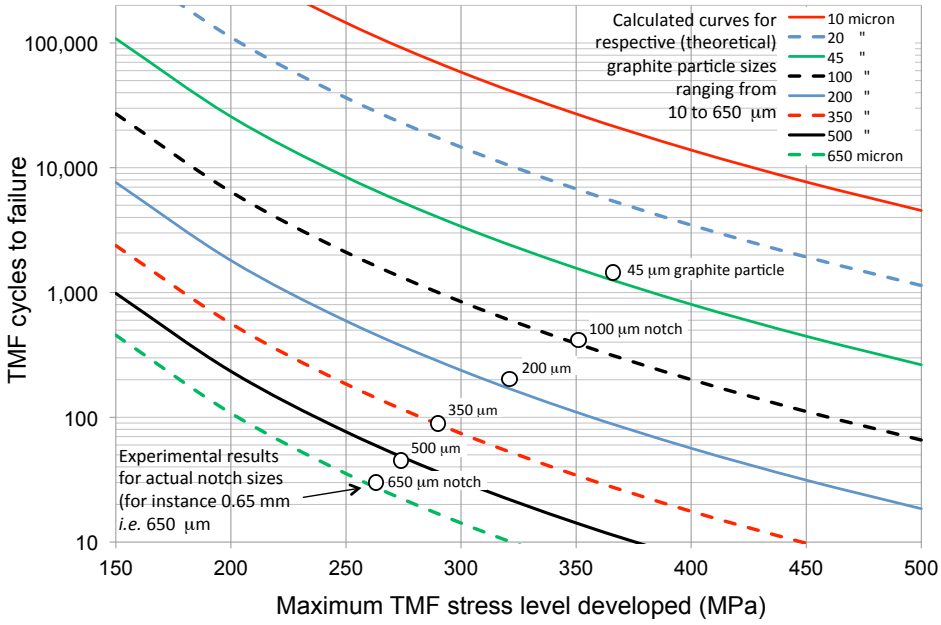

Figure 5.9 Calculated lifetime as a function of nominal maximum stress level for different notch sizes (or theoretical graphite particle sizes).

Scatter in TMF Lifetimes as a Function of Notch Depth

For notch depths of 0.35, 0.50 and 0.65 mm, only two tests were performed per notch depth and a statistical evaluation of the scatter with respect to a single set of duplicate tests is not realistic. However, since the duplicate tests for all notch depths mentioned above consistently show a low level of scatter, and also since the average N_{10} values show a clear correlation with the notch depth, the reproducibility found for the notched tests mentioned is considered to be relatively high. The scatter in the results of the 0.1 mm notches is noticeably larger, and this was also the reason that two additional tests were performed. The reason for this increased scatter is probably the fact that a 0.1 mm notch is not much larger than the average size of the graphite particles (≈ 45 µm).
It should be mentioned that during the progress of this study it was occasionally found useful to perform TMF tests using 0.2 mm notched specimen. These additional test results are also included in Table 5.1 and Figure 5.8.
To address the observed scatter, the role of the graphite particles near to the root of the notch must be considered. The effective notch size will deviate from the actual size, due to the presence of graphite particles at or close to the root of the notch, locally extending the notch depth. This will happen at several locations along the circumferential notch, governed by the spatial and the size distribution of the graphite particles. Consequently, crack growth at the notch starts at varying rates, thus affecting TMF lifetime.

An average graphite particle size of 45 μm has been established by measuring the size of 2126 graphite particles; a typical micrograph used for this analysis is shown in Figure 4.1 (*cf.* chapter 4). In this analysis the standard deviation of the graphite particle size distribution was found to be 25 μm. The scatter in the test results can be quantified by using the Paris crack growth equation and comparing calculated lifetimes for the actual notch with those for a notch extended by this standard deviation of the particle size, *i.e.* 25 μm.

The lifetimes for a 0.1 mm and a 0.125 mm notch are calculated as 389 and 262 cycles, respectively, representing a reduction in lifetime of 33%. Likewise, the calculated lifetimes for a 0.65 mm and a 0.675 mm notch are 27.5 and 24.3 cycles, respectively, representing a decrease of 12%. In comparison, the standard deviations in the experimental results for a 0.1 mm and a 0.65 mm notch are 40% and 7%, respectively. It is recognized that the small number of test results does not allow a solid statistical evaluation, but the agreement between calculated and experimental scatter is striking. It should be noted, that the calculated scatter can also be read from the slopes of the respective lifetime curves in Figure 5.8.

It is interesting to also estimate the scatter that is to be expected in testing smooth specimens. Comparing a notch of 45 μm with one of 70 μm leads to a calculated lifetime reduction from 1278 to 580 cycles. This reduction of 53% is of the same order of magnitude as the standard deviation of the test results for smooth specimens (37%).

The evaluation of scatter in measured TMF lifetimes, as given above, was based on the idea that graphite particles locally extend the notch depth with a local increase of the initial crack growth rate. However, the graphite particles at the notch tip could also be interpreted as an average notch depth extension, effective with regard to the TMF mechanism. This matter was evaluated by repeating TMF lifetime calculations for extended notch depths. For instance, calculating lifetimes with notch depth values, extended by an amount of 25 μm (*i.e.* standard deviation of the graphite particle size distribution), were found to also give a good fit between calculated and measured TMF lifetimes. It should be mentioned that this involved small adaptations to the values of the C and m Paris parameters, compared to the values used for the original calculations (see Table 5.1 and Figure 5.8). However, the new fit did not result in a noticeable improvement leading to a better correlation between calculated and measured TMF lifetimes. Also the effect of other notch extensions, with values ranging from 10 μm to 45 μm, were analyzed but were found to give similar results. It was concluded that the use of the real notch depth as initial crack length is a good practice for modeling TMF lifetimes.

In summary, the results of Figure 5.8 lead to the conclusion that a major portion of the TMF lifetime of CGI is consumed by crack growth. The crack growth can be described by the Paris' crack growth equation. Therefore, the use of notched specimens for evaluating TMF properties of cast iron is a promising technique. Results are obtained in shorter testing time, with a lower scatter. For instance it was possible to perform tests with a long holding time per cycle while the total testing time was kept within reasonable time frames by using notched specimens (see chapter 6).

5.3.3 Crack Growth Measurements

The numerical crack growth model (Paris), as described in the previous section, is based on the comparison of experimental TMF lifetime results (notched specimens) and numerical calculations. It was considered useful to have a more direct verification of the Paris model by measuring crack extensions and calculating crack growth rates.
Using the Paris model, it can be established that an initial crack extension of 0.2 mm consumes approximately 80% of total lifetime, both for smooth and notched specimens. Therefore, the crack growth rates occurring during this range of crack extension to a large extent determine TMF lifetime.
The initial aim was to measure crack growth rates that are of the same order of magnitude as the crack growth rates that control TMF failures of real parts (or smooth specimens). A smooth specimen was loaded for about 800 cycles and cross sections were made to evaluate cracks, which were expected to grow from graphite particles at or near the surface of the gauge region. Indeed, cracks emanating from graphite particles could be observed, but without a clear relation between the presence and size of graphite particles and emanating cracks. It was recognized that the visible size of a graphite particle may not represent its maximum size, since only an arbitrary cross section through the particle is visible. Hence, it was considered not realistic to measure crack growth rates using smooth samples.
As an alternative, notched specimens were employed, forcing cracks to initiate from the notch tip. Relatively small notch depths were used to stay in the low crack-growth rate regime, while the scatter in crack growth rates is expected to be reduced compared to the situation of a smooth sample. Notches of 0.20, 0.25 and 0.50 mm were chosen in order to obtain three distinctly different crack growth rates. Using the Paris model, the number of cycles was calculated necessary for the crack to grow about 0.1 mm from the notch tip. The specimen was subjected to the usual TMF conditions (cf. chapter 3, section 3.2.2.) for this calculated number of cycles, and subsequently the test was stopped and cross sections were made.
Table 5.2 summarizes the test conditions and the average measured crack extensions for the three specimens. Also the crack growth rates, calculated using the secant method described in [24], are listed. All measured crack growth rates were found to be approximately 30% smaller compared to the values predicted by the Paris model. Factors influencing the precision of obtained crack growth rates are discussed in section 11 of [24]. It mentions that for fatigue tests performed within one laboratory and using highly homogeneous materials, the variability of measured *da/dN* values on average is of the order of ±27%. Appendix X3 of [24] also addresses the additional difficulties in measuring *da/dN* when dealing with small cracks. In view of these considerations, the measured values of *da/dN* are within reasonable agreement with the calculated values of the Paris model, *i.e.* for the three tests that were used for validation here.

Table 5.2 Crack extensions and crack growth rates, both measured and calculated according to the Paris crack growth model. *Cf.* Appendix E for the abbreviations in this table columns 1 to 12.

TMF test data				Crack extension		da/dN		Statistical data			
				Meas.	Paris	Meas.	Paris				
1)	2)	3)	4)	5)	6)	7)	8)	9)	10)	11)	12)
a_0	N_{TMF}	σ_{max}	K_{max}	Δa_{avg} (st. dev.)	Δa_{Paris}	$\frac{\Delta a_{avg}}{N_{TMF}}$	$\left(\frac{da}{dN}\right)_{Paris}$	n_{meas}	Δa_{min}	Δa_{max}	Δa_{stdev}
[mm]	-	[MPa]	[MPa√m]	[µm]	[µm]	[µm/ cycle]	[µm/ cycle]	-	[µm]	[µm]	[µm]
0.20	125	316	10.50	89 (7)	150	0.71	1.10	48	21	245	48
0.25	100	303	11.50	117 (11)	180	1.17	1.60	30	3	268	61
0.50	30	264	13.80	108 (10)	150	3.60	4.70	50	9	355	72

Precision of the Crack Size Measurement Technique Used

The crack extension was intentionally aimed to be small (*i.e.* 150 µm) in order to limit the change in ΔK between the start and end of the crack growth. In this way, the calculated crack growth rate is not smoothed too much by using the secant method described in [24]. It should be noticed that using optical microscopy at high magnification, each individual crack length could be measured within an accuracy of about 0.1 µm.

The measured crack extensions show a standard deviation of 60 µm, which is relatively large. This large scatter is not related to the measurement precision, but represents actual variations in the sizes of cracks at different locations in the material. The cause of this variation in local crack size was discussed in section 5.3.2. Clearly, making one cross section in a specimen with one circumferential notch, would enable two crack extension measurements only, which does not lead to a reliable value for *da/dN*. The procedure used here, using multiple cross sections and three notches per specimen, resulted in 48, 30 and 50 crack extension measurements. Assuming a random variation of the measured values, the calculated average crack extension has an accuracy inversely proportional to the root of the number of measurements, and is estimated to be only 10 µm.

5.3.4 Effect of Bulk Cyclic Plasticity on Crack Growth

The individual test results shown in Figure 5.8 cover an extended range of TMF lifetimes, from N_{10} = 30 to 1400 cycles to failure. Obviously, accumulated cyclic plasticity of bulk material also ranges significantly at these different lifetimes. Nevertheless, the lifetimes of all 'smooth' and notched TMF tests could be predicted by a single Paris equation with identical values for *C* and *m*. This indicates that TMF crack growth might not be significantly affected by the amount of cyclic plasticity of the bulk material. To evaluate

this matter further tests were performed on notched specimens of pre-cycled material, *cf.* section 5.2.
The number of pre-cycles must be chosen high enough to produce some distinct cyclic plasticity, but low enough to prevent the development of a large macroscopic crack. According to the Paris model, the maximum size of a TMF crack after 400 cycles is about 100 µm, when considering crack growth starting from a relatively large graphite particle (for instance 70 µm, which is the average size of the graphite particles extended by the standard deviation of graphite particle size distribution) at or near the surface of a smooth specimen. With 400 as the number of pre-cycles, a notch depth of 0.2 mm was chosen, because this notch depth can be expected to be dominant relative to TMF cracks that will have developed during the pre-cycling. Three replicate tests were performed for both pre-cycled and reference material (all using a 0.2 mm notch size). It should be mentioned that these tests were performed on specimens taken from a single individual cylinder head, in order to minimize possible effects arising from variations in castings.
The results of the tests are listed in Table 5.3. It was found that the lifetimes of the pre-cycled and notched specimens were similar to the lifetimes of the notched specimens of initial material, *i.e*. $N_{10} \approx 200$. As can be seen in this table, the pre-cycled samples which had 400 cycles more compared to the reference notched samples exhibit higher stress levels due to strain hardening, which leads to slightly shorter lifetime. It is concluded that the TMF crack growth rate in CGI is not significantly affected by the level of accumulated cyclic plasticity of the bulk material. The cyclic plasticity in the crack tip region apparently is dominant for TMF crack growth in CGI. It was confirmed by microscopic observation that the final TMF crack originated from the notch tip, and not from cracks present near the specimen surface.

Table 5.3 TMF lifetimes and maximum stresses of notched specimens (0.2 mm) for pre-cycled bulk specimens (400 cycles) and specimens of virgin material.

	N_{10}	σ_{max} (MPa)	Averaged N_{10}	Averaged σ_{max} (MPa)
Pre-cycled and subsequently notched (0.2 mm)	232	332	195	334
	158	337		
	195	332		
Reference notched tests (0.2 mm)	200	330	222	327
	245	331		
	221	320		

5.4 Conclusions

In the present chapter the lifetime was measured in Thermo Mechanical Fatigue (TMF) tests under total constraint on pearlitic Compacted Graphite Iron (CGI), with temperatures cycling between 50 °C and 420 °C. As TMF lifetimes could be measured in

a shorter period of time with relatively low scatter on notched specimens, while results are still representative for TMF failures of smooth specimens, it is concluded that working on notched specimens is a promising approach to study TMF behavior of CGI. The inherent graphite particles are found to act as internal notches from which a TMF crack almost immediately starts to grow during the first TMF cycles. Hence, it was established that TMF lifetime in CGI is governed by crack growth and not by crack initiation.

By considering the notch depth as an initial crack length, TMF lifetimes were reproduced numerically using the Paris equation for fatigue crack growth. For one distinct set of the Paris parameters *C* and *m*, the calculated lifetimes were found to be in good agreement with all experimental results, covering a wide range of TMF lifetimes from 30 to 1400 cycles. Even for smooth specimens the Paris model worked well by taking the typical graphite particle size as the notch depth. The relevance of the Paris growth law was further confirmed by meticulously measuring the actual crack growth rates for three typical ΔK values. The resulting average crack growth rates proved to be in reasonable agreement with the predicted values according to the Paris model. It was further shown that the cyclic plasticity of the bulk material, accumulated during TMF cycles, does not have a noticeable effect on TMF crack growth rates (*i.e.* on TMF lifetime).

5.5 References

[1] Trampert S, Gocmez T, Pischinger S. Thermomechanical fatigue life prediction of cylinder heads in combustion engines, J. Eng. Gas Turbines Power, 2008; 130: 012806-1 (10 pages).

[2] Hallstein R, Lang K.H, Löhe D, Macherauch E. Thermal-Mechanical Fatigue Behaviour of Vermicular Cast Iron, Proceedings of the 8th International Conference on Mechanical Behaviour of Materials (ICM8), Ellyin F., Provan J.W. (Editors), 1(Victoria, Canada), May 16-21, 1999; 301–306.

[3] Charkaluk E, Rémy L. " Fatigue of Materials and Structures, Application to Design and Damage", In Bathias, C., &Pineau A. (Eds.), Chapter 7: Thermal fatigue, John Wiley & Sons Inc., USA, 2011; 271-338.

[4] Christ H-J. Effect of environment on thermomechanicalfaigue life, Mater. Sci. Eng. A, 2007; 468–470: 98–108.

[5] Rémy L. Fatigue and thermomechanical fatigue at high temperature, Encyclopedia of Materials: Science and Technology, 2001; 2866-2877.

[6] Huang Z.W, Wang Z.G, Zhu S.J, Yuan F.H, Wang F.G. Thermomechanical fatigue behavior and life prediction of a cast nickel-based superalloy, Mater. Sci. Eng. A, 2006; 432: 308–316.

[7] Nagesha A, Valsan M, Kannan R, BhanuSankaraRao K, Bauer V, Christ H-J, Singh V. Thermomechanical fatigue evaluation and life prediction of 316L(N) stainless steel, Int. J. Fatigue 2009; 31: 636–643.

[8] Gocmez T, Awarke A, Pischinger S. A new low cycle fatigue criterion for isothermal and out-of phase thermomechanical loading, Int. J. of Fatigue 2010; 32: 769-779.

[9] Cavallini M, Bartolomeo O. Di, Iacoviello F. Fatigue crack propagation damaging micromechanisms in ductle cast irons, Engineering Fracture Mechanics 2008; 75: 694-704.

[10] Hübner P, Schlosser H, Pusch G, Biermann H. Load history effects in ductile cast iron for wind turbine components, Int. J. of Fatigue 2007; 29: 1788–1796.

[11] Seifert T, Riedel H. Mechanism-based thermomechanical fatigue life prediction of cast iron, Part I: Models, Int. J. Fatigue, 2010; 32: 1358-1267.
[12] Seifert T, Maier G, Uihlein A, Lang K, Riedel H. Mechanism-based thermomechanical fatigue life prediction of cast iron, Part II: Comparison of model predictions with experiments, Int. J. Fatigue, 2010; 32: 1368-1377.
[13] Rémy L, Haddar N, Alam A, Koster A, Marchal N. Growth of small cracks and prediction of lifetime in high-temperature alloys, Mater. Sci. Eng. A, 2007; 40-50: 468-470.
[14] Riedler M, Leitner H, Prillhofer B, Winter G, Eichlseder W. Lifetime simulation of thermo-mechanically loaded components, Meccanica 2007; 42:47–59.
[15] McClung R. C. *et al.* Behaviour of small fatigue cracks, Applications Where Small Cracks Are Important,ASM Handbook (online), vol. 19, Fatigue and Fracture, Copyright © 2002 ASM International®.
[16] Murakami Y, Endo M. Effect of defects, inclusions and inhomogeneities on fatigue strength, Int. J. of Fatigue 1994; 16:163-182.
[17] Hähner P, *et al.*, Research and development into a European code-of-practice for strain-controlled thermo-mechanical fatigue testing, Int. J. Fatigue 2008; 30: 372-381.
[18] Ghodrat S, Riemslag A.C, Kestens L.A.I, Petrov R.H, Janssen M, Sietsma J. Effects of Holding Time on Thermo-Mechanical Fatigue Properties of Compacted Graphite Iron through Tests with Notched Specimens, Metallurgical and Materials Transactions A 2013; 44: 2121-2130.
[19] Ritchie R.O. Mechanisms of fatigue-crack propagation in ductile and brittle solids, International Journal of Fracture 1999; 100: 55–83.
[20] Heil M.L, Nicholas T, Haritos G.K, Crack growth in alloy 718 under thermal-mechanical cycling, thermal stress, material deformation, and thermo-mechanical fatigue, Sehitoglu H, Zamrik S.Y, Ed., American Society of Mechanical Engineers, 1987; 23-29.
[21] Riemslag A.C. Fatigue testing of high-density polyethylene and polycarbonate with crack length measurement using image processing techniques, J. Test. Eval. 1994; 22: 410-419.
[22] Herzberg R.W, Manson J.A. Fatigue of Engineering Plastics. London: Academic press INC. ISBN 0-12-343550-1, Chapter 3, 1980; 74-149.
[23] Tada H, Paris P.C, Irwin G.R. The Stress Analysis of Cracks Handbook, 2nd ed., Paris Productions INC., 1985; p. 27.1a.
[24] ASTM E 647-00 Standard Test Method for Measurement of Fatigue Crack Growth Rates, 2000.

6

Effects of Holding Time on Thermo-Mechanical Fatigue Properties of Compacted Graphite Iron through Tests with Notched Specimens

"The best scientist is open to experience and begins with romance, the idea that anything is possible".

Ray Bradbury

TMF tests using notched specimens were reported in the previous chapter and were found to give relatively short testing times with a low scatter, while still being representative for TMF lifetimes of smooth specimens.
In this chapter[1], a detailed study is presented on the effect of the fatigue cycle holding time on the thermo-mechanical fatigue behavior of CGI. By using notched specimens, the effect of prolonged holding times on TMF lifetimes was studied while total testing time was kept within reasonable limits.
During TMF tests with extended holding times higher maximum stress levels were developed and the reason for this is evaluated in this chapter. For all holding times, TMF lifetimes were also calculated by using the Paris crack growth model (*cf.* chapter 5) using the same maximum stress levels. This enabled to distinguish the isolated effect of different holding times on TMF lifetimes, without being obscured by dissimilar stress levels.
Microstructural changes associated with the stress relaxation phenomenon were evaluated by analyzing quantitative data sets obtained by orientation contrast microscopy based on Electron Backscatter Diffraction (EBSD).

[1] This chapter is based on: S. Ghodrat, A.C. Riemslag, L.A.I. Kestens, R. H. Petrov, M. Janssen, and J. Sietsma, Effects of Holding Time on Thermo-Mechanical Fatigue Properties of Compacted Graphite Iron through Tests with Notched Specimens, Metallurgical and Materials Transactions A 44 (2013) 2121-2130.

6.1 Introduction

Multiple mechanisms take place during a thermo-mechanical out-of-phase cycle: plastic deformation, creep, oxidation, changes of the microstructure and crack initiation and propagation [1, 2]. These damage mechanisms significantly depend on the material, temperature, frequency, stress levels and the environment [3]. The main damage mechanisms are mechanical damage by fatigue, viscous phenomena by stress relaxation/creep and environmental damage by oxidation [4]. In damage models, the oxidation process is defined as a function of strain range, strain rate, strain-temperature phasing and oxidation kinetics. Likewise, creep damage is based on stress, temperature, strain-temperature phasing and time [4]. Both mechanical and oxidation damage mechanisms are temperature and time dependent, which is relevant for TMF, since this takes place during prolonged periods of time at various temperatures. In addition to these phenomena, in the case of cast iron, the graphite particles affect the deformation. As discussed by Seifert *et al.* [5,6], graphite particles in cast iron weaken the material in tension by decreasing the stiffness, since the graphite particles partly delaminate from the matrix. In compression interfacial microcracks are closed and a higher stiffness results. This leads to an asymmetrical tension-compression behavior of cast iron [5]. It was found that in compression the Young's modulus on average is 5% larger than in tension [7].

Generally, an in-service thermal cycle of a diesel engine includes an extended holding time during the heating and cooling phases. In OP-TMF, the maximum compressive stress occurs during the upper cycle temperature. The influence of the holding time at maximum operating temperature has been evaluated by many researchers and was first reported by Gundlach [8]. In order to study the response of cast iron undergoing thermal cycling, he performed TMF tests on different types of cast irons. His results revealed that during thermal cycling, the compressive stress at maximum temperature decreased with the number of cycles, while the tensile stress at minimum temperature increased. Consequently, Gundlach concluded that stress relaxation was taking place, ultimately reducing the TMF life of specimens. It is reported that cast irons under TMF conditions undergo short-term stress relaxation within time periods of the order of only minutes [9]. Results of relaxation experiments performed for nodular cast iron, show that after half an hour the stress decreased by 30% at 450 °C and 50% at 500 °C [6].

In the case of TMF under total constraint conditions, stress relaxation during the compressive part of a TMF cycle causes a higher tensile stress to develop in the subsequent tensile part of the TMF load cycle together with an increase of inelastic deformation as a result of the decrease of elastic stress. These conditions are considered to induce damage and hence reduce TMF lifetime. The matter of increasing tensile stresses due to relaxation of compressive stresses is discussed in more detail in section 6.3.1.

With regard to testing procedures, as addressed in chapter 5, an alternative TMF test method for CGI was introduced using notched specimens, resulting in shorter testing times with a reduced amount of scatter.

In the current research, the effect of holding time on the TMF behavior of CGI is studied using notched specimens. In this way, the total testing time is kept reasonably short, in spite of the extended holding times (up to 5 h) per cycle.
For an effective reduction of scatter, the notch depth must be notably larger than the typical graphite particle size (*i.e.* 50 µm) and in this respect, a notch depth of 0.2 mm is suitable. Choosing a larger notch depth would reduce both scatter and testing time even more. However, the testing time must remain sufficiently long for the environment to interact with the TMF micromechanisms. Therefore, a notch depth of 0.2 mm provides a balance between a reduced scatter and a sufficiently long testing time.
In the current research, the microstructural evolution of CGI is investigated by the powerful technique of orientation contrast microscopy, which is based on Electron Backscatter Diffraction (EBSD). More precisely, with this technique it is intended to reveal very subtle microstructural changes induced by microplastic strain and ensuing recovery during a typical first TMF cycle. Orientation contrast microscopy allows observing minute orientation changes (of the order of less than 1°), which are reminiscent and characteristic of the phenomena under consideration.

6.2 Experimental Procedures

Basic information about CGI material and specimens used are addressed primarily in chapter 3. However, an additional test procedure, involving EBSD measurements, is used for evaluating microstructural evolution during the holding time of a TMF cycle. This procedure is described in detail in the following.
Standard TMF tests were performed with holding times of 30 s, by cycling the temperature between 50 °C and 420 °C (under total constraint) resulting in out-of-phase (OP) TMF loading, as shown schematically in Figure 3.4 of chapter 3. A holding time of 30 s (as already used in standard TMF tests) is considered the minimum value to ensure a homogenous temperature distribution at the minimum and maximum temperature. In this chapter also longer holding times were introduced to represent (and evaluate) the in-service conditions that valve bridges of cylinder heads are subjected to. Preferably, holding times should not lead to unpractical testing times and in this respect four different holding times were chosen *i.e.* 30, 480, 1800 (30 min) and 18000 s (5 h). The extended holding times were applied during the maximum temperature (*i.e.* 420 °C) in combination with 30 s for the minimum temperature of 50 °C. Using different holding times at 420 °C allows stress relaxation to occur to different extents.

Stress Relaxation Test and Microstructural Evolution Measured by Orientation Contrast Microscopy
The microstructural evolution during a typical TMF heating stage was evaluated by performing EBSD measurements in order to find the mechanisms associated with the stress relaxation phenomenon. To this purpose a CGI sample with a rectangular cross section of 9 x 7 mm^2, and a height of 17 mm was fabricated, which is designated as a parallelepipoid-shaped specimen. The small size of the specimen accommodates the positioning of the specimen within the chamber of the Scanning Electron Microscope (SEM).

The Electron Backscatter Diffraction (EBSD) measurements were performed for three conditions of the CGI, being (A) as-cast (B) heated in total constraint before holding and (C) heated in total constraint with a holding time of 1800 s and cooling. The conditions A, B, and C are also shown in Figure 6.1. To enable the EBSD measurements, one side of the parallelepipoid-shaped specimen (9 x 17 mm^2) was prepared by manually polishing the surface for 40 minutes with OPS (0.25 µm). In the center of the polished surface, three micro-indentions were made to mark a specific location. At this location EBSD measurements were performed, characterizing the situation of the as-cast state of the material and the subsequent conditions (points A, B and C in Figure 6.1).

To obtain condition B of the CGI (*cf.* Figure 6.1), two cylindrical pushing rods (diameter 12 mm) were clamped in the grips of the TMF machine. The parallelepipoid-shaped specimen was placed between the ends of the cylindrical pushing rods and heated to 420 °C (at the rate of 9 °C s^{-1}) under total constraint. When reaching the temperature of 420 °C, a peak compressive stress was obtained and the test was stopped, after which the specimen was removed. One side of the specimen was then polished and analyzed by EBSD, giving microstructural information on the condition represented by point B, *cf.* Figure 6.1. The EBSD measurements were done at the same location as was done for the as-cast condition.

Finally, to characterize condition C (*cf.* Figure 6.1), the specimen was again placed in the TMF machine and heated to a temperature of 420 °C (at the rate of 9 °C s^{-1}), after which the peak compression level of condition B was applied, whilst maintaining the temperature of 420 °C. At the point of reaching the peak compressive stress, the strain was kept constant for a period of 1800 s, allowing stress relaxation to occur (point C in Figure 6.1). After this holding time, the test was ended and the specimen surface was repolished for observation by EBSD at exactly the same location as studied before. The EBSD measurements were done on a scanning area of 430×300 μm^2 with a step size of 1.4 µm.

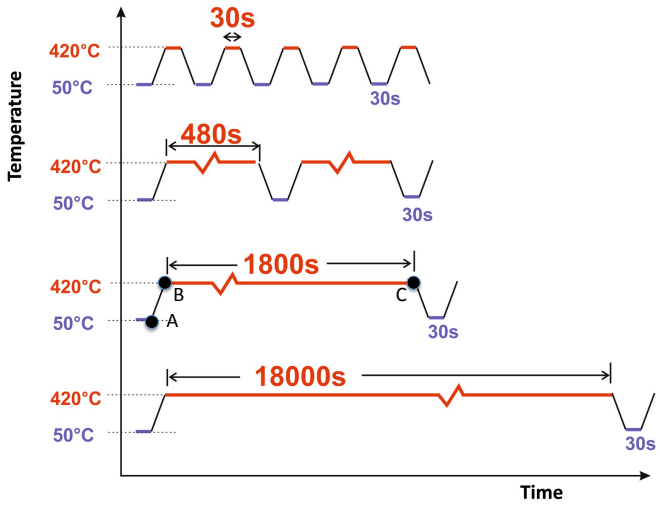

Figure 6.1 Four different holding times at maximum temperature 420 °C of 30, 480, 1800 and 18000 s were chosen in combination with 30 s for the minimum temperature 50 °C.

6.3 Results and Discussion

6.3.1 Lifetime (N_f), Stress and Plastic Strain Evolutions with Holding Times

Results of tests with different holding times are listed in Table 6.1. In this table the TMF measured lifetime N_{10} is defined as the number of cycles at which the maximum (tensile) stress (σ_{max}) has decreased by 10% relative to its maximum value. In appendix C, the underlying reasons for using N_{10} as the lifetime criterion are discussed in more detail. The TMF-lifetime results for different holding times show a clear reduction in lifetime at prolonged holding times (*cf.* Table 6.1). Relative to the lifetime at 30 s holding (*i.e.* 213 cycles), the lifetimes for the 480 s, 1800 (30 min) and 18000 s (5 h) holding times show a reduction of 27%, 57% and 60% respectively.

Table 6.1 Experimental and calculated results for TMF tests. Stresses are nominal values, *i.e.* based on a circular cross section of 6 mm diameter.

	Experimental Values				Calculated Values	
Holding time	Lifetime N_{10}	Avg. lifetime N_{10}	Max. stress level	Avg. max. stress level	C_{Paris} *)	Corrected lifetime N_{Paris} **)
s	cycles	cycles	MPa	MPa	***)	cycles
30	208	213	326	324	$7.3\ 10^{-12}$	213
	218		323			
480	162	154	323	331	$9.0\ 10^{-12}$	172
	169		339			
	130		332			
1800	96	91	346	348	$1.2\ 10^{-11}$	132
	85		346			
	93		352			
18000	75	84	347	344	$1.3\ 10^{-11}$	118
	92		342			

*) C_{Paris} values are calculated with the Paris law, chapter 5, equation (5.1), such that the lifetime corresponds to the average experimental lifetime, using the actual stress levels and assuming $m = 5$.
**) Lifetimes are calculated using a maximum stress level of 324 MPa.
***) C_{Paris} values give da/dN in m/cycle, when ΔK is expressed in MPa√m.

The effect of holding time can also be evaluated in relation to the developed stress levels during the progress of the TMF experiment. In Figure 6.2, a typical development of the minimum, mean and maximum stress is shown as a function of elapsed TMF cycles,

for these holding times tested. The development of stress levels can be divided into three distinct regions [3].

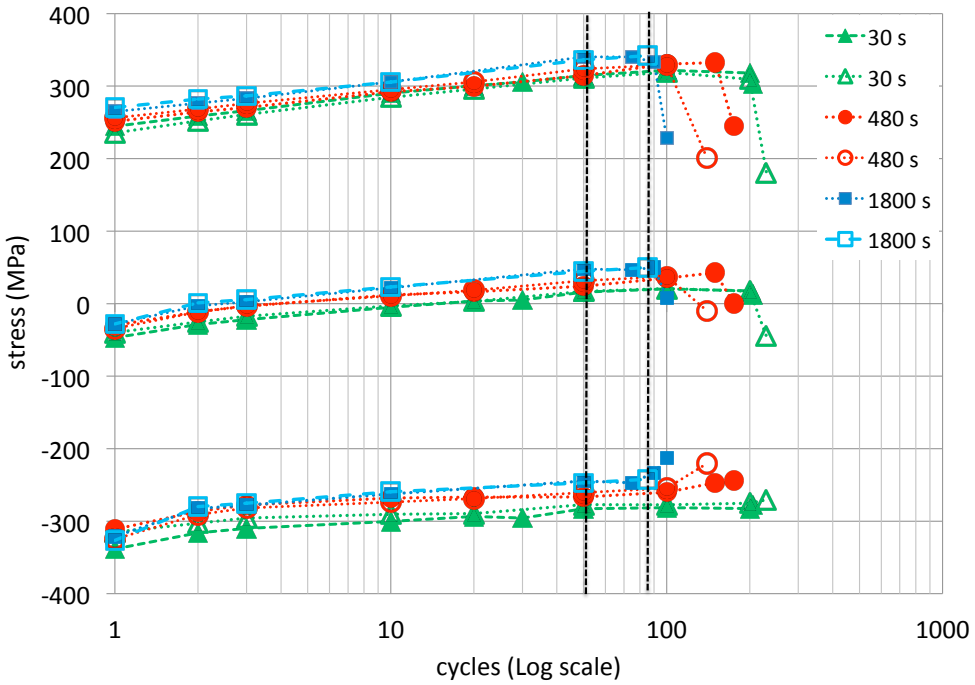

Figure 6.2 Maximum, mean and minimum stresses as a function of TMF cycles with holding times of 30 s, 480 s, and 1800 s.

The first region is characterized by increases in minimum and maximum stress level for subsequent TMF cycles. In the second region the maximum stress level remains more or less stable. Finally, in the third region, a decrease in stress level is observed. For the total constraint tests applied here, the decrease in maximum tensile stress is induced by a decrease in specimen stiffness, associated with the opening of a macroscopic crack. Therefore, the drop in stress level can be used to detect a macroscopic crack and can be applied as a criterion to define TMF lifetime. TMF testing under total constraint is equivalent to cyclically inducing a specific amount of mechanical strain. This amount is equal (and opposite in sign) to the value of the thermal strain, which was 0.6% for the TMF tests under consideration, corresponding to the temperature range of 50 °C to 420 °C (*cf.* chapter 3, section 3.2.2).

Therefore, during the entire duration of the TMF tests, the CGI is exposed to cyclic mechanical strain changes of 0.6%, in the tensile direction during cooling and the compressive direction during heating. The resulting stress levels largely depend on the initial stress levels from which individual strain excursions start. Therefore, the development of tensile and compressive stresses during a TMF test, under conditions of total constraint, are mutually dependent.

As can be seen in Figure 6.2, for all holding times the mean stress level shifts towards a tensile value during the progress of the TMF test. This is typical for the out-of-phase nature of the TMF loading condition of total constraint. One reason for the shift is that the material exhibits a lower yield strength in the compressive region (at high

temperature) compared to the value in the tensile region (at low temperature). In addition, the compressive stress may decrease during the holding time at high temperatures because of stress relaxation. As a consequence, the strain cycle associated with cooling starts at a relatively low compressive stress, and will thus produce a relatively high tensile stress. Moreover, the subsequent heating cycle starts from this relatively high tensile stress, resulting in a relatively low compressive stress. This process is repeated, until the ratio of tensile and compressive stresses settles to a certain stable value.

The stress-mechanical strain hysteresis can also give useful information about the TMF behavior. The mechanical strains calculated as a function of stress for one of the specimens (N_{10} = 96, *cf.* Table 6.1) with a 1800 s holding time are shown in Figure 6.3. The black circle indicates the parts of the TMF cycles where the compressive stress relaxes. It can also be observed that the lower the compressive stress, the higher the tensile stress in the next cycle, confirming the interdependency of tensile and compressive stress levels, as described before.

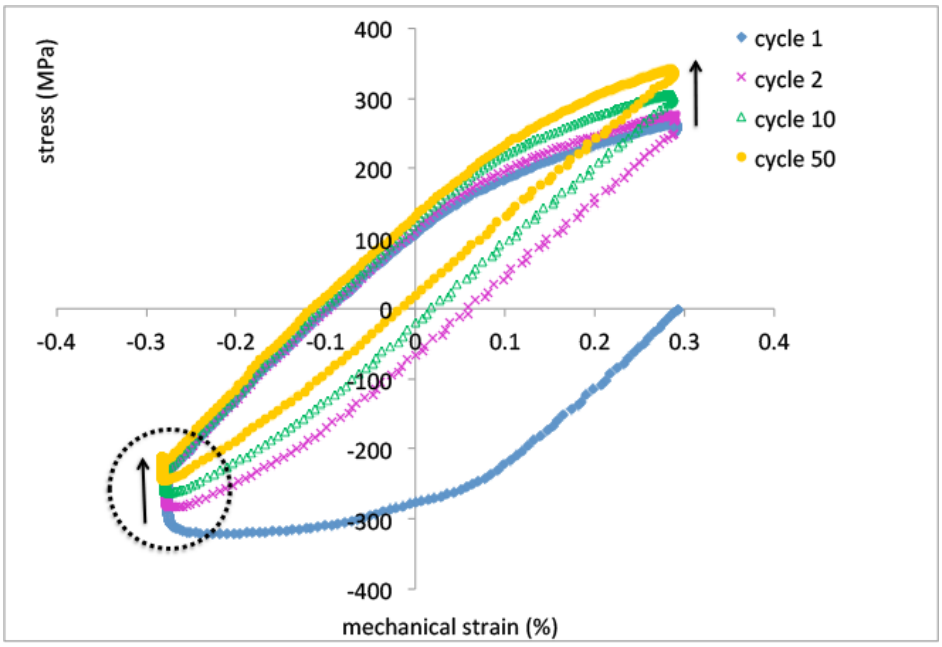

Figure 6.3 Stress–mechanical strain hysteresis loops for a specimen with 1800 s holding time (N_{10} = 96, *cf.* Table 6.1), revealing the development of the maximum tensile stress with increasing cycles due to stress relaxation in compression.

With progressing TMF cycles, the degree of stress relaxation at 420 °C gradually decreases and the shape of the hysteresis loop becomes narrower, indicating a reduction of cyclic plasticity. In Figure 6.4, the stress is plotted as a function of time for two cycles (55 and 56) for the specimen discussed above (*cf.* Figure 6.3). The stress relaxation at 420 °C for these two cycles is approximately 22 MPa. On the other hand, the increase of σ_{max} by changing the holding time from 30 s to 1800 s is approximately 24 MPa (*cf.* Table 6.1). Therefore, it can be inferred that the higher stress relaxation occurring during 1800 s holding time is responsible for the increase of σ_{max}.

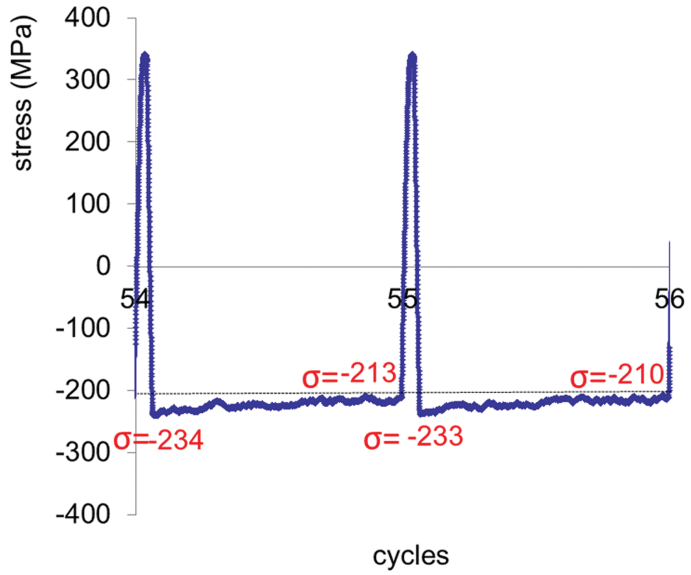

Figure 6.4 Stress as a function of time for two cycles (55 and 56) of a specimen with 1800 s holding time (N_{10} = 96).

The evolution of the degree of stress relaxation during the holding time under compression with the number of TMF cycles is plotted for all four holding times in Figure 6.5. This stress relaxation is calculated as the stress change from the moment the temperature has stabilized at 420 °C (after 10 s exposure) until the last moment of exposure to 420 °C. As can be seen, the stress relaxation for the 480 s and 1800 s holding times show a similar trend, starting at a high level of about 50 MPa and reducing to a level of about 22 MPa after 50 cycles, and remaining at that level. The stress relaxation for the specimen with 30 s holding time started with a value of 20 MPa in the first cycle and then decreased to a value of about 10 MPa for the rest of the TMF test. Relaxation of stresses is thought to be related to viscous phenomena and recovery processes [3]. This is investigated by EBSD techniques and will be discussed in section 3.4.

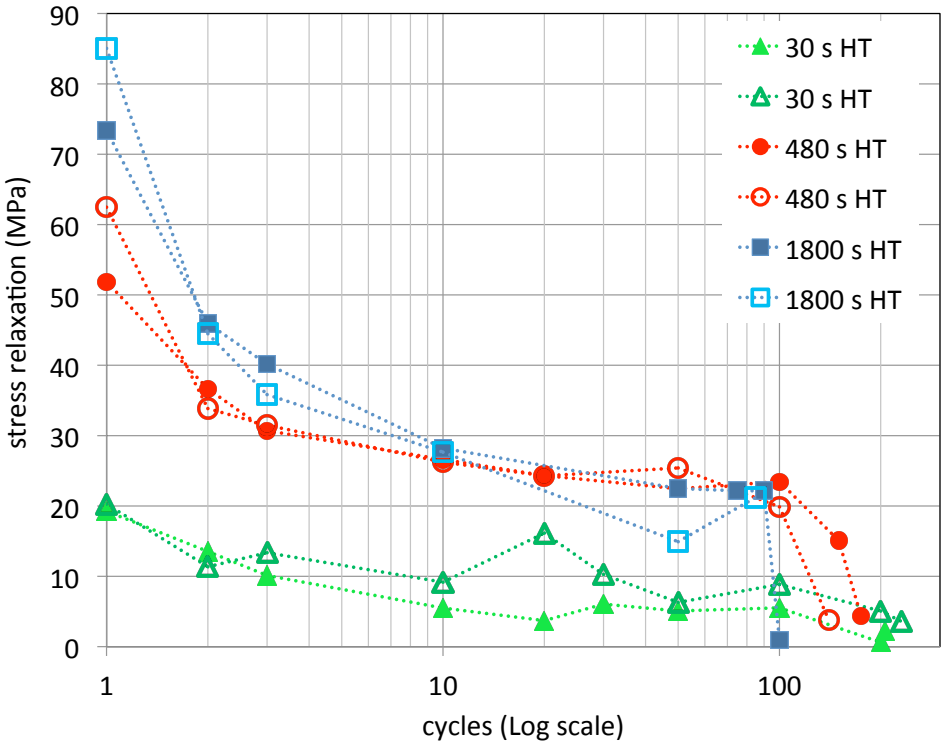

Figure 6.5 Stress relaxation vs number of cycles, compared for three specimens with 30 s, 480 s, and 1800 s holding time.

In Figure 6.3 the decrease in cyclic plastic strain can already be observed, but in Figure 6.6 the reduction of cyclic plasticity is presented explicitly. The calculated plastic strain range versus the number of elapsed cycles is plotted for all four holding times. The plastic strain range is calculated by subtracting the elastic strain range from the mechanical strain range. The maximum and minimum elastic strains needed to calculate the elastic strain range are calculated as the maximum and minimum stresses divided by the Young's moduli at the minimum and maximum temperature respectively.

All holding times show a similar trend of a rapidly decreasing plastic strain range in the first few cycles, continuing to decrease at a somewhat lower pace in the first tens of cycles, saturating at a nearly constant value from 50 cycles onwards, and increasing somewhat at the end of the test. The reduction in cyclic plasticity is in accordance with an increase in yield strength found at increased numbers of cycles. This increase in strength indicates the occurrence of cyclic strain hardening. It should be noted, that at the start of the test the total constraint condition was applied at the minimum temperature, and consequently, the first TMF cycle produces a large compressive plasticity in the CGI. In the 2nd cycle (the first complete cycle) the plastic strain range, $\Delta\varepsilon_p$ is already significantly lower.

The levels of cyclic plastic strain differ for the different holding times, with the highest cyclic plasticity for the longest holding time. It seems likely, that a high cyclic plasticity contributes to the shorter lifetime at prolonged holding times.

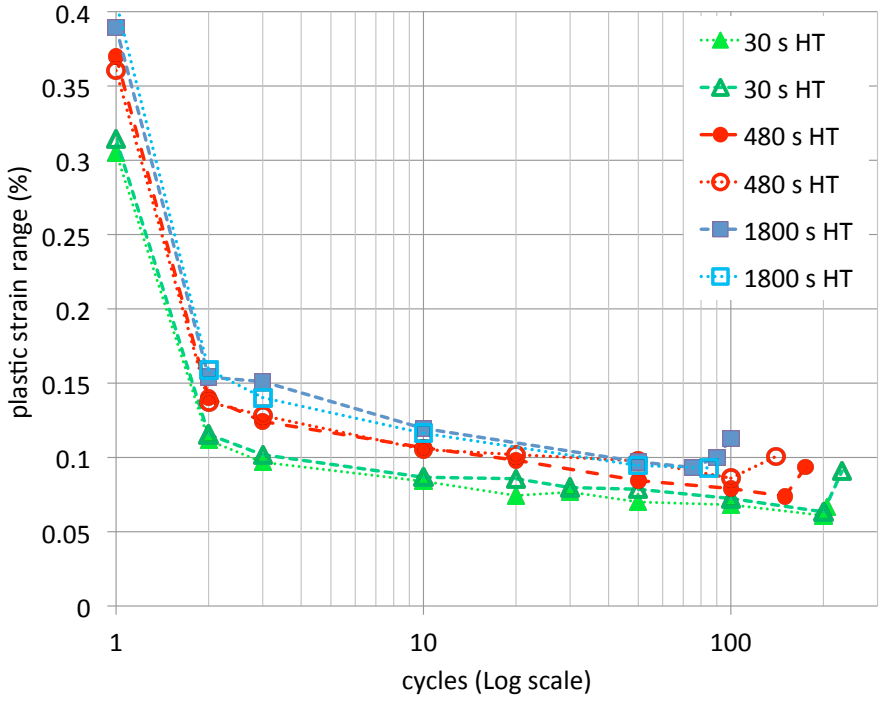

Figure 6.6 Plastic strain range vs number of cycles, compared for three specimens with 30 s, 480 s, and 1800 s holding time.

6.3.2 Correction for Dissimilar Maximum Stress Levels, Using the Paris Crack Growth Law

In chapter 5, the failure times were calculated successfully by applying Paris' fatigue crack growth law. As can be seen in Table 6.1 and in Figure 6.2, increasing the holding time leads to higher maximum stress levels and shorter lifetimes. In order to see the isolated effect of holding time, without the influence of the increased stress level, two approaches are used, both involving the Paris crack growth model (*cf.* chapter 5). The Paris model accounts for the maximum stress level developed, enabling to establish the theoretical effect of different maximum stress levels found at different holding times.

In the first approach, for each TMF test series performed with a particular holding time, the value of the Paris parameter C was determined that gives comparable values for the calculated and measured lifetimes (*cf.* Table 6.1, designated as C_{Paris})[2]. The values of C_{Paris} determined in this way were found to decrease consistently with increasing holding times, reflecting a holding time dependency of the TMF mechanism. For instance, at holding times of 30 s and 18000 s, the determined values for the C_{Paris} parameter are 7.3 10^{-12} and 1.3 10^{-11} respectively (*i.e.* a increase of about 44 %).

In the second approach, a corrected lifetime is calculated using the same reference

[2] The m parameter value is assumed to be 5, as was used in chapter 5. For the lifetime calculation actual maximum stress levels developed during individual tests were used.

It must be noted that the C value for the 30 s holding time, $7.3 \cdot 10^{-12}$, is not the same as found earlier in chapter 5, section 5.3.2, *i.e.* $9.5 \cdot 10^{-12}$. The difference is probably related to the fact that the tested specimens were sampled from different cylinder heads with different batch properties.

stress level for all holding times, while using the respective C_{Paris} values for each holding time, as mentioned in Table 6.1. The reference stress level was chosen to be the value that occurred for the shortest holding time, *i.e.* 324 MPa. The corrected calculated lifetimes (N_{Paris}) are shown in the last column of Table 6.1. Here, the corrected TMF lifetimes of the 18000 s and 30 s holding times were found to be 118 and 213 cycles (*i.e.* an increase of about 45 %).

Both approaches account for the different maximum stress developed at different holding times and give comparable results. It implies that if there were only a material effect and no additional stress effect then N_{Paris} would have decreased by 45%. The fact that an actual reduction in N_f was observed by 60 % (from 213 to 84 cycles) is due to the accumulated effect of stress and material behavior. It is assumed here that the entire stress effect is captured by stress intensity factor ΔK, whereas the parameter C is exclusively material dependent.

Figure 6.7 shows the experimental N_{10} values and the calculated N_{Paris} values for the four holding times under consideration. Hence, we can draw the conclusion that more than half of the drop in lifetime can be attributed to the material effect. As reported in Table 6.1, for each holding time there is a calculated C_{Paris}, which increases at prolonged holding times. This trend is also presented in Figure 6.8, in which the measured lifetime (N_{10}) is plotted as a function of C_{Paris} and holding time. This might point to an additional effect related to microstructural recovery during holding at elevated temperature, which will be looked at in more detail in the next section.

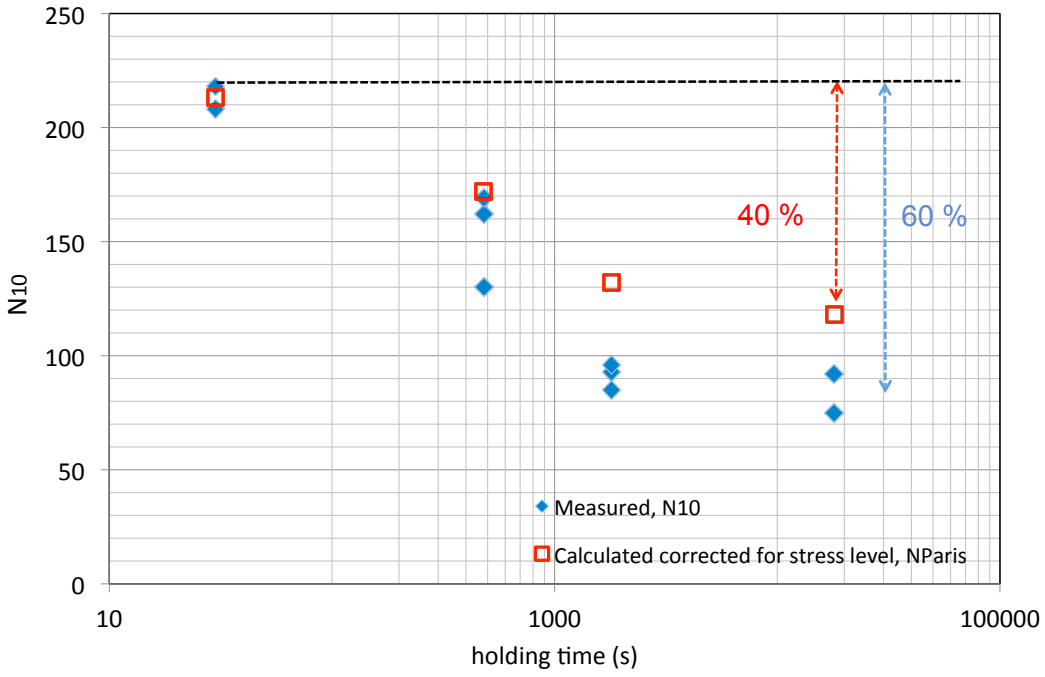

Figure 6.7 Measured lifetimes and lifetimes calculated while correcting for stress level, both as a function of holding time.

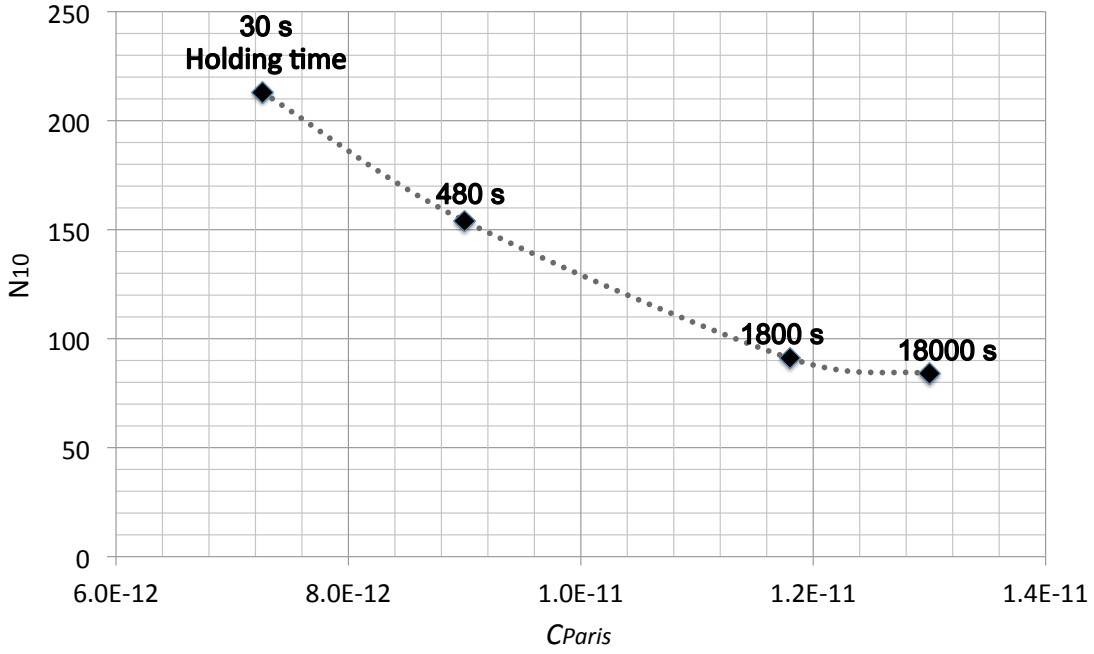

Figure 6.8 Measured lifetimes as a function of C_{Paris} and holding time.

6.3.3 EBSD Results

The evolution of crystal misorientation angle in the range between 2 to 10° ([3]) is an indication of local strains induced in the microstructure by the compressive stresses involved in these thermomechanical treatments. Such stresses produce plastic deformation involving dislocation glide in the metal matrix. The dislocations remaining in the microstructure configure themselves in cells or subgrains, which will give rise to small orientation gradients that can be measured accurately by orientation contrast microscopy (EBSD with angular resolution of the order of less than 1°).
Table 6.2 contains the length fraction (approximately equal to area fraction in 3D) of low angle grain boundaries (LAGB) measured with EBSD at a specific location of the parallelepipoid-shaped CGI specimen in 3 conditions. As can be seen in this table, the as-cast condition gives 64% of LAGB length fraction, whereas after heating to 420 °C in total constraint (1st step) this has increased to 73%, clearly showing the effect of the plasticity to which the sample was subjected. However, after a holding time of 1800 s (2nd step), the LAGB length fraction has regressed to the initial value. Alternatively this trend can also be observed in Figure 6.9, exhibiting the Image Quality (IQ) maps of the three conditions under consideration (the IQ factor represents a quantitative measure of the band contrast in the EBSD pattern, and therefore is indicative of the local density of crystal defects). In these maps LAGBs (2-15°) together with HAGBs (high angle grain boundary, 15-180°) are indicated by red (thin) and blue (thick) lines, respectively.

[3] Misorientation angles below 2° were attributed to background noise and therefore were excluded from the data set.

Table 6.2 Quantitative data obtained from EBSD scans: length fraction of LAGBs (0-10°) and kernel average misorientation.

Specimen condition	Length fraction of LAGBs with misorientation 2-10° (%)	Kernel average misorientation (degree) (st. dev.)
As-cast condition (point A in Figure 6.1)	64	0.62 (2.44%)
1st-step: Heating to 420 °C under total constraint (point B in Figure 6.1)	73	0.73 (2.21%)
2nd-step: After 1800 s holding time at 420 °C (point C in Figure 6.1)	65	0.68 (2.15%)

Local misorientation can also be characterized using a misorientation kernel approach, which quantifies the average misorientation of a data pixel in the EBSD scan with regard to its 1st, 2nd, or nth nearest neighbors within the misorientation tolerance of a grain (*e.g.* 5° tolerance. The resulting parameter of this analysis is the so-called Kernel Average Misorientation (KAM) value associated with each individual data point.

Table 6.2 lists the average KAM values for 1st nearest neighbors for the entire scan (excluding the graphite phase) observed in the three conditions considered. It can be seen that the average KAM value is sensitive to the plastic strain occurring after heating the sample from 50 °C to 420 °C, as its value increases from 0.62° to 0.73°. After a holding time of 1800 s at this temperature the average KAM value drops to 0.68°, which is precisely half way the value of the 1st step and the as-cast condition, *cf.* Table 6.2.

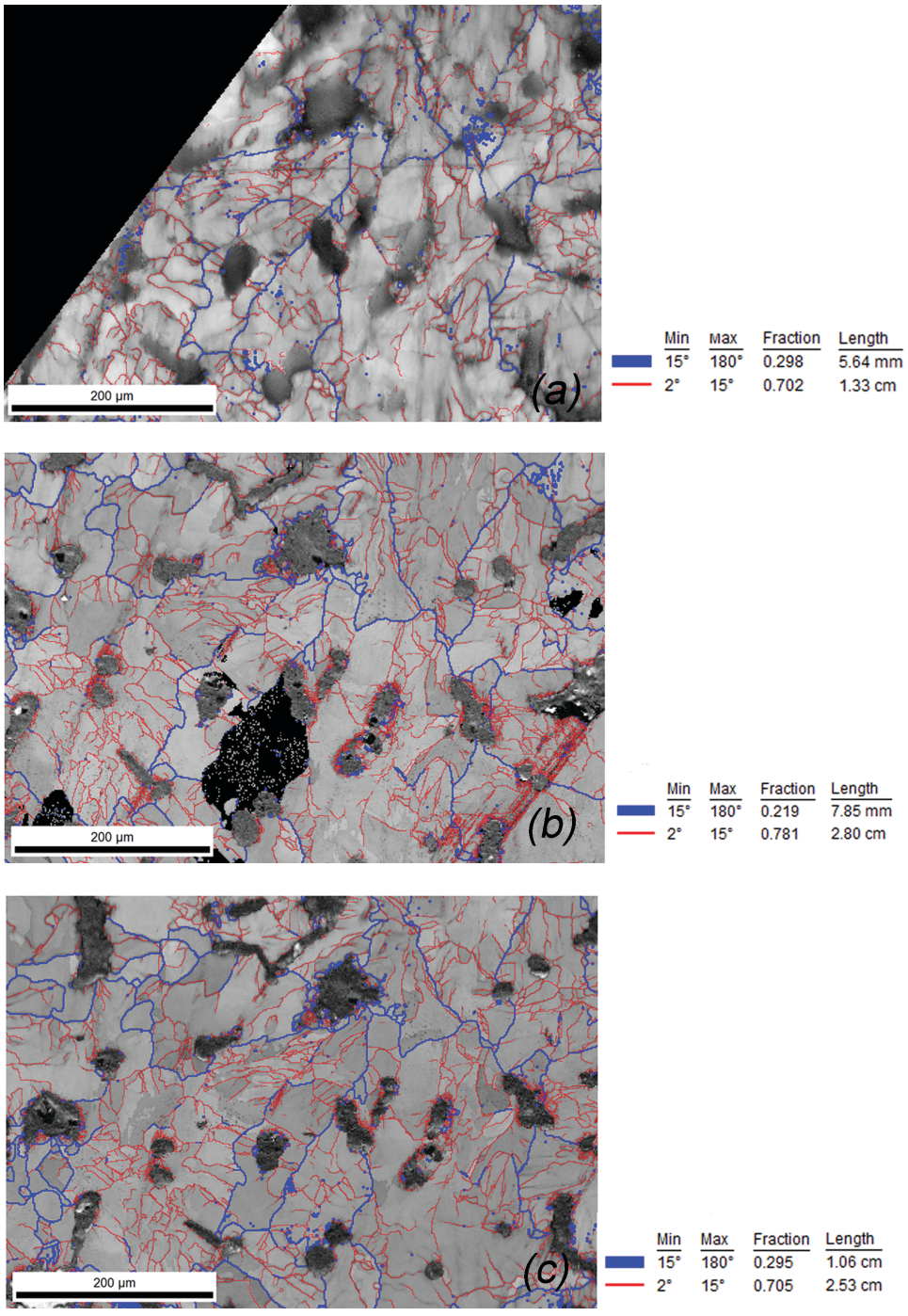

Figure 6.9 Image quality maps of three conditions under consideration: (a) as-cast condition, (b) 1st step: heating to 420 °C in total constraint, and (c) 2nd step: after 1800 s holding time at 420 °C.

Figure 6.10 also displays the KAM distributions between 0 and 5° for the three conditions under consideration. It can be observed that there is a slight difference in the tail end of the distribution in the range of 1 to 3°, between the samples that were subjected to a plastic strain of 0.4% (imposed by the mechanical constraint) and the initial sample in as-cast condition. After holding for 1800 s at high temperature, the peak

position and the distribution average is affected by the stress relaxation during isothermal holding time, *i.e.* one may readily assume that the sample was subjected to stress-relieve recovery. By close inspection of the KAM distribution profiles, it can be observed that this gave rise to a slight shift of the distribution peak from 0.44° at the start to 0.31° at the end of the holding. This is also reflected in a decrease of the average KAM value from 0.73° to 0.68°. This may be associated with the fact that the deformation substructure, established by plastic deformation, is predominantly reflected in the high tail end of the distribution, whereas statistical scatter of short-range distribution gradients more affects the core of the distribution. In this sense, one may draw the conclusion that the relaxation processes have left the plastic deformation structure unchanged, but have reduced to some extent the local orientation scatter, corresponding to the well-known recovery of statistically stored dislocations in the metal matrix [12]. Whether these minute changes are truly representative for the underlying microstructural changes needs to be confirmed in further study.

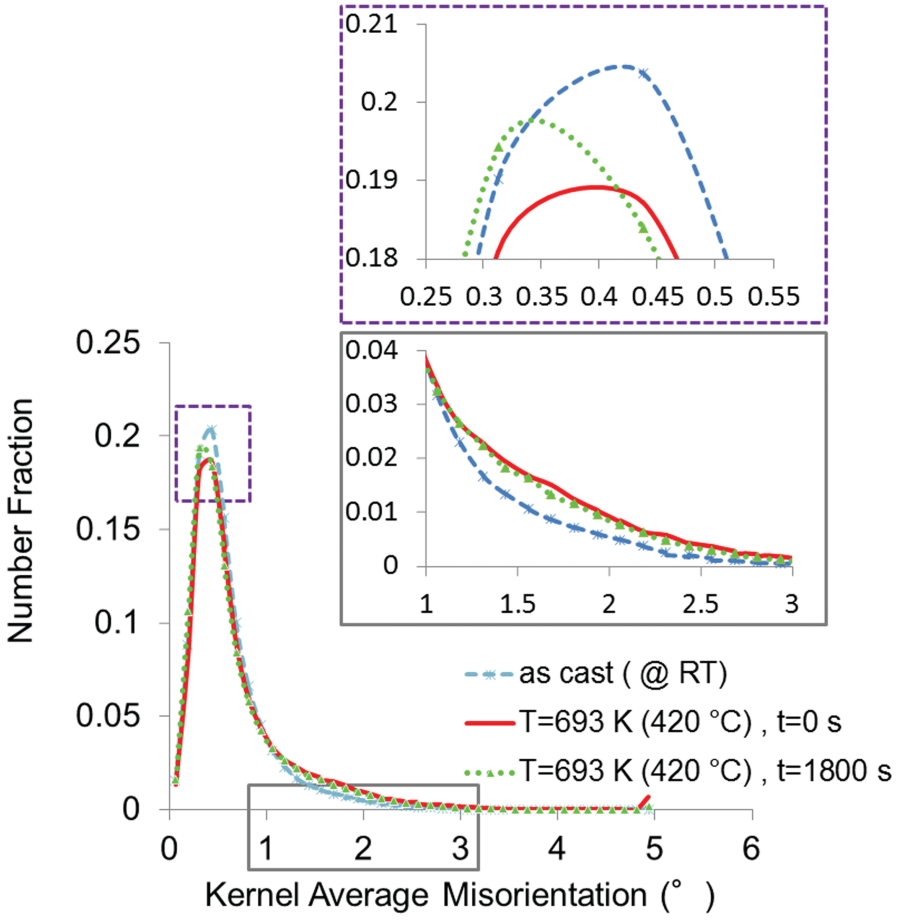

Figure 6.10 KAM distribution for the three conditions under consideration: as-cast, heating to 420 °C in total constraint, and after 1800 s holding time at 420 °C.

6.4 Conclusions

Using a notch depth of 0.2 mm, the effect of prolonged holding times (HT) on TMF lifetime was studied and a clear effect was found, *cf.* a 60% reduction of lifetime when the holding time was increased from 30 s to 18000 s (5 h). Extended holding times were also found to be accompanied by a pronounced relaxation of compressive stresses, causing higher tensile stresses to develop in the subsequent low temperature stages of the TMF cycles.

Using short holding times of 30 s (at T = 420 °C) is useful to reduce TMF testing times, but was found to give somewhat optimistic estimates for TMF lifetimes, compared to using "in field" holding times.

The Paris fatigue crack growth model was used to calculate lifetimes, taking into account the different stress levels that developed at prolonged holding times. The calculations showed a 45% reduction in lifetime when increasing the holding time from 30 s to 18000 s (5 h), and ignoring the effects of increasing maximum tensile stress at low temperature. As in reality a 60% drop in lifetime was measured, this implies a combined effect of (tensile) stress and microstructural evolution during TMF.

It should be noted that the tests with extended holding times (18000 s or 5 h) only became feasible by the use of notched specimens (notch depth of 0.2 mm). Using notched specimens involved about 20 days per test, whereas using smooth specimens would have taken about 200 days per test and would also require more replicate tests because of the increased scatter in test results inherent to smooth specimens.

Microstructural changes were evaluated by analyzing quantitative data sets obtained by orientation contrast microscopy based on Electron Backscatter Diffraction (EBSD).

Quantitative data obtained from EBSD scans confirmed that after heating to 420 °C under total constraint, the induced strain gives rise to higher LAGB area fraction, while after 1800 s holding time, this fraction has regressed to the initial value. This may be indicative of the recovery process during holding. The recovered state is different from the initial state, though, as the high end tail of the KAM distribution function does not revert to the initial as-cast condition. Therefore, it can be concluded that recovery modifies the plastically strained condition, but does not bring it back to the undeformed state.

6.5 Reference

[1] Trampert S., Gocmez T., Pischinger S., J. Eng. Gas Turbines Power, 2008; 130: 012806-1 (10 pages).

[2] Löhe D., Beck T., Lang K., In: PD. Portella, H. Sehitoglu, K. Hatanaka (eds), Fifth International Conference on low cycle fatigue, LCF5. DVM, Berlin, pp. 161- 175, Berlin.

[3] Charkaluk E., Remy L., Fatigue of Materials and Structures, Application to Design and Damage, In C. Bathias, & A. Pineau (Eds.), Chapter 7: Thermal fatigue, pp. 271-338, John Wiley &

Sons Inc., USA, 2011.
[4] Gocmez T., Awarke A., Pischinger S., Int. J. Fatigue 2010; 32: 769-779.
[5] Seifert T., Riedel H.: Part I, Int. J. Fatigue 2010; 32: 1358-1267.
[6] Seifert T., Maier G., Uihlein A., Lang K., Riedel H., Part II, Int. J. Fatigue 2010; 32, 1368-1377.
[7] Ghodrat S., Riemslag A.C., Janssen M., Sietsma J., Kestens L.A.I., Measurement and Characterization of Thermo-Mechanical Fatigue in Compacted Graphite Iron, International Journal of Fatigue 2013; 48: 319–329.
[8] Gundlach R., AFS Trans. 1979; 61: 551-560.
[9] Zieher F., Langmayr F., Engine Simulation in View of Reduced Development Time. Technical, Paper Code: F02V081, AVL List GmbH, Austria, 2002.
[10] Zuidema J., Wijnmaalen L., van Eldijk C.: Fatigue '99, Pechino 1999,3, pp. 2071-2076.
[11] Hähner P., *et al.*, Int. J. Fatigue, 2008; 30: 372-381.
[12] Humphreys F.J., Hatherly M., Recrystallization and Related Annealing Phenomena, Chapter 6: Recovery after Deformation, pp. 169-213, Elsevier Ltd, (2nd edition), 2004.

7

Microstructural Characterization of Compacted Graphite Iron with Orientation Contrast Microscopy

"With EBSD we look straight at the planes and directions of the crystal lattice, as if they are pulled out of the crystal towards our macroscopic world."

Leo Kestens

The Last section of chapter 6 (section 6.3.3) presented microstructural changes during plastic deformation and stress relaxation, evaluated by analyzing quantitative data sets obtained by orientation contrast microscopy based on the Electron Backscatter Diffraction (EBSD) technique. In the present chapter, a detailed account is presented on 3D analysis of the crack path evolution induced in Compacted Graphite Iron (CGI) during Thermo-mechanical Fatigue conditions (TMF). Orientation contrast microscopy was employed to provide a deep insight in the complex TMF crack morphology of CGI. To meticulously characterize TMF crack paths, in relation to microstructural features, in more detail and to find out how and by which mechanisms the cracks develop, a 3D microscopy analysis was carried out[1].

7.1 Background: Orientation Contrast Microscopy

Under cyclic loading, crystal anisotropy of polycrystalline metals causes heterogeneities of stresses and strains, whereas crystal orientations change on the micro-scale. Investigations on steel have shown that cyclic behavior near the yield strength is closely related to microplastic strain in the grain boundary region [1]. To determine the strain localizations and grain fragmentation that are the potential regions of damage initiation, orientation contrast microscopy has been frequently employed on free sample surfaces or on internal surfaces of sectioned samples.

[1] H. Pirgazi, S. Ghodrat, L.A.I. Kestens, Three-Dimensional EBSD Characterization of Thermo-Mechanical Fatigue Crack Morphology in Compacted Graphite Iron, submitted to the Journal of Materials Characterization.

Only very few EBSD studies have been conducted so far on cast iron [1, 2], neither in an as-cast form nor after mechanical loading. One reason for this shortage of studies is that obtaining the orientation of graphite with EBSD is difficult, due both to the low atomic number of the carbon and also the softness of the graphite [1]. Since no pattern from graphite can be revealed, it is not clearly known whether the graphite is a single crystal or polycrystalline. However, determining the local orientation in the microstructure of ferrous alloys containing austenite, martensite, pearlite, ferrite and combinations of these, has been carried out successfully by EBSD in the last decade [1-6]. EBSD allows a clear identification of grains, grain boundaries and grain orientations and the relation of orientation between the matrix and inclusions.

Pearlite morphology and structure in steel and ferrous alloys has a significant influence on mechanical properties. The strength of pearlite depends on interlamellar spacing, pearlite colony size, prior austenite grain size, as well as other microstructural features, *e.g.* the concentration of elements in solid solution and the dislocation density in ferrite [4]. The lamellar structure in a pearlite colony contains various types of substructures. The influence of the substructures of the pearlite lamellae and the crystallographic orientation pattern in the pearlite colonies have been investigated with EBSD analysis by Takahashi et al. [4]. They addressed the issue of the distribution of Geometrically Necessary Dislocations (GNDs) involved in the formation of subgrains in each pearlite colony. Density can be quantified precisely by monitoring local orientation changes in the crystals [4]. It is known that the pearlite colony containing a large density of dislocations, cells, or subgrains may show higher strength than a colony with small defect density.

The Kernel average misorientation (KAM) map reveals short-range orientation gradients, *cf.* chapter 6, section 6.3.3. This allows one to relate localized orientation changes and certain spatial misorientation patterns to dislocation substructures such as cells or subboundaries. For instance, Takahashi et al. [4] observed that inside pearlite regions in a hypoeutectoid steel pronounced misorientation gradient exist, whereas almost no misorientation gradients can be found inside the ferrite grains surrounding the pearlite colony (*cf.* Figure 7.1). Figure 7.1b shows the inverse pole figure (IPF) map of the area shown in Figure 7.1a; it can be observed that the cementite layers are not distinguishable in the pearlite colonies.

This misorientation is the characteristic of the presence of some substructures, that accommodates gradual orientation change, such as provided by polarized dislocation arrangements also known as GNDs [4]. GNDs are formed due to deformation gradients induced by externally imposed constraints associated with plastic deformation or during phase transformation. Figure 7.1c exhibits the short-range orientation gradients between 0° and 4°. It can be observed that specific patterns of orientation change are visible as regions of more intense orientation gradients can be distinguished from almost homogenous orientation areas. At first sight there is no direct link between these patterns and the morphology of the pearlite colonies in terms of cementite direction or lamellar spacing. However, when long-range orientation gradients are considered

between 0° and 20°, *cf.* Figure 7.1e, it can be observed that the direction of orientation change is roughly parallel to the direction of the cementite lamella. Moreover, it appears that a sudden orientation gradient appears where there is a (slight) discontinuity or increased curvature of the pearlitic lamella.

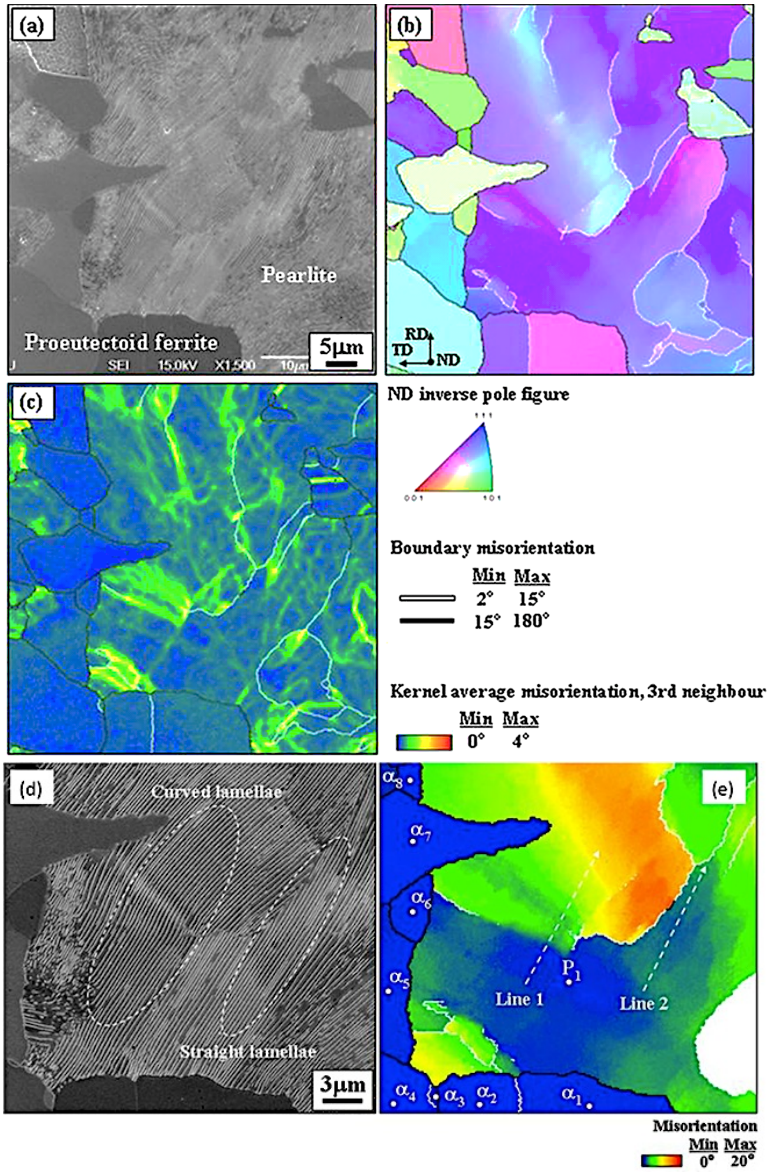

Figure 7.1 (a) A SEM micrograph of a typical ferrite and pearlite microstructure in a hypoeutectoid steel when subjected to slow cooling from the austenite state. (b) The inverse pole figure map obtained from the corresponding area of (a). (c) Kernel average misorientation map of the same area. (d) Magnified SEM image of the middle part of image (a). (e) Corresponding grain internal misorientation map. Line 1 is placed in the curved lamellae with a strong crystallographic curvature and line 2 in a region with a much weaker crystallographic curvature. The colors represent the misorientation measured from each reference point inside the colony [4].

The information of the above-mentioned study is valuable and useful since it provides quantitative, systematic and representative characterization of substructure in pearlite colonies of steel. Although this type of study [4] and other studies [1-3, 5, 6] have been carried out for as-cast, heat-treated, or statically loaded conditions, *i.e.* not dynamically loaded conditions.
To the present purpose of understanding the TMF mechanism, not only the microstructure aspect of the ligament is of interest, but also the precise characteristics of the crack features in relation to the local microstructure. Therefore, an extensive SEM and EBSD study was carried out on CGI loaded under TMF conditions. The results of this research are presented in the sections 7.2 and 7.3.

7.2 2D-Characterization

In-situ Tensile Test and Crack Path Observation with Scanning Electron Microscopy

One of the important aspects of the simulation model for CGI is that it should be able to predict what happens at the interface between the (pearlitic) matrix and the graphite when this interface is loaded mechanically and thermally.
To this aim, an in-situ experiment was designed and performed to observe interface processes during mechanical loading. Hence, an experiment was carried out on a small tensile device, *i.e.* Deben® micro-tensile machine, which was placed inside a scanning electron microscope.
In order to measure the strain while applying load, microhardness indentations were used as markers on the surface of the polished specimen (*cf.* Figure 7.2). By applying appropriate loads while observing the surface, phenomena like delamination and microcracking along the graphite-matrix interface and also cracking through the graphite layers can be made visible at the early stage of loading. By applying increasing loads particularly after yielding, above the stress and strain values of 340 MPa and 0.5% respectively, cracks propagate along the graphite/matrix interfaces as well as through layers of the graphite particles. At strains above 2.4 % and stresses exceeding 500 MPa, cracks successively grow through the matrix from one graphite particle to a neighboring one (*cf.* Figure 7.3).

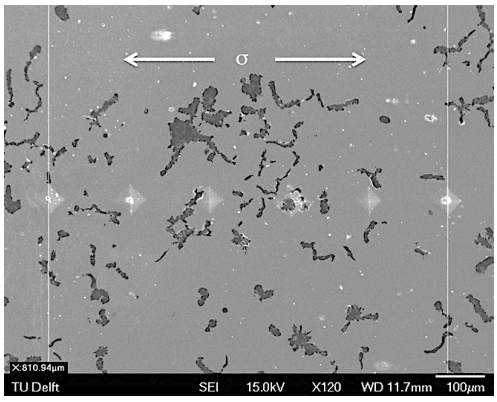

Figure 7.2: Microhardness indentations used as a markers on the polished surface of the tensile specimen before loading.

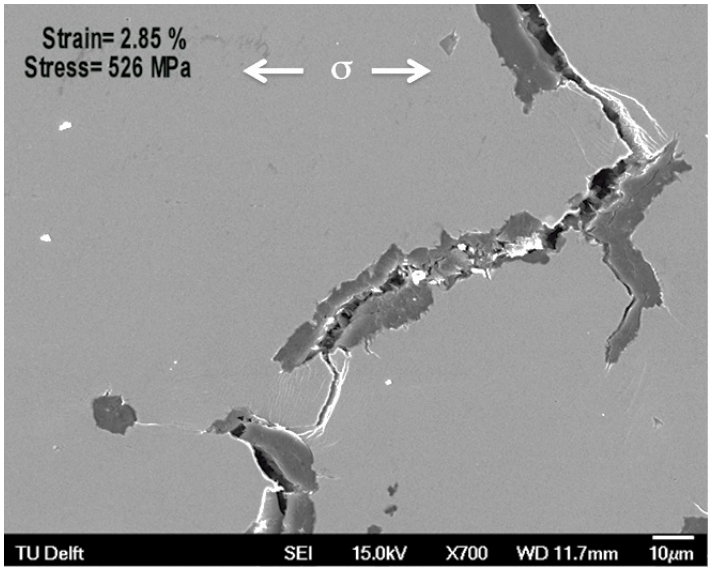

Figure 7.3: Microstructural observation during an in-situ tensile test at an overall strain of 2.85% and a corresponding stress of 526 MPa showing cracks developing at the graphite-matrix interface and also through the graphite layers and growing through the matrix from one graphite phase to another.

Characterizing the CGI Crack Path under TMF Loading by Orientation Contrast Microscopy

A TMF sample tested with the "standard" TMF test, chapter 3, section 3.2.2, with 30 s holding time and N_{10}= 254 cycles was studied here.
From single grain orientation contrast maps shown in Figure 7.4 (b), it appears that the crack propagates between pearlite grains (*i.e.* intergranular). However, at close inspection, we found that in reality crack propagation occurred transgranularly. The wrong impression given by the unique grain colored maps arises from the fact that the crack itself is considered as a grain by the data post-processing software. However, IPF maps in Figure 7.4 (d) which reflect the true crystal orientation, leave no doubt about the transgranular propagation. They show that the TMF cracks in CGI propagate transgranularly through the pearlitic colonies. This observation confirms the earlier literature [7] and corresponds to the conventional features of cleavage fracture.

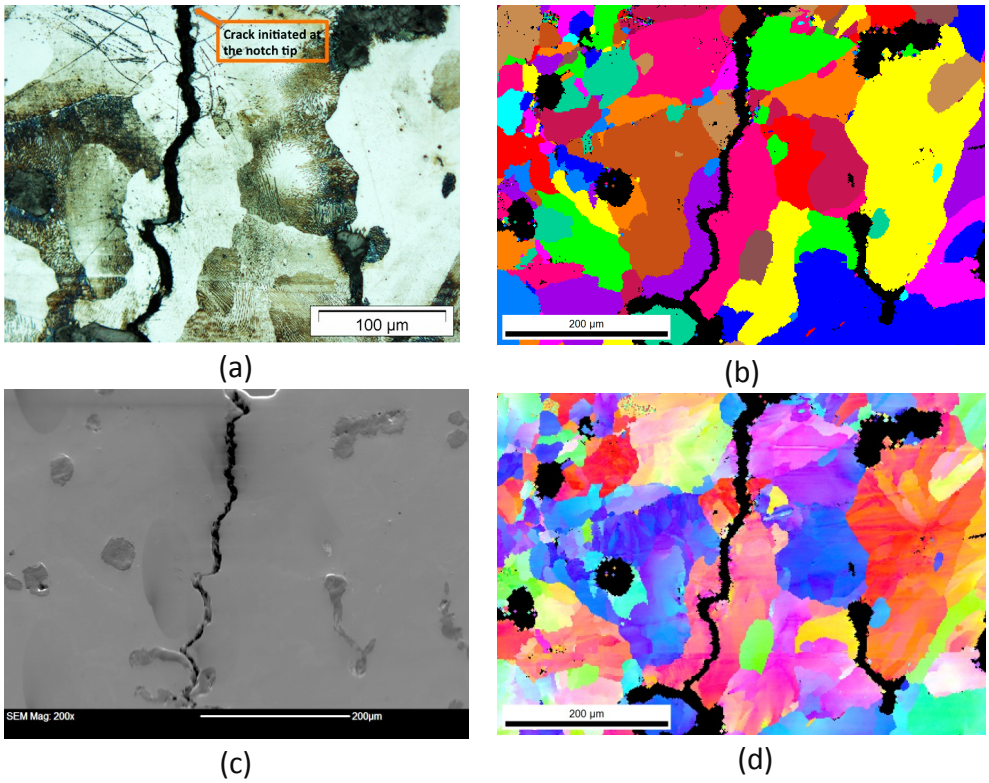

Figure 7.4 (a-d) Optical microscopy, unique grain colored map, SEM and IPF maps at the notch tip of a propagating crack. The crack is observed on a TMF sample tested with the "standard TMF test", chapter 3, section 3.2.2, with 30 s holding time, N_{10}= 254 cycles.

Figure 7.5 shows the fracture surface of a TMF loaded sample after approximately 1000 cycles, which obviously predominantly displays brittle features. It is known from the literature that brittle fracture in BCC metals, *e.g.* in steel, occurs on {001} cleavage planes [8]. These observations were generally limited to single phase ferrite steels [8]. It remains to be verified, however, whether or not this still applies to brittle fracture as observed in the fine pearlitic matrix of the current CGI material under investigation.

Therefore, in order to verify the crystallographic features of the brittle fracture, a further quantitative study of the crack path was carried out by means of EBSD. Figure 7.6 shows the IPF map of the material along the crack path making its way through the CGI microstructure. The 2D microscopically cross section does not allow us to directly observe the fracture plane. What is observed in the IPF map (Figure 7.6) is the cross section of the fracture plane with the plane of the observation. Nevertheless, if the fracture plane is a {001} plane, then all crystal traces <*uvw*> parallel to the crack path should be parallel to the {001} plane, *cf.* Figure 7.7. Mathematically this can be

expressed by the condition that the scalar product of the crystal vector <*uvw*> and the <001> vector, normal to the {001} planes, must be zero. The angular deviation θ between the <*uvw*> trace and the {001} plane is given by the following equation (7.1):

$$\theta = Min\ \{\text{asin}(u'), \text{asin}(v'), \text{asin}(w')\} \qquad (7.1)$$

where [u' v' w'] is the normalized equivalent of [u v w]. If the hypothesis of {001} cleavage planes were to be confirmed, then this angle should be close to zero. The schematic drawing of the crack plane and a {001} plane with θ and ω angles is shown in Figure 7.7. In this figure, ω is angle between the normal of crack plane and the {001} plane, which only can be observed in a 3D image (*cf.* infra). In our analysis, we calculated the deviation angle θ for nearly 600 traces of crack path segments, and it was found that the average value of θ is equal to 13.4˚ with a standard deviation of 8.5˚, which compares very well to the average value of 15.0˚ for a random distribution of traces.

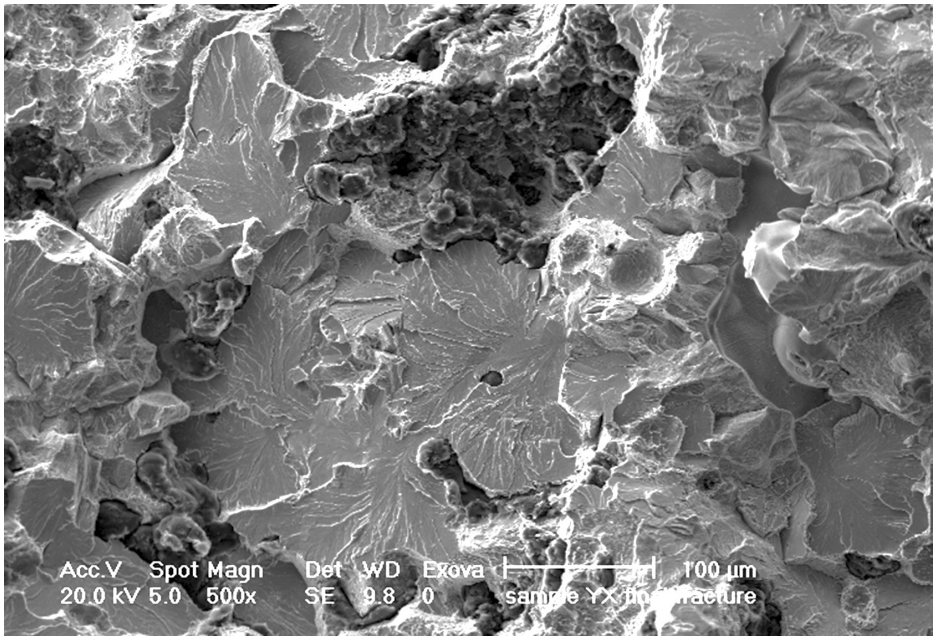

Figure 7.5 Brittle fracture features observed on the fracture plane after fatigue failure of a smooth TMF specimen tested 30 s HT, N_{10}=986.

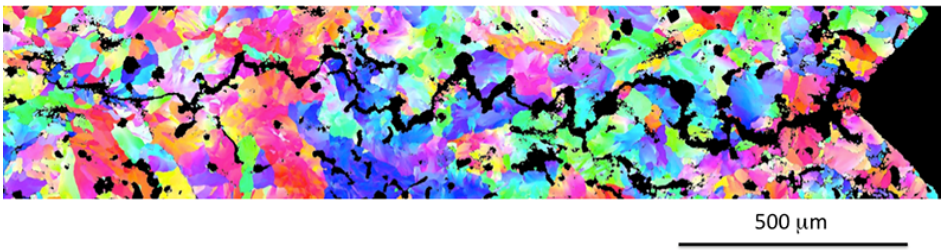

Figure 7.6 IPF map displaying the cross section of the fracture plane with the plane of observation. The crack propagated from the notch (right hand side of the map) through the CGI microstructure in a TMF standard tested sample N_{10}=195. Color coding is according to inverse pole figure legend 7.4.

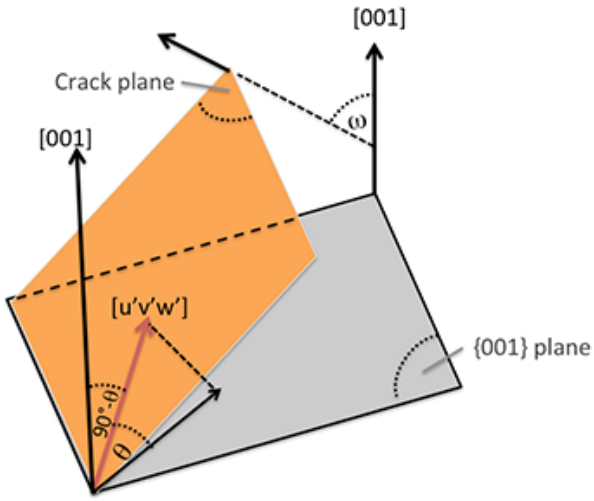

Figure 7.7 Schematic drawing of the crack plane and a {001} plane with θ and ω angles.

The measured distribution of θ is shown in Figure 7.8. This figure also exhibits the random distribution of θ, which has to be compared with the measured distribution. This random distribution was calculated by averaging the deviation angles between an arbitrary trace direction and the closest <100> direction. As it can be seen, the measured distribution of θ approximately resembles the random distribution of θ. Therefore, it cannot be concluded that there is a tendency that the crack path trace is included in the {001} plane. In order to obtain a more detailed view of the crack path, it requires a 3D observation. This is treated in the next section 7.3.

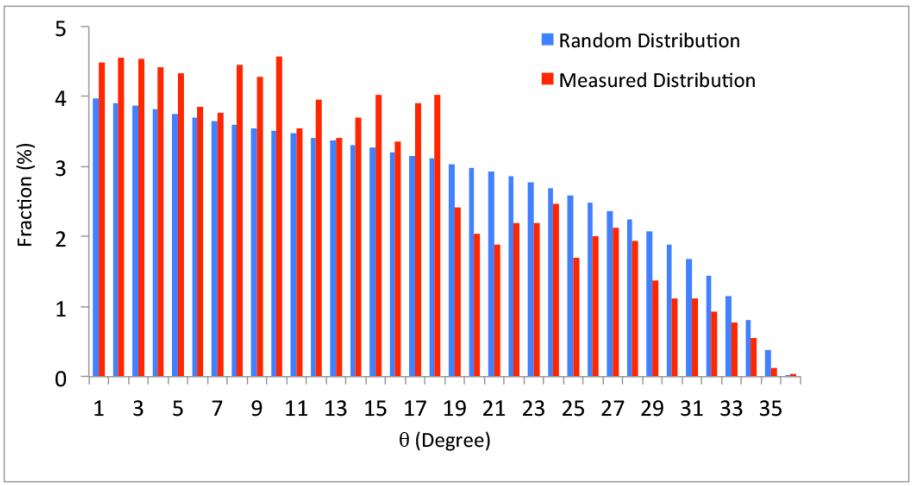

Figure 7.8 Measured deviation angle θ distribution for more than 600 traces of crack path segments (red distribution), and the random θ distribution (gray distribution).

7.3 3D-SEM-EBSD Imaging, Characterizing and Quantitative Analysis of the CGI Crack Path under TMF Loading[2]

Methodology

To have a better understanding of the effect of the crystallographic orientation on the TMF crack growth path, a TMF loaded sample (*cf.* table 7.1 for history of loading), was investigated by 3D-EBSD measurements using a manual serial sectioning technique.

Table 7.1 History of TMF tested specimen with the "standard TMF test" (*cf.* chapter 3, section 3.2.2, with 30 s holding time).

TMF specimen	N_{10}	σ_{max} *(MPa)*
Pre-cycled (400 cycles) then notched (0.2 mm)	195	332

This technique consists of the reconstruction of several consecutive 2D EBSD sections. Each EBSD measurement was carried out in the middle of the gauge length of the TMF loaded sample in an area of 6000 × 700 µm^2 (*cf.* Figure 7.9). For each section two adjacent EBSD scans with dimensions of 3000 × 700 µm^2 were merged. These

[2] H. Pirgazi, S. Ghodrat, L.A.I. Kestens, Three-Dimensional EBSD Characterization of Thermo-Mechanical Fatigue Crack Morphology in Compacted Graphite Iron, submitted to the Journal of Materials Characterization.

measurements were performed with an in-plane step size of 3 µm which was sufficient for the detection of the relevant microstructural details for this material.
After each scan, the sample was finely polished with oxide polishing suspension (OPS) solution with an automatic polishing machine (*cf.* chapter 3, section 3.3.2, EBSD: Sample Preparation). The removal rate of each layer was approximately 1 µm per minute. Several micro-Vickers indentations on the sample were used to control the plane-parallelism and the thickness of the removed layer. In total, 30 consecutive slices were measured with a *Z* distance of 8.0±0.5 µm from a 3D volume with the dimensions of 6000 × 700 × 240 μm^3.
The first step to reconstruct the 3D microstructure is the alignment of the sections. Different alignment algorithms have been proposed already and the most important ones are based on the maximization of mutual information of two adjacent sections. In this study an algorithm which is based on the minimization of the average misorientation between two adjacent sections was used. According to the method applied here, it was observed that for a particular alignment of two sections, always a well defined minimum exists and this minimum is taken into account as the correct alignment position [9].
After alignment, another graphical algorithm, called marching cubes, was used to reconstruct the 3D microstructure. Marching cubes is a method to obtain smooth reconstructed surfaces, which can be appropriatly used for viewing the 3D data [10]. This algorithm produces a continuous triangular mesh from a series of discrete points and produces an analytical surface representation. The inverse pole figure (IPF) map of the reconstucted volume after applying the above mentioned algorithm is presented in Figure 7.10.

Figure 7.9 Large scale EBSD measurement through the entire thickness, the size of this scan is 6000 × 700 μm^2. Color coding is according to inverse pole figure legend of Figure 7.4.

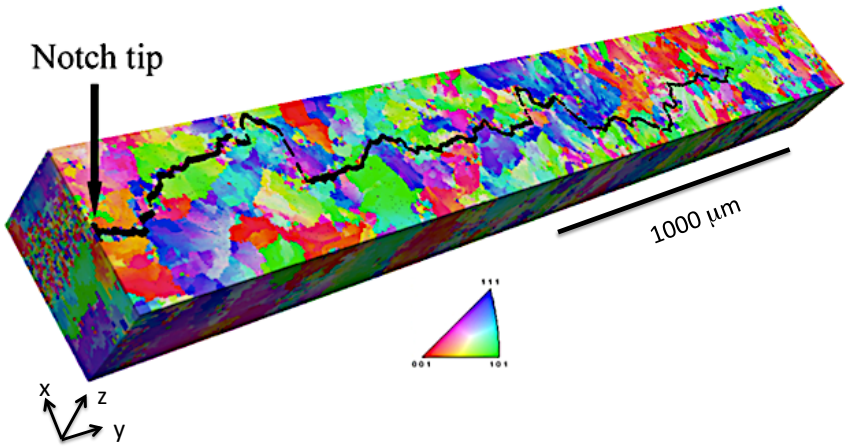

Figure 7.10 Reconstructed microstructure after applying alignment and marching cube algorithms.

3D-SEM View of the TMF Crack

The EBSD measurements provide extensive microstructural information, especially about the crystallographic orientation. However, because of the low indexation rate in the vicinity of the crack because of plastic deformation, it was not possible to precisely determine the morphology of the crack from the EBSD scans. For this reason, in addition to the EBSD scans, high resolution secondary electron SEM imaging was also performed on each section. For each section 15 secondary electron images with a magnification of 700 X were collected over the entire surface and were merged to show a high-resolution large-scale view of the surface (*cf.* Figure 7.11a). As it can be seen from Figure 7.11b, crack and graphites were separately highlighted with different colors using a MATLAB image processing toolbox and some manual corrections. This marking allows obtaining a sharp separation between metal matrix, graphite partlicles and the crack.

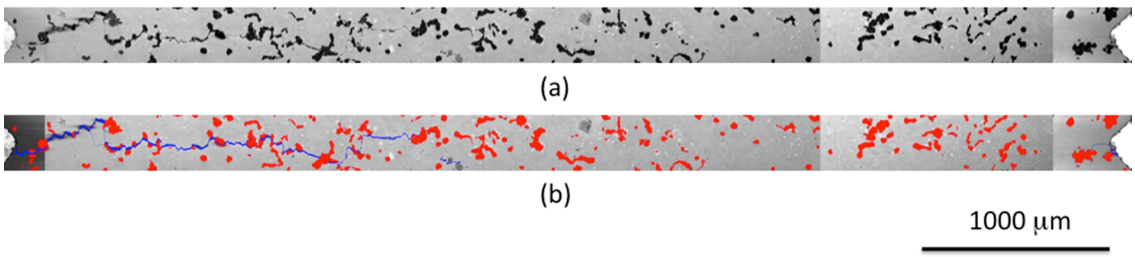

Figure 7.11 (a) Secondary electron SEM image through the entire thickness, this image consist of several individual images. The horizontal length of the image is 6 mm. (b) The same image with highlighted crack (blue) and graphite (red).

The SEM image of each section with highlighted crack and graphite was used to generate an artificial EBSD scan file. To this purpose, it was assumed that each pixel of the image represents one OIM data point. The X and Y coordinates in the scan file were derived directly from the X and Y coordinates of the pixels in the SE image and random values were assigned to Euler angles, confidence index and image quality (chapter 3, section 3.3.2) in order to obtain a complete record of an OIM data point. To distinguish between crack, graphite and metal matrix in the EBSD dataset, they were artificially considered as three different crystallographic phases. This helps us later to look at crack and graphite separately in the Paraview® software, which is used for 3D image reconstructon (*cf.* Figure 7.12).

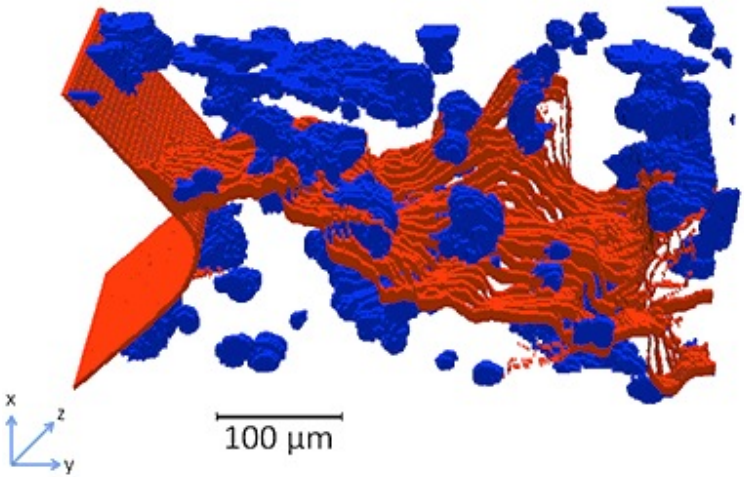

Figure 7.12 3D Reconstructed image of crack and graphite together with individual view of graphite particles (blue) and crack surface (red).

3D-EBSD View of the TMF Crack

Subsequently, the artificially generated files with graphite and crack as two phases were merged with real EBSD scans. In order to do this, the scan information of graphite and crack from the artificial file (derived from the SE image) was substituded in the real EBSD scan (*cf.* Figure 7.13a and b). This produces a new file with 3 phases (iron, crack and graphite) and the crystallographic orientations of the iron phase. The 3D reconstructed volume of these files can be extensively used for further evaluation of the relative effects of texture and graphite morphology on the TMF crack growth path, of which one side is shown in Figure 7.13c. It can be observed that the IPF map of figure 7.13a, which represents the combined SE and EBSD image, exhibits a much sharper crack profile compared to the pure EBSD image of Figure 7.9.

(a)

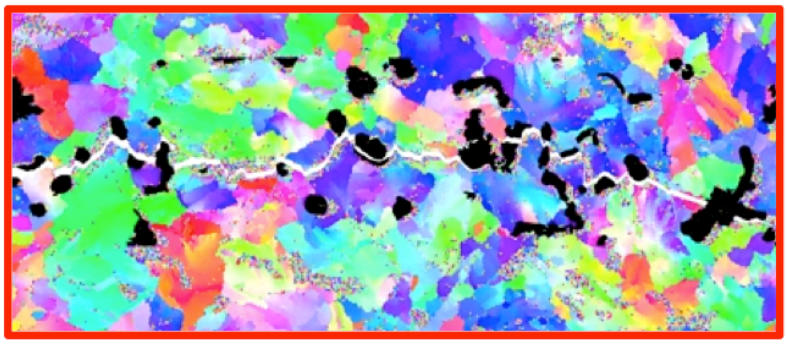

(b)

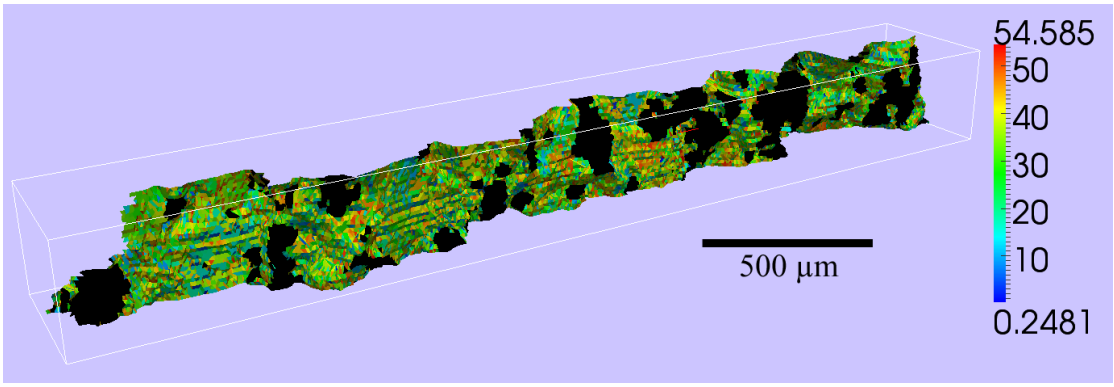

(c)

Figure 7.13 (a) The IPF map after merging the artificial scan file (with crack as white and graphite as black) with the EBSD scan. (b) close-up of the part of the crack shown in the red box (a). (c) Lateral view of the crack path exhibiting ω angles according to the color code of the legend, together with the black graphite particles. Color coding for (a) and (b) is according to inverse pole figure legend of Figure 7.4.

7.4 Results and Discussion

The measured distribution of the angle ω (*cf.* Figure 7.7) between the normal on the crack plane and the normal on the closest {001} plane is shown in Figure 7.14 together with the random distribution of ω.
Similar as for the θ distribution, this random distribution was calculated by considering the deviation angles between an arbitrary sample direction and the closest {001} plane. Also in this case it can be observed that the measured distribution of ω closely resembles the random distribution of ω. We calculated the average ω angle and it was found to be equal to 32.5˚ with the standard deviation of 11.7˚, which is near to the average of the random distribution being 36.5˚.
This shows that there is no preferred crystal plane that is parallel to the crack plane. This 3D data analysis confirms the 2D trace analysis (*cf.* Figure 7.8). The present analysis strongly suggests that the brittle fracture in CGI does not occur on the traditional {001} cleavage planes [8], even though the crack grows transgranularly (*cf.* Figure 7.4). This may be related with the fact that the pearlite metal matrix does not represent a continuous volume of BCC crystal, but a fine mixture of BCC ferrite and orthorhombic cementite (Fe_3C).

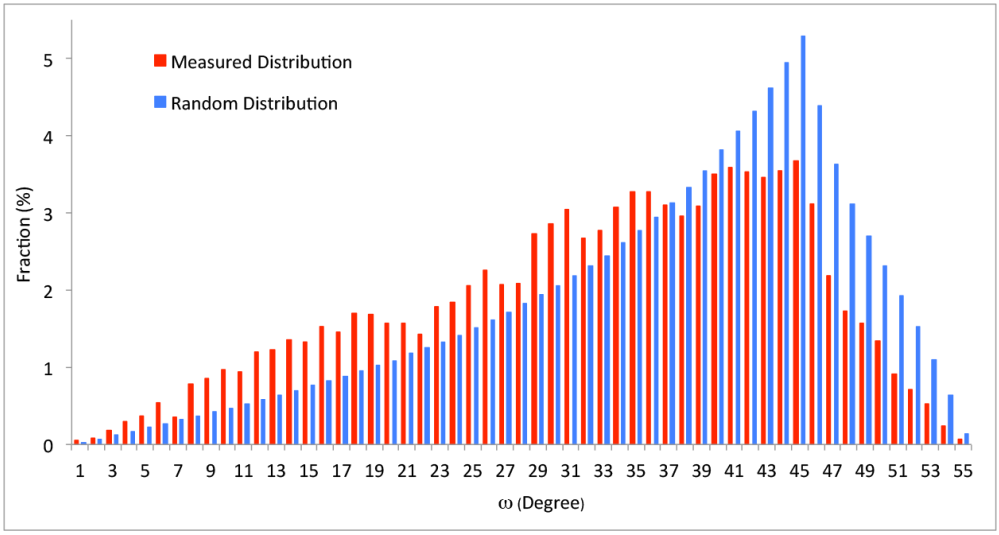

Figure 7.14 Measured and random distribution of ω angle as derived from 3D-EBSD data.

We would like to emphasize that the crack plane normal directions were directly determined on the triangulated surface, without employing the marching cube algorithm, which was only used to the purpose of 3D image reconstruction. Figure 7.15 shows part of the triangulated crack surface in which the color of the triangles scales with the ω angle. If the crack path is parallel to the {001} plane, then most of the triangles would appear in blue. It obviously can be seen in Figure 7.15 that this is not the case, *i.e.* the data shows that there is no preferential alignment of the crack plan with {001} plan.

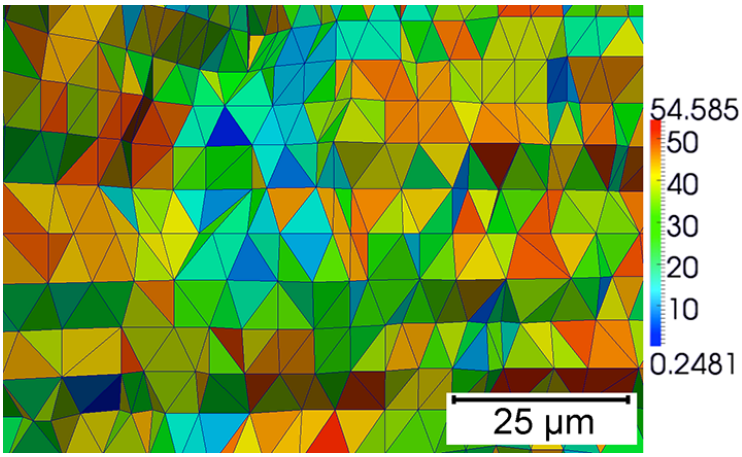

Figure 7.15 Part of the triangulated crack surface as measured by 3D EBSD revealing the distribution of ω angles on the crack surface.

In order to check the hypothesis of crystal orientation effect on the crack path, a further analysis was carried out. In the previous evaluation it was found that there was no overal influence of crystal orientation on the crack propagation. It still remains to be verified, though, if the crystal orientation might have a *local* effect far away from the graphite particles, where there is no influence of the graphite morphology. To this purpose, the value of ω was evaluated as a function of distance to the nearest graphite particle (*cf.* Figure 7.16). If the crystal orientation effect were to play a role far away from the graphite particles, one would expect a negative slope of the curve that represents the ω value vs. the distance to the nearest graphite particle. The measured data, however, derived from the 3D data set do not show such a decending slope, but nearly a constant ω value (~32˚) that very well approximates the avarge of the random distribution (~36˚).

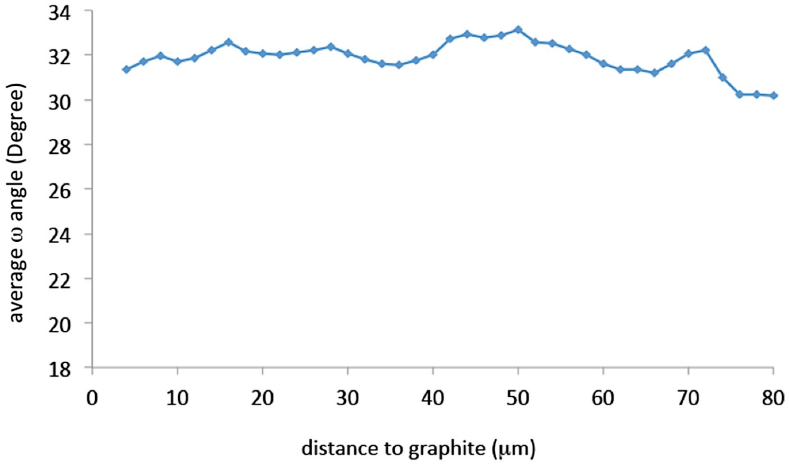

Figure 7.16 Measured deviation angle ω as a function of the distance from graphite particles. Each data point in this graph represents the average of dozens observations.

The data analysis, so far, suggests that the local crystallography does not play a role in the crack path propagation. Hence, one may wonder what is the role of graphite particles, as it appears that the crack path jumps from one graphite particle to the neighbering one and crystal orientation is not of importance.
It was established that the total area fraction of crack plane covered by graphite partcles is equal to 23.9%. However, this number has to be compared with the average fraction of graphite particles covered in arbitrary planes. From our 3D analysis, we found that the area fraction of graphite particles is equal to 9.4% (3.9% stdev) for a number of more than 1000 arbitrary sections. Furthermore, we compared the measured area fraction of graphite of 23.9% in the crack path with the average area fraction of graphite in the planes parallel to the crack path (excluding the crack path itself). The latter value was found to be equal to 9.6%, which implies that the graphite morphology is nearly isotropic.
From the present study, based on the precise quantitative microstructural analysis we can derive the conclusion that graphite particles do not only play a crucial role in the crack *initiation* (see chapter 5), but also are of primary significance for crack *propagation*. However, it remains to be determined by which interaction mechanism the crack is guided through the metal matrix aiming for the maximum area fraction of graphite particles.
In this respect, two main mechanisms might play a role: either the stress concentration field around a graphite particle interacts with the stress frield at the crack tip, or a delaminated zone at the graphite metal interface represents a small microcrack in the bulk of the metal matrix equally exhibiting a local stress distribution that will interact with the main crack on the local microstructural scale. Given the observation of graphite delamination (*cf.* section 7.2), the second hypothesis appears to be more probabale.
This finding may have important technological consequences. In CGI, the graphite particles are of a vermicular morphology randomly distributed in space. The present study tells that graphite particles enhance crack growth. Thus, if it would be possible to design a cast iron with anisotropic distribution of graphite particles in such a way that there are less particles in the direction of crack propagation, perpendicular to the direction of maximum stress then better crack resistance might be obtained. Such an approach only makes sence if the direction of maximum load coincides with the direction of heat transfere.

7.5 Conclusions

Orientation contrast microscopy was employed to provide a deeper insight in the complex TMF crack path morphology in CGI during TMF conditions. To meticulously characterize TMF crack paths, in relation to microstructural features and to find out how and by which mechanisms the cracks predominantly develop, 2D and 3D microscopy observations were employed. It was found that TMF crack propagation occurred

transgranularly. In order to verify the crystallographic features of brittle fracture, a further quantitative study of the crack path in 2D and 3D was carried out with the help of EBSD.

The obtained results did not indicate a particular crystallographic preference of fracture plane, *i.e.* the crystal plane parallel to the fracture plane was nearly of random orientation. We came to this conclusion on the basis of extensive 3D microstructural characterization, in which the entire material volume in the vicinity of the crack was mapped by orientation contrast microscopy. Whether or not the fracture plane was considered in the vicinity of a graphite particle did not have any effect on this conclusion.

Based on the precise quantitative microstructural analysis we could derive the conclusion that graphite particles do not only play a crucial role in the crack *initiation*, but also are of primary significance for crack *propagation*. Quantitative analysis with EBSD in 2D and 3D showed that the density of graphite particles on the fracture plane is more than double as high as in any other arbitrary plane of the structure. Hence it obviously revealed that crack growth is enhanced by the presence of graphite particles.

7.6 References

[1] Campos M.F. et al. Texture and microtexture studies in different types of cast irons, Materials Science and Engineering 2005; A 398: 164-170.

[2] Rivera G., Calvillo P.R., Boeri R., Houbaert Y., Sikora J., Examination of the solidification macrostructure of spheroidal and flake graphite cast irons using DAAS and EBSD, Materials Characterization 2008; 59: 1342–1348.

[3] Rehrla C., Kleber S., Antretter T., Pippan R., A methodology to study crystal plasticity inside a compression test sample based on image correlation and EBSD, Materials Characterization 2011; 62: 793–800.

[4] Takahashi T., Ponge D., Raabe D., Investigation of Orientation Gradients in Pearlite Hypoeutectic Steel by Use of Orientation Imaging Microscopy, Max-Planck-Institut für Eisenforschung GmbH, 2008.

[5] Calcagnotto M., Ponge D., Demir E., Raabe D., Orientation gradients and geometrically necessary dislocations in ultrafine grained dual-phase steels studied by 2D and 3D EBSD, Materials Science and Engineering A 2010; 527: 2738–2746.

[6] Peranio N., Roters F., Raabe D., Microstructure evolution during recrystallization in dual-phase steels, Materials Science Forum 2012; 715-716: 13-22.

[7] Rémy L. Fatigue and thermomechanical fatigue at high temperature, Encyclopedia of Materials: Science and Technology 2001; 2866-2877.

[8] Randle V., Davies P., Crystallography of Brittle Fracture and Deformation Twinning in Ferritic Steels, Materials Science and Technology 2005; vol. 21 No 11: 1275-1281.

[9] Lee S.B., Rolleh A.D., Three dimensional microstructure reconstruction using FIB-OIM, materials Science Forum 2007; 558-559: 915-920.

[10] William E. Lorensen, Harvey E. Cline, Marching Cubes: A High Resolution, 3D Surface Construction Algorithm, Computer Graphics, vol. 21, No 4, July 1987.

8

Conclusions and Recommendations

I think and think for months and years. Ninety-nine times the conclusion is false. The hundredth time I am right.

Albert Einstein

In cylinder heads made of Compacted Graphite Iron (CGI), heating and cooling cycles can lead to localized cracking due to Thermo-Mechanical Fatigue (TMF). In order to prevent cracking, it is important to characterize the microstructural evolution and TMF behavior under realistic thermal and mechanical loads. The fundamental aim of this research was to find the damage micro-mechanisms of TMF in CGI, to predict the TMF lifetime and increase the reliability of diesel truck cylinder heads.

In this Ph.D. research, a mechanical test setup was designed to monitor TMF behavior of CGI under well-controlled laboratory conditions. Various series of such TMF tests were performed between 50 °C and 420 °C under total constraint (leading to out-of-phase loading) with different holding times. This TMF test procedure is intended to replicate the thermal and mechanical conditions observed in cylinder heads. The cycling temperature mimics the situation during the start-stop cycles during the operational life of the engine. In this way, the TMF test results are likely to represent potential TMF processes in real engines.

With regard to microstructural characterization, and more specifically with the purpose of revealing fatigue micromechanisms and subtle microstructural changes in the material under investigation, several techniques were employed. These techniques include X-ray 3D-computed tomography, scanning electron microscopy combined with energy and wave-length dispersive X-ray analysis and the powerful technique of orientation contrast microscopy, *i.e.* Electron Back Scattering Diffraction (EBSD).

8.1 Conclusions

Growth Phenomena in Compacted Graphite Iron at Elevated Temperature Annealing

In the first series of experiments, time and temperature induced microstructural changes in CGI were characterized, in view of their possible role in the TMF behavior of CGI.

During open air annealing of CGI at 420 °C microstructural changes take place in the material, which gave rise to volume expansion (labeled "*growth*") and weight increase. It was observed that after 4557 h (189.8 days) of cyclic exposure, the length increase is +0.11 % and the mass increase due to oxide scaling is +0.012 kg/m^2. However, after this exposure time, only a minor fraction (less than 16 %) of pearlite has decomposed into ferrite and graphite, *i.e.* a complete decomposition of pearlite needs longer exposure times than the presently applied 4557 h at 420 ˚C. It was also found that internal oxidation largely inhibited the progress of pearlite decomposition and therefore much smaller growth rates were obtained as compared to the ones observed under vacuum conditions. After 16 h of annealing at 700 ˚C, comparable in terms of carbon diffusion to 1754 h at 420 ˚C, a vacuum condition exhibited 10 times faster growth kinetics. The observed oxide layers at the internal metal/vapour interface of cavities (left behind by denuded graphite) cause the obstruction of carbon diffusion and thus hindering of the pearlite decomposition process.

In addition, the distance from the surface where cavities are formed was measured to be approximately 115 µm after 120 h. The oxide penetration depth saturates at the value of approximately 240 µm after 570 h of exposure time.

By X-ray computed tomography, it was assessed that the eutectic cell size (*i.e.* the volume in which graphite particles are interconnected) of CGI was of the order of 160 µm, which is close to the observed penetration depth at saturation. This suggests that the interconnectivity of the graphite has a dominant influence on the kinetics of the oxidation process.

Microstructural Dependence of Tensile and Fatigue Properties of Compacted Graphite Iron at Room Temperature

An extended annealing treatment of 720 h at 420 °C was carried out to generate different initial conditions of the CGI microstructure. It can be concluded that this extended annealing treatment causes an increase in yield strength, and at the same time an increase in ductility during static tensile loading at room temperature. During stress-controlled cyclic loading at room temperature an increase of lifetime was observed. These variations of mechanical properties were measured both after annealing under atmospheric and vacuum conditions, but were far more pronounced after vacuum

annealing. In the fatigue tests a decrease in cyclic plastic strain was associated with the increase in yield strength obtained by the extended annealing, which in turn has produced an increase of lifetime, with the strongest increase observed for the specimens annealed in vacuum. Specimens annealed in vacuum show the least plastic strain after the first cycle compared to specimens in the as-cast condition and annealed in open air. In the vacuum-annealed material this behavior can be explained by the decomposition of the pearlite during annealing and the formation of new ferrite at the graphite/metal interface. It is assumed that the ferrite/graphite interface exhibits a stronger bond than the pearlite/graphite interface. As this stronger bond will be better resistant to delamination it will strengthen the material both in static and dynamic loading. That such effects were far less pronounced in the open-air annealed material could be associated with the fact that it was shown that internal oxidation strongly reduced the kinetics of decomposition.

Measurement and Characterization of Thermo-Mechanical Fatigue in Compacted Graphite Iron

For smooth and notched specimens, the lifetime of pearlitic CGI was measured in TMF tests under total-constraint conditions, with temperatures cycling between 50 °C and 420 °C.

By considering the notch depth as an initial crack length, TMF lifetimes were reproduced numerically using the Paris equation for fatigue crack growth ($da/dN = C\,(\Delta K)^m$). For a single set of the Paris parameters C and m, the calculated lifetimes were found to be in good agreement with all experimental results, covering a wide range of TMF lifetimes from 30 to 1400 cycles. Also for smooth specimens the Paris model worked well by taking the typical graphite particle size as notch depth.

It is one of the main conclusions of this work that graphite particles act as internal notches from which a TMF crack almost immediately starts to grow during the first TMF cycles. Hence, it was established that TMF lifetime in CGI is governed by crack growth and not by crack initiation.

The relevance of the Paris growth law was further confirmed by meticulously measuring the actual crack growth rates for three typical ΔK values. The resulting average crack growth rates proved to be in reasonable agreement with the predicted values according to the Paris model.

It was further shown that the cyclic plasticity of the bulk material, accumulated during TMF cycles, does not have a noticeable effect on TMF lifetime (*i.e.* crack growth rates are not affected).

Effects of High Temperature Holding Time on Thermo-Mechanical Fatigue Properties of Compacted Graphite Iron through Tests with Notched Specimens

Using short holding times of 30 s (at T = 420 °C) is useful to reduce TMF testing times, but was found to give somewhat optimistic estimates for the TMF lifetime, compared to using *in field* holding times.

It should be noted that the tests with extended holding times (5 h or 18000 s) only became feasible by the use of notched specimens. Using notched specimens involved about 20 days per test, whereas using smooth specimens would have taken about 200 days per test and would also require more replicate tests because of the increased scatter in test results inherent to smooth specimens.

With a notch depth of 0.2 mm, the effect of prolonged holding times on TMF lifetime was studied and a clear effect was found. Extended holding times were also found to be accompanied by an increased relaxation of compressive stresses, causing higher tensile stresses to develop in the subsequent low temperature stages of the TMF cycles.

The Paris fatigue crack-growth model was used to calculate lifetimes, taking into account the different stress levels that developed as a result of prolonged holding times. The calculations showed a 45% reduction in lifetime when increasing the holding time from 30 s to 18000 s (5 h), and ignoring the effects of increasing maximum tensile stress at low temperature. As in reality a 60% decrease in lifetime was measured, this implies a combined effect of (tensile) stress and microstructural damage evolution during TMF.

Microstructural evolutions were evaluated by analyzing quantitative data sets obtained by orientation contrast microscopy based on Electron Back Scattering Diffraction (EBSD). It was observed that already in the initial material, before loading, a distinct substructure was present in the form of a network of low-angle grain boundaries. The area fraction of low-angle grain boundaries significantly increased after heating to 420 °C under full constraint conditions due to thermally induced plastic deformation, after holding for 30 min this area fraction was reduced to the initial value as a result of recovery processes. Other substructural parameters, though, related to the mechanisms of microplasticity at elevated temperature did not revert to the initial value, which is reminiscent of the fact that recovery does not fully restore the material to its initial state.

Microstructural Characterization with Orientation Contrast Microscopy

Orientation contrast microscopy was employed to provide a deeper insight in the complex TMF crack-path morphology in CGI during TMF conditions. To meticulously characterize TMF crack paths in relation to microstructural features and to find out how and by which mechanisms the cracks predominantly develop, 2D and 3D microscopy observations were employed. It was found that TMF crack propagation occurred transgranularly. In order to verify the crystallographic features of brittle fracture, a

further quantitative study of the crack path in 2D and 3D was carried out with the help of EBSD.
The obtained results did not indicate a particular crystallographic preference of the fracture plane, *i.e.* the crystal plane parallel to the fracture plane was nearly of random orientation. We came to this conclusion on the basis of extensive 3D microstructural characterization, in which the entire material volume in the vicinity of the crack was mapped by orientation contrast microscopy. Whether or not the fracture plane was considered in the vicinity of a graphite particle did not have any effect on this conclusion.
Based on the precise quantitative microstructural analysis we could derive the conclusion that graphite particles do not only play a crucial role in the crack *initiation*, but also are of primary significance for crack *propagation*. Quantitative analysis with EBSD in 2D and 3D showed that the density of graphite particles on the fracture plane is more than twice as high as in any other arbitrary plane of the structure. Hence it revealed that crack growth is enhanced by the presence of graphite particles.

8.2 Recommendations for Future Research

The current project mainly focused on fundamental aspects of failure micro-mechanisms of thermo-mechanical fatigue in compacted graphite iron. Implementing the material knowledge and TMF test results into a microstructural-based model is one of the main goals of future research in this area. In order to realize this objective, it is recommended to invest efforts on the following topics:

- Characterization of thermo-mechanical fatigue crack morphology in compacted graphite iron by 3D orientation contrast microscopy

With the help of 3D orientation microscopy, it is possible to evaluate the crack path in relation to the microstructural features (*e.g.* graphite shape, size, morphology, matrix characteristics, and so on). Such numerical data are required to develop a microstructural-based TMF model.

- Evaluating the environmental effects

In order to evaluate the effect of environment on TMF lifetime of CGI, it is recommended to carry out TMF tests under controlled environmental conditions. This may include a neutral atmosphere such as vacuum or protective gas or otherwise a corrosive environment, *e.g.* exhaust gases to simulate the real condition of a diesel engine in operation. In this context also the effect of protective coatings on the cylinder heads can be examined.

- More precise characterization of the CGI dominant constituent phases: graphite and pearlite

By measuring TMF lifetimes through TMF testing and also by numerically calculating crack growth rate using the Paris model for a purely pearlitic steel, it is possible to obtain a better profile of the metal matrix TMF properties (*e.g.* crack growth rate) and hence also to better assess the role of the graphite particles in the CGI composite.
With regard to the graphite particles the crystallographic nature of the graphite particle structure (*e.g.* single vs. polycrystalline) is as yet poorly understood. A better structural knowledge of the graphite particles is required to obtain a more physically based description of their mechanical role during loading.

- In-situ tensile testing at elevated temperatures in order to study the mechanical response controlled by the evolving microstructure

One of the important aspects of a microstructural-based model for CGI is that it should be able to predict what happens at the interface between the (pearlitic) matrix and the graphite particles if this interface is loaded mechanically and thermally. To this aim, an in-situ tensile device can be placed inside a scanning electron microscope. By applying appropriate loads while observing the surface, phenomena like delamination, microcracking and crack propagation can be evaluated. For instance, it is of relevance to know whether the crack propagates through the graphite particles or along the metal/particle interface.

- Evaluating the effect of the size of compacted graphite particles on TMF lifetime

It was found in the present work that graphite particles in CGI are of key importance, both for crack initiation and for crack growth. For instance, using the Paris model, it can be predicted that when the average graphite size decreases from 45 µm to 10 µm, the lifetime may increase from 1000 to 20 000 cycles in the reference TMF test developed in this work. This fact could lead to a new design strategy in search for TMF-resistant materials. Hence, testing CGI with smaller average size of graphite particles is recommended.

Appendices

Appendix A

The Relevance of Notch Size Accuracy

In chapter 5, the Paris crack growth equation is used to discuss the relation between notch depth and TMF lifetimes (see chapter 5, section 5.3.2, scatter in TMF lifetimes as a function of notch depth). Especially for small notches (*i.e*. 0.1 and 0.2 mm) TMF lifetimes are shown to be sensitive to variations in notch size. For example, a 10% increase in notch depth from 0.10 to 0.11 mm is found to result in an equal reduction (calculated) in TMF lifetime of 10%, indicating the relevance of an accurately machined notch. It should be mentioned that all TMF specimens were machined in one batch per cylinder head, while later on some of those specimens were provided with an additional notch, using another lathe machine. Having two separate turning operations can introduce an asymmetry in notch depth[1], since alignments of the lathe machines used are likely to have a small mismatch. Therefore, before notching the radial eccentricity of the specimen was checked to be within a tolerance[2] of 0.01 mm, which theoretically corresponds to a maximum variation in notch depth of 0.005 mm.

[1] The most accurate notch depth would be obtained when the notch is machined in one run with the actual fabrication of the specimen, without being re-gripping in between. However, this was not feasible in the current research program.

[2] Adjusting the radial alignment was performed by providing the turning machine with a chuck having four radial jaws that could be adjusted independently. This procedure involved the measurement of radial positions of the specimen using a micrometre probe, while manually rotating the specimen one revolution and adjusting the four jaws for an optimal alignment.

Appendix B

Stopping the TMF Test in a Controlled Manner

Ultimate TMF failures occur when the crack has reached a critical length, resulting in a sudden failure of the CGI specimen. The failure is a rather brutal process, possibly damaging the extensometer and also sometimes causing a shutdown of the system. It was preferred to end the test in a more controlled way[3] by using the fact that the formation of a macroscopic crack is accompanied by a drop in the maximum load level (developed during the cooling parts of the OP TMF cycles). For instance, tests with smooth specimens typically developed a maximum load level of about 10 kN and tests were automatically stopped when the maximum load level dropped to a value of about 6 kN. The choice of 6 kN as "test stop" criterion is not critical since its only purpose is to end the test before failure occurs[4]. For each TMF cycle the maximum and minimum loads are always (and automatically) detected in the background of the test program. Using the so called "peak-valley change detector" of the MPT™ software, it is possible to define two bandwidths for peak values, in compression and tension respectively. For instance, bandwidths of [-12 kN to -5 kN] and [6 kN to 13 kN] were typically used in most TMF tests performed. Detected peak values outside this range generate a trigger signal used to interrupt the looped TMF "group procedure". Subsequently, the MPT™ procedure includes actions to automatically abort the constant-strain condition and switch to a load-control mode. Finally, the load is ramped to a zero level (and maintained there) and the temperature set-point is ramped to 20 °C [5].

[3] Also, microscopic study of crack paths is facilitated by keeping the specimen (containing a crack) in one piece.

[4] The "test stop" criterion does not represent the TMF lifetime, for which a 10% load drop criterion is used (*cf.* appendix C). The "test stop" and lifetime criteria are only related in the sense that the test should not be stopped before the lifetime can be determined from recorded test data.

[5] The automatic stopping of the TMF test could also happen during the absence of the operator.

Appendix C

The Relation Between Extensometer Position and Load Drop Behavior

In chapter 6, section 6.3.1, it is discussed that the load drop related to the development of a macroscopic crack is not always consistent. Sometimes, a considerable degree of load drop occurred before final fracture, while in some other cases sudden fracture took place without any load drop. It should be mentioned that the (final) main crack is typically asymmetrical (*cf.* Figure C-1) and is initiated at a random position with respect to the position of the extensometer. Therefore, the extensometer could be positioned at the crack mouth location or opposite to it. To analyze this matter, we marked the extensometer position on the tested specimens. From this, we observed a relation between the aforementioned load drop behavior and the position where the main fatigue crack developed relative to the extensometer. Typically, when the crack mouth of the final crack was on the same side as the extensometer, a substantial load drop occurred before failure, and the final crack lengths were relatively large.

The effect of the extensometer position can be related to the asymmetry of the dominant fatigue crack, which introduces a bending component in the specimen. If the crack develops at the extensometer position, the displacement experienced by the extensometer during tensile loading is relatively large, due to opening of the crack. In this case, the control system applies only a relatively low tensile load on the specimen to maintain the total-constraint condition at low temperature. Since the crack is now loaded to a lesser extent, it can grow to a larger size before it becomes critical and leads to failure. More cycles are needed for failure to occur, during which the maximum tensile load will drop substantially as a result of the decreasing specimen stiffness. Conversely, when the dominant crack develops diametrically opposed to the extensometer the opposite observation can be made. The extensometer now experiences relatively low displacements and correspondingly high applied tensile loads are required to maintain the total-constraint condition. Failure will occur at a shorter length of the dominant crack, involving only a small load drop.

In order to reduce the influence of the extensometer position on TMF lifetime, the failure criterion for TMF lifetime is defined as the number of cycles at a 10% load drop. At such a small load drop, the crack is still relatively short and the bending effect will be less pronounced and consequently the effect of the extensometer position will be effectively reduced.

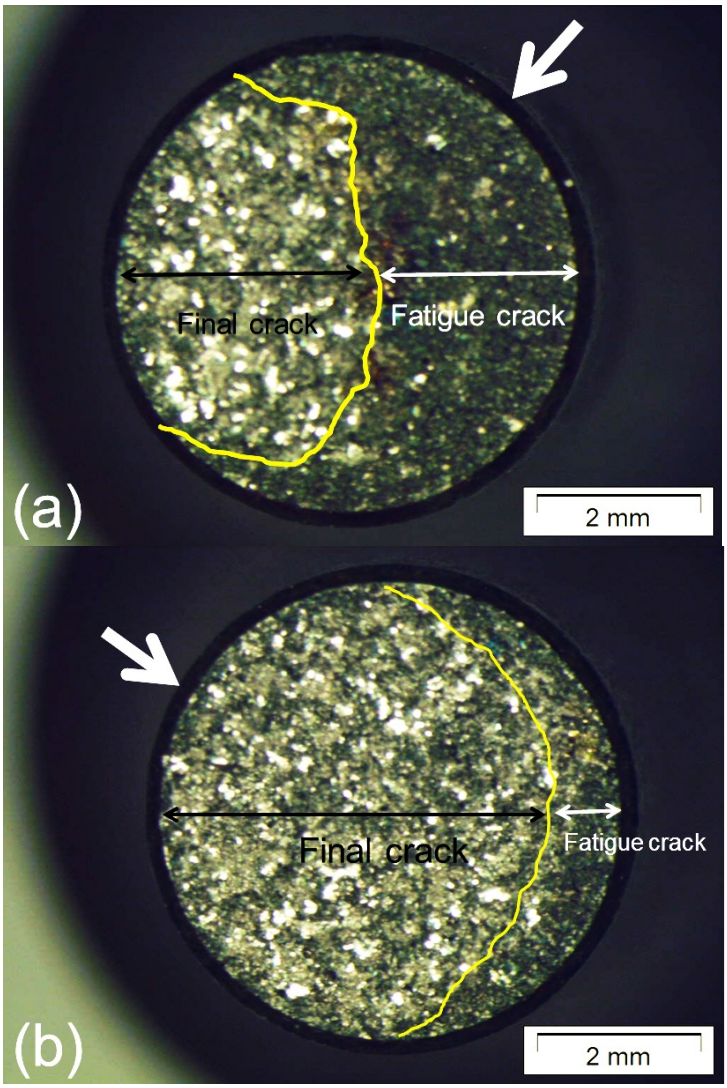

Figure C-1 TMF-tested specimens with 1800 s holding time: (a) N_{10} = 96, with the extensometer at the crack mouth and (b) N_{10}= 85, the extensometer is at the opposite side of the crack.

Appendix D

Equations Used to Calculate Radial Crack Extension Values with Symbols Shown in Figure 5.1 of Chapter 5.

D =Outer diameter (or 2R = 6mm)

Δa' = Crack extension measured from the grinded and polished surface by optical microscopy, at magnifications up to 500x.

h = Distance from surface to center of specimen.
(known from the removed polymer sample height)

$\mathbf{a_o}$ =Notch depth.
(an accurately machined value)

$$\mathbf{R_n} = 0.5D - a_o$$

$$\beta = \arcsin\left(\frac{h}{R}\right)$$

$$B' = 2R\cos(\beta)$$

(can also measured directly from the surface)

$$\gamma = \arcsin\left(\frac{h}{R_n}\right)$$

$$bn' = R_n\cos(\gamma)$$

$$a_o' = 0.5B' - bn'$$

$$a' = a_o' + \Delta a'$$

$$ba' = 0.5B' - a'$$

$$\omega = \arctan\left(\frac{h}{ba'}\right)$$

$$\mathbf{R_a} = \frac{h}{\sin(\omega)}$$

$$\Delta a = R_n - R_a$$

(radial crack extension from notch)

$$a = a_o + \Delta a$$

(radial crack length)

Appendix E

List of Abbreviations Used in Table 5.2 of chapter 5.

1) a_0 ..... The depth of the machined notch.

2) N_{TMF}..... The number of TMF cycles after which the test was stopped.

3) σ_{max} ..... The maximum stress level that developed during the TMF test.

4) K_{max} ..... The maximum stress intensity range at a crack length of (a_0 + ½ Δa_{avg}).

5) Δa_{avg}..... The average value of all crack extension values measured. (the crack extension Δa is defined as the distance between notch tip and crack tip).
The standard deviation of the averaged value is taken (Δa_{stdev} / $\sqrt{n_{meas}}$)

6) Δa_{Paris} ..... The numerically calculated value of the crack extension using Paris' model with parameters
$C = 9.5 \cdot 10^{-12}$ and $m = 5$. (notch depth a_0 is taken as initial crack length).

7) $\frac{\Delta a_{avg}}{N_{TMF}}$ ..... The crack growth rate, calculated by the secant method as mentioned in Appendix X1.1 of lit. [11] *i.e.* $\left(\frac{da}{dN}\right)_{\bar{a}} = \frac{(a_{i+1} - a_i)}{(N_{i+1} - N_i)}$
In case of the current TMF crack extension measurements
For $(a_{i+1} - a_i)$ the average of all measured crack extensions (Δa_{avg}) per sample is taken.
For $(N_{i+1} - N_i)$ the total number of elapsed TMF cycles (N_{TMF}) is taken.

8) $\left(\frac{da}{dN}\right)_{Paris}$ ..... The calculated crack growth rate according to Paris' crack growth model, using parameters values $C = 9.5 \cdot 10^{-12}$ and $m = 5$.
The value of ΔK is calculated at a crack length a = a_0 + (½·Δa_{avg}), using the value of σ_{max} as stress level, see also 4).

9) n_{meas} ..... The number of crack extension measurements performed on one TMF specimen.
(in some cases a crack could not be distinguished from a graphite particle, and those observations were just omitted from the measurement series).

10) Δa_{min} ..... The minimum and maximum value of all crack extension measurements
11) Δa_{max} ..... performed on one TMF specimen.

12) Δa_{stdev}..... The standard deviation of all crack extension measurements performed on one TMF specimen.

Summary

Cast iron components in combustion engines, such as cylinder blocks and heads of trucks, are exposed for long periods of time to elevated temperatures. Moreover, the engines are started and stopped frequently during their operational life, constituting a large number of heating and cooling cycles. In geometrical complex components the sudden heating (starting the engine) and cooling (stopping the engine) lead to thermal gradients and thermal mismatch within the material, resulting in the local development of high stress levels. The many start-stop operations and their associated alternating stress levels can lead to a localized cracking phenomenon known as Thermo-Mechanical Fatigue (TMF).
Compacted Graphite Iron (CGI) is a common material of choice for diesel engine cylinder heads of heavy trucks and is a type of graphitic cast iron, consisting of vermicular graphite particles embedded in a metal matrix of pearlite. This material provides a suitable combination of thermal and mechanical properties, satisfying the functional requirements of these engine components.
The main aim of this research is to identify and understand the damage micro-mechanisms that control thermo-mechanical fatigue phenomena in cast iron (CGI). The acquired knowledge is of relevance for predicting the lifetime, improving the properties and increasing the reliability of diesel truck cylinder heads.
The work of this study can roughly be categorized into three main subjects: (i) Microstructural evolutions of CGI at elevated temperatures, (ii) TMF crack growth characterization and (iii) precise microstructural analysis of the TMF-crack path.

Microstructural Evolutions of CGI at Elevated Temperatures
In a first series of experiments, time and temperature induced microstructural changes in CGI were characterized, in view of their possible role in the TMF behavior of CGI. During open air annealing of CGI at 420 °C microstructural changes take place in the material, which gave rise to volume expansion and weight increase. The weight increase can be explained by considering the formation of an oxide scale whereas the volume expansion can be attributed to the decomposition of pearlite into ferrite and graphite. It was observed that the atmosphere is of crucial importance in this process. Annealing in an open-air atmosphere produced ten times less volume expansion as compared to annealing in vacuum conditions. Internal oxidation was observed during annealing under atmospheric conditions and the presence of an internal oxidation layer largely inhibited the progress of pearlite decomposition. The observed oxide layers at the internal metal/vapour interface of cavities (left behind by denuded graphite) cause the obstruction of carbon diffusion and thus the suppression of the pearlite decomposition process. In addition it was found that the depth of the oxidized zone near the surface (the oxide penetration depth) was of the same order of magnitude as the eutectic cell size, *i.e.* the volume in which graphite particles are interconnected. This suggests that the interconnectivity of the graphite has a dominant influence on the kinetics of the oxidation process.
The microstructural dependence of tensile and fatigue properties of CGI at room temperature were evaluated by an extended annealing treatment of 720 h at 420 °C. This extended annealing treatment leads to better tensile (increase in yield strength, ductility) and dynamic properties (fatigue lifetime) at room temperature. The variations of mechanical properties were observed

both after annealing under atmospheric and vacuum conditions, but were more pronounced after vacuum annealing. This can be explained by the decomposition of the pearlite phase during annealing and the formation of new ferrite at the graphite/metal interface. It is assumed that the ferrite/graphite interface exhibits a stronger bond than the pearlite/graphite interface. As this stronger bond will be better resistant to delamination, it will strengthen the material both in static and dynamic loading. Such effects were far less pronounced in the open-air annealed material, which could be associated with the fact that it was shown that internal oxidation strongly reduced the kinetics of decomposition.

TMF Crack Growth Characterization

An important part of this study was to measure and analyze the TMF lifetime of CGI. For smooth and notched specimens, the TMF lifetime was measured in TMF tests under total-constraint conditions, with temperatures cycling between 50 °C and 420 °C. By considering the notch depth as the initial crack length, TMF lifetimes were reproduced numerically using the Paris equation for fatigue crack growth ($da/dN = C\,(\Delta K)^m$). The calculated lifetimes were found to be in good agreement with all experimental results, covering a wide range of TMF lifetimes from 30 to 1400 cycles. Also for smooth specimens the Paris model worked well by considering the typical graphite particle size as notch depth. It is one of the main conclusions of this work that graphite particles act as internal notches from which a TMF crack almost immediately starts to grow during the first TMF cycles. Hence, it was established that TMF lifetime in CGI is governed by crack growth and not by crack initiation.

The relevance of the Paris growth law was further confirmed by meticulously measuring the actual crack growth rates for three typical values of the stress intensity factor. The resulting crack growth rates proved to be in reasonable agreement with the predicted values according to the Paris model. It was further shown that the cyclic plasticity of the bulk material, accumulated during TMF cycles, does not have a noticeable effect on TMF lifetime (*i.e.* crack growth rates are not affected).

The notched dog-bone specimen geometry is proposed in this work as a valid alternative for monitoring the TMF behavior of CGI. By applying standard TMF tests with notched specimens, it was possible to significantly reduce both testing time and experimental data scatter, whilst preserving a realistic estimation of the lifetime of the smooth sample.

The effect of prolonged holding times (HT) on TMF lifetime was studied by using notched specimens and a clear effect was observed. Extended holding times were accompanied by an increased relaxation of compressive stresses, causing higher tensile stresses to develop in the subsequent low temperature stages of the TMF cycles. So, extended HTs had an adverse effect on the sample lifetime with a saturating effect for HTs above 1800 s. The Paris fatigue-crack-growth model was used also to estimate the impact of extended HTs. According to the Paris growth law, using a fixed value of tensile stress at low temperature, it was estimated that an increase of holding time from 30 s to 18000 s (5 h) produced a drop of 45% in lifetime. In reality a 60% drop in lifetime was measured, though, which implies that a combined effect of (tensile) stress and microstructural evolution during TMF is responsible for the reduction of lifetime.

Precise Microstructural Analysis of the TMF Crack Path

To the purpose of precise characterization of the complex TMF-crack-path morphology in CGI in relation to local microstructural features and to find out how and by which mechanisms the cracks predominantly develop, 2D and 3D orientation contrast imaging was carried out on wide field sample volumes, covering several mm^3 of imaged material. The data analysis revealed that the crystal planes that are parallel to the (local) crack plane are essentially of a random orientation. Conversely, it was found that graphite particles do not only play a crucial role in the crack initiation, but also are of primary significance for crack propagation. Quantitative analysis of the EBSD data in 2D and 3D showed that the distribution of graphite particles is very important for the crack propagation, as it was revealed that graphite particles enhance crack growth. It was statistically proven that the density of graphite particles in the crack plane is more than double of the density in an arbitrary plane. Our materials knowledge, based on the interpretation of test results in terms of quantifiable microstructural data functions, is of crucial importance to develop a microstructurally based TMF model.

Samenvatting

Gietijzeren onderdelen van verbrandingsmotoren, zoals cilinderblokken en –koppen van vrachtwagens, worden gedurende lange tijd blootgesteld aan hoge temperaturen. Daarnaast worden de motoren in hun levensduur ook vaak gestart en uitgeschakeld, wat gepaard gaat met een groot aantal thermische cycli van het constructiemateriaal. In geometrisch complexe componenten veroorzaken de snelle opwarming (bij het starten van de motor) en afkoeling (na het uitschakelen van de motor) thermische gradiënten en thermische incompatibiliteit, waardoor zich plaatselijk hoge spanningen in het materiaal ontwikkelen. De wisselende spanningsniveaus als gevolg van het starten en stoppen van de motor kunnen lokaal scheurvorming veroorzaken. Dit fenomeen staat bekend als Thermo-Mechanische Vermoeiing (Engelse afkorting: TMF).
Vermiculair gietijzer (Engelse afkorting: CGI) is een veel gebruikt constructiemateriaal voor cilinderkoppen van dieselmotoren. De microstructuur van CGI bestaat uit wormvormige (*c.q.* vermiculaire) grafietdeeltjes die zijn ingebed in een metaalmatrix van perliet. De samenstelling van dit materiaal bevat een geschikte combinatie van thermische en mechanische eigenschappen voor de functionele eisen van voornoemde motoronderdelen.
Het primaire doel van dit onderzoek was het verkrijgen van inzicht in de micromechanismen die verantwoordelijk zijn voor het optreden van thermo-mechanische vermoeiing in vermiculair gietijzer. De verworven kennis is van belang voor het voorspellen van de levensduur, het verbeteren van de eigenschappen en het verhogen van de betrouwbaarheid van de betrokken motoronderdelen.
De werkzaamheden in deze studie kunnen grofweg worden ingedeeld in drie onderwerpen: (i) de verandering van de microstructuur bij verhoogde temperatuur, (ii) karakterisatie van scheurgroei als gevolg van thermo-mechanische vermoeiing en (iii) een nauwgezette analyse van het gevolgde pad van de scheur tijdens thermo-mechanische vermoeiing.

Veranderingen in de microstructuur van CGI bij verhoogde temperatuur
Een eerste reeks experimenten had als doel om microstructurele veranderingen te karakteriseren die optreden als functie van tijd en temperatuur tijdens een gloeibehandeling. Een juist begrip van deze processen is van cruciaal belang gezien hun mogelijke rol in het thermo-mechanisch vermoeiingsgedrag van CGI. Tijdens gloeien onder atmosferische omstandigheden van CGI bij 420 °C vinden microstructurele veranderingen plaats in het materiaal, die aanleiding geven tot gewichtstoename en volumevergroting. De gewichtstoename kan worden verklaard door de vorming van een oxidehuid, terwijl de volumetoename kan worden toegeschreven aan het uiteenvallen van perliet in ferriet en grafiet. Bovendien is geconstateerd dat de omringende atmosfeer van cruciaal belang is bij dit proces. Gloeien in lucht gaf aanleiding tot een tien keer kleinere volume-expansie in vergelijking met gloeien in vacuüm. Bij het gloeien in lucht treedt interne oxidatie op en de aanwezigheid van een interne oxidelaag is grotendeels verantwoordelijk voor het onderdrukken van de perlietontbinding die verantwoordelijk is voor de volume-expansie. De waargenomen oxidelagen in de interne holtes (achtergelaten door verbrand grafiet) aan metaal-luchtgrensvlakken belemmeren koolstofdiffusie van perliet naar grafiet en onderdrukken hierdoor de perlietontbinding.

Bovendien is waargenomen dat de diepte van de geoxideerde zone nabij het oppervlak (oxidatie-indringdiepte) van dezelfde ordegrootte is als de eutectische celgrootte (d.w.z. het volume waarin grafietdeeltjes onderling zijn verbonden). Dit suggereert dat het netwerk van verbonden grafietdeeltjes een doorslaggevende invloed heeft op de kinetiek van het oxidatieproces.
De treksterkte en vermoeiingseigenschappen bij kamertemperatuur, en het mogelijk verloop hiervan als gevolg van veranderingen in de microstructuur van CGI, zijn beoordeeld aan de hand van een uitgebreide gloeibehandeling gedurende 720 uur bij 420 °C. De gloeibehandeling leidt tot betere mechanische eigenschappen (statisch en dynamisch), d.w.z. dat bij kamertemperatuur een toename in treksterkte, vervormbaarheid en vermoeiingslevensduur is waargenomen. De mechanische eigenschappen zijn bepaald, zowel na het uitgloeien onder atmosferische omstandigheden als ook onder vacuüm, maar de variaties waren meer uitgesproken na vacuümgloeien. Dit kan worden verklaard door het uiteenvallen van de perlietfase tijdens het uitgloeien en de vorming van nieuw ferriet aan het grafiet-metaalgrensvlak. Aangenomen wordt dat het ferriet/grafiet-grensvlak een sterkere cohesie bezit dan het perliet/grafiet-grensvlak. Als gevolg van deze sterkere cohesie is het ferriet/grafiet grensvlak beter bestand tegen delaminatie, waardoor het materiaal verstevigt, zowel onder statische als dynamische belasting. Dergelijke effecten waren veel minder uitgesproken in het atmosferisch gegloeide materiaal, wat verklaard kan worden door het feit dat als gevolg van interne oxidatie de kinetiek van perlietontbinding sterk gereduceerd wordt.

Karakterisatie van thermo-mechanische vermoeiingsscheurgroei
Een belangrijk deel van deze studie is gewijd aan het meten van de TMF levensduur van CGI. Voor het bepalen van de TMF-levensduur is gebruik gemaakt van zowel gladde als gekerfde proefstaven. Voor beide typen proefstaven zijn de TMF-proeven uitgevoerd onder een starre inklemming van de proefstaaf, waarna de temperatuur cyclisch wordt gevarieerd tussen 50 °C en 420 °C. Door de kerfdiepte als initiële scheurlengte te beschouwen, blijkt de vermoeiings-scheurgroei gemodelleerd te kunnen worden volgens de scheurgroeiwet van Paris ($\mathrm{d}a/\mathrm{d}N = C(\Delta K)^m$). De aldus berekende levensduur zijn in goede overeenstemming met de experimentele resultaten over een breed bereik in levensduren, variërend van 30 tot 1400 cycli (voor respectievelijk diep en ondiep gekerfde proefstaven). De scheurgroeiwet van Paris blijkt ook te gelden voor gladde proefstaven (d.w.z. ongekerfd), waarbij aangenomen is dat de grootte van de grafietdeeltjes beschouwd mag worden als initiële kerfdiepte. Het is één van de belangrijkste conclusies van deze studie dat grafietdeeltjes fungeren als inwendige kerven van waaruit een TMF scheur bijna onmiddellijk begint te groeien tijdens de eerste TMF cycli. Hieruit kan ook worden afgeleid dat de TMF levensduur in CGI wordt bepaald door scheurgroei en niet door scheurinitiatie.
De geldigheid van de Paris-scheurgroeiwet is bevestigd door een nauwkeurige microscopische meting van werkelijke scheurgroeisnelheden voor drie karakteristieke waarden van de spanningsintensiteitsfactor. De gemeten scheurgroeisnelheden zijn gebleken in redelijke overeenstemming te zijn met de voorspelde waarden volgens het Paris-model. Bovendien is aangetoond dat de cyclische plasticiteit van het bulkmateriaal, opgebouwd tijdens TMF-cycli, geen merkbaar effect heeft op de TMF-levensduur.

In deze studie wordt TMF-beproeving met gebruik van gekerfde proefstaven voorgesteld als een efficiënt alternatief voor de klassieke TMF-beproeving aan gladde proefstaven. De gekerfde proefstaven geven een aanzienlijke verkorting in testduur en verkleinen bovendien de spreiding in meetresultaten (bij duplo-beproevingen). Daarnaast zijn de resultaten van gekerfde proefstaven nog steeds representatief voor de TMF-levensduur van gladde proefstaven.
De invloed van een verlengde wachttijd (in iedere TMF-cyclus) is onderzocht aan gekerfde proefstaven en hierbij is een duidelijk effect op de TMF-levensduur vastgesteld. Gedurende een verlengde expositie van het materiaal (tijdens de hoge-temperatuurfase van een TMF-cyclus) relaxeren opgebouwde drukspanningen zich meer. Paradoxaal genoeg ontstaan hierdoor echter hogere (trek)spanningen in de navolgende lage-temperatuurfase van de TMF-cyclus, met een verkorting van de levensduur als gevolg. Boven een tijdsduur van 1800 s (tijdens de hoge-temperatuurfase) stabiliseert dit effect zich, en neemt de TMF-levensduur niet verder af.
Het Paris-scheurgroeimodel is ook toegepast om het effect van verlengde wachttijden in te schatten, door gebruikmaking van een vaste waarde van de trekspanning in het model (zoals optreedt bij lage temperatuur). Hierbij bleek dat een verlenging in wachttijd (tijdens de hoge-temperatuurfase van de cycli) van 30 s tot 18000 s (5 uur) volgens de berekeningen een daling veroorzaakt van 45% van de TMF levensduur. In werkelijkheid, is echter een daling van 60% gemeten, hetgeen impliceert dat een *gecombineerd* effect van spanning en microstructurele veranderingen verantwoordelijk is voor de vermindering van de levensduur.

*Nauwgezette analyse van het gevolgde pad van de scheur tijdens thermo-mechanische vermoe*iing
Om de complexe morfologie van het TMF-breukvlak te karakteriseren in relatie tot de lokale microstructuur en om de mechanismen van scheurgroei te bestuderen, werden 2D- en 3D-oriëntatie-contrastmetingen uitgevoerd op een relatief groot monstervolume van meerdere mm^3. Uit de data-analyse is gebleken dat de kristalvlakken die lokaal evenwijdig zijn aan het breukvlak in feite een willekeurige oriëntatie vertonen. Het microscopische onderzoek heeft echter aan het licht gebracht dat grafietdeeltjes niet alleen een cruciale rol spelen in de scheurinitiatie, maar ook van essentieel belang zijn voor de scheurgroei. Een statistische analyse van de EBSD-data heeft bevestigd dat de oppervlaktedichtheid van grafietdeeltjes in het scheurvlak meer dan het dubbele bedraagt van de dichtheid in een willekeurig vlak. Onze kennis van het materiaalgedrag, gebaseerd op een kwantitatieve analyse van testresultaten, is van cruciaal belang voor de ontwikkeling van een microstructureel TMF-model.

Publications

- Ghodrat S., Riemslag A.C., Janssen M., Sietsma J. and Kestens L.A.I. Measurement and Characterization of Thermo-Mechanical Fatigue in Compacted Graphite Iron, International Journal of Fatigue 48 (2013) 319–329.

- Ghodrat S., Riemslag A.C., Kestens L.A.I., Petrov R.H., Janssen M. and Sietsma J., Effects of Holding Time on Thermo-Mechanical Fatigue Properties of Compacted Graphite Iron through Tests with Notched Specimens, Metallurgical and Materials Transactions A 44 (2013) 2121-2130.

- Ghodrat S., Janssen M., Kestens L.A.I. and Sietsma J., Microstructural Features of Oxidation Induced Volume Change of Compacted Graphite Iron at Elevated Temperature Annealing, Oxidation of Metals, March 2013, (DOI) 10.1007/s11085-013-9406-y.

- Ghodrat S., Janssen M., Petrov R.H., Kestens L.A.I. and Sietsma J., Microstructural Evolution of Compacted Graphite Iron under Thermo-Mechanical Fatigue Conditions, Published in Advanced Materials Research, 409, 757-762, © (2012) Trans Tech Publications, Switzerland,
DOI: 10.4028/www.scientific.net/AMR.409.757.

- Pirgazi H., Ghodrat S. and Kestens L.A.I., Three-Dimensional EBSD Characterization of Thermo-Mechanical Fatigue Crack Morphology in Compacted Graphite Iron, submitted to Materials Characterization.

- Ghodrat S. and Shabestari S.G., Assessment of Modification and Formation of Intermetalic Compounds in Aluminum Alloy using Thermal Analysis, Materials Science and Engineering A, 467 (2007), PP. 150-158.

Acknowledgment

Notwithstanding the challenging nature of the endeavor, working on this PhD has been a great pleasure for the most part. Not only because it gave me the opportunity to delve deeper into a subject which captured my scientific interest, but also because of all the inspiring people I have met during this journey. They have contributed to this work in many different ways, and I sincerely want to thank them for that. I would like to mention some of them in particular.

First and foremost, I would like to acknowledge my promoters, Prof. Dr. Ir. Leo Kestens and Prof. Dr. Ir. Jilt Sietsma. I was honored and pleased to have worked under their supervision. Their thoughts and comments, stemming from rich experience and vision in research, have inspired me with fruitful ideas and innovative concepts. They taught me that innovation in research comes from within and by continuously challenging and questioning the limits of one's knowledge and understanding. They exemplify the true sense of what it means to be a research scientist. Leo, Jilt, without your guidance my dissertation and ultimately my research would not have been possible!

I would like to thank my supervisor Dr. Ir. Michael Janssen for his guidance, insightful comments and feedback towards my research. I have learnt a lot from his critical questions and comments. He taught me many things and believed in me and my abilities and provided opportunities for me to grow during varying stages of my career. Michael, many thanks!

I would also like to extend my appreciation to Dr. Roumen Petrov for helping me to employing the orientation contract microscopy technique, preparing samples for EBSD measurements, interpreting the results by giving valuable and encouraging comments. Roumen, thank you!

I would like to single out my mentor and friend Dr. Ir. Ton Riemslag. I want to thank him for his continuous support in my Ph.D. research, for mentoring me, for his patience, enthusiasm, and insights in knowledge. A great deal of my dissertation is owed to his guidance. Ton, it was a great pleasure working under your supervision! I also enjoyed early morning coffee at the TMF machine or after running a test, specially the ones that were not easy to run.

I am also grateful to the committee members, Prof. Dr. Ir. Thomas Pardoen, Prof. Dr. Ian Richardson, Dr. Stephan Zaefferer, Dr. Ir. Johan Zijp for their critical comments to this thesis and their willingness to be part of the promotion committee.

This research was carried out under project number MC2.06270b in the framework of the research program of the Dutch Materials innovation institute (M2i). I would like to thank M2i for the financial support for this project. Without the assistance of the entire M2i staff, it would have been all but impossible to solve many of the practical issues faced during my stay in the Netherlands. Special thanks to Monica Reulink, Irina Bruckner, Monika Hoekstra, Gitty Bouman, Marjolein Blankenstein, Margo Poelman, Oscar Ruigrok, Ilona Versteeg and Ciska van 't Hof. Thank you all for your help, support and kindness. Monica, many thanks for everything during these four years also for our unforgettable time we shared in lunches and coffee breaks.

The motivation for this research project was triggered from the challenges faced by the

industry. I was lucky enough to have in-depth input and readily available help from my industrial partner, the Central Lab of N.V. DAF Trucks, Eindhoven, especially Frank Mertens, Nico Kamperman, Paul Steuten and Eric van Velthooven for their contributions and ready provision of material for this research. Special thanks to Frank, who kindly advised and guided me in several meetings and discussions with his valuable feedbacks and comments. Also I would like to extend my appreciation to Marc Walz from Fritz Winter foundry in Germany for providing the materials, taking part in the meetings and sharing the knowledge on cast irons.

I extend my thanks to Eindhoven University of Technology (TU/e), and more specifically to the Mechanics of Materials department for their collaboration on modeling research. Especial thanks to Prof. Dr. Ir. Marc Geers, Dr. Varvara Kouznetsova and Juan Carlos Pina, PhD candidate in the modeling team. I would like to particularly appreciate Prof. Marc Geers, leader of this research group, for his advice and guidance with his deep knowledge on the subject. Marc, your comments and ideas were so important to me and helped me a lot in analyzing the results.

I am indebted to the MTS staff, particularly Jaap Dorsman, Cor Goudriaan and Helmut Schubauer for their cooperation in installing the TMF testing setup for the first time in our Material Science and Engineering (MSE) department, at Delft University of Technology (DUT).

Special thanks to Dr. Xiaomin Wu (Jason) for introducing me to X-ray computed tomography (CT) to the purpose of revealing the fascinating 3D structure of the graphite network. I thank him for all his support during scanning and data analysis. Jason, you were a great help, thanks a lot!

Also my sincere thanks to Wim Verwaal from CITG and Marc van Maris from TU/e for their contributions in CT scanning and measurements.

I am grateful to the timely contributions made by Hans Drop (TUDelft workshop) and the people at DEMO and electrical services, mainly Leon Roessen, for their help in manufacturing specimens for this project.

I also would like to extend my sincere thanks to the laboratory staff: Kees Kwakernaak, Ruud Hendrikx, Niek van der Pers, Hans Hofman, Nico Geerlofs, Frans Bosman and Jurriaan van Slingerland, Freek Brakel and Erik Peekstok[†].

Also thanks to our secretaries of the MSE department: Anneke van Veen, Marian Smit, Olga Wens-van Swol, Annemart Berendse, Linda Ruigrok and Ilse Vercruysse (UGent).

I would like to acknowledge the MSc and BSc students whom I supervised during my PhD: Maureen de Gastines (summer 2010), Marion Cadet (summer 2011), Karel-Alexander Duerloo (September 2010 - January 2011), Ayesha Khan (September 2010 - January 2011), Rogier Sulkers (September 2010 - January 2011), Nils Verkleij (September 2010-August 2011), Yaxun Wu (started February 2013)- supervising you was one of the most rewarding parts of my research.

Thanks to my former officemates Yu Pan, Fengwei Sun and my current officemate, Vera Popovich. I enjoyed their companionship (during long and tough working hours). I extend my thanks to my colleagues and friends: Gozdeh, Farideh, Andrea, Patricia, Masoud, Chuangxin, Abbas, Maryam, Vahid, Mehdi, Muru, Tungky, Alexis, Tuan, Kirk, Maria, Pina, Orlando, Jurij, Edgar, Tricia, Jai, Hemant, Lie, Richard, Lucia, Marcel, Yulia, Yaiza, He, Rangan and Yunhe.

Also thanks to Peyman and Farid for all their help during the thesis submission and the preparation work for the final printing, Peyman, Farid: “Sepase faravan!”.
And of course, Hadi Pirgazi at Ghent University for his great contribution to 3D microscopy analysis and presenting our work in TMS 2013 conference, Hadi: “Kheili mamnoon!”
Pim Kerssemakers, thanks for designing the cover of my thesis, which I find equally informative and attractive.
I was also very fortunate to have the support and inspiration of my four spiritual mentors and friends, my “Gurus” Mehrdad Fadaiee, Jila Toofan, Bella Hakhverdian and Laleh Akbarzadeh who encouraged me a lot on the road to self-awareness and self-empowerment. Amoo Mehrdade mehraboon, khale Jilaye aziz, Bella joon va Laleh nazaninam, your pure and everlasting love and support helped me to overcome the demanding and stressful situations during past four years.
I would like to thank my friends: Farid, Sima, Sepideh & Hamed, Seyran & Nader, Sara & Pooyan, Nasim & Farzad, Mahsa & Dr. Nikookar, Mahshid, Kathy, Berta, Kameila, Negin, Gijsje and all my other friends (here in Delft, Iran and everywhere in the world) who helped me both intellectually and emotionally during past four years, I wish I could list all your names here, but you know that your names are engraved in my heart and I have the blessing of having you any time and anywhere I need, in difficulties and in happiness!
I would love to express my deepest gratitude to my family: my mother Foroogh, my father Alireza and my older brother Mohammad Ali who afforded me an inspiring environment that helped me grow and instilled within me the desire to advance both in knowledge and in contribution towards society. Maman va babaye azizam, despite the physical distance and missing each other, you continued to be present for me and gave me your love and care in every step of my life. I would also like to express my gratitude to my parents-in-law, Ghodsi Mirmoez and Mohammad Maleki: thank you for all your care, concern and encouragement!
And I would like to remember my lovely aunt Farkhondeh, who has always been and still continues being my source of energy. I cannot believe that I have lost her.
Last, but never the least, my husband Ammar, of whom I have had his patience, friendship and understanding in happiness and sorrow. Ammar, your continuous support in pursuing my study is so valuable to me, mamanoon baraye hamechiz!
Thank you all for being with me in this never-ending journey!

Yours,
Sepideh
Delft, 14 May 2013

About the Author

Sepideh Ghodrat was born in March 1978 in Shiraz, Iran. After graduating from secondary school in 1996, she started the bachelor's program in Metallurgy and Material Engineering, Industrial Metallurgy at the University of Tehran. She obtained her B.Sc. degree in September 2000, after which she started her M.Sc in Materials Science and Engineering at Iran University of Science and Technology (IUST). She completed her M.Sc in September 2003 with a thesis on assessment of modification and intermetallic formation of AS5U3G Aluminium alloy by thermal analysis.

She has five years of working experience in the automotive, oil and gas industrial sectors as material specialist and quality engineer in Tehran, Iran.

In February 2009, Sepideh started her doctoral research at the Material innovation institute (M2i), associated with the Materials Science and Engineering (MSE) Department of Delft University of Technology (TU Delft). With the objective to predict the lifetime and increase the reliability of diesel truck cylinder heads she has focused her doctoral research on the study of microstructural damage mechanisms that are responsible for thermo-mechanical fatigue in compacted cast iron, which is the material of choice for such diesels engines.

Since February 2013, Sepideh has started working as a postdoctoral researcher at Delft University of Technology (TU Delft). In her postdoc she will continue and expand the microstructural characterization of thermo-mechanical fatigue crack morphology in compacted graphite iron with the innovative technique of wide-field 3D orientation contrast microscopy.